Growth of hybrid piezoelectric/magnetostrictive systems for magnetic devices based on surface acoustic wave resonators

Vincent Polewczyk

THÈSE

Pour l'obtention du titre de :

Docteur de l'université de Lorraine

Spécialité: *Physique*

Présentée par :

Vincent Polewczyk

Growth of hybrid piezoelectric/magnetostrictive systems for magnetic devices based on surface acoustic wave resonators

Thèse soutenue publiquement le 06 juillet 2018 à Nancy devant le jury composé de :

Mme. Nathalie Viart	Professeur, Université de Strasbourg	Rapporteur
M. Jean Juraszek	Maître de conférences, Université de Rouen	Rapporteur
M. Sergei Zhgoon	Professeur, Moscow Power Engineering Institute	Examinateur
M. Omar Elmazria	Professeur, Université de Lorraine	Examinateur
Mme. Karine Dumesnil	Chargé de recherche, Université de Lorraine	Examinateur
M. Michel Hehn	Professeur, Université de Lorraine	Directeur de thèse

Institut Jean Lamour – UMR 7198 – Département P2M – Equipe 101
Campus Artem – 2 allée André Guinier – 54011 Nancy Cedex
Université de Lorraine – Pôle M4 : matière, matériaux, métallurgie, mécanique

"Notre gibier est une goutte de clarté." – René Char

Acknowledgements/Remerciements

For the acknowledgements, I have decided to write in English the parts relative to non-French speakers and in French for the others. I also want to precise that there is no special order in the acknowledgements.
Pour la partie remerciements, j'ai décidé de rédiger en anglais les parties concernant des personnes ne parlant pas français et en français pour les autres. Je précise qu'il n'y a pas d'ordre spécial dans les remerciements.

Undertaking a PhD could not have been possible without the presence of many people throughout the years as it is more a certain achievement of a part of my life than a three-year challenging experience.

First and foremost, I wish to thank the reading committee members; Nathalie Viart and Jean Juraszek for their time, interest and helpful comments. I would also like to thank the two other members of my oral committee; Omar Elmazria and Sergei Zhgoon for their time and insightful questions.

My sincere thanks also go to my supervisors Karine Dumesnil and Michel Hehn, whose thorough scientific demand prevented me from leaning towards any kind of lazy thinking or lack of rigour. I have been very fortunate to have them as a guiding influence for the past years. The "coupling" occurs and it will be the same for a long time!

I wish to thank my colleagues and collaborators who have constantly stimulated my work and provided help and support in many forms; the best team leader Stéphane Mangin who allowed me to work in his team; Sylvie Robert and Pascal Boulet for the X-ray diffraction measurements; Arnaud Hillion and Ludovic Pasquier for the MBE setup; Laurent Badie, Gwladys Lengaigne and François Montaigne for the clean rooms training; Nicolas Tiercelin, Oliver Bou Matar, Albdelkarim Talbi, Sami Hage-Ali, Hamid M'Jahed for the understanding of SAW devices; Sylvie Migot and Jaafar Ghanbaja for their expertise during TEM measurements; Thomas Hauet, Stéphane Suire and Crosby Soon Chang for the marvelous CC-magnetism. Moreover, Isabelle Fournelle and Christine Sartori for their administrative works but also for being friends of mine. Finally, I am especially grateful to Harshad Mishra for cooperative work and Sébastien Petit-Watelot for any kind of help and more during my Ph.D.

As said, there are many more people who helped me along my way. It begins during my last year of master degree with Hugo, Fahad, Tom, Flo and Sarah. I wish to thank them for their guidance and encouragement through the ups and downs of my life.

Of course this thesis would not be possible without beers, and when I speak about beer, I always think about incredible people who sharing them with me; Christopher, Olivier, Guillaume, Maryam, Danielle, Gauthier, Kosseila, Stéphane, Ludo, Séb and Carlos. Guys, I feel privileged having built such an amazing friendship (and of course, not only due to beers) with you!

Il en est forcément de même pour tous les autres DCCE de l'université. Je suis vraiment heureux de vous avoir rencontré, Hugo, Amaury, Apolline, Max, Bisch.

Next, I would like to express my gratitude to the rest of the laboratory who spiced up my Ph.D; Kathleen, Sebastien, Mohammed, Yassine, Yannis, Cécile, Thibaud, Pierre, Alexandre, Philippe, Daniel, Gregory, Jon, Helene, Marion, Damien, Mathias, Anton, Marwan, Christine and all those I forgot.

Bien sûr, mes pensées vont aussi pour mes colocataires de bureau. Comme je pars bientôt, ils seront heureux de savoir que je cesserai de perturber leurs longues discussions « scientifiques »… ou pas !

Now, a special paragraph must be devoted to a guy, who becomes a huge friend; Charles Guillemard. I cannot summarize our friendship in few sentences but I really want to express my admiration to you. You will definitely be part of my life in the future.

Je suis aussi très reconnaissant envers mes amis hors laboratoire. Que ce soit pour m'avoir supporté, pour m'avoir fait travailler, pour m'avoir changé les idées, pour m'avoir fait faire du sport, pour m'avoir fait…! En soit, il n'est pas nécessaire que je les nomme car ils savent pertinemment que je les aime ! Mais bon, histoire que ce soit gravé dans la roche ; Grivor, Vrat, Moscat', Antho', Hip', Prendesventdenvshreft, Dalouf, Dagz, Dennis, Amélie, Yann, Zoé, Yannis, Tonnon, Ju', Max, Marc, toute la pulp', tous les mougrou mais surtout… l'ODLC!

Et pour finir, le noyau dur, la famille; Véronique Ricardi, Françis Polewczyk, Louise Polewczyk, Monique Ricardi and Franck "Sauveur" Polewczyk. Je tiens profondément à vous remercier de m'avoir toujours soutenu dans mes décisions et surtout de m'avoir transmis une légèreté d'esprit qui m'a permis d'affronter toutes les épreuves de la thèse. Il en est de même pour ma copine, qui a toujours su être patiente, encourageante et dévouée; Barbara Rubino. Tu as tant contribué à mon épanuissement ces dernières années, par ta sagesse, ton courage et ton intelligence. Sache que je t'aime du plus profond de mon cœur.

Je tiens finalement à rajouter une dernière phrase concernant mon pot. Encore une fois, ma famille, ma copine et ses amis ont su rendre ce moment unique. Je ne me suis occupé de rien, mais vous vous êtes occupés de tout. Cela n'a pas de prix et je vous en remercie.

List of abbreviations and terms

AFM	Atomic-Force Microscopy
AR	Asymmetrical Reflections
BAW	Bulk Acoustic Wave
EA	Easy Axis
FWHM	Full Width at Half Maximum
HA	Hard Axis
IDT	InterDigital Transducer
IP	In-Plane
KS	Kurdjumov-Sachs
LNO	Lithium NiObate ($LiNbO_3$)
M	Magnetization
M_s	Magnetization at saturation
MBAW	Magnetic Bulk Acoustic Wave
MBE	Molecular Beam Epitaxy
MFM	Magnetic-Force Microscopy
MSAW	Magnetic Surface Acoustic Wave
MR	Metallization Ratio
NW	Nishiyama-Wassermann
OOP	Out Of Plane
OR	Orientation Relationships
QSHSAW	Quasi Shear Horizontal Surface Acoustic Wave
QSVSAW	Quasi Shear Vertical Surface Acoustic Wave
RE	Rare Earth
RF	Radio Frequency
RHEED	Reflection High-Energy Electrons Diffraction
RW	Rayleigh Wave
SAW	Surface Acoustic Wave
SIMS	Secondary Ion Mass Spectroscopy
T_C	Curie temperature
T_N	Néel temperature
UHV	Ultra High Vacuum

Contents

Introduction

A ferroic order implies that a material has a spontaneous long range alignment of some microscopic property, leading to a macroscopic spontaneous property, named the order parameter. A necessary property of ferroic materials is that a suitable external field is able to switch the direction of the order parameter. Another important characteristic of ferroic materials is the existence of the spontaneous macroscopic property in the absence of any external field. In ferroelastic materials, the microscopic property is the unit cell deformation and the macroscopic property is called mechanical strain (ε). An external stress field (σ) can modify the strain direction. In ferroelectrics, the gravity center of the positive charges does not coincide with that of the negative charges and leads to the existence of a permanent dipole moment in a unit cell, which in turn produces a macroscopic electrical polarization (P). An external electric field (E) can alter the polarization direction. Electronic spins carry the microscopic magnetic moment in ferromagnets and produce a macroscopic magnetization (M) that can be switched by a magnetic field (H). Ferroelastic, ferroelectric and ferromagnetic display hysteresis phenomena that disappear above a temperature called Curie temperature.

In favorable cases, ferroic order parameters can be coupled to each other, which leads to additional functionalities (Figure 1). The link between an applied stress and the polarization for instance is called piezoelectricity. Piezoelectricity describes a change in polarization as a linear function of applied stress (piezoelectric effect), or a strain that occurs as a linear function of applied electric field (inverse piezoelectric effect). This effect occurs only in a particular class of dielectrics (non centro-symmetric crystals). A quadratic effect can also link the polarization and stress or the electric field and strain: the electrostriction. Some materials, such as the ferroelectrics, can exhibit both piezoelectricity and electrostriction. Electrostriction occurs in all dielectric materials (regardless of crystal symmetry), but the electrostrictive strains being much smaller than the piezoelectric ones, the materials are simply refered as piezoelectric.
Magnetostriction and piezomagnetism are the magnetic equivalent of electrostriction and piezoelectricity, but for stress and magnetization. The first effect corresponds to the occurence of a strain independent of the sign of the applied magnetic field (quadratic effect), while some non centro-symmetric crystals may exhibit piezomagnetism. Nevertheless, piezomagnetism is seldomly encountered because both adequate crystallographic symmetry conditions and magnetic symmetry conditions must be met, which is rarely the case. Piezomagnetism is usually produced when the applied stress changes the magnetic symmetry of an antiferromagnetic crystal in such a way that a weak ferromagnetism arises.
Finally, the link between (H,M) and (E,P) is the so-called magnetoelectric coupling. This one is particularly attractive and arouses a strong interest since it lets envision the electric field-controlled magnetic data storage.

Multiple ferroïc orders/properties can coexist in a single phase material, which is the so-called intrinsic multiferroism. The materials combining coupled ferroelectric and magnetic orders are however relatively rare. They are classified into two families. Type I multiferroics are compounds where the phase transitions of the ferroic orders are distinct; ferroelectricity and magnetism are independent in origin, as for example in the antiferromagnetic/ferroelectric perovskite compound $BiFeO_3$ [WAN03]. Type II multiferroics are compounds in which the phase transitions of the different ferro-orders appear at the same temperature because one causes the other, *i.e.* magnetism causes ferroelectricity or ferroelectricity results in magnetism. In these materials, the magnetoelectric coupling is strong but the polarization (magnetization) induced by the magnetic (electric) order is generally weak. These compounds are very rare but we can cite the antiferromagnetic/ferroelectric perovskite compound $TbMnO_3$ [KIM03]. Rarity arises from the fact that the ferromagnetism requires an invariance of space symmetry as well as a break of time symmetry, while the ferroelectricity requires an invariance of time

symmetry as well as a break of space symmetry. Another point is that most ferromagnetic compounds are metallic, whereas a ferroelectric compound must be insulating [HIL00, HIL02].

Hybrid systems whose ferromagnetic and ferroelectric properties would result from independent sub-networks are therefore developed, for example by alternating a ferromagnetic compound and a ferroelectric compound in multilayer or nanocomposite stack. These materials are called hybrid multiferroics. The main issue in that case is to achieve a reasonable coupling between electric and magnetic order parameters.
The coupling can first occur via an *electric field effect*. It was thus proved that the variation of polarization could possibly influence the magnetic properties of the ferromagnetic material (anisotropy, magnetic order…). Vaz *et al.* [VAZ10] for example shows that the LSMO magnetization at the LSMO/PZT interface depends on the orientation of the PZT polarization, through the modulation of the charge-carrier density.
Another way to induce a coupling between electric and magnetic order parameters is to use an indirect path *via the lattice strains*, in taking advantage of both piezoelectric and magnetostrictive properties. The electrostatic potential generates a strain in the piezoelectric layer that can be elastically transferred to the magnetostrictive layer and influence the magnetic properties. Such hybrid systems could be used in magnetic logic and memory. Based on such a coupling mechanism, it was theoretically predicted that the magnetization of an anisotropic piezoelectric/ferromagnetic multiferroic nanomagnet can be switched by 180° with a small voltage applied to the piezoelectric layer [BIS14].
The coupling between magnetic and piezoelectric properties via lattice strains and magnetoelastic effects is also largely used in the so-called Magnetic Surface Accoustic Wave (MSAW) devices, where dynamical contributions have to be considered. Surface Acoustic Waves (SAW) generated by inverse piezoelectric effect can directly act on spin waves via an effective dynamical magnetoelastic field, and elastically drive magnetization dynamics and magnetic resonance, as it has been shown by several authors [THE14, WEI11]. Reciprocally, the static magnetization configuration and the induced magnetization dynamics modify the SAW characteristics, which can be exploited to develop magnetic field sensors [KAD11, ELH16]. This PhD work being mainly focused on MSAW devices, these specific aspects and physical mechanims will be detailed in the core of the manuscript.

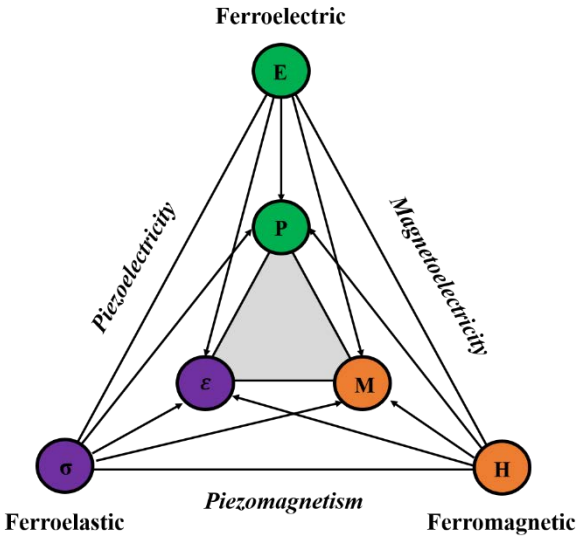

Figure 1. Scheme of different ferroics and multiferroics (ferromagnetic / ferroelectric / ferroelastic) [inspired by SPA05].

In the general context described above, the first aim of this work is to synthetize hybrid systems combining magnetostrictive and piezoelectric materials, with the specificity to investigate the possible growth of a strongly magnetostrictive materials ($TbFe_2$ [CLA80]) in crystalline/single crystalline form on a $LiNbO_3$ piezoelectric substrate (common and efficient for SAW applications). The combination of high magnetostriction and epitaxial growth could let expect a large coupling between the two

components and a good sensitivity of the device to an external field. Other magnetic materials are also used as simple reference examples or for specific purposes. The objective is then to pattern magnetic surface acoustic wave devices in a resonator geometry and to perform a carefull investigation of the MSAW response (different types of SAW) under field in various devices (different wavelength, wave propagation directions...) in close connection with the magnetic properties. The choise is to focus on the incidence of the external magnetic field on the SAW characteristics and to explore several aspects of interest for the possible development of sensors.

This document is divided into three main parts.
The first part concerns the general properties of the different materials involved in the hybrid systems: the ferroelectric/piezoelectric properties of Lithium Niobate that is used as a substrate, and the magnetic and magnetostrictive properties of the materials chosen as magnetic component, in particular $TbFe_2$. The main energy terms are described in details and a specific paragraph is devoted to magnetic thin films in which supplementary energetic contributions have to be taken into account.

The second part covers the various growth steps to get piezoelectric/magnetostrictive systems.
Since one objective of this work is to grow crystalline $TbFe_2$ on different cuts of Lithium Niobate, a first chapter recalls the main studies dealing with the $TbFe_2$ epitaxial growth, first on sapphire substrates and then on $LiNbO_3$ (Z-cut) substrates.
The second chapter presents in some details the various LNO substrates that have been used throughout this study. It is namely important for the following of this part to have a clear idea of the structural characteristics of the different LNO cuts (Z-, 128Y- and 41Y- cuts).
The following chapters concern the MBE growth of $TbFe_2$ on LNO Z (chapter 3) and LNO 128Y and 41Y (chapter 4). Detailed informations are given on both the buffer layers' growth and on the $TbFe_2$ growth. Those are obtained from the combined Reflection High-Energy Electrons Diffraction (RHEED) and X-ray diffraction analysis. Magnetic characterization of these films are also given for different directions of the applied magnetic field, mainly to analyse the magnetic anisotropy in these systems.
The last chapter (chapter 5) gathers the results concerning the structural and magnetic properties of the Ni films (sputtered on the three different LNO cuts) and of the [Co/IrMn] multilayers (sputtered on LNO 41Y).

The third part reports on the magnetic surface acoustic waves devices patterned from the hybrid stacks presented previously.
The first chapter gives a general introduction to acoustic waves and surface acoustic wave devices, presenting the two main geometries (delay line and resonator) and the specific case of magnetic devices. A paragraph is devoted to the previous studies performed on MSAW devices, in order to explain the underlying physical phenomena and to highlight the two main research directions in the field, *i.e.* the development of magnetic field sensors and the elastic/accoustic manipulation of magnetization and magnetization dynamics. This permits to position our objective in this topic.
The chapter 2 describes the nano-fabrication steps, the first basic characterizations of the patterned resonator devices and the configurations in which the measurements under field are systematically performed. The chapter 3 is essentially devoted to the results obtained on the 50 nm thick Nickel-based devices patterned on various LNO cuts. The magneto accoustic responses (frequency variations versus field) are explored for different types of SAW and different directions of the applied magnetic field first in the case of devices on LNO 41Y. A piezomagnetic equivalent model is used to understand the role of the magnetic anisotropy in the in-plane magneto acoustic responses. Complementary results are then provided for devices on LNO 41Y with a different wavelength or wave propagation direction and for devices on LNO 128Y. A wireless remote experiment is finally presented.
The chapter 4 presents how the MSAW responses can be designed and controled in tailoring the IDT magnetic properties. The shape anisotropy is a first lever of interest in the resonator geometry. The specific choice and design of the magnetic component in the hybrid system can be also exploited according to the required MSAW behavior: for example for the development of high field or out-of-plane magnetic field.

The last chapter (chapter 5) gathers supplementary results for devices in non-conventionnal geometries: 200 nm thick Nickel-based devices, where the easy magnetization axis is perpendicular to the SAW propagation plane with strong stripes domains configurations, and SAW devices (both magnetic and non-magnetic), where a strong and isotropic field sensitivity has been observed for a Bulk Accoustic Wave (BAW).

References

[BIS14] A. K. Biswas, S. Bandyopadhyay and J. Atulashimha, *Complete magnetization reversal in a magnetostrictive nanomagnet with voltage generated stress: A reliable energy-efficient non-volatile magneto-elastic memory*, Appl. Phys. Lett. **105**, 072408, (2014).
[CHO12] R. V. Chopdekar, V. M. Malik, A. F. Rodriguez, Y. Takamura, A. Scholl, D. Stender, C. W. Schneider, C. Bernhard, F. Nolting and L. J. Heyderman, *Spatially resolved strain-imprinted magnetic states in an artificial multiferroic*, Phys. Rev. B. **86**, 014408, (2012).
[CLA80] A. E. Clark, *Magnetostrictive RFe2 intermetallic compounds*, Chap. 15, in Handbook on the physics and chemistry of rare earths, North Holland Publishing Company, (1980).
[ELH16] M. Elhosni, O. Elmazria, S. Petit-Watelot, L. Bouvot, S. Zhgoon, A. Talbi, M. Hehn, K. Ait Aissa, S. Hage-Ali, D. Lacour, F. Sarry and O. Boumatar, *Magnetic field SAW sensors based on magnetostrictive-piezoelectric layered structures: FEM modeling and experimental validation,* Sensors and Actuators A: Physical**. 240**, 41-49, (2016).
[HIL00] N. A. Hill, *Why are there so few magnetic ferroelectrics?,* J. of Phys. Chem. B**. 104**, 6697-6709, (2000).
[HIL02] N. A. Hill and A. Filippeti, *Why are there any magnetic ferroelectrics?*, J. Mag. and Magn. Mat**. 242**, 976-979, (2002).
[KAD11] M. Kadota, S. Ito, Y. Ito, T. Hada and K. Okaguchi, *Magnetic Sensor Based on Surface Acoustic Wave Resonators,* Jap. J. of Appl. Phys**. 50**, 07HD07, (2011).
[KIM03] T. Kimura, T. Goto, H. Shintani, K. Ishizaka, T. Arima and Y. Tokura, *Magnetic control of ferroelectric polarization*, Nature. **426**, 55-58, (2003).
[SPA05] N. A. Spaldin and M. Fiebig, *The renaissance of magnetoelectric multiferroics*, Science**. 309**, 391-392, (2005).
[THE14] L. Thevenard, C. Gourdon, J. Y. Prieur, H. J. Von Bardeleben, S. Vincent, L. Becerra, L. Largeau and J. Y. Duquesne, *Surface acoustic wave driven ferromagnetic resonance in (Ga,Mn)(As,P) epilayers*, arXiv. 1406, (2014).
[VAZ10] C. A. F. Vaz, J. Hoffman, Y. Segal, J. W. Reiner, R. D. Grober, Z. Zhang, C. H. Ahn and F. J. Walker, *Origin of the magnetoelectric coupling effect in* $Pb(Zr_{0.2}Ti_{0.8})O_3/La_{0.8}Sr_{0.2}MnO_3$ *multiferroic heterostructures,* Phys. Rev. Lett**. 104**, 127202, (2010).
[WAN03] J. Wang, J. B. Neaton, H. Zheng, V. Nagarajan, S. B. Ogale, B. Liu, D. Viehland, V. Vaithyanathan, D. G. Schlom, U. V. Waghmare, N. A. Spaldin, K. M. Rabe, M. Wuttig and R. Ramesh, *Epitaxial* $BiFeO_3$ *multiferroic thin film heterostructures*, Science**. 299**, 1719-1722, (2003).
[WEI11] M. Weiler, L. Dreher, C. Heeg, H. Huebl, R. Gross, M. S. Brandt and S. T. B. Goennenwein, *Elastically driven ferromagnetic resonance in Nickel thin films*, Phys. Rev. Lett. **106**, 117601, (2011).

First part: Ferroelectric/piezoelectric and ferromagnetic materials towards the development of hybrid multiferroics

This chapter gives some general informations on the physical processes underlying the properties of the ferroic materials combined in hybrid multiferroics, *i.e.* ferroelectric/piezoelectric and ferromagnetic materials in our case. The chapter 1 is devoted to ferroelectric/piezoelectric materials and their properties. The piezoelectricity, which is taken advantage of into strain mediated hybrid multiferroics is especially emphasized, with specific details on $LiNbO_3$. The chapter 2 gathers important informations on magnetic materials: the origin of magnetism in rare earth element and transition metals, the different energy contributions governing their magnetic properties, as well as the main effects to be considered in the case of a magnetic thin film. A specific paragraph deals with magnetostriction, another key ingredient in strain-mediated hybrid multiferroics.

Chapter 1: Ferroelectric/piezoelectric materials

A ferroelectric material is characterized by the occurrence of a spontaneous polarization in absence of an electric field, below a critical temperature, called Curie temperature (Tc). An external electric field can reverse the polarization and the behavior under electric field is generally described by a so-called hysteresis loop. Above the Curie temperature, the ferroelectric material enters a paraelectric phase in which it no longer possesses a spontaneous polarization. In most cases, the transition between these two states is related to a structural transition from a non-centrosymmetric to a centrosymmetric structure.
Considering the 32 classes of symmetry in crystals (Figure 2), ferroelectric materials belong to the non-centrosymmetric ones and are also pyroelectric and piezoelectric. Pyroelectricity is the variation of a spontaneous polarization by a change of temperature while piezoelectricity refers to the apparition of an induced polarization and the accumulation of electric charges under the application of an external mechanical stress. Since this piezoelectric character is one of the key ingredients for the development of strain-mediated hybrid multiferroics, the following paragraph mainly focus on piezoelectric materials and especially $LiNbO_3$.

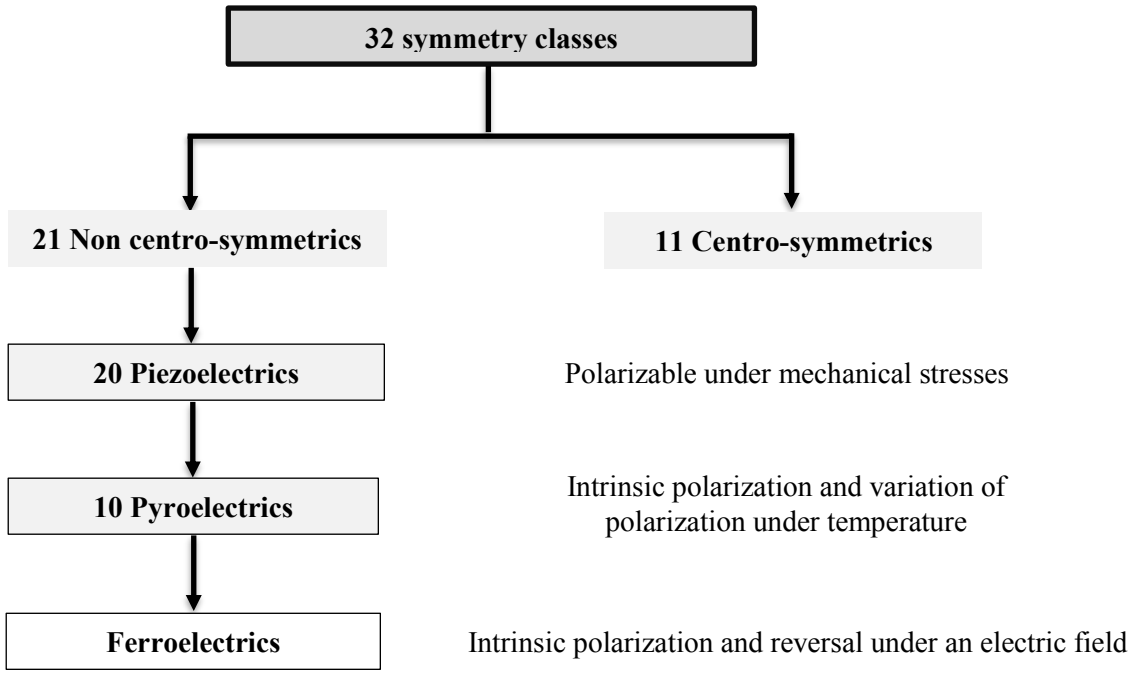

Figure 2. Classification of crystals showing the classes with piezoelectric, pyroelectric and ferroelectric effects. Ferroelectricity is a subgroup of the 10 pyroelectric classes.

1. Different piezoelectric materials

The piezoelectric effect is generally described as a linear electromechanical interaction between the mechanical and the electrical states in materials with no inversion symmetry. Four main classes of materials exhibit piezoelectric behavior: crystals, ceramics, polymers and composites.

1.1. Crystals

An external mechanical stress causes strain in the crystal structure and thus relative displacements of the electric charges of the ions. These displacements give rise to a polarization in the material. Without external stress, gravity centers of positive and negative charges are at the same position, which means no polarization. Quartz was one of the first piezoelectric crystal commercialy used. Nevertheless, quartz properties are unattractive for transducer applications: its acoustic impedance is relatively high and its electromechanical coupling factor, characterizing the ability to convert the electric energy into mechanical energy and reciprocally, is very small. Other crystals, such as Lithium Niobate ($LiNbO_3$) or Lithium Tantalate ($LiTaO_3$) exhibit similar acoustic impedance but much higher electromechanical coupling.

1.2. Ceramics

Piezoelectric ceramics are polycrystals that are produced by sintering a mixture of oxides and their composition can be modulated during manufacturing process in order to adjust their dielectric, mechanical and piezoelectric properties. These ceramics exhibit high electromechanical coupling but also huge acoustic impedance. However, they are generally used because of their relatively low cost, they are easy to transform and they offer a very wide range of performances due to the existence of many different compositions with specific properties for peculiar applications. For instance, the most widely used is Barium Titanates (BTO) which exists for five to six different compositions.

1.3. Polymers

Some polymers such as PVDF (PolyVynilDiFluoride) also possess piezoelectric properties. The elementary (monomer) unit which constitutes the material is repeated according to formula (CH_2CF_2), with the Fluorine and Hydrogen atoms constituting an electrostatic dipole. On the same chain, the directions of these dipoles vary and they are oriented in all directions. The individual dipole contributions compensate each other and there is no polarization. A remanent polarization can be achieved by aligning the chains of molecules with a stress in applying an intense electric field at high temperature. Compared to ceramics and crystals, PVDF is much more flexible, lightweight, and supports larger strains. The flexibility of the film gives good properties to electronic devices. On the other hand, the electromechanical coupling factor is lower than that observed in other materials and it stiffness makes it difficult to adapt acoustic impedance with rigid structures.

1.4. Composites compounds

In order to get rid of various problems inherent to ceramics (fragility and stiffness), many works are currently done in order to combine ceramic piezoelectric fibers (the quality of manufacture and the lifetime of the ceramic is much better in this form) to an array of suitable electrodes (*i.e.,* orthogonal to the fibers). The whole is embedded in an epoxy matrix, which protects and ensures the mechanics of the assembly. By choosing the shape of the electrodes, it is possible to obtain a polarization of the material allowing good electromechanical coupling. The idea is to get a polarization in the direction of the fibers. Composites have shown their interest with respect to conventional ceramics in the field of high-frequency acoustic transducers for imaging. Their better electromechanical coupling factor and their more suitable acoustic impedance make it possible to improve the resolution of the images [LEE14].

2. Lithium Niobate

Lithium Niobate ($LiNbO_3$, LNO or often called LN) is a well-known ferroelectric material, intensively studied and applied in technology [KAL02, HAU09, HAU11, LI08] since it was synthesized in 1965 by Fedulov [FED65] in the USSR and by Ballman [BAL65] in the USA.

2.1. Crystallographic structure

$LiNbO_3$ is chemically stable in its crystalline state and belongs, as Lithium Tantalate ($LiTaO_3$), to the ABO_3-type ferroelectrics. This material has a trigonal crystal structure, which may be represented by a rhombohedral or by an hexagonal unit cell. Our choice was to use the hexagonal unit cell of $LiNbO_3$ (Figure 3). It possesses six formula units (30 atoms) in its unit cell.

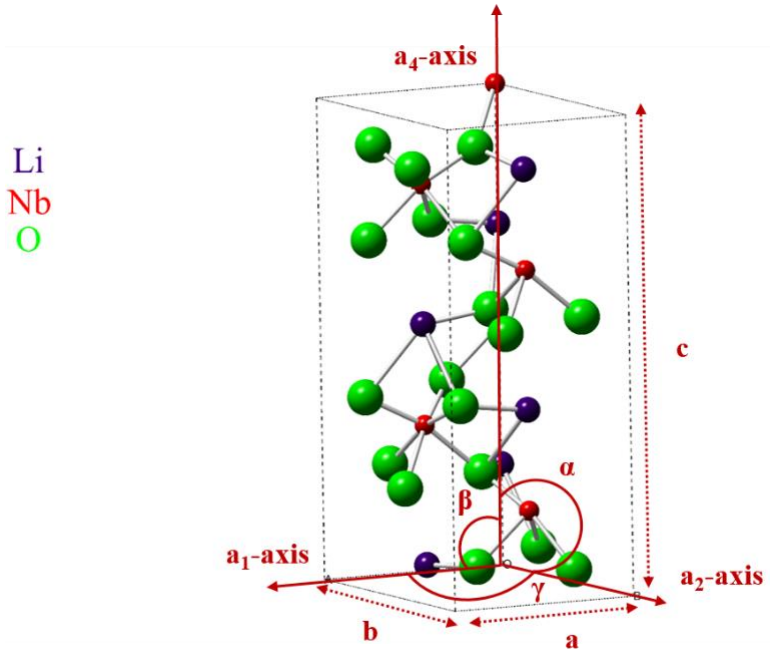

Figure 3. Hexagonal unit cell of $LiNbO_3$ in the ferroelectric. α is the angle between a_2 and a_4-axis, β is the angle between a_1 and a_4-axis, and γ is the angle between a_1 and a_2-axis. The size ratio between the different ions are obtained from their ionic radii values [SHA76].

In this convention, a = b = 0.5149 nm and c = 1.386 nm with $\alpha = \beta = 90°$ and $\gamma = 120°$. In the hexagonal coordinate system, the a_1-axis and a_4-axis corresponds to $< 11\bar{2}0 >$ and $< 0001 >$ crystallographic directions respectively.

The structure consists of planar sheets of Oxygen atoms in a distorted hexagonal close-packed configuration and perpendicular to the a_4-axis. A significant difference is however observed between the structures above and below the ferroelectric Curie temperature (≈ 1200 °C varying with composition (Figure 4). In the paraelectric phase (above T_C), the Lithium ions are located in the Oxygen planes and the Niobium ions are located between the Oxygen planes. This centrosymmetric structure belongs to the trigonal space group $R\bar{3}c$ with point group $\bar{3}m$. In the ferroelectric phase (below T_C and thus at RT), the elastic forces force the Li and Nb ions into new positions relative to the Oxygen planes; they move from the median planes defined by the Oxygen ions, producing a charge separation and consequently a spontaneous polarization along the a_4-axis. The distorted octahedral interstices formed in this structure are one third filled by Lithium ion, one-third filled by Niobium ion, and one-third vacant. This non-centrosymmetric structure belongs to the trigonal space group $R3c$ with point group $3m$.

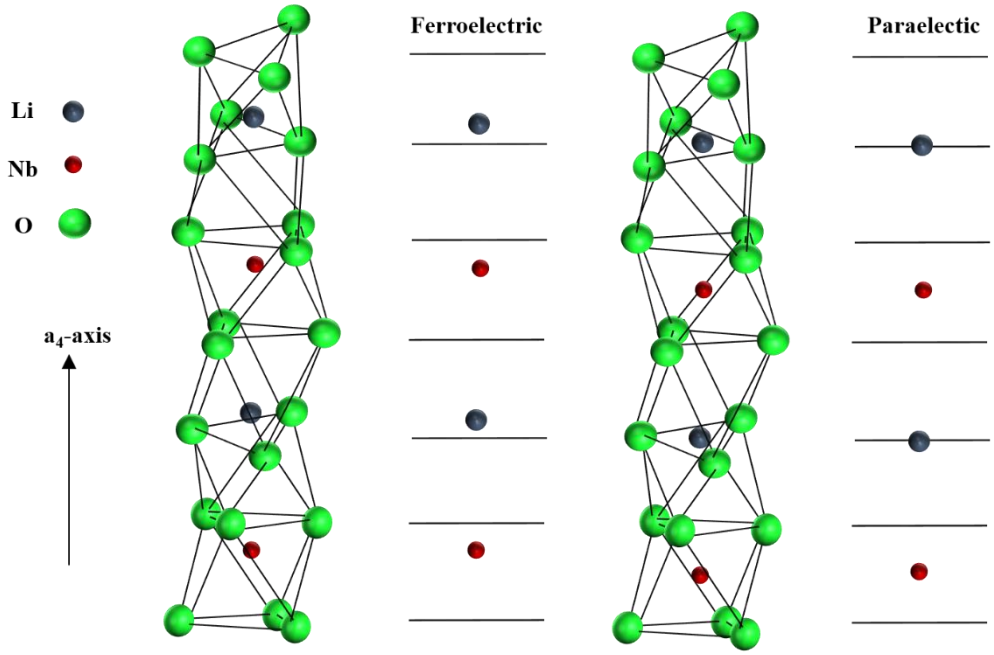

Figure 4. $LiNbO_3$ structure along a_4-direction in the ferroelectric phase (T<Tc) and in the paraelectric phase (T>Tc). The size ratio between the different ions are obtained from their ionic radii values [SHA76].

2.2. Growth of Lithium Niobate crystals

Lithium Niobate crystals have a strong tendency to non-stoichiometry and their actual composition presents a deficit of Lithium which is at the origin of the presence of intrinsic defects in the crystal lattice (these defects can be atom vacancies or excess atoms placed outside of normal lattice positions). This can be explained by the fact that the Lithium ion bonds have a more ionic character than the Niobium ion bonds, which are essentially covalent. The Li^+ ions are therefore less bound to the crystal than the Nb^{5+} ions. Lithium ions can migrate more easily during crystal growth, resulting in a deficit of Lithium in the synthesized crystal [MIG10].
Thus, depending on the manufacture process, different LNO compositions can be obtained, the so-called congruent and stoichiometric LNO that may exhibit significantly different properties. In both cases, the growth of LNO crystals is achieved at a temperature above its Curie temperature (between 1130 °C and 1250 °C depending on the pressure) for which the crystal is in its paraelectric phase.

Congruent LNO
LNO crystals are mainly produced using Czochralski method. The method consists of direct solidification from a small monocrystalline germ. The molten material is at a temperature just above the congruent melting point, with a controlled temperature gradient. At the congruent melting point, composition of the liquid is the same as the composition of the solid. The germ is placed in a "shuttle" suspended above the liquid by a stem. The liquid solidifies, keeping the same crystalline organization as the germ is pulled upwards while rotating (at very slow speed).
The operation takes place under a neutral atmosphere in order to avoid oxidation [BAL65]. Oxygen comes from the material and not from the atmosphere. In fact, a melt containing 48.5 mol % of Li_2O and 51.5 mol % of Nb_2O_5, is used to grow congruent LNO single crystals (Figure 5). The ratio of the concentration (in mol %) of the cations [Li] and [Nb] determines the composition of the resulting crystal. Ratio obtained is R = [Li] / [Nb] ≈ 0.969. Another option to describe the composition is to calculate the Li content by the formula C = [Li] / [Li] + [Nb] ≈ 0.485 (see Figure 5).

Stoichiometric LNO

A more sophisticated technique, namely the double-crucible Czochralski method, is used to grow near-stoichiometric single crystals with a ratio C ≈ 0.498 (Figure 5). In this technique, another crucible containing Lithium is used to diffuse into the crystal during the process at the congruent melting point. The number of intrinsic defects is much smaller in these crystals compared to congruent LNO with a Li deficit and, as mentioned previously, this has a significant impact on various properties.

For instance, the permittivity coefficients change from κ_{33} = 28.7 F.m^{-1} in congruent LNO to 41.7 F.m^{-1} in stoichiometric LNO [NIK05]. Another example is the magnitude of the coercive field (Ec). Congruent LNO coercive field is approximately 210 kV.cm^{-1} while it is reduced to approximatively 40 kV.cm^{-1} at room temperature for stoichiometric LNO [KIM02]. This difference is attributed to the role of defects on domain walls pinning [AGR06].

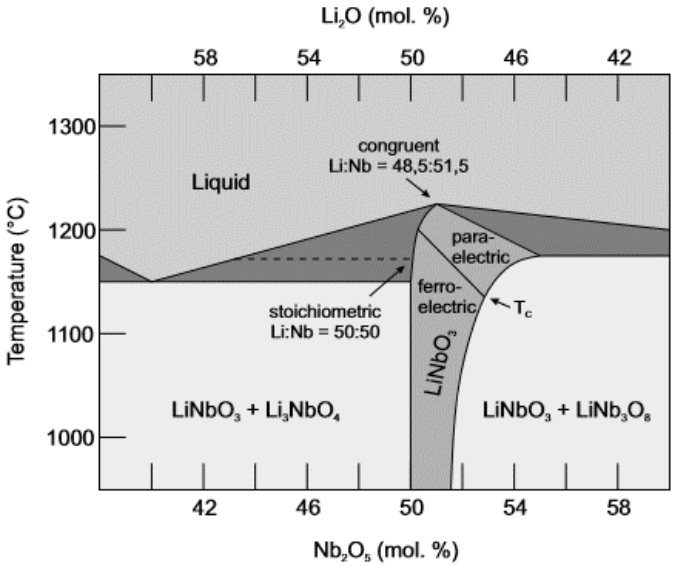

Figure 5. Phase diagram of the Li_2O-Nb_2O_5 system at atmospheric pressure.

2.3. Lithium Niobate properties through some important effects

Instead of using the hexagonal coordinate system, an orthogonal basis as sketched in Figure 6 is used to describe following properties. The X-axis is set parallel to a_1, the Z-axis is set parallel to a_4 and the Y-axis is defined with respect to the right hand rule.

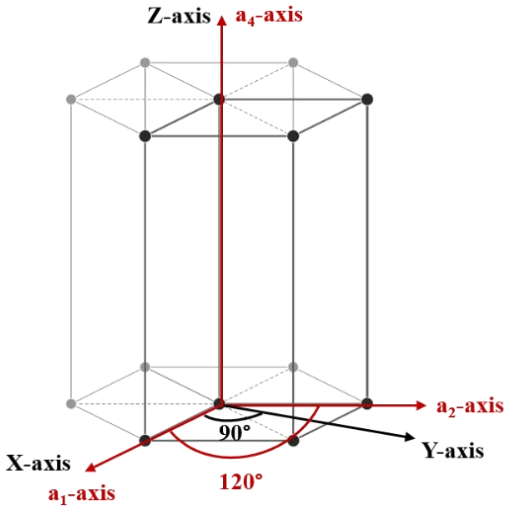

Figure 6. Hexagonal (red) and orthogonal (black) bases.

Since the Lithium Niobate crystal possesses 3m point group symmetry below the Curie temperature, any tensor describing its physical properties must have at least this symmetry, as asserted by Neumann in 1833 [NYE57].
By convention, each physical constant of these tensors has two subscripts. The first and the second indicate respectively the direction of the applied force and the direction perpendicular to the applied force. The two subscripts are expressed in the orthornomal basis (X,Y,Z). Directions X, Y and Z correspond to the subscript 1, 2 and 3 respectively. Shear about one of these axes is represented by the subscript 4, 5 and 6 respectively.

2.3.1. Pyroelectricity

The relation between the change in spontaneous electric polarization ($\Delta\vec{P}$) and the change in temperature ($\Delta\vec{T}$) is given by:

$$\Delta\vec{P} = \bar{p}\Delta\vec{T}$$

where $\bar{p}$ is the first-rank pyroelectric tensor.
Since Li and Nb ions can only move along the Z-axis, the pyroelectric tensor has only one non-zero component:

$$p_i = \begin{bmatrix} 0 \\ 0 \\ p_3 \end{bmatrix}$$

where p_3=-6.8×10^{-3} μC.K^{-1}.cm^{-2} in congruent LNO [SEI11]. The negative value indicates that the magnitude of spontaneous polarization decreases with heating the crystal.

2.3.2. Piezoelectricity

We will introduce here the equations that describe the electromechanical properties of piezoelectric materials, based on the IEEE standard of piezoelectricity [IEE87].

The quantities playing a role in the piezoelectric effect are:
(i) The stress tensor $\bar{\bar{\sigma}}$ of order 2 (components σ_{ij}), expressed in N.m^{-2} (or Pa). The stress tensor can be represented by a 3x3 matrix:

$$\sigma_{ij} = \begin{bmatrix} \sigma_{11} & \sigma_{12} & \sigma_{13} \\ \sigma_{21} & \sigma_{22} & \sigma_{23} \\ \sigma_{31} & \sigma_{32} & \sigma_{33} \end{bmatrix}$$

σ_{ij} is defined as the stress component on the face with normal i and acting in the direction j. It must be noticed that in some studies, this definition could be reversed. The stress tensor includes both the normal and shear stresses acting on the material. There are three normal stresses ($i = j$), related to tensile or compressive forces and six shear stresses ($i \neq j$).
(ii) The strain tensor $\bar{\bar{\varepsilon}}$ of order 2, with dimensionless components ε_{ij}. Strain is related to change in dimensions and shape of a material. When a material is stretched, the change in length and the strain are positive. When it is compressed, the change in length and strain are negative. This definition refers to normal strains that change the dimensions of a material but not its shape, *i.e.* angles do not change. The strains involving angles' changes (but no length) are known as shear strains. A sketch of normal and shear strains is given in Figure 7.

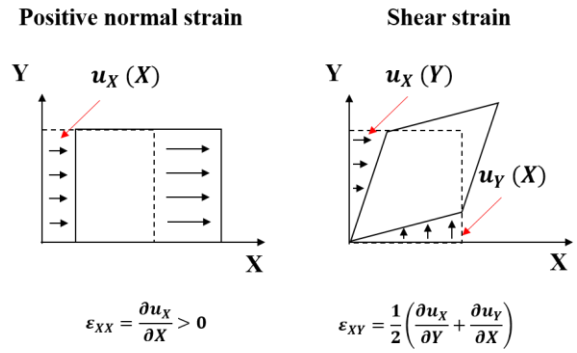

Figure 7. Positive normal and shear strains applied on a 2D body. Black thin arrows represent the displacement u.

(iii) The electric displacement field $\vec{D}$ with components D_i expressed in C.m^{-2}.
(iv) The electric field $\vec{E}$ with components E_i, expressed in V.m^{-1}.

In order to derive the constitutive equations of a piezoelectric material, different types of thermodynamic potentials can be used. We have chosen the electric Gibbs energy (electric enthalpy) $Ge = Ge(E_i, \varepsilon_{ij})$. From the first principle of thermodynamics, which stipulates the existence of an internal energy U and the conservation of the energy, it is shown that at constant temperature:

$$\sigma_{ij} = \left(\frac{\partial Ge}{\partial \varepsilon_{ij}}\right)_E \text{ and } D_i = -\left(\frac{\partial Ge}{\partial E_i}\right)_\varepsilon$$

As we are only interested in a linear theory, Ge is defined by the sum of mechanical (U_{MM}), piezoelectric (U_{ME}) and electrical (U_{EE}) energies:

$$Ge = U_{MM} + U_{ME} + U_{EE} = \frac{1}{2}C_{ijkl}\varepsilon_{ij}\varepsilon_{kl} - e_{ijk}E_i\varepsilon_{jk} - \frac{1}{2}\kappa_{ij}E_iE_j \text{ with } (i,j,l,k) \in \{X,Y,Z\}$$

where $\bar{\bar{e}}$ is the third-rank piezoelectric tensor expressed in C.m^{-2} and $\bar{\kappa}$ is the second-rank permittivity tensor. C_{ijkl} are the elastic constants expressed in N.m^{-2} or Pa.

The relationships describing the piezoelectricity thus are:

$$\begin{cases} \sigma_{ij} = C_{ijkl}\varepsilon_{kl} - e_{kij}E_i \\ D_i = e_{ijk}\varepsilon_{jk} + \kappa_{ij}E_j \end{cases}$$

Several points can be noticed:
(i) From the linear electrical behavior in a dielectric, the relation between the electric displacement field ($\vec{D}$), the polarization ($\vec{P}$) and the electric field ($\vec{E}$) is given by: $\vec{D} = \kappa_0\vec{E} + \vec{P} = \bar{\kappa}\vec{E}$. In the absence of an electric field, *i.e.* $\vec{D} = \vec{P}$, the piezoelectric effect gives: $\vec{P} = \bar{\bar{e}}\bar{\bar{\varepsilon}}$.

(ii) For a strain-free crystal, *i.e.* $\bar{\bar{\varepsilon}} = 0$, the inverse piezoelectric effect gives: $\bar{\bar{\sigma}} = -\bar{\bar{e}}\vec{E}$.

(iii) In order to write the piezoelectric and elastic tensors in the form of a matrix array, Voigt notations are introduced. Thus, the ij subscripts are reduced to a single subscript:
$ij = 11 = 1\ ;\ ij = 22 = 2\ ;\ ij = 33 = 3\ ;\ ij = 23/32 = 4\ ; ij = 31/13 = 5\ ;\ ij = 12/21 = 6$
The application of Neumann's principle to these tensors followed by the use of the reduced-subscript notation allows to express the e_{ijk} tensor as a 3×6 matrix and the C_{ijkl} tensor as a 6×6 matrix:

$$e_{ijk} = \begin{bmatrix} 0 & 0 & 0 & 0 & e_{15} & -2e_{22} \\ -e_{22} & e_{22} & 0 & e_{15} & 0 & 0 \\ e_{31} & e_{31} & e_{33} & 0 & 0 & 0 \end{bmatrix}$$

$$C_{ijkl} = \begin{bmatrix} C_{11} & C_{12} & C_{13} & C_{14} & 0 & 0 \\ C_{12} & C_{11} & C_{13} & -C_{14} & 0 & 0 \\ C_{12} & C_{13} & C_{33} & 0 & 0 & 0 \\ C_{14} & -C_{14} & 0 & C_{44} & 0 & 0 \\ 0 & 0 & 0 & 0 & C_{44} & C_{14} \\ 0 & 0 & 0 & 0 & C_{14} & \frac{C_{11} - C_{12}}{2} \end{bmatrix}$$

In the case of our supplier (congruent LNO from Roditi):

$$e_{ijk} = \begin{bmatrix} 0 & 0 & 0 & 0 & 3.7 & -5 \\ -2.5 & 2.5 & 0 & 3.7 & 0 & 0 \\ 0.23 & 0.23 & 1.33 & 0 & 0 & 0 \end{bmatrix} [C.m^{-2}]$$

$$C_{ijkl} = \begin{bmatrix} 203 & 57.3 & 75.2 & 8.5 & 0 & 0 \\ 57.3 & 203 & 75.2 & -8.5 & 0 & 0 \\ 57.3 & 75.2 & 242.4 & 0 & 0 & 0 \\ 8.5 & -8.5 & 0 & 59.5 & 0 & 0 \\ 0 & 0 & 0 & 0 & 59.5 & 8.5 \\ 0 & 0 & 0 & 0 & 8.5 & 72.9 \end{bmatrix} [GPa]$$

(iv) In the $\bar{\bar{\kappa}}$ tensor, the only non-zero components are the diagonal elements. In the plane perpendicular to the Z-axis, the permittivity components have the same value. Thus the permittivity tensor can be represented by a 3×3 matrix as:

$$\kappa_{ij} = \begin{bmatrix} \kappa_{11} & 0 & 0 \\ 0 & \kappa_{11} & 0 \\ 0 & 0 & \kappa_{33} \end{bmatrix}$$

In the case of our supplier (Roditi), the dielectric constants ($\kappa_{rij} = \kappa_{ij}/\kappa_0$, with κ_0 the permittivity of free space (8.854×10^{-12} F.m^{-1})) for congruent LNO are:

$$\kappa_{rij} = \begin{bmatrix} 85.2 & 0 & 0 \\ 0 & 85.2 & 0 \\ 0 & 0 & 28.7 \end{bmatrix}$$

(v) Non-dimensional electromechanical coupling factors are generally used to characterize the amplitude of the piezoelectric effect. They characterize the energy transduction from electrical to mechanical energy or vice versa through the piezoelectric effect [IEE87].

This coupling factor is written as:

$$K_{ij}^2 = \frac{Piezoelectric\ constant^2}{Elastic\ constant.Permittivity\ constant}$$

The first subscript to K^2 denotes the direction along which the input force is applied and the second denotes the direction along which the output energy is developed.

For instance, in our case (congruent LNO from Roditi), $K_{33} = \frac{e_{33}}{\sqrt{C_{33}\kappa_{33}}} = 17\%$ (coupling factor for longitudinal case), $K_{31} = \frac{e_{31}}{\sqrt{C_{11}\kappa_{33}}} = 3\%$ (coupling factor for transverse case) and $K_{15} = \frac{e_{15}}{\sqrt{C_{55}\kappa_{11}}} = 55\%$ (coupling factor for shear case).

Chapter 2: Ferromagnetic materials

Ferromagnetism refers to the ability of some materials to exhibit a spontaneous magnetization even in the absence of an external magnetic field. The spontaneous magnetization is related to the alignment of magnetic moments due to the exchange interaction. Other contributions, described in the following, can affect the direction of the spontaneous magnetization. The application of an external magnetic field, via the supplementary Zeeman contribution, can lead to a complete aligned order called magnetic saturation. This state can be reversed by the application of an equally strong opposite magnetic field. The reversal process is usually not reversible and can be described by the so-called magnetic hysteresis loop.
Beyond a critical temperature (Curie temperature), ferromagnets lose their magnetic properties and enter a paramagnetic state. In the paramagnetic state, magnetic moments are disordered in the absence of an applied magnetic field due to thermal fluctuations.

At the atomic level, the magnetic properties of a material are due to the contributions of the spin and orbital magnetic moments giving rise to the atomic magnetic moment. The case of solids strongly depends on the localized/delocalized character of the electrons carrying most of the magnetization and two main classes of magnetic materials have to be distinguished: Rare Earth (RE) metals and Transition Metals (TM).
The first section recalls the main features related to the magnetism of these materials before dealing with the interesting case where RE and TM are combined in $RETM_2$ compounds. Two paragraphs are devoted to magnetostriction, a key ingredient for strain-mediated multiferroics, and to the specific energy contributions to be considered in magnetic thin films compared to bulk materials.

1. Different magnetic materials

1.1. Localized magnetism in lanthanide metals (4f)

The series of rare earth metals, or lanthanides, extends from Lanthanum to Lutetium, and corresponds to the progressive filling of the 4f orbital. Rare earths whose 4f orbit is not half filled are called light rare earths; those for which the number of 4f electrons is larger than 7, *i.e.* for more than half filled layer, are called heavy rare earths.
Rare earths have an electronic configuration of type [Xe] $4f^n$ $5d^1$ $6s^2$ where n=0 for Lanthanum and n=14 for Lutetium. In their metallic state, the 5d and 6s electrons are delocalized and form the conduction band. 4f electrons are highly localized and are only slightly affected by the state of the conduction electrons. The interaction between 4f electrons is very strong. In this 4f orbital, the Coulomb interaction is stronger than the spin-orbit coupling and the description of the magnetic moments is performed following:
(i) A coupling occurs for orbital angular momentum and another one for spin moments of the 4f electrons, which gives rise to the total orbital angular momentum ($\vec{L}$) and total spin moments ($\vec{S}$).
(ii) Spin-orbit coupling, strong in rare earths, leads to the formation of the total angular momentum $\vec{J} = \vec{L} + \vec{S}$.
The values of S, L and J are given classically by Hund's rules (under which the spin of a system must be maximum). The heavy rare earths are characterized by $J = L + S$ while in the light rare earths $J = |L - S|$.

The magnetic properties are governed by the various terms appearing in the magnetic component of the Hamiltonian: the exchange interaction, the magnetocrystalline anisotropy and the magnetostriction.

(i) Because of the localized character of 4f electrons carrying the magnetic moment, the exchange coupling in RE metals is indirect and occurs via polarization of the conduction electrons. It is the so-called RKKY (Ruderman, Kittel, Katsuya and Yosida) interaction. The overlap between the 4f wave functions centered on two neighboring sites is namely too small to enable a significant direct exchange. The overlap between 4f and 5d wave functions is however sufficient to allow direct exchange between the local moment and the conduction electrons. This direct exchange between 4f electrons and conduction electrons mediates the indirect exchange between the magnetic moments of neighboring atoms. This is a long-range interaction that oscillates with the distance and decreases as r^{-3}.
(ii) The magnetocrystalline anisotropy results from the Coulomb electrostatic interaction between the electronic 4f cloud and the crystal field due to neighbor ions of the crystal lattice. The orientation of the 4f orbital tends to minimize the energy by bringing the electrons closer to the positive ions of the lattice. This preferred orientation of the 4f orbital yields a preferred direction for magnetic moment respect to the crystal lattice.
(iii) The magnetostriction describes the change/strain in the crystal lattice due to the magnetic state of the material. The magnetostrictive strains result from the balance between a magnetoelastic term (linear in strain) that may favor a lattice distortion and a purely elastic term (quadratic in strain) that always limits the lattice strain. Magnetostrictive effects are described in details in paragraph 2.

1.2. Magnetism of transition metals (3d)

The magnetic properties of the transition metals are linked to the existence of *d* electronic shells gradually filled when the atomic number increases. In these metals, the magnetism is described in terms of itinerant magnetism.
In the band structure model, the magnetization M is related to unequal numbers of electrons with spin up $n_{\uparrow}$ and electrons with spin down $n_{\downarrow}$ at Fermi level and M is given by:

$$M = \mu_B.(n_{\uparrow} - n_{\downarrow})$$

where μ_B is the Bohr magneton.

The crystal field energy in TM is about 100 times larger than the spin-orbit coupling and plays thus a major role, one major consequence being the quench of the orbital angular momentum.
(i) Due to the strong overlap of spatially extended 3d orbitals, the exchange interaction between magnetic moments in transition metals is direct. This results in a strong TM-TM interaction and to Curie temperatures much higher than in RE metals.
(ii) The magnetocrystalline anisotropy being directly related to crystal field and orbital angular momentum is generally low in 3d metals where the orbital angular momentum is partly quenched ($\vec{L}$ close to zero).
(iii) The magnetostriction in 3d transition metals is also small, essentially for the same reasons as for magnetocrystalline anisotropy, *i.e*. the weak spin-orbit coupling.

1.3. $REFe_2$ alloys (4f/3d)

Rare earth/Iron alloys present the strong interest to combine specific properties from rare earth and transition metals. They especially benefit both from the strong magnetocrystalline anisotropy and magnetostriction related to RE moments and from the strong exchange related to Fe moments [DUC97]. Among the various RE/Fe compounds that can be stabilized (see Figure 8 for TbFe compounds [ENG99]), $REFe_2$ have risen a particular interest due to their record room temperature magnetostriction. This section aims to recall the $REFe_2$ structure, as well as the exchange process and magnetocrystalline anisotropy in these compounds.

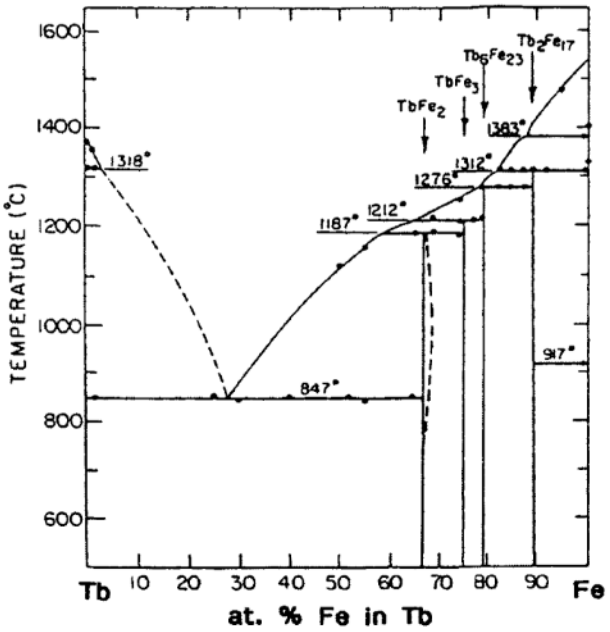

Figure 8. Binary phase diagram of TbFe at atmospheric pressure.

1.3.1. Structure

$REFe_2$ compounds crystallize in the so-called "Laves phase" cubic structure (space group $Fd\bar{3}m$) sketched in Figure 9. The rare earth atoms (in gold) form a diamond structure where half of the tetrahedron sites are occupied by rare earth atoms, the other half being occupied by regular tetrahedron of Fe atoms (in black). The lattice constant for $TbFe_2$ (also called Terfenol) at the center of this work is equal to 0.7345 nm at room temperature.

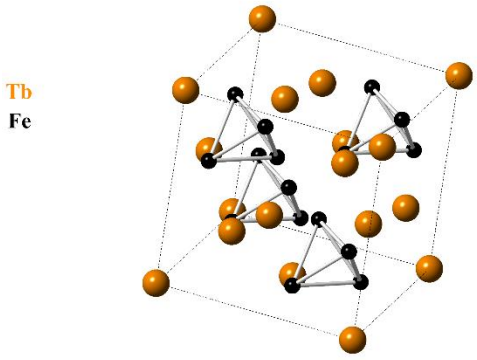

Figure 9. $TbFe_2$ Laves phase structure. Fe atoms are presented in black and Tb atoms in gold. The size ratio between the different atoms are obtained from their crystal radii values [SHA76].

1.3.2. Exchange energy

Three different exchange interactions of unequal importance take place in $REFe_2$:
(i) The RE-RE interaction is the weakest one and, as in RE metals, of RKKY type.
(ii) The TM-TM interaction is the strongest one and, as in TM, the large spatial extension of 3d orbitals can lead to an overlap between neighboring Fe atoms.
(iii) The RE-TM interaction remains relatively low compared to the TM-TM interaction but still plays a significant role in the magnetic structure of the compound. Campbell [CAM72] was the first to point out that the RE-TM interaction, although indirect, could not be of the RKKY type. He proposed a different mechanism involving two types of interactions:

A direct intra-atomic positive coupling between the 4f and 5d moments of the rare earth. This 4f -5d interaction acts as an intense field and contributes to increase the RE 5d moment.
A direct inter-atomic negative coupling between the 3d TM and the 5d RE spins. It relies on the hybridization of the 3d and 5d conduction bands, and the polarization of the 5d electrons. According to Campbell, and confirmed by Brooks *et al.* [BRO91], this direct 3d TM - 5d RE exchange interaction controls the RE-TM coupling and the nature of the coupling between RE and TM moments depends on the light or heavy character of the RE. Since the RE moment is dominated by the 4f orbital contribution L, the RE-TM coupling is eventually parallel in the case of light RE where 4f L and S are antiparallel and antiparallel in the case of heavy RE where 4f L and S are parallel (Figure 10).

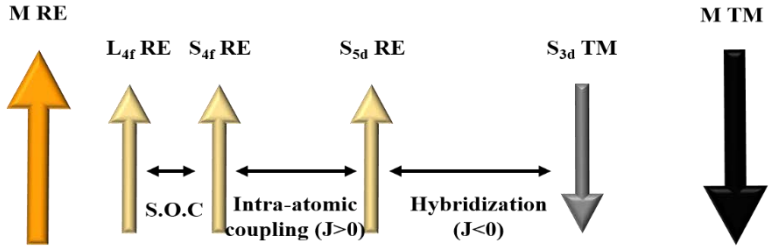

Figure 10. Schematic representation of the interactions between heavy RE and TM magnetic moments. S.O.C represents the spin-orbit coupling and J the exchange constant.

$TbFe_2$ compound is therefore ferrimagnetic with a Curie temperature of 425 °C [CLA80]. Contrary to other $REFe_2$ compounds based on heavy RE, $TbFe_2$ doesn't exhibit any compensation temperature where Tb and Fe moments would be opposite and of equal values. The Tb moments are dominant over the entire temperature range where the compound is magnetically ordered.
The Tb and Fe magnetic moments are reported to be 7.58 μ_B/at. and 1.6 μ_B/at. [CLA80] respectively at room temperature, leading to a saturation magnetization of 800 $kA.m^{-1}$ [CLA80].

1.3.3. Magnetocrystalline anisotropy

In the cubic symmetry, the phenomenological expression of the magnetocrystalline anisotropy energy density is:

$$E_{m.a} = K_1\left(\alpha_x^2\alpha_y^2 + \alpha_x^2\alpha_z^2 + \alpha_y^2\alpha_z^2\right) + K_2\left(\alpha_x^2\alpha_y^2\alpha_z^2\right) + K_3\left(\alpha_x^4\alpha_y^4 + \alpha_x^4\alpha_z^4 + \alpha_y^4\alpha_z^4\right) + \cdots$$

where $K_{1,2,3}$ are the magnetocrystalline anisotropy constants and $\alpha_{x,y,z}$ are the magnetization direction cosines.

The easy magnetization axis is obtained from the minimization of this energy respect to the direction cosines. By limiting the development at the order 6 of the direction cosines, the easy magnetization directions are parallel to one of the main crystallographic directions, *i.e.* $< 100 >$, $< 111 >$ or $< 110 >$, depending on the signs and relative values of K_1 and K_2 [ATZ76]. Considering higher order terms may lead to more complex easy magnetization directions, away from the main crystal axis.
$REFe_2$ magnetocrystalline anisotropy constants are highly dependent on temperature and K_3 constants are generally smaller than K_1 by more than one order of magnitude at RT [MOU99]. Table 1 gathers the room temperature constants reported in the literature for $TbFe_2$ and $Tb_{0.3}Dy_{0.7}Fe_2$ in comparison to those reported for hcp Co, fcc Ni and bcc Fe.

These values emphasize the large magnetocrystalline anisotropy encountered in $REFe_2$ compounds, one or two order of magnitude larger than in TM.
In $TbFe_2$, this set of anisotropy constants leads to an easy magnetization direction parallel to $< 111 >$, as reported by Clark at room temperature [CLA80].

Compound	K_1 (J.m^{-3})	K_2 (J.m^{-3})
Co (hcp)	5.13×10^5 [1]	1×10^3 [1]
Fe (bcc)	4.8×10^4 [1]	1×10^3 [1]
Ni (fcc)	-6×10^3 [1]	-3×10^3 [1]
$TbFe_2$ (fcc)	-6.3×10^6 [2]	6×10^5 [2]
Terfenol-D ($Tb_{0.3}Dy_{0.7}Fe_2$) (fcc)	-3×10^5 [2]	-1.7×10^5 [2]

Table 1. Magnetocrystalline anisotropy constants $K_{1,2}$ (in J.m^{-3}) for different bulk compounds at room temperature according to [SAN04] [1] and [ODE96] [2].

2. Magnetostriction

The distortion of the crystal lattice associated with a change in the magnetic state is called magnetostriction. As mentioned previously, TM magnetostrictive properties are rather unattractive because the strains generated by magnetic changes are very small. The interest in magnetostrictive materials was revived in the 1960's due to the discovery of giant magnetostriction in rare earth metals. In 1963, magnetostrictive strains in the basal plane of the hexagonal structure of Dysprosium and Terbium have been reported: they reach 1%, 100 times to 10000 times larger than those encountered in the TM [CLA80]. Unfortunately, the magnetic order temperatures of magnetostrictive RE are too low (- 51 °C for Tb and - 185 °C for Dy [ENG99]) for room temperature applications.
The development of materials with high magnetostriction at room temperature began in the 1971, when some researchers from the Naval Ordnance Laboratory (US Navy), among which A. E. Clark, had the idea of combining a rare earth (Terbium) with a transition metal (Iron).

When dealing with magnetostriction, several underlying physical effects have to be distinguished:
(i) The volumic magnetostriction. It is isotropic and due to the onset of magnetic order. It arises from the strain dependence of the exchange interaction among electrons, provided these electrons are magnetically polarized. A supplementary contribution to this exchange magnetotriction arises under an external magnetic field that adds to the intrinsic exchange field. It is the so-called forced magnetostriction.
(ii) The Joule magnetostriction. It is anisotropic and arises from the strain dependence of the interaction between the electrons and their atomic environment (spin moments with crystal field through the spin orbit coupling). The Joule magnetostriction contribution becomes constant after reaching magnetic saturation.
(iii) The deltaE-effect. A stress applied to a ferromagnetic material induces a magnetization reorientation (inverse Joule magnetostriction) which in turn leads to an additional magnetostrictive strain (direct Joule magnetostriction). The resulting strain shifts from the strain expected from the Hook law, which leads to a change of the effective Young modulus (E). This effect was discovered from Honda and Terada's work in 1907 and it is defined as [CLA75]:

$$\Delta E = \frac{E_s - E_o}{E_o}$$

where E_s and E_0 are Young's modulus at magnetic saturation and at zero magnetic field respectively. Once again, the deltaE-effect contribution becomes constant after reaching magnetic saturation. This effect is small in Iron and Nickel, being on the order of 0.4 to 18 % [CLA75]. However, Clark and Savage reported deltaE-effects as large as 240 % in 1975 for giant magnetostrictive materials such as $TbFe_2$ [CLA75].

As mentioned previously, the magnetostriction results from a crystal distortion that can lower the magnetoelastic energy (linear in strains ε_{ij}) but that always increases the elastic energy (quadratic in strains ε_{ij}).
The expressions of both the magnetoelastic ($E_{m.e}$) and the elastic (E_{el}) energy densities are the following:

$$E_{m.e} = b_0(\varepsilon_{xx} + \varepsilon_{yy} + \varepsilon_{zz}) + b_1(\alpha_x^2\varepsilon_{xx} + \alpha_y^2\varepsilon_{yy} + \alpha_z^2\varepsilon_{zz}) + b_2(\alpha_x\alpha_y\varepsilon_{xy} + \alpha_x\alpha_z\varepsilon_{xz} + \alpha_y\alpha_z\varepsilon_{yz})$$

$$E_{el} = \frac{1}{2}C_{11}.(\varepsilon_{xx}^2 + \varepsilon_{yy}^2 + \varepsilon_{zz}^2) + C_{12}.(\varepsilon_{xx}\varepsilon_{yy} + \varepsilon_{xx}\varepsilon_{zz} + \varepsilon_{yy}\varepsilon_{zz}) + 2C_{44}.(\varepsilon_{xy}^2 + \varepsilon_{xz}^2 + \varepsilon_{yz}^2)$$

where b_i are the magnetoelastic coefficients, ε_{ij} the components of the strain tensor in a Cartesian coordinate system, C_{ij} the elastic constants (= C_{ijkl} using Voigt notation) and α_i the magnetization direction cosines.

For a given magnetization direction, strains at equilibrium are those that minimize the sum of the magnetoelastic and elastic energies respect to ε_{ij}. They are given by:

$$\varepsilon_{ii}^{eq} = \frac{-b_1\alpha_i^2}{C_{11} - C_{12}} + \frac{-b_0}{C_{11} + 2C_{12}} + \frac{C_{12}b_1}{(C_{11} + 2C_{12})(C_{11} - C_{12})}$$

and

$$\varepsilon_{ij}^{eq} = \frac{-b_2\alpha_i\alpha_j}{C_{44}}$$

From these equilibrium strains, one can calculate the magnetostrictive strain $\frac{\Delta l}{l}$ along an arbitrary direction defined by direction cosines β_i with respect to the orthogonal reference axes [KIT49]:

$$\frac{\Delta l}{l} = \sum_{i,j} \varepsilon_{ij}^{eq}\,\beta_i\beta_j$$

Substituting the equilibrium strains in the above expression and keeping only order two terms and no residual terms leads to:

$$\frac{\Delta l}{l} = -\frac{b_1}{C_{11} - C_{12}}\left(\alpha_x^2\beta_x^2 + \alpha_y^2\beta_y^2 + \alpha_z^2\beta_z^2 - \frac{1}{3}\right) - \frac{b_2}{C_{44}}\left(\alpha_x\alpha_y\beta_x\beta_y + \alpha_y\alpha_z\beta_y\beta_z + \alpha_z\alpha_x\beta_z\beta_x\right)$$

One can deduce the magnetostrictive strains along [100] for magnetization fully aligned along [100] ($\alpha_x = \beta_x = 1$ and $\alpha_y = \alpha_z = \beta_y = \beta_z = 0$):

$$\frac{\Delta l}{l}_{[100]} = -\frac{2b_1}{3(C_{11} - C_{12})} = \lambda_{100}$$

and the magnetostrictive strains along [111] for magnetization fully aligned along [111] ($\alpha_x = \alpha_y = \alpha_z = \beta_x = \beta_y = \beta_z = {}^1/_{\sqrt{3}}$):

$$\frac{\Delta l}{l}_{[111]} = -\frac{b_2}{3C_{44}} = \lambda_{111}$$

The magnetostrictive strain $\frac{\Delta l}{l}$ along an arbitrary direction can thus be also given by the so-called equation of magnetostriction:

$$\frac{\Delta l}{l} = \frac{3}{2}\lambda_{100}\left(\alpha_x^2\beta_x^2 + \alpha_y^2\beta_y^2 + \alpha_z^2\beta_z^2 - \frac{1}{3}\right) + 3\lambda_{111}\left(\alpha_x\alpha_y\beta_x\beta_y + \alpha_y\alpha_z\beta_y\beta_z + \alpha_z\alpha_x\beta_z\beta_x\right)$$

In the case where the magnetostriction is measured in the same direction as the magnetization, *i.e.* as the magnetic field, this expression reduces to:

$$\frac{\Delta l}{l} = \lambda_{100} + 3(\lambda_{111} - \lambda_{100})(\alpha_x^2a_y^2 + \alpha_y^2\alpha_z^2 + \alpha_z^2\alpha_x^2)$$

Finally, in a randomly oriented polycrystalline (with no preferred grain orientation) cubic crystal, the magnetostriction is calculated in averaging the effects and the formula simplifies further to:

$$\frac{\Delta l}{l} = \frac{2}{5}\lambda_{100} + \frac{3}{5}\lambda_{111}$$

Table 2 gathers the magnetoelastic constants b_1 and b_2 at room temperature, the values of λ_{100} and λ_{111} at room temperature and Curie temperatures for different crystalline magnetic materials. One can notice the huge room temperature magnetostriction obtained in $TbFe_2$ in comparison to moderate values reported for TM. Moreover, b_1 constants are negligible in comparison to b_2 in $REFe_2$.

Compound	b_1 (J.m^{-3})	b_2 (J.m^{-3})	λ_{100} (10^{-6})	λ_{111} (10^{-6})	T_C (°C)
Co (hcp)	-8.1×10^6 [1]	-2.9×10^7 [1]	---	---	1115 [2]
Fe (bcc)	-3.43×10^6 [1]	7.83×10^6 [1]	24.1 [1]	-22.7 [1]	770 [2]
Ni (fcc)	9.38×10^6 [1]	1×10^7 [1]	-64.5 [1]	-28.3 [1]	355 [2]
$TbFe_2$ (fcc)	-1.2×10^7 [6]	-3.7×10^8 [3]	100 [6]	2460 [4]	425 [4]
Terfenol-D ($Tb_{0.3}Dy_{0.7}Fe_2$) (fcc)	-1.03×10^7 [6]	-2.3×10^8 [5]	90 [6]	1600 [4]	380 [4]

Table 2. Magnetoelastic constants b_1 and b_2 at room temperature, magnetostriction constants λ_{100} and λ_{111} at room temperature and Curie temperatures T_C of some crystalline materials according to [SAN99] [1], [KEF66] [2], [ODE96] [3], [CLA80] [4], [MOU99b] [5] and [DUF10] [6].

3. Magnetic thin films

The case of magnetic thin films has to be specifically considered because, beyond the usual magnetic contributions that have been described above (exchange, magnetocrystalline anisotropy, magnetoelastic and elastic), additional contributions to the energy have to be taken into account. They are briefly described in this paragraph.

3.1. Shape anisotropy

The magnetic dipolar anisotropy, or shape anisotropy is mediated by the dipolar interaction. This interaction is long range and its contribution is thus dependent upon the shape of the sample.
The magnetization inside a ferromagnetic system is responsible for the appearance of magnetic charges at the surface of the magnetic material that create a dipolar magnetic field, also called demagnetizing field. In the case of a homogeneous magnetization in an ellipsoid, the dipolar field is defined as:

$$\overrightarrow{H_D} = -\overline{\overline{N}}\vec{M}$$

where $\vec{M}$ is the magnetization and $\overline{\overline{N}}$ is the positive demagnetizing field tensor which in the case of a uniformly magnetized sample can be written:

$$\overline{\overline{N}} = \begin{bmatrix} N_{xx} & 0 & 0 \\ 0 & N_{yy} & 0 \\ 0 & 0 & N_{zz} \end{bmatrix}$$

with $N_{xx} + N_{yy} + N_{zz} = 1$.

These demagnetizing coefficients depend on the dimension of the ellipsoid.
The associated demagnetizing field energy density is given by:

$$E_D = -\frac{\mu_0}{2}\vec{M}.\overrightarrow{H_D}$$

where μ_0 is the magnetic permeability of vacuum.

A thin film with a very small thickness compared to lateral dimension is treated as a flattened ellipsoid and in this case, the only non-zero term is $N_{zz} = 1$ (Z is the perpendicular to the film).
The demagnetizing field energy density is then written:

$$E_D = \frac{\mu_0}{2}{M_s}^2 cos^2\theta$$

where θ is the angle between the magnetization and the perpendicular to the sample surface.
This term thus leads the magnetization lying in the film plane since its maximum occurs when the magnetization is perpendicular to the plane.

3.2. Surface anisotropy

The surface/interface of a magnetic film is a very peculiar region due to the symmetry breaking, the specific morphology (roughness, steps…), the possible hybridization with a neighbor material. These features can give rise to a supplementary magnetic anisotropy contribution directly linked to the film surface/interface. The resulting volumic effective anisotropy constant is thus:

$$K_{eff} = K_v + 2K_s/t$$

where K_v (J.m^{-3}) is the volume contribution, K_s (J.m^{-2}) the surface contribution and t the thickness of the magnetic layer. For small thicknesses, the surface contribution may become preponderant over volume contribution.

3.3. Influence of the strain state

Another important parameter to consider in the case of thin films is the strain state of the crystal lattice. These strains may come from different sources but some of them are predominant: (i) The pseudomorphic epitaxial growth of the material. When there is a perfect match to the substrate or buffer layer lattice, the film in-plane lattice constant is different from the bulk one which induces lattice strains both in-plane and consequently along the growth direction. Those strains generally relax above a given critical thickness because of the increase of the associated elastic energy. (ii) The difference between the thermal dilatation coefficients of the deposited film and the substrate may also lead to lattice strains in the case of high temperature deposition. The deposited film lattice is relaxed at the deposition temperature but is eventually strained during the temperature decrease to room temperature. These strains should not depend on the film thickness, but only on the deposition temperature and on the difference between thermal dilatation coefficients [WAN96].
Lattice strains generated in the deposited film can significantly modify the magnetoelastic contribution to the total energy and thus induce changes of the spontaneous magnetization direction. Wang *et al.* [WAN96] have shown that (111) $TbFe_2$ films tensively strained in the plane (sapphire substrate with smaller dilatation coefficient) exhibit an in-plane magnetization, whereas those compressively strained in the plane (CaF_2 substrate with larger dilatation coefficient) exhibit a perpendicular magnetization. Avisou *et al.* [AVI08] have reported a similar effect for (111) $SmAl_2$ films. Since the $SmAl_2$ b_2 magnetoelastic constant is however positive (while it is negative for $TbFe_2$), the situation is reversed with a perpendicular magnetization in the case of in-plane expansion (sapphire substrate) and an in-plane magnetization in the case of in-plane compression (CaF_2 substrate).
The appendix B presents the calculation to determine the easy magnetization axis depending on the lattice strain for $TbFe_2$ films. They are performed for [110] and [111] growth directions in taking both magnetocrystalline and magnetoelastic contributions into account.
Finally, lattice strains generated in the deposited film can also influence the above mentioned surface anisotropy term. Perpendicular magnetization direction observed in Cu/Ni/Cu [001] textured systems [BOC96] and in Co/Ni (111) superlattices [GOT12] has been namely attributed to a strain-dependent contribution to the surface anisotropy energy.

References

[AGR06] A. Agronin, Y. Rosenwaks and G. Rosenman, *Direct observation of pinning centers in ferroelectrics*, Appl. Phys. Lett. **88**, 072911, (2006).
[AVI08] A. Avisou, C. Dufour and K. Dumesnil, *Control of magnetic anisotropy in (111) $SmAl_2$ films*, J. Appl. Phys. **103**, 07E135, (2008).
[ATZ76] U. Atzmony and M. P. Daniel, *Non major cubic symmetry axes of easy magnetization in rare-earth-iron Laves compounds*, Phys. Rev. B. **13**, 4006, (1976).
[BAL65] A. A. Ballmann, *Growth of piezoelectric and ferroelectric materials by the Czochralski technique*. J. Am. Ceram. Soc. **48**, 112–113, (1965).
[BOC96] G. Bochi, A. A. Ballentine, H. E. Inglefield, C. V. Thompson and R. C. O'Handley, *Evidence for strong surface magnetoelastic anisotropy in epitaxial Cu/Ni/Cu(001) sandwiches*, Phys. Rev. B. **53**, 4, (1996).

[BRO91] M. S. S. Brooks, L. Nordstrom and B. Johansson, *Magnetism of RFe_2 compounds*, J. Appl. Phys. **69**, 5683, (1991).
[CAM72] I. A. Campbell, *Indirect exchange for rare earths in metals*, Elsevier Science, (1972).
[CLA75] A. E. Clark and H. T. Savage, *Giant magnetically induced changes in the elastic modulus in $Tb_{0,3}Dy_{0,7}Fe_2$*, IEEE Trans. Sonics and Ultrasonics**. 22**, (1975).
[CLA80] A. E. Clark, *Magnetostrictive RFe2 intermetallic compounds*, Chap. 15, in Handbook on the physics and chemistry of rare earths, North Holland Publishing Company, (1980).
[DUC97] N. H. Duc, *Handbook on the Physics and Chemistry of Rare Earths*, Phys. Lett. **81**, 81, (1997).
[DUF10] C. Dufour, *Directions de facile aimantation dans quelques composés $TRFe_2$*, Rapport de stage de R. Isenbart et G. Rollin, Université H. Poincaré, Nancy, (2010).
[ENG99] G. Engdahl and I. Mayergoyz, *Handbook of Giant Magnetostrictive Materials*, Elsevier, Science, (1999).
[FED65] S. A. Fedulov, Z. I. Shapiro and P. B. Ladyzhinskii. Sov. Phys. Crystallography. **10**, 218, (1965).
[GOT12] M. Gottwald, S. Andrieu, F. Gimbert, E. Shipton, L. Calmels, C. Magn, E. Snoeck, M. Liberati, T. Hauet, E. Areholz, S. Mangin and R. E. Fullerton, *Co/Ni(111) supperlattices studied by microscopy, x-ray absorption and ab initio calculations,* Phys. Rev. B. **86**, 014425, (2012).
[HAU09] A. Haubmann, P. Milde, C. Erler and L. M. Eng, *Ferroelectric lithography: Bottom-up assembly and electrical performance of a single metallic nanowire*. Nano Lett. **9**, 763, (2009).
[HAU11] A. Haubmann. *Ferroelektrische Lithografie auf magnesium dotierten Lithium niobat-Einkristallen*. PhD thesis, Technische Universität Dresden, (2011).
[IEE87] American National Standards Institute, *Standard on piezoelectricity*, ANSI/IEEEStd. **176**, (1987).
[KAL02] S. V. Kalinin, D. A. Bonnell, T. Alvarez, X. Lei, Z. Hu, J. H. Ferris, Q. Zhang and S. Dunn, *Atomic polarization and local reactivity on ferroelectric surfaces: A new route toward complex nanostructures*, Nano Lett. **2**, 589, (2002).
[KEF66] F. Keffer, Handbuch der Physik, New York: Springer-Verlag.18, (1966).
[KIM02] S. Kim, V. Gopalan and A. Gruverman*, Coercive fields in ferroelectrics: A case study in lithium Niobate and lithium tantalate,* Appl. Phys. Lett. **80**, 2740, (2002).
[KIT49] C. Kittel*, Physical theory of ferromagnetic domains,* Rev. Mod. Phys. **21**, 541, (1949).
[LEE14] H. J. Lee, S. Zhang, Y. Bar-Cohen and S. Sherrit, *High temperature, high power piezoelectric composite transducers,* Sensors. **14**, 8, (2014).
[LI08] D. Li and D. A. Bonnell, *Ferroelectric lithography*, Ceram. Int. **34**, 157 – 164, (2008).
[MIG10] S. Mignoni, *Investigation par spectroscopie Raman des propriétés microstructurales et photoréfractives de $LiNbO_3$ dopé*, PhD thesis, Université de Metz-Supélec, (2010).
[MOU99] A. Mougin, *Nanosystèmes magnétostrictifs de $TRFe_2$ (110) (TR=terre rare): croissance, morphologie et propriétés magnétiques*, PhD dissertation, Université H. Poincaré, Nancy, (1999).
[NIK05] D. N. Nikogosyan, *Nonlinear optical crystals*, Springer, (2005).
[NYE57] J. F. Nye, *Physical Properties of Crystals: Their representation by tensors and matrices,* Oxford Science Publications, p. 115, (1957).
[ODE96] V. Oderno, *Croissance de couches minces épitaxiées de phases de Laves TR-Fe_2 (TR=Y, Tb, Dy et Er). Influence des déformations épitaxiales sur l'anisotropie magnétique*, PhD dissertation, INPL, Ecole des mines de Nancy, (1996).
[SAN04] D. Sander, *The magnetic anisotropy and spin reorientation nanostructures and nanoscale films*, J. Phys. Condens. Matter**. 16**, 603-636, (2004).
[SAN99] D. Sander, *The correlation between mechanical stress and magnetic anisotropy in ultrathin films*, Rep. Prog. Phys**. 62**, 809-858, (1998).
[SHA76] R. D. Shannon, *Revised effective ionic radii and systematic studies of interatomic distances in halides and chalcogenides*, Acta. Cryst**. A32**, (1976).
[SEI11] J. Seidel, D. Fu, S. Y. Yang, E. Alarcon-Llado, J. Wu, R. Ramesh and J. W. Ager, *Efficient photovoltaic current generation at ferroelectric domain walls*. Phys. Rev. Lett. **107**, 126805, (2011).
[WAN96] C. T. Wang, B. M. Clemens and R. L. White, *Effects of substrate on the magnetic properties of epitaxial $TbFe_2$ (111) films*, IEEE Trans. Magn. **32**, 4752, (1996).

Second part: Synthesis of piezoelectric/magnetostrictive heterostructures-Magnetic properties

This part reports on the synthesis of the piezoelectric/ magnetostrictive heterostructures. As mentioned previously, the general context is the development of hybrid multiferroics, and more specifically of nanosystems in which the magnetization would influence the dynamical acoustic properties, such as the propagation of surface acoustic waves (these analysis are extensively detailed in the following part). For this purpose, $LiNbO_3$ substrates have been chosen because of their well-known properties and suitable electromechanical coupling for the development of SAW-based devices. After recalling some important results previously reported on the epitaxial growth of $TbFe_2$ and on the crystalline growth on $LiNbO_3$ substrates (chapter 1), the chapter 2 is specifically devoted to the various types of $LiNbO_3$ substrates that have been used. The following chapters summarize the results obtained for the crystalline growth by molecular beam epitaxy of $TbFe_2$ on LNO-Z cut (chapter 3), on LNO-128Y and 41Y cuts (chapter 4), and for the growth of Ni and [Co/IrMn] by sputtering on similar substrates (chapter 5). In these various cases, we present the results of the structural (RHEED and X-ray scattering) and magnetic (VSM) characterization. Those were undertaken to unravel the sometimes complex Orientation Relationships (OR), to analyze the quality of the magnetostrictive material and obtain a good knowledge of its magnetic properties, which appears essential for the understanding of SAW devices.

The information on the growth techniques and various experimental setups are given in appendices A, C and E.

Chapter 1: State of the art

1. $TbFe_2$ growth on a sapphire substrates

The epitaxial growth requires the use of a suitable substrate and possibly of buffer layer(s) to get the suitable in-plane symmetry and lattice constants. The role of buffer layers is also to minimize chemical reactions with the substrate, most often an oxide. Those points are particularly significant in the case of $REFe_2$ since RE are known to be strongly sensitive to Oxygen and their epitaxial growth requires high temperature deposition. This part focuses on the epitaxial growth achieved on $\alpha-Al_2O_3$ corundum (also called sapphire). Different Al_2O_3 orientations and buffer layers have been used to get different growth planes: (110), (111) or even (211).

(110) $REFe_2$ epitaxial growth on Al_2O_3 ($11\bar{2}0$)

The (110) $REFe_2$ epitaxial growth on Al_2O_3 ($11\bar{2}0$) (a-plane) is well known in the group of Nancy [ODE96b, MOU99a]. After outgassing the substrate at 800 °C, a 50 nm thick Nb (110) buffer layer is deposited at 700 °C, followed by a 1.5 nm thick Fe layer deposited at 500 °C. This original process enables, via inter-diffusion between Nb and Fe, the formation of a surface alloy (called NbFe-α) that has the symmetry required for the epitaxy of the (110) Laves phase plane. This surface alloy reduces the lattice mismatch between the buffer layer and the Laves phase in the [001] direction, which favors the growth of single crystalline $REFe_2$ (110). In this case, the in-plane epitaxial relationships are: [001] $REFe_2$ // [001] Nb and [$1\bar{1}0$] $REFe_2$ // [$1\bar{1}0$] Nb. Deposition temperatures are ranged between 460 °C and 660 °C with an optimal temperature of 550 °C. Growth is of Stranski-Krastanov type (few monolayers then relaxation and formation of islands). For low thicknesses, the islands are oriented with a preferential orientations along the [$1\bar{1}0$] direction. As the thickness increases, the islands get closer and form a continuous film but the process depends on the deposition temperature. As shown in [MOU01], increasing the deposition temperature delays the formation of full film by increasing the coalescence of deposited atoms towards islands. Independently of the $REFe_2$ film thickness in the 5 – 100 nm range, these films are systematically compressed by -0.4 % in the growth direction and expanded by +0.6 % in the plane, which has been attributed to the high deposition temperature and to a thermal dilatation coefficient smaller for the sapphire substrate than for the $REFe_2$ compounds.
The growth of $REFe_2$ along the [110] direction was also achieved directly on a 50 nm thick Ta (110) buffer layer deposited at 1000 °C on Al_2O_3 ($11\bar{2}0$) [HUT98b]. The deposition of $TbFe_2$ or $DyFe_2$ is performed at 680 °C and for a growth rate of 0.02 $nm.s^{-1}$. A tensile strain in the (110) plane of +0.5 % is obtained at room temperature.

From the magnetic point of view, in both cases, the $TbFe_2$ magnetization lies in the (110) plane: two equivalent $< 1\bar{1}1 >$ axis favored by the magnetocrystalline anisotropy are in the growth plane, and the magnetoelastic term due to lattice compression along the growth direction also favors in-plane directions (appendix B), as does the shape anisotropy. Furthermore, the magnetic response is strongly correlated to morphology. In fact, when the layer is composed of islands, the in-plane response is isotropic. In contrary, the response is anisotropic for a continuous film (in the case of $DyFe_2$ [MOU00]). The morphology can also alter the coercive field value. Finally, magnetization at saturation varies between 600 $kA.m^{-1}$ and 800 $kA.m^{-1}$ at room temperature depending on $REFe_2$ coumponds and studies [MOU99, ODE96].

(111) $REFe_2$ epitaxial growth on *Al_2O_3*

The (111) $TbFe_2$ epitaxial growth can also be obtained on Al_2O_3 $(11\bar{2}0)$ using a (110) Mo buffer layer deposited at 750 °C as shown by Huth *et al.* [HUT98a]. The $TbFe_2$ growth is obtained for deposition temperatures in the [450 °C - 680 °C] range and a growth rate of 0.02 $nm.s^{-1}$. In-plane orientation relationships are: $[11\bar{2}]$ $TbFe_2$ // [001] Mo and $[1\bar{1}0]$ $TbFe_2$ // $[1\bar{1}0]$ Mo, which corresponds to the so-called R30 OR between fcc (111) and bcc (110) planes [HOM87]. Those OR are recalled in appendix D. As in the case of (110) $TbFe_2$ films, these (111) $TbFe_2$ films are under a perpendicular strain of -0.4 % and in-plane tensile strain of approximatively +0.5 %, which is also attributed to the different thermal dilatation coefficients of $TbFe_2$ and sapphire substrate. (111) $TbFe_2$ films were also obtained on a Al_2O_3 (0001) c-plane covered by a (111) Nb buffer layer deposited at 750 °C [HUT98b]. This buffer is however of reduced structural quality due to the presence of facets because of very low surface free energy for (110) Nb.
From the magnetic point of view, the $< 1\bar{1}1 >$ directions at 20° off the plane are energetically favored for the magnetization orientation, due to the combination of shape and magnetoelastic contributions.

(211) $REFe_2$ epitaxial growth on *Al_2O_3*

The (211) $TbFe_2$ growth has been achieved on faceted α-Al_2O_3 $(10\bar{1}0)$ (m-plane) substrates using a 50 nm thick Nb or Mo buffer deposited at 850 °C covered by a 1.5 nm thin Fe seed layer at 530 °C [OST05]. α-Al_2O_3 $(10\bar{1}0)$-oriented substrates show microscopically large facets ($(10\bar{1}\bar{2})$ and $(10\bar{1}1)$ facets parallel to the in-plane [010] axis) after one day at high temperature annealing in air. Nb and Mo both exhibit a twin-free (211) oriented growth with in-plane epitaxial relationships:

$$Nb/Mo\ [01\bar{1}]\ //Al_2O_3\ [010]$$
$$Nb/Mo\ [\bar{1}11]\ //\ Al_2O_3\ [001]$$

The $TbFe_2$ grows on (211) Nb along the same [211] direction and the crystalline orientation is cube to cube with regard to the Nb buffer layer. Those films are less strained than those deposited on sapphire a-plane since the difference between perpendicular and in-plane strains has been measured around -0.4 %. The easy magnetization direction lies in the plane, along the $[\bar{1}11]$ axis favored by magnetocristalline anisotropy, as well as shape and magnetoelastic contributions. On (211) Mo, the $TbFe_2$ grows with the formation of multiple domains and no magnetic results are shown. Nevertheless, these authors express that one result of this multiple domains growth is that $TbFe_2$ films show small coercive fields, small saturation fields and vanishing magnetic anisotropy in the plane. Another interesting point raised in this paper [OST05] is the fact that the epitaxial relationship of Nb/Mo on faceted sapphire m-plane fits into the established three dimensional epitaxial relationship of the Nb/Mo-sapphire non faceted system.

2. Growth on Lithium Niobate substrates

A large amount of studies using $LiNbO_3$ as a substrate (the different LNO orientations/cuts will be presented in further details in chapter 2) for magnetic or non-magnetic film deposition can be found in the literature. However, in most of these studies, the deposition is performed at room temperature and results in amorphous or polycrystalline films.

Concerning the deposition of magnetic films, one can mention:
(i) 200 nm thick Ni on LNO128 Y-cut by RF-sputtering at room temperature and using a 250 nm thick insulating ZnO or Al_2O_3 as buffer layer [ELH16]. No structural information is provided. The magnetization of the Ni thin film exhibits an isotropic in-plane response. No OOP magnetic characterization has been done.
(ii) 850 nm thick Ni on LNO Y-cut [GAN76]. The deposition technique is unknown. Neither structural nor magnetic information are provided.

(iii) [$TbCo_2$/FeCo] multilayers on LNO Y-cut by RF-sputtering [ZHO14]. No structural information is provided. A magnetic anisotropy axis of order 2 is reported and attributed to the deposition geometry.
(iv) 2500 nm thick $TbFe_2$ deposited on a LNO Y-cut at RT by RF-sputtering [YAM79, YAM80]. The deposition takes 4 hours. They perform an annealing at a pressure of 10^{-5} Torr at 240 °C for 1 hour to relieve internal stress induced in the deposition process, but do not provide any information on structural and magnetic properties.

Few studies however report on the epitaxial growth on LNO, achieved by MBE or by sputtering, and performed at relatively high temperature.
(i) (0002) ZnO on LNO Z-cut (RF-sputtering) at 550 °C [MAT99]. The authors report on a reasonable cystal quality with a Full Width at Half Maximum (FWHM) across the (0002) Bragg peak of 0.47°. The in-plane epitaxial relationship is: $[11\bar{2}0]$ ZnO // $[1\bar{1}00]$ $LiNbO_3$. Along this direction, the lattice mismatch predicted is 9.3 % between ZnO and LNO.
(ii) (0001) GaN films on LNO Z-cut (MBE) at 650 °C [NAM11]. To produce atomically flat surfaces, the LNO substrate is first annealed in the air at 1000 °C for two hours in quartz tube of furnace system. It is then cleaned with organic solvents, rinsed with de-ionized water and outgassed in vacuum at 200 °C for 1 hour. Prior to the GaN gowth, a 100 nm thick AlN buffer layer is grown at 600 °C. AlN seems to be a good barrier against possible diffusion. The authors indeed warn the community about Lithium rise and degradation of the LNO at the interface with the appearance of non-stoichiometric LNO due to the high temperature required for epitaxy.
(iii) (111) $TbFe_2$ on LNO Z-cut at 550 °C using a double Ti/Mo buffer layer by MBE [HUT99]. The LNO substrate is first cleaned with basic and organic solvents, and then annealed for 12 hours in vacuum at 350 °C. The 50 nm thick (0001) Ti buffer layer is then grown at 100 °C (0.1 $nm.s^{-1}$). The following 50 nm thick (110) Mo buffer is grown at 750 °C (0.03 $nm.s^{-1}$). The authors report a 1° tilted growth and an increased roughness for the Mo surface but do not provide any information on in-plane orientation relationships. The deposition of (111) $TbFe_2$ is finally achieved at 550 °C. This film is submitted to a perpendicular tensile strain and an in-plane compressive strain (-0.4 %) attributed to the larger thermal expansion coefficient of LNO compared to $TbFe_2$. This in-plane compression induces a magnetoelastic term that overcomes the shape anisotropy and stabilizes perpendicular magnetization (appendix B). Despite the success in growing $TbFe_2$ on LNO Z-cut, the authors emphasize the difficulties related to the low stability of LNO at high temperature with the possible Li diffusion. The double Ti/Mo buffer is supposed to form an efficient chemically inert diffusion barrier. The saturation magnetization at RT reaches 90% of the bulk value. Temperature variations during the growth process are fast (15 minutes between Ti and Mo, 10 minutes between Mo and $TbFe_2$) to limit the time at high temperature.

From these different studies, one can underline that most of the magnetic layers deposited on LNO exhibit a polycrystalline or amorphous structure and didn't benefit from a comprehensive structural and magnetic characterization. Due to the difficulties inherent to this material, high temperature MBE growth studies on LNO remain rare, the work by Huth and Flynn [HUT99] being an exception. It's also to note that, to the best of our knowledge, only the specific LNO Z-cut orientation has been used as a substrate for MBE epitaxial growth.

One objective in this PhD thesis is to go beyond Huth and Flynn first success in two main directions:
(i) To reproduce the (111) $TbFe_2$ growth on LNO Z-cut in undertaking a careful analysis of orientation relationships between buffer layers and LNO, and between $TbFe_2$ and buffer layers, in the case of single and double templates.
(ii) To extend the $TbFe_2$ MBE growth to deposition on other LNO orientations, more specifically 128Y- and 41Y-cuts, the properties of which let envision the development of SAW-based devices. Those non-conventional surfaces would add some complexity to the growth process and the determination of related OR.

Chapter 2: The $LiNbO_3$ substrates

All LNO substrates used in this work belong to the congruent type. Among them, we have tried both the commonly called "white" and "black" LNO. White LNO corresponds to the congruent LNO described in first part, while black LNO has been chemically reduced after Czochralski production, which gives this peculiar color (because of a significant increase of the optical absorption of the crystal [STA98]). The degree of depletion depends on the reduction temperature and atmosphere. This process strongly reduces the pyroelectric effect by increasing the conductivity (from 2.63×10^{-15} $\Omega^{-1}.cm^{-1}$ in white LNO to 4.17×10^{-11} $\Omega^{-1}.cm^{-1}$ in black LNO). The piezoelectric properties should be identical in white and black LNO but one could mention an increase of the average surface roughness from 0.4 nm in white LNO to 1.7 nm in black LNO.
Since the structural characterizations of the layers deposited on black or white LNO are very similar, no distinction will be done in this thesis.

1. Different cuts of Lithium Niobate

Crystal cuts of LNO are of prime importance because they dictate the surface properties (piezoelectric properties, optical properties…).
By using the orthogonal basis defined in Figure 6, the direction of a cut is specified with the name of the substrate. In this work, three different LNO cuts/orientations have been used.
(i) LNO Z-cut (Figure 11 (a)). The cut is performed perpendicular to the Z-axis, which is consequently the perpendicular to the surface plane. This substrate cut exhibits an hexagonal surface symmetry and has already been used for $TbFe_2$ growth, as shown in the state of the art [HUT99].
(ii) LNO 128 Y-cut (Figure 11 (b)). This cut indicates that the crystal is cut at the plane 128° rotated from the Y-plane about the X-axis (counterclockwise rotation). The Z-axis, *i.e.* a_4-axis of the crystal is thus tilted by -38° from the normal to the surface. This substrate exhibits a medium electromechanical coupling factor (intermediate band filter) for non-leaky SAW in SAW devices [HAS00].
(iii) LNO 41 Y-cut (Figure 11 (c)). This cut indicates that the crystal is cut at the plane 41° rotated from the Y-plane about the X-axis (counterclockwise rotation). The Z-axis, *i.e.* a_4-axis of the crystal is thus tilted is thus tilted by +49° from the normal to the surface. This substrate exhibits a high electromechanical coupling factor (large band filter) even if SAW are leaky in SAW devices [HAS00].

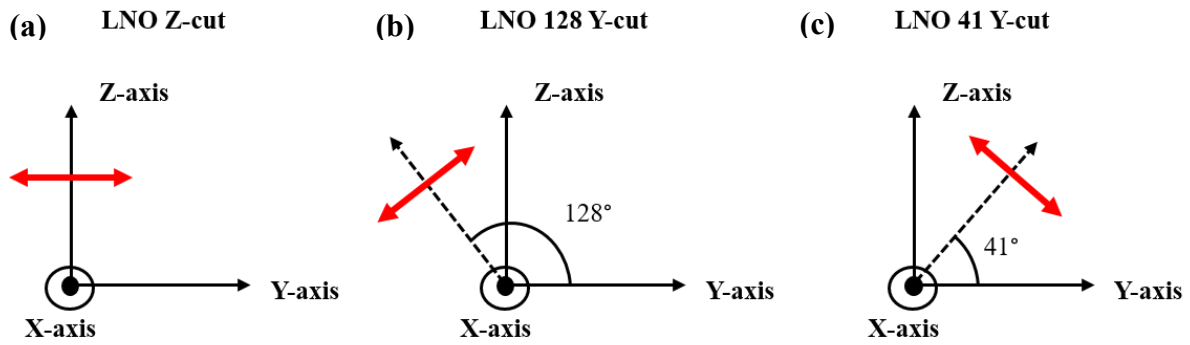

Figure 11. Sketch of different LNO cuts (parallel to red arrows) with respect to the orthogonal basis.

In our LNO cuts, it must be noticed that except the LNO Z-cut, which contains after crystal cut X- and Y-axes in its surface plane, other LNO cuts will contain only X-axis. The in-plane axis perpendicular to X will be refer as X+90°-axis.

Figure 12 presents two convenient ways that will be used in the following to analyze and discuss the orientation of these different cuts and of the deposited layers.
The first one (Figure 12 (a)) corresponds to the relative positions of (0001) Bragg reflections in the reciprocal space in the case where the three different LNO surface planes are parallel (black); the surface normal is vertical and the X direction points out. The (0001) reflection for the LNO Z-cut (red) is along the specular direction, while they are rotated by +49° and -38° respectively for LNO 41 Y-cut (green) and LNO 128 Y-cut (blue). For those two latter cuts, the Bragg reflections close to or on the specular direction have been also added. The $(10\bar{1}4)$ reflection for LNO 128 Y-cut is on the specular direction since those planes are parallel to the surface. The surface of LNO 41Y-cut doesn't correspond to any specific crystallographic plane, but $(01\bar{1}2)$ planes are tilted by -8° from the surface, which gives rise to the $(01\bar{1}2)$ reflection, close to the specular direction.
The second way to present the relative orientations of those LNO cuts (Figure 12 (b)) is to use stereographic projections (appendix C). This figure is the superimposition of the stereographic plots corresponding to the three different cuts with the common X-axis horizontal. The central pole corresponds to the surface normal while the poles on the outer circle (90° from the center) correspond to in-plane directions. For each cut, the 0001 pole and the main poles contained in the (0001) plane (hexagonal symmetry), *i.e.* the $< 11\bar{2}0 >$ (direction link the atom of the center to an atom of the hexagon edge) and $< 1\bar{1}00 >$ directions are presented.

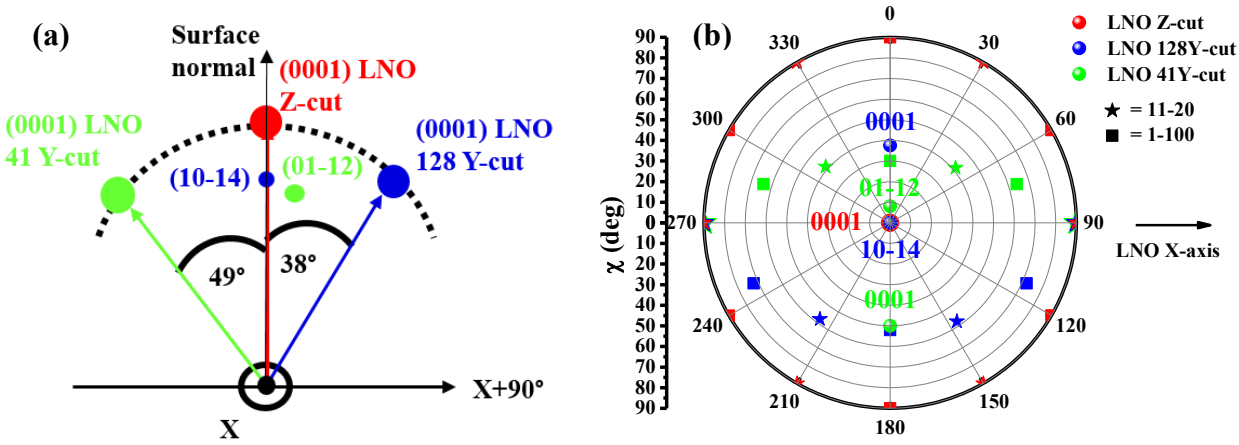

Figure 12. Relative positions of (0001) Bragg reflections expected for parallel LNO Z (red), 128 (blue) and 41 (green) Y-cuts. Additional reflections close to, or on the specular direction are added for LNO 128Y and LNO 41Y cuts (a). Positions of high symmetry crystallographic directions for LNO substrates (same color code) on stereographic projections. Stars ($< 11\bar{2}0 >$) and squares ($< 1\bar{1}00 >$) represent the directions contained in the LNO (0001) planes (b).

For all experiments presented in this part, the Lithium Niobate substrates are first cleaned with acetone and isopropanol and rinsed with de-ionized water. Since Nam *et al.* [NAM11] warn about a deterioration of the LNO at high temperature (1000° in air), the outgas process in the UHV chamber was limited to one hour at 500 °C. At this temperature, no change in RHEED patterns could be observed and residual gas analyzer shows no increase of pressure.

1.1. LNO Z-cut

This orientation of LNO corresponds to a (0001) surface that exhibits an hexagonal symmetry, as it is sketched in Figure 13 (a). In Figure 13 (b) are recalled the equivalent in-plane directions in the (0001) plane with $< 1\bar{1}00 >$ and $< 11\bar{2}0 >$ in red and blue respectively (conventional hexagonal coordinate system with 4 subscripts (a_1, a_2, a_3, a_4)).

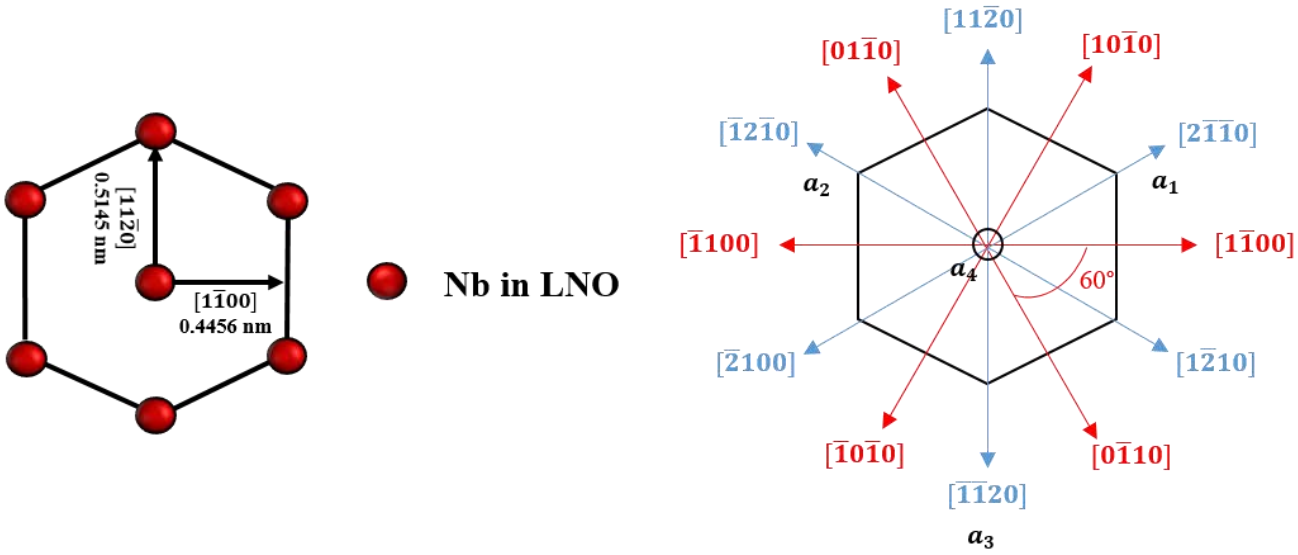

Figure 13. Representation of the LNO Z-cut surface (Nb plane) (a). Equivalent in-plane directions [hk-(h+k)l] in the (0001) plane using the hexagonal coordinate system (a_1, a_2, a_3, a_4) (b).

The RHEED analysis of this surface (Figure 14) is consistent with the hexagonal symmetry and with the observation of two different types of patterns separated by 30° and reproduced every 60°. The measurement of relative inter-streaks distances yields a ratio of 1.73 and permits to identify the main [11$\bar{2}$0] and [1$\bar{1}$00] azimuthal directions.
One can underline that the RHEED measurement is relatively difficult due to the insulating nature of the substrate, but remains possible when increasing the temperature and grounding the substrate holder.

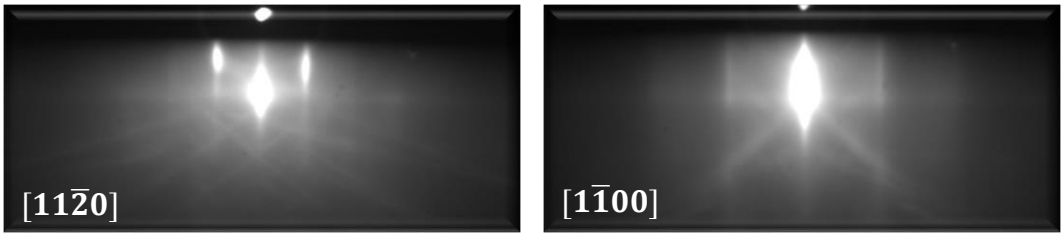

Figure 14. RHEED patterns collected for LNO Z-cut at 500 °C along two azimuths rotated by 90°.

A large number of tilted and symmetrical lines with respect to the vertical can be observed. These are the so-called Kikuchi lines, due to incident electrons that have been "channeled" following a first quasi-elastic diffusion in the crystallographic structure of the material (thus in depth) and that emerge in precise directions. They are more visible when the material exhibits a high crystallographic quality and when the material is a bad conductor [AND05].

1.2. LNO 128 Y-cut

As mentioned previously, the LNO 128 Y-cut corresponds to (10$\bar{1}$4) surface planes. Nb atoms form a rectangular mesh, as sketched in Figure 15.

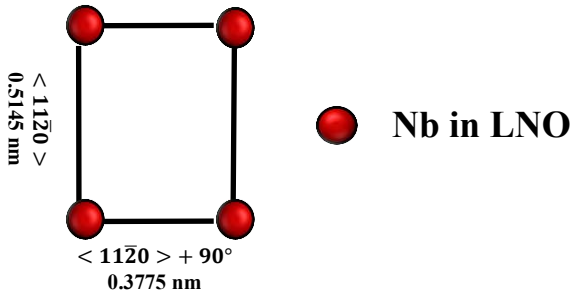

Figure 15. Representation of the LNO 128 Y-cut surface (Nb plane).

The RHEED analysis of this surface (Figure 16) is consistent with the expected rectangular symmetry. The main directions are separated by 90°. The measurement of relative inter-streaks distances yields a ratio of 1.36 and permits to identify the main $< 11\bar{2}0 >$ and $< 11\bar{2}0 > + 90°$ azimuthal directions. Once again, the existence of Kikuchi lines attests for the good crystalline order.

Figure 16. RHEED patterns collected for LNO 128 Y-cut at 500 °C along two azimuths rotated by 90°.

1.3. LNO 41 Y-cut

The surface corresponding to the 41 Y-cut doesn't correspond to any specific crystalline plane, which makes the RHEED observation and analysis very hazardous, as it can be seen in Figure 17. The determination of the $< 11\bar{2}0 >$ azimuthal direction is only possible from the orientation information provided by the supplier and is verified from X-ray diffraction experiments. One can however notice along $< 11\bar{2}0 >$ the presence of tilted streaks, approximately ± 8.26° off the normal to the surface. Those might be related to the diffraction in the close $(01\bar{1}2)$ planes since the electron beam lies along the $< 11\bar{2}0 >$ zone axis, *i.e.* along possible step edges (appendix E).

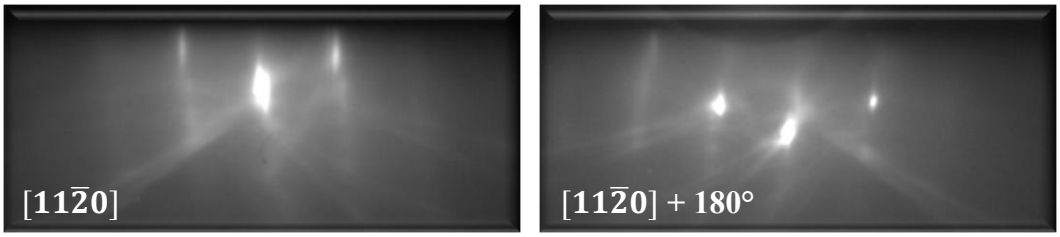

Figure 17. RHEED patterns collected for LNO 41 Y-cut at 500°C along two azimuths rotated by 180°.

2. Effect of temperature

Previous studies have reported on specific issues linked to the heating of LNO, especially the depletion in Lithium and Oxygen [NAM05]. This depletion can lead to a surface rearrangement, increased roughness, a new surface chemistry and it can also oxidize the upper layers.

The dissociation reaction of $LiNbO_3$ is described by:

$$3LiNbO_3 \rightarrow LiNb_3O_8 + Li_2O$$

where the $LiNb_3O_8$ phase (Lithium Triniobate) forms at $LiNbO_3$ surface for temperatures in the 300 °C - 900 °C range in air by decomposition of Li_2O [NAM05]. At T > 900 °C, the Lithium Niobate becomes monophasic ($LiNb_3O_8$ precipitates are absorbed onto the substrate surface via a retransformation to the $LiNbO_3$ phase) and the surface changed to a stepped surface morphology with low roughness and with the same initial symmetry [NAG97].
It must be noted that the monoclinic phase of Lithium Triniobate (a = 1.5262 nm, b = 0.5033 nm and c = 0.7457 nm with $\alpha = \gamma = 90°$ and $\beta = 107.34°$) precipitates epitaxially on LNO substrates. Mostly, it's $LiNb_3O_8$ $(20\bar{6})$ for LNO Z-cut. The mutual orientations between the two materials is characterized by the parallel nature of the directions:

$$LiNb_3O_8\ [010]\ //LiNbO_3\ [11\bar{2}0]$$

regardless of the substrate orientations. The $LiNb_3O_8$ islands are aligned such that the single symmetry face of the Lithium Triniobate coincides with each of the three symmetry planes of LNO by using variant [MCC94].

In order to check this problem of stability, several experiments have been carried out to analyze the LNO after heating in UHV.
(i) Secondary Ion Mass Spectroscopy (SIMS) analysis performed during etching of SAW-based devices has confirmed the rise of Lithium after heating. Oxygen has not been observed since its signal is too small.
(ii) X-ray diffraction experiments have evidenced a diffraction peak associated to Lithium Triniobate in a LNO Z-cut substrate after a one hour heating at 700 °C under UHV (black curve in Figure 18). This peak is cleary absent for a pristine LNO Z-cut substrate (red curve).

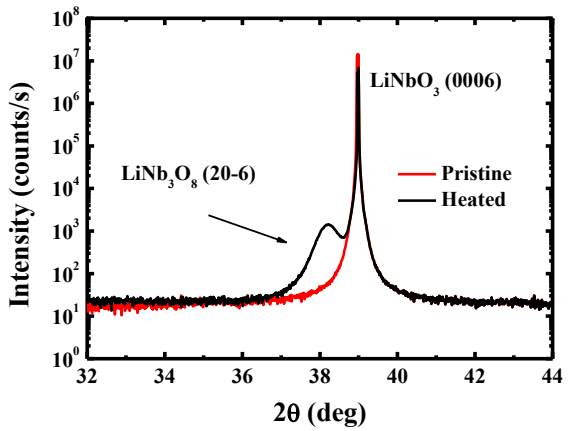

Figure 18. Large angle X-ray specular scans measured for a LNO Z-cut substrate before (red) and after one hour annealing at 700 °C in UHV (black).

This peak correspond to $(20\bar{6})$ Lithium Triniobate. The full width at half maximum of the rocking curve across the (0006) LNO Bragg peak also significantly increases from 0.02° before heating to 0.6° after heating.
Finally, it should be noted that the X-ray diffraction experiments performed for LNO 41Y and 128 Y cut substrates also suggest some degradation process with the occurrence of multiple peaks appearing upon heating and depending on the annealing temperature (not reported here).
(iii) Transmission Electron Microscopy (TEM) permits to directly visualize the deteriorated layer at the substrate surface (Figure 19). The sample presented here corresponds to a multilayer stack deposited on LNO Z-cut at temperatures up to 500 ° C for at least 5 hours in vaccum.

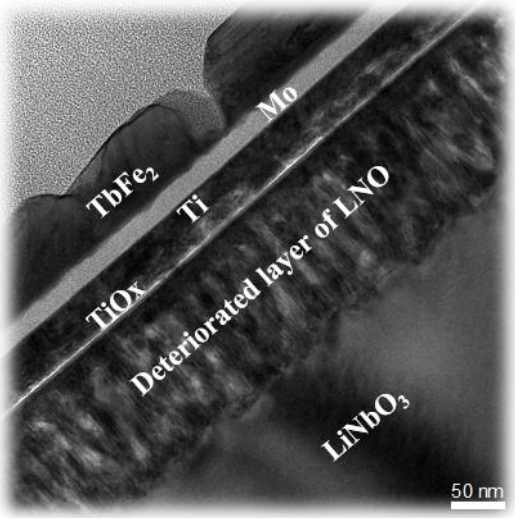

Figure 19. TEM image of the LNO Z-cut after being heated up to 500 °C during 5 hours in UHV.

LNO is degraded over a 140 nm thick layer at the interface. Energy-Dispersive X-ray spectroscopy (EDX) measurements suggest that the composition has strongly changed in this deteriorated layer. The measurement accuracy is however not good enough to allow us determining an exact composition.
The Lithium and Oxygen atoms diffusing from LNO can of course lead to the deterioration of the deposited layers, which fully jusitifies the need of efficient buffer layers when dealing with high temperature growth.

Chapter 3: Growth of $TbFe_2$ on LNO Z-cut

This chapter summarizes the results concerning the $TbFe_2$ growth experiments performed on LNO Z-cut by molecular beam epitaxy. Since different buffer layers have been used (single Ti, Mo or Nb layers, or Ti/Nb and Ti/Mo bilayers), we have chosen to first detail the growth of these various templates before reporting the growth of $TbFe_2$. In-situ RHEED (appendix E) and ex-situ X-ray experiments (appendix C) have been mainly carried out to determine the OR between successive crystal lattices, the possible occurrence of multiple domains and to estimate the structural quality of the deposited layers. The magnetic characterization of the $TbFe_2$ layers deposited on LNO Z-cut were performed by VSM to analyze the magnetic anisotropy in connection with our knowledge of structural characteristics.

1. Buffer layers

The use of buffer layers in the process of thin metallic film deposition is very common for various reasons depending on the metallic film that has to be grown, among which one can mention: (i) to form a chemical diffusion barrier between the substrate (most of the time an oxide) and the metallic layers, (ii) to help the adhesion of the layer onto the substrate, (iii) to promote a specific surface symmetry and thus favor specific growth planes, if low surface free energy conditions are fulfilled, (iv) to reduce a lattice mismatch and favor epitaxial growth, (v) to impose a given lattice mismatch and control the strain state of the film…
From the study by Huth *et al.* [HUT99], the epitaxial growth of $TbFe_2$ on LNO is particularly challenging and an optimal process requires a Ti/Mo bilayer both to initiate the growth and limit the diffusion of Lithium and Oxygen during the deposition. For the development of hybrid piezoelectric/magnetostrictive multiferroics where the magnetoelectric coupling should occur via the interface mechanical coupling between both functional materials, the use of thick intermediate templates could be prohibitive. It can reduce the propagation of strain and also increases the time spent at high temperature during deposition, with the related problematic effect on the chemistry and structure of the LNO interface region.

One goal is thus to revisit the growth of a single template directly on LNO: Ti, Mo and Nb. As Mo and Nb were shown to be suitable buffers for high quality growth on Al_2O_3 $(11\bar{2}0)$ [MOU99a], nothing was up to now reported concerning their direct growth on LNO (except Ti/Mo bilayer in [HUT99]). Double Ti/Mo and Ti/Nb templates have been then synthetized and characterized.
Although various thicknesses of buffer layers have been used in the [10 - 100 nm] range, the results presented here concern the 50 nm thick layers because no significant structural differences were observed.

1.1. Single buffer layers

1.1.1. Titanium growth

As proposed by Huth and Flynn [HUT99], the Titanium deposition is performed with the substrate kept at 100 °C, for deposition rates between 0.04 and 0.1 $nm.s^{-1}$ without a clear incidence of this parameter on the crystalline quality.
The in-situ RHEED analysis performed during the deposition process exhibits features after approximately 1-2 nm. Two typical RHEED patterns obtained at 100 °C after the deposition of 50 nm

thick Ti are presented in Figure 20 (c and d). Those are measured along the two main azimuthal directions of LNO Z-cut reported above (Figure 20 (a and b)).

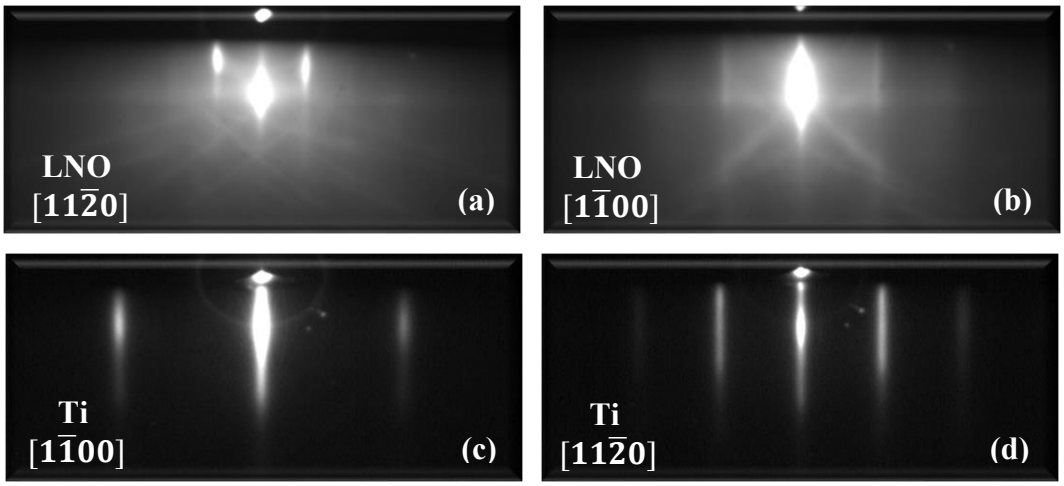

Figure 20. RHEED patterns for LNO Z-cut (a and b) and 50 nm thick Ti (c and d) collected at 100 °C along two azimuthal directions rotated by 90°.

The Ti RHEED patterns exhibit continuous streaks characteristic of a relatively smooth surface (appendix E). Two successive RHEED patterns measured in rotating the sample around its normal direction reveal an hexagonal symmetry with two main directions rotated by 30°, each being reproduced every 60°. From the relative inter-streak distances, it is possible to confirm the 1.73 ratio expected from the (0001) plane and the $[1\bar{1}00]$ and $[11\bar{2}0]$ azimuthal directions, as noted in Figure 13.

A specular θ/2θ X-ray scattering scan (Figure 21) confirms the diffraction by (0001) planes, parallel to the sample surface and to LNO (0001) planes. The rocking curve across the (0002) Ti Bragg peak exhibits a full width at half maximum of 0.8°, which is a sign of a reasonable crystalline quality. The coherence length (appendix C) is approximatively 25 nm. The possible $LiNb_3O_8$ peak is most likely hidden in the Ti Bragg peak since they are very close.

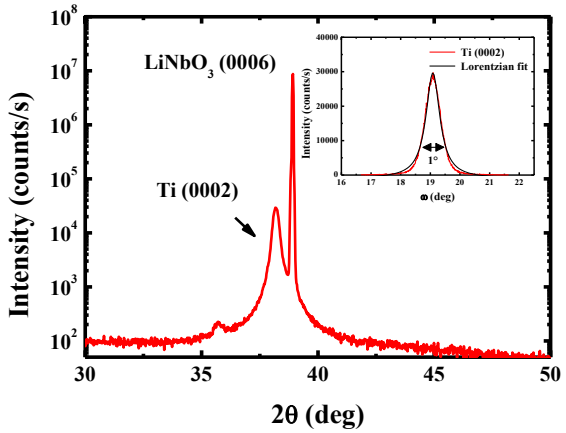

Figure 21. θ/2θ X-ray scattering scan measured for a 50 nm thick Ti layer deposited at 100 °C on LNO Z-cut (rocking curve across the (0002) Ti Bragg peak in inset).

The epitaxial relationships can thus be described as follows:

$$Ti\ (0001)\ //\ LNO\ (0001)$$

with:

$$Ti\ [11\bar{2}0]\ //\ LNO\ [1\bar{1}00]$$
$$Ti\ [1\bar{1}00]\ //\ LNO\ [11\bar{2}0]$$

This 30° rotation between LNO and Ti basal planes lattices (sketched in Figure 22) enables a relatively good crystalline match, with a 1 Ti : 1 LNO coincidence between atomic rows perpendicular to the LNO $[11\bar{2}0]$ direction and a 3 Ti : 1 LNO coincidence between atomic rows perpendicular to the LNO $[1\bar{1}00]$ direction.

Along LNO $[11\bar{2}0]$, the lattice mismatch is: $\frac{a_{LNO}-\sqrt{3}a_{Ti}}{\sqrt{3}a_{Ti}} = 0.704\ \%$.

Along LNO $[1\bar{1}00]$, the lattice mismatch is: $\frac{\sqrt{3}a_{LNO}-3a_{Ti}}{3a_{Ti}} = 2.13\ \%$.

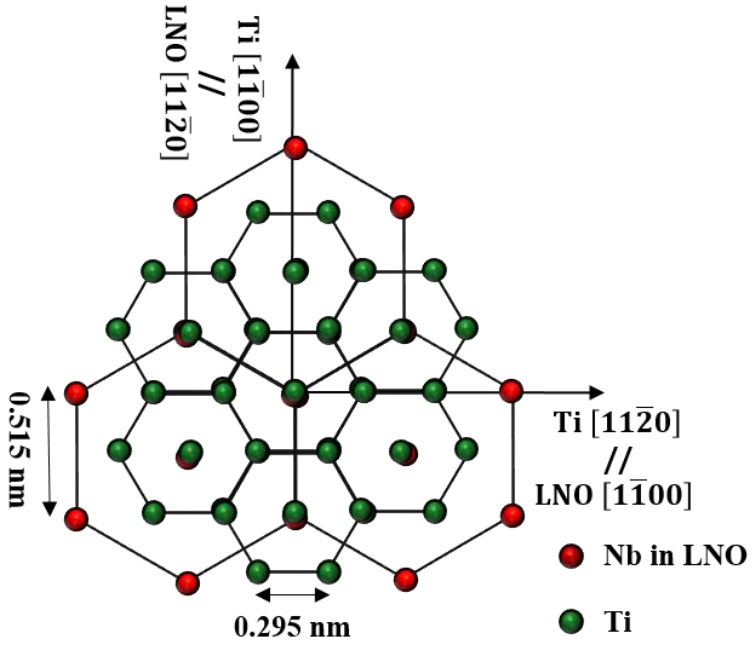

Figure 22. Sketch of the Ti (0001) surface (green) on LNO (0001) surface (Nb atoms of LNO in red).

As mentioned previously, the above results correspond to a Ti film deposited at 100 °C. The growth of the next layer, another buffer layer or the $TbFe_2$ layer however requires an increase in temperature than can reach 600 °C - 700 °C for the time required to grow the layer. In order to explore the incidence of this heating on the LNO/Ti system, complementary experiments have been performed by recording X-ray scans at successive temperatures in heating the system by 16.5 °C/min under atmospheric pressure (Figure 23).

These measurements reveal the progressive degradation of the Ti layer with first the appearance of a TiO_2 (Anatase) (004) Bragg peak above 300 °C and then the occurrence of several contributions most likely attributed to different TiO_x + Ti compositions. As reported previously, a Lithium Triniobate layer develops at the LNO surface when the substrate is heated to in air [NAG97]. In this experiment, the same effect seems to occur.
Although these experiments do not exactly correspond to the UHV deposition process, they provide important informations on the degradation/oxidation of the Ti layer, either by Oxygen from the atmosphere or by Oxygen diffusing from the substrate.
The oxidation of the Ti layer under UHV is confirmed by TEM experiments that reveals the rise of Oxygen in the Ti layer from the substrate (Figure 19). From chemical analysis (EDX), approximatively 60% of the Titanium layer seems to be oxidized.

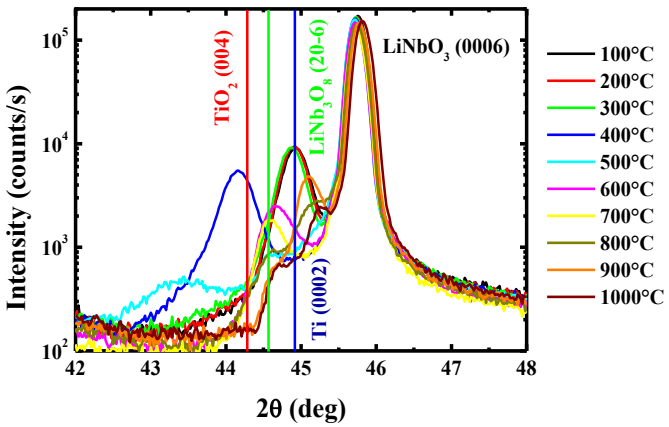

Figure 23. θ/2θ X-ray scattering scans (Cobalt wavelength) measured in increasing temperature (16.5 °C/min) under atmospheric pressure for a 50 nm thick Ti deposited on LNO Z-cut.

1.1.2. Niobium and Molybdenum growth

Niobium and Molybdenum deposition have been performed using various deposition rates in the [0.02 $nm.s^{-1}$ – 0.07 $nm.s^{-1}$] range without a clear incidence of this parameter on the crystalline quality. The deposition temperatures have been varied in the [400 °C - 800 °C] range. High temperatures, above 700 °C, are generally reported as optimal for the deposition of high quality Nb or Mo films on sapphire substrates [KWO86, HUT98a, HUT98b] but the specificities of LNO led us to test and decrease these deposition temperatures to lower temperatures.
In contrast to the results obtained on sapphire, deposition temperatures above 500 °C yield a lower crystallization quality (as observed by X-ray diffraction) than deposition temperatures under 500 °C. For temperature below 500 °C, two distinct RHEED patterns rotated by 30°, each being reproduced every 60°, could be observed (Figure 24), both for Nb (c and d) and Mo (e and f) deposits.

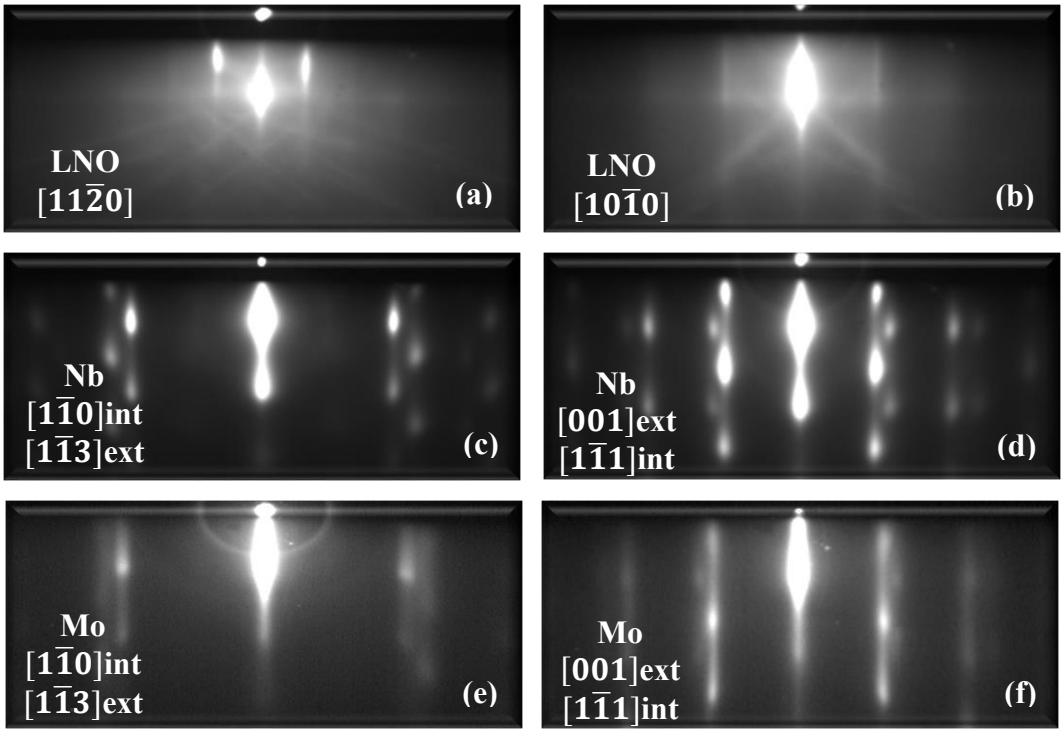

Figure 24. RHEED patterns of LNO Z-cut (a and b), 50 nm thick Nb deposited at 450 °C (c and d) and 50 nm thick Mo deposited at 450 °C (e and f) collected along two azimuths rotated by 30°.

These two typical patterns are rather similar for both elements although they are more dotted for Nb, revealing a stronger 3D character, *i.e.* an increased surface roughness (appendix E). In both cases, one can observe the clear superposition of several diffraction patterns that could not be separated in tilting the azimuth angle and that could not be simply identified.

Specular θ/2θ X-ray scattering scans (not shown here) reveal that the Nb and Mo layers grow along the [110] direction, which is the one generally stabilized because of the very low surface free energy for (110) planes. The FWHM determined from the rocking curves are relatively large: 1.75° for Mo and 3° for Nb. Coherence length are 25 and 13 nm for Mo and Nb respectively.
φ scans on Asymmetrical Reflections (AR) (appendix C) were performed to unravel the in-plane orientation relationships between Nb/Mo and LNO (Figure 25 (a and b respectively)).

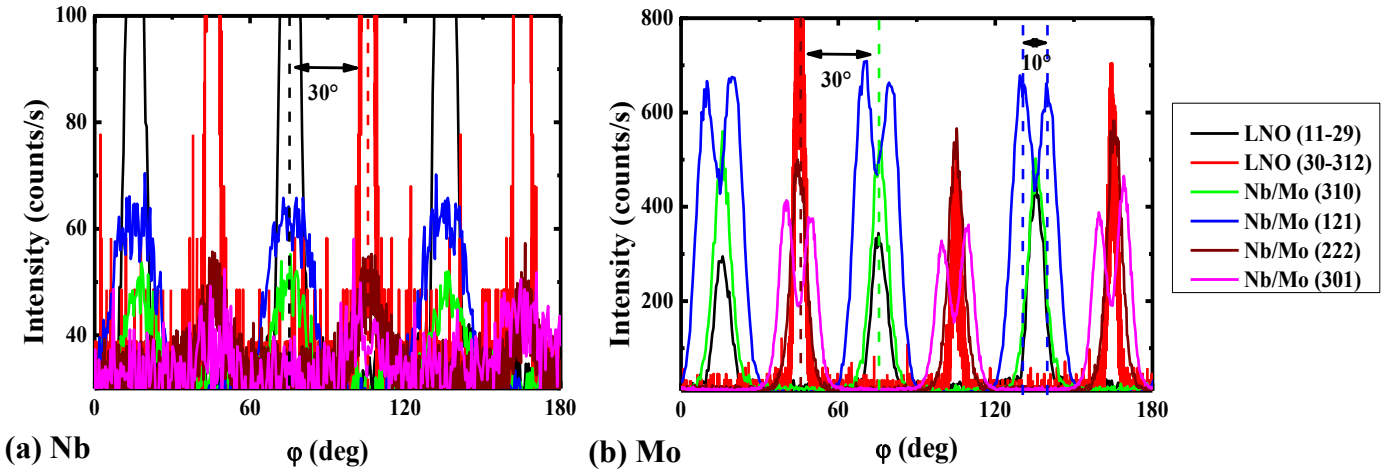

Figure 25. φ scans for asymmetrical reflections measured for Nb (a) and Mo (b) deposited on LNO Z-cut. AR are also measured for LNO in both cases.

As explained in appendix C, the observation of asymmetrical Bragg reflections peaks is possible for a given in-plane orientation of the crystal lattice only when the in-plane direction shared by the surface planes and the asymmetrical diffracting planes is perpendicular to the scattering plane. The Table 17 presented in appendix C recalls which in-plane direction can be identified via the measurement of a given asymmetrical reflection.
As expected for LNO Z-cut, 30° separate the AR related to $< 1\bar{1}00 >$ and $< 11\bar{2}0 >$ in-plane directions. For the Mo and Nb films, the φ scans permit to identify three $< 001 >$ (rotated by 60°) and three $< 1\bar{1}0 >$ directions (rotated by 60°) over the 180° angular range. These reveal the occurrence of three (110) domains rotated by 60° and the following in-plane OR respect to the LNO lattice:

$$Mo\ or\ Nb\ [001]\ //\ LNO\ [1\bar{1}00]$$
$$Mo\ or\ Nb\ [1\bar{1}0]\ //\ LNO\ [11\bar{2}0]$$

Consistently with this OR, $< 1\bar{1}1 >$ directions (resp. $< 1\bar{1}3 >$ directions) are localized at approximatively ± 5° from $< 001 >$ directions (resp. $< 1\bar{1}0 >$ directions), as shown in appendix D. One can however underline the poorer quality of the Nb film for which the larger in-plane dispersion doesn't enable the clear observation of the distinct reflections separated by 10°. The Nb (301) reflections can by the way be measured only with a very grazing incidence of 0.2°.

The observed RHEED patterns (Figure 24) correspond to the superposition of the diffraction patterns related to the occurrence of the three domains and to a relatively wide spread of crystal orientation in the surface plane. As expected from the [110] growth direction, the ratio between inter-streaks distances have been checked to be 1.41 for $[1\bar{1}0]$ and [001] azimuths and 1.92 for $[1\bar{1}1]$ and $[1\bar{1}3]$ azimuths.

The three distinct domains for Nb or Mo deposited on LNO Z-cut are presented in Figure 26 (Nb or Mo atoms in blue, Nb atoms of LNO in red).

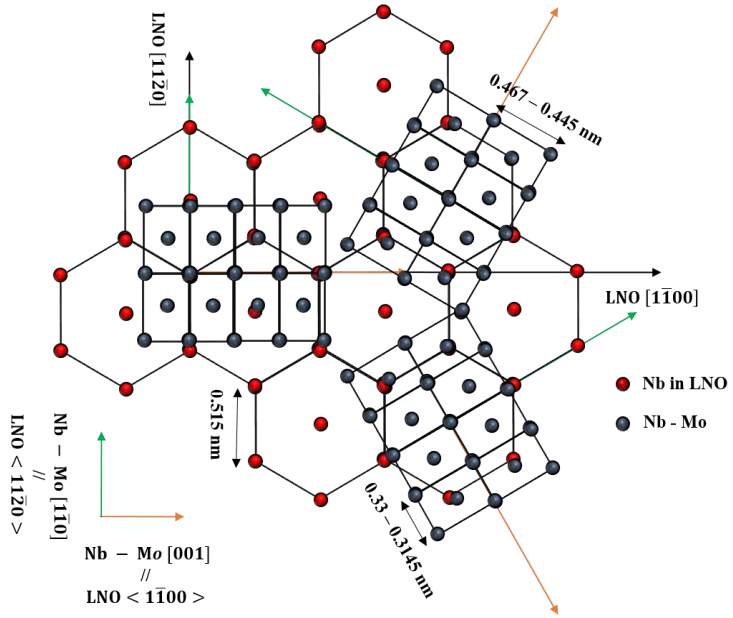

Figure 26. Superimposition of the three domains observed for the Niobium - Molybdenum (110) surface (blue) on R30-orientation with respect to LNO (0001) (Nb atoms of LNO in red).

This specific OR between the Nb/Mo (110) lattice and the LNO (0001) lattice is different from the most common OR reported between (110) bcc and (111) fcc lattices (or (0001) hcp lattice), *i.e.* the Nishiyama-Wassermann and the Kurdjumov-Sachs OR (appendix D). These orientations are basically predicted by the rigid-lattice theory and depend on the ratio between nearest neighbor distances in the surface plane. The currently observed OR, so-called R30 (bcc $[1\bar{1}0]$ // fcc $[1\bar{1}0]$), has been already theoretically predicted and observed in Ce/V bilayers [HOM87] .
As in the case of NW-OR, the underlying hexagonal symmetry gives rise to the occurrence of three (110) domains, but tilted by 30° compared to the domains observed in NW orientation.
In the case of Nb/Mo (110) on LNO (0001), the R30-OR corresponds to the approximate match of:
1 Nb/Mo : 1 LNO atomic rows perpendicular to LNO $[11\bar{2}0]$ with a resulting mismatch:

$$\frac{a_{LNO} - \sqrt{2}a_{Nb/Mo}}{\sqrt{2}a_{Nb/Mo}} = +10.24\% \text{ for Nb} \qquad \text{and} \qquad +16.21\% \text{ for Mo}$$

3 Nb/Mo : 1 LNO atomic rows perpendicular to LNO $[1\bar{1}00]$ with a resulting mismatch:

$$\frac{\sqrt{3}a_{LNO} - 3a_{Nb/Mo}}{3a_{Nb/Mo}} = -9.94\% \text{ for Nb} \qquad \text{and} \qquad -5.65\% \text{ for Mo}$$

The ratios between nearest neighbor distances (x_{bcc}/y_{LNO}) in the surface plane are $r_{Mo/LNO} = 0.529$ and $r_{Nb/LNO} = 0.556$, which is relatively far from the ideal value of 0.61 reported for the R30-OR (appendix D). If one however considers the above mentioned 3:1 match of atomic rows perpendicular to LNO $[1\bar{1}00]$, the optimal ratio is deduced in equalizing the distances between these atomic rows:

$$\frac{\sqrt{3}y_{LNO}}{2} = \frac{3x_{Nb/Mo}}{\sqrt{3}}$$

This leads to a ratio $x_{Nb/Mo}/y_{LNO}$ of 0.5 that can explain the stabilized R30-OR experimentally observed.

1.2. Double buffer layers (Ti/Nb and Ti/Mo)

In a second step, the synthesis of double Ti/Nb and Ti/Mo templates was studied by varying the deposition rates in the [0.03 nm.s^{-1} – 0.1 nm.s^{-1}] range without a clear incidence of this parameter on the crystalline quality.
In contrast to the results published by Huth and Flynn [HUT99] on LNO, deposition temperatures above 500 °C didn't permit the suitable growth of multilayers because of adhesion problems on the LNO surface. Cracks that can lead to the partial removal of the layer were systematically observed after the deposition process.
Deposition temperatures in the [100 °C - 500 °C] range enabled the crystalline growth and the adhesion of Nb/Mo on Ti, but the crystalline quality decreases when decreasing the temperature with the rise of a diffuse background in the RHEED pattern and a tendency to form a polycrystalline structure. The results reported in the following correspond to the films deposited at 450 °C.

Figure 27 presents the RHEED patterns collected for Ti (a and b), Nb on Ti (c and d) and Mo on Ti (e and f) along the two main azimuthal directions of (0001) Ti.

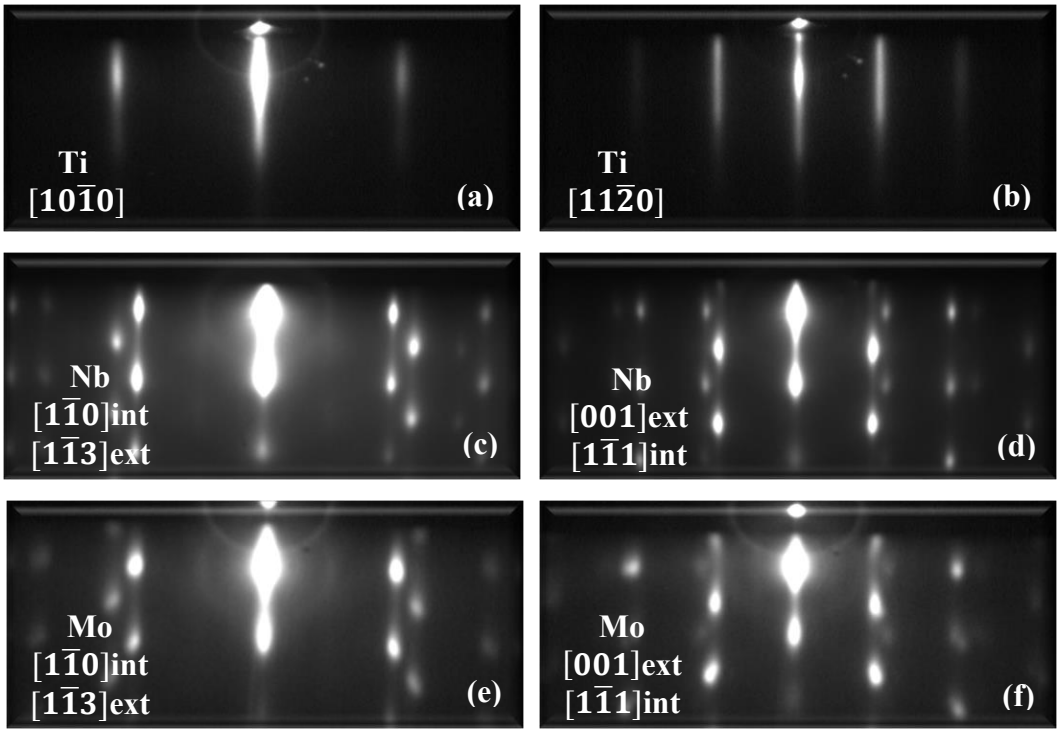

Figure 27. RHEED patterns collected along two azimuths rotated by 30° for 50 nm thick Ti deposited at 100 °C (a and b), 50 nm thick Nb deposited at 450 °C on Ti (c and d) and 50 nm thick Mo deposited at 450 °C on Ti (e and f).

As in the case of direct growth of Nb or Mo on LNO, two different RHEED patterns rotated by 30° and reproduced every 60° are observed. They obviously also correspond to the superposition of several diffraction patterns and reveal a significant surface roughness.

Large angle specular X-ray scans (not reported here) reveal a [110] growth direction. Although the position of the Nb (110) and Ti (0002) diffraction peaks at approximatively the same 2θ position does not help the deconvolution of them, the FWHM for the rocking curves across (110) Bragg reflections are 0.9° for Mo and 1.2° for Nb. The coherence lengths are 32 nm for Mo and 18 nm for Nb, both features suggesting a better quality than for single buffer layers directly grown on LNO.
φ scans on asymmetrical reflections (AR) were performed to unravel in-plane OR with respect to the underlying Ti lattice (Figure 28 ((a) for Ti/Nb and (b) for Ti/Mo)).

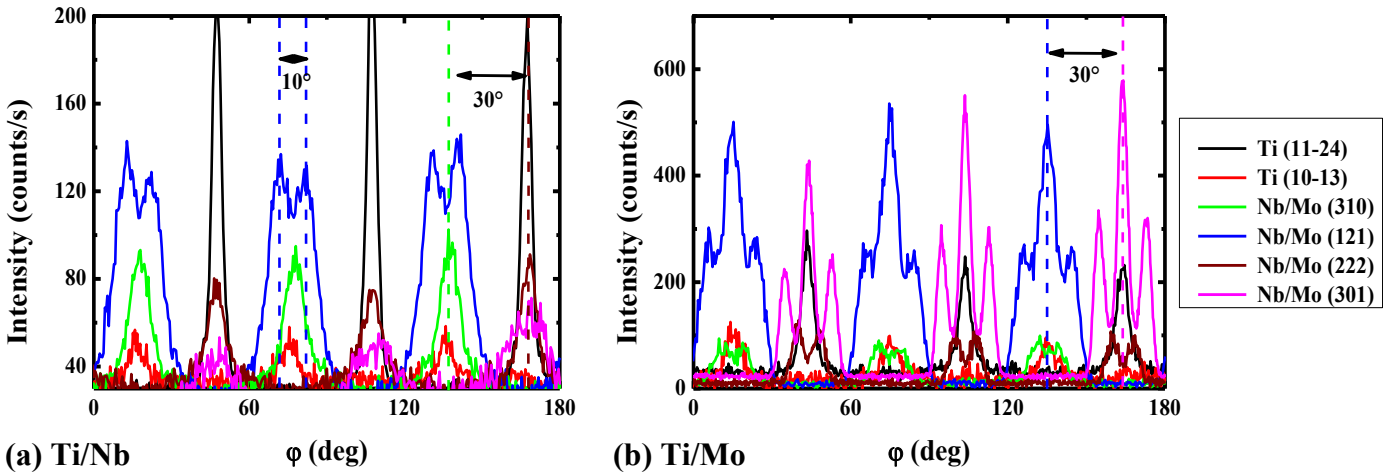

Figure 28. φ scans for asymmetrical reflections for Ti/Nb (a) and Ti/Mo (b) deposited on LNO Z-cut.

One can first notice the expected 30° separation for the Ti AR related to $< 1\bar{1}00 >$ and $< 11\bar{2}0 >$ in-plane directions. Despite relatively similar RHEED patterns, φ scans obviousy reveal different OR for Mo/Ti and Nb/Ti systems.
For Nb, three in-plane $< 001 >$ (rotated by 60°) and three in-plane $< 1\bar{1}0 >$ directions (rotated by 60°) can be identified over the 180° angular range. They reveal the occurrence of three (110) domains rotated by 60 ° and the following in-plane OR respect to the Ti lattice:

$$Nb\ [001]\ //\ Ti\ [11\bar{2}0]$$
$$Nb\ [1\bar{1}0]\ //\ Ti\ [1\bar{1}00]$$

This corresponds to the Nishiyama-Wassermann (NW) OR (bcc [001] // fcc $[1\bar{1}0]$) [HEL98] and consistently with this OR, $< 1\bar{1}1 >$ directions (resp. $< 1\bar{1}3 >$ directions) are localized at approximatively ± 5 ° of $< 001 >$ directions (resp. $< 1\bar{1}0 >$ directions), as shown in appendix D.
It must be noted that intensity and resolution of Nb asymmetrical reflections (AR) are improved for bilayer buffer (Ti/Nb) respect to single buffer (Nb).

For Mo, six $< 001 >$ and six $< 1\bar{1}0 >$ directions can be identified over the 180° angular range, revealing the formation of six (110) domains. In this case, the comparison of φ angles related to Ti and Mo AR leads to the following in-plane OR between Mo and Ti lattices:

$$Mo\ [1\bar{1}1]\ //\ Ti\ [11\bar{2}0]$$
$$Mo\ [1\bar{1}3]\ //\ Ti\ [1\bar{1}00]$$

These correspond to the Kurdjumov-Sachs (KS) OR (bcc $[1\bar{1}1]$ // fcc $[1\bar{1}0]$) [HEL98], where each alignment of Mo $< 1\bar{1}1 >$ on the three equivalent Ti $< 11\bar{2}0 >$ gives rise to two domains because of the occurrence of two equivalent $< 1\bar{1}1 >$ directions in the Mo (110) plane. The succession of in-plane directions identified by AR is fully consistent with the relative orientation of the six domains, as detailed in appendix D.

For both Nb deposited in NW-OR and Mo deposited in KS-OR, RHEED patterns collected along the main Ti azimuthal directions result from the same superposition of diffraction patterns. The KS-OR for Mo on Ti should however lead to a wider angular range where this superposition is visible. This was not clearly the case in our experiments, most likely due to a poorer in-plane orientation (wider dispersion) for Nb.

Figure 29 presents the OR between Nb and Ti lattices (a) and between Mo and Ti lattices (b). Only one domain is sketched here for each case.

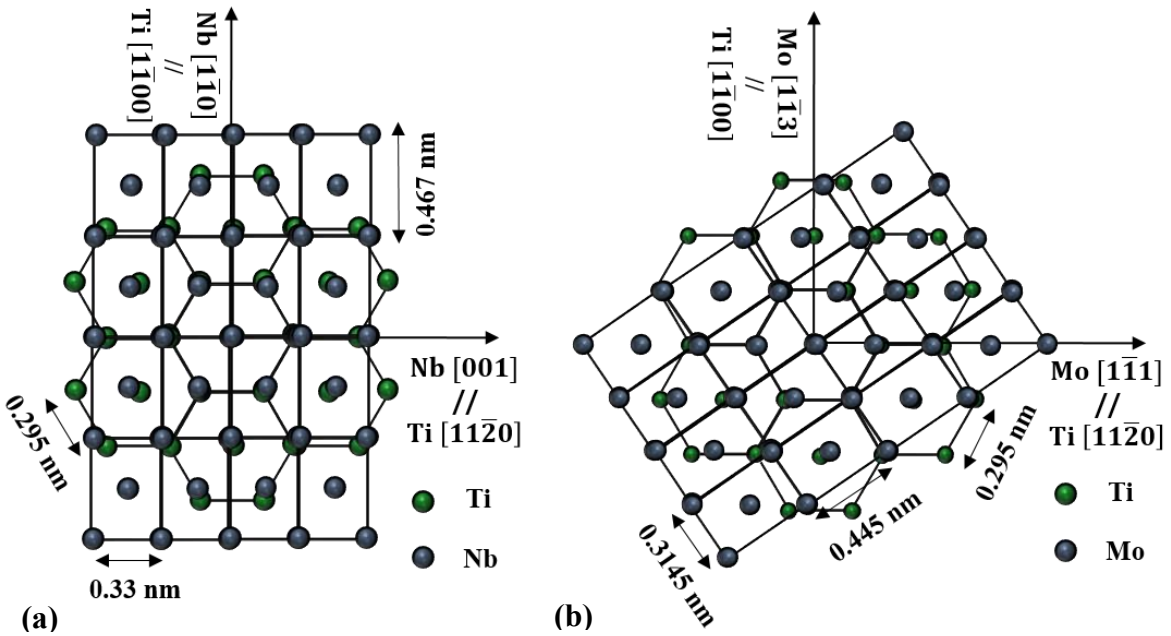

Figure 29. Superimposition of the Nb (110) plane in NW-OR with the Ti (0001) plane (green) (a) and of the Mo (110) plane in KS-OR with the Ti (0001) plane (green) (b). One bcc domain is sketched for each case.

The ratios between nearest neighbor distances (x_{bcc}/y_{Ti}) in the surface plane are $r_{Nb/Ti}$ = 0.968 and $r_{Mo/Ti}$ = 0.923, which is consistent with the occurrence of NW-OR for Nb (110) on Ti (0001) and of KS-OR for Mo (110) on Ti (0001) (appendix D). The corresponding mismatches are the following:

For Nb (110) on Ti (0001):

$\frac{a_{Ti}-a_{Nb}}{a_{Nb}} = -10.58\ \%$ along Ti [11$\bar{2}$0] with 1 Nb : 1 Ti

$\frac{\sqrt{3}a_{Ti}-\sqrt{2}a_{Nb}}{\sqrt{2}a_{Nb}} = +9.52\ \%$ along Ti [1$\bar{1}$00] with 1 Nb : 1 Ti

For Mo (110) on Ti (0001):

$\frac{a_{Ti}-\frac{\sqrt{3}}{2}a_{Mo}}{\frac{\sqrt{3}}{2}a_{Mo}} = +8.37\ \%$ along Ti [11$\bar{2}$0] with 1 Mo : 1 Ti

$\frac{\frac{\sqrt{3}}{2}a_{Ti}-\frac{\sqrt{2}}{\sqrt{3}}a_{Mo}}{\frac{\sqrt{2}}{\sqrt{3}}a_{Mo}} = -0.48\ \%$ along Ti [1$\bar{1}$00] with 1 Mo : 1 Ti

1.3. Summary on the buffer layers' growth

The growth of the different buffer layers on LNO Z-cut can be summarized in Table 3 that gathers the various OR reported in the previous paragraphs.

As mentioned previously, these OR are consistent with the orientations that could be expected from the ratio between nearest neighbor distances in the overlayer and underlayer surface planes presented previously. From the structural analysis (FWHM of rocking curve, coherence length…), it appears that Nb and Mo quality is improved when Nb and Mo are deposited on Ti compared to the direct deposition on LNO. This might be related both to a better matching to the Ti (0001) lattice and to a reduced chemical interaction with the underlying layer. The Mo layer by the way exhibits systematically better characteristics than the Nb layer, although the occurrence of six different domains when deposited on Ti might be a severe limitation for subsequent $TbFe_2$ growth.

One can recall at this stage that Huth and Flynn [HUT98] reported the Mo (110) growth on LNO/Ti(0001) at 750 °C without alluding to the occurrence of in-plane multiple domains. They mention "a well-ordered layer" with a "higher degree of surface roughness than is observed for high-quality Mo (110) layers grown directly on sapphire". They do not give specific informations on the surface symmetry obtained from in-situ RHEED experiments. Despite several trials for different deposition temperatures, we could never get a Mo (110) single domain but always the sixth KS domains governed by the Ti (0001) surface lattice constant and symmetry. The growth process can be different for several reasons and the lower deposition temperature in our case may contribute to the development of domains. Some tests were thus performed at higher deposition temperatures despite the adhesion problems encountered above 500 °C (not faced by Huth & Flynn), but similar RHEED patterns and KS-OR have been obtained.

Material	Structure in the growth direction	In-plane orientation relationships	Growth type
Titanium	Ti (0001)	$Ti\ [1\bar{1}00]\ //\ LNO\ [11\bar{2}0]$ $Ti\ [11\bar{2}0]\ //\ LNO\ [1\bar{1}00]$	30° rot. hexagon 1 domain
Niobium	Nb (110)	$Nb\ [001]\ //\ LNO\ [1\bar{1}00]$ $Nb\ [1\bar{1}0]\ //\ LNO\ [11\bar{2}0]$	R30 3 domains
Molybdenum	Mo (110)	$Mo\ [001]\ //\ LNO\ [1\bar{1}00]$ $Mo\ [1\bar{1}0]\ //\ LNO\ [11\bar{2}0]$	R30 3 domains
Titanium / Niobium	Nb (110) // Ti (0001)	$Nb\ [001]\ //\ Ti\ [11\bar{2}0]\ //\ LNO\ [1\bar{1}00]$ $Nb\ [1\bar{1}0]\ //\ Ti[1\bar{1}00]\ //\ LNO\ [11\bar{2}0]$	NW 3 domains
Titanium / Molybdenum	Mo (110) // Ti (0001)	$Mo\ [1\bar{1}1]\ //\ Ti\ [11\bar{2}0]\ //\ LNO\ [1\bar{1}00]$ $Mo\ [1\bar{1}3]\ //\ Ti\ [1\bar{1}00]\ //\ LNO\ [11\bar{2}0]$	KS 6 domains

Table 3. Summary of growth directions, in-plane orientation relationships and growth types for different buffer layers deposited on LNO Z-cut.

2. $TbFe_2$ growth

$TbFe_2$ was deposited on single (Ti, Nb and Mo) and double buffer layers (Ti/Nb and Ti/Mo) described in the previous paragraphs.
Several deposition temperatures were used but in term of the crystalline quality visualized by RHEED patterns and X-ray diffraction experiments, 650 °C seems to be the best choice. Below 600 °C, $TbFe_2$ films are polycrystalline with a preferential [111] growth direction, as attested by the observation of rings during RHEED analysis. One can underline that the optimal deposition temperature in this study is thus higher than the temperature reported by Huth [HUT99] for the growth on LNO Z-cut (550 °C) and the temperature reported for the growth on sapphire with Nb or Mo buffer layers (450 °C – 680 °C) [HUT98a, HUT98b].
The results presented in this section correspond to 50 nm thick films deposited at 650 °C. The deposition rates are summarized in appendix A.

2.1. $TbFe_2$ on single buffer layer

2.1.1. $TbFe_2$ on Titanium

The RHEED patterns obtained after the $TbFe_2$ deposition on Ti (0001) are presented in Figure 30 (c and d), together with those collected for Ti along the same azimuthal directions (a and b).

The $TbFe_2$ RHEED images exhibit spotty streaks with a relatively high diffuse background that can be related to both disorder and roughness at the surface. One can also notice the presence of extra spots and tilted streaks that don't seem to belong to a single diffraction pattern. They could be linked to the presence of multiple domains but also to the occurrence of crystalline facets at the surface, as it has

already be reported for the growth of $DyFe_2$ on Al_2O_3/Nb [OST05]. This specific point of surface morphology was not investigated in further details in the current study.

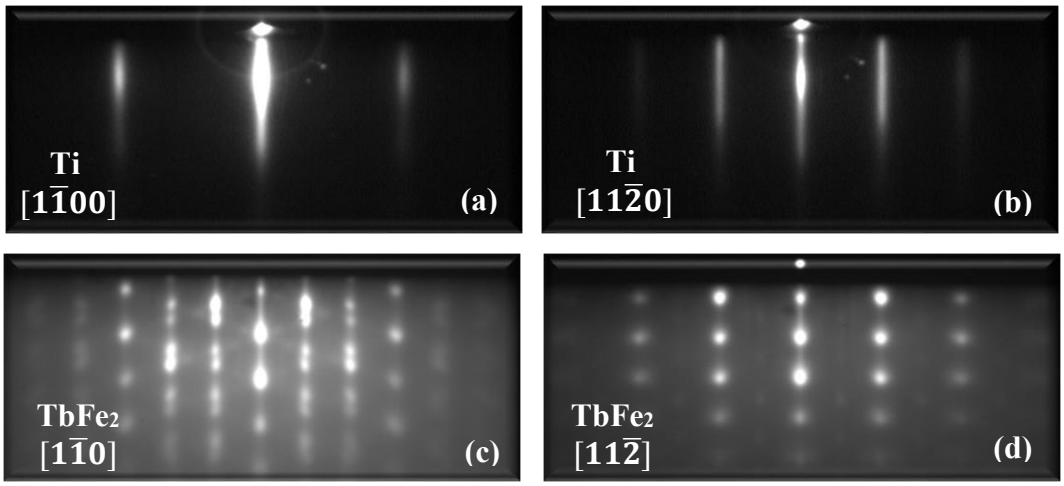

Figure 30. RHEED patterns collected along two azimuths rotated by 90° for a 50 nm thick Ti deposited at 100 °C on LNO (a and b) and for a 50 nm thick $TbFe_2$ deposited at 650 °C on LNO/Ti (c and d).

Two distinct diffraction patterns are observed, they are separated by 30° and each pattern is recovered every 60°.
The in-plane symmetry together with the relative inter-streaks distances (a ratio of 1.73) enable us to conclude to the occurrence of a (111) growth plane ($TbFe_2$ (111) // Ti (0001)) with the following epitaxial relationships:

$$TbFe_2\ [11\bar{2}]\ //\ Ti\ [11\bar{2}0]$$
$$TbFe_2\ [1\bar{1}0]\ //\ Ti\ [1\bar{1}00]$$

Those are confirmed by the X-ray measurements of specular and asymmetrical Bragg reflections (φ scans), as presented in Figure 31 (a and b), and sketched in Figure 32. Note that the FWHM of rocking curve across the $TbFe_2$ (111) Bragg peak is 1.5°, which is a sign of reasonably quality. A supplementary contribution can be observed on the right side of the $TbFe_2$ (222) peak but its origin couldn't be determined up to now.
φ scans for the $TbFe_2$ ARs show diffraction conditions every 60°, while 120° are expected from the [111] orientated Laves phase structure. They reveal the presence of two variants rotated by 60° around the [111] growth direction. Both variants give rise to the same in-plane OR with respect to the underlying Ti (0001) plane (Figure 31 (b)).

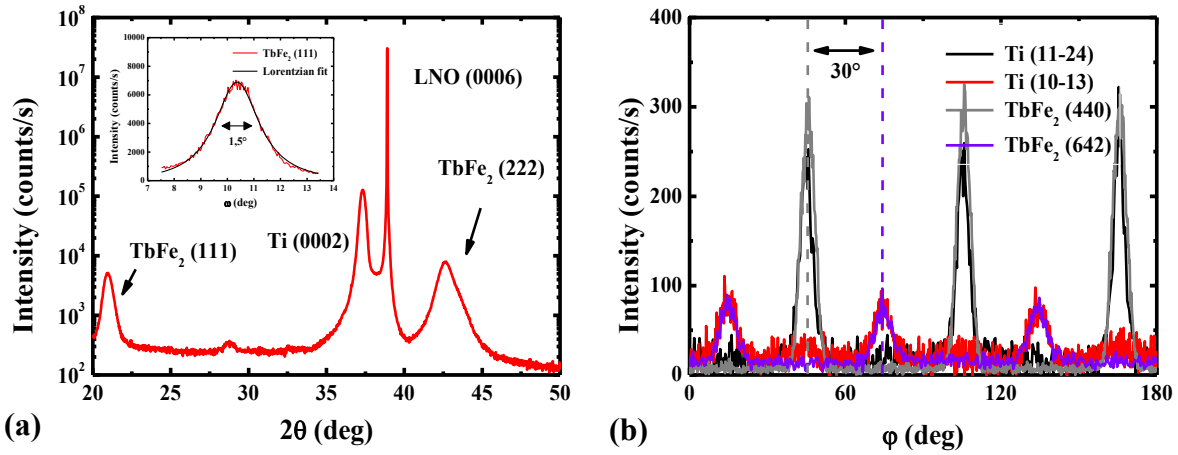

Figure 31. Specular X-ray diffraction scan performed for a 50 nm thick $TbFe_2$ layer deposited on LNO Z /Ti (rocking curve across the $TbFe_2$ (111) Bragg peak is shown in inset) (a) and φ scans for Ti and $TbFe_2$ asymmetrical reflections (b).

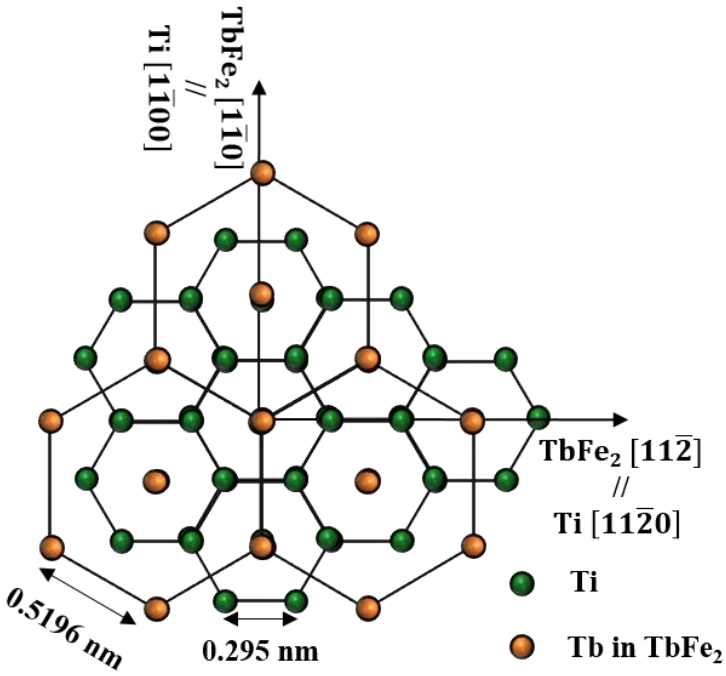

Figure 32. Superimposition of the (111) Tb in $TbFe_2$ (gold) and (0001) Ti planes (green).

The observed in-plane epitaxial relationships lead to the same lattice mismatches along the main in-plane directions:

$\frac{3a_{Ti}-\frac{\sqrt{6}}{2}a_{TbFe_2}}{\frac{\sqrt{6}}{2}a_{TbFe_2}} = -1.56\ \%$ along Ti $[11\bar{2}0]$, for a 1 $TbFe_2$: 3 Ti coincidence between atomic rows.

$\frac{\sqrt{3}a_{Ti}-\frac{\sqrt{2}}{2}a_{TbFe_2}}{\frac{\sqrt{2}}{2}a_{TbFe_2}} = -1.56\ \%$ along Ti $[1\bar{1}00]$, for a 1 $TbFe_2$: 1 Ti coincidence between atomic rows.

2.1.2. $TbFe_2$ on Niobium or Molybdenum

The RHEED images obtained for $TbFe_2$ deposited on LNOZ/Nb (a-d) or LNOZ/Mo (e-h) are given in Figure 33, together with those collected for the underlying buffer surface along the same azimuths.

As attested by the ring patterns in (c) and (d), the deposition on LNOZ/Nb results in the formation of a polycrystalline compound, whatever the deposition parameters (deposition temperature, deposition rates…). The reason could be the weak crystallographic quality of the Nb buffer layer. Also, the ratio between in-plane nearest neighbor distances (bcc/fcc) is 0.55 and doesn't fit to the ideal values calculated for the R30-OR or for the 1 fcc : 3 bcc R30-OR.
The LNOZ/Mo template however enables the crystalline growth with diffraction patterns consistent with a [111] growth direction, as observed on Ti (0001). The streaks appear less spotty in this case, but one can mention the occurrence of inter-streaks on 1/3 positions, usually attributed to a surface reconstruction or a surface structure.

Specular X-ray scattering experiments (Figure 34 (a)) confirm the [111] growth direction with a FWHM of the rocking curve around 2°, but also shows a residual contribution attributed to (110) planes parallel to the surface, as it has already been observed on sapphire [MOU99a].
φ scans on asymmetrical reflections (Figure 34 (b)) are consistent with the occurrence of two [111] $TbFe_2$ variants rotated by 60° with following in-plane orientation relationships with respect to the underlying Mo template, as sketched in Figure 35:

$TbFe_2$ $[11\bar{2}]$ // Mo $[001]$
$TbFe_2$ $[1\bar{1}0]$ // Mo $[1\bar{1}0]$

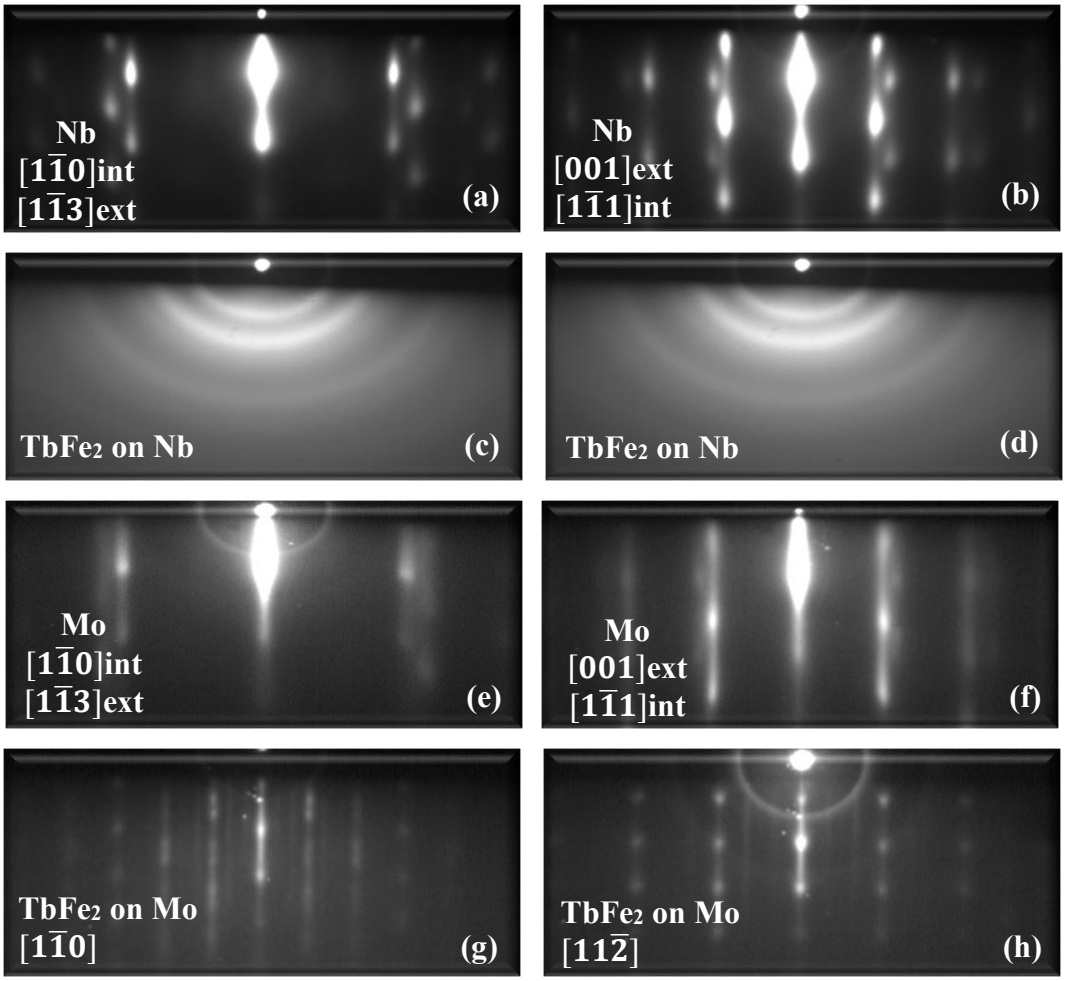

Figure 33. RHEED patterns collected along the same two azimuths rotated by 90° for a 50 nm thick Nb on LNOZ at 450 °C (a and b), a 50 nm thick $TbFe_2$ on LNOZ/Nb at 650 °C (c and d), a 50 nm thick Mo on LNOZ at 450 °C (e and f) and a 50 nm thick $TbFe_2$ on LNOZ/Mo at 650 °C (g and h).

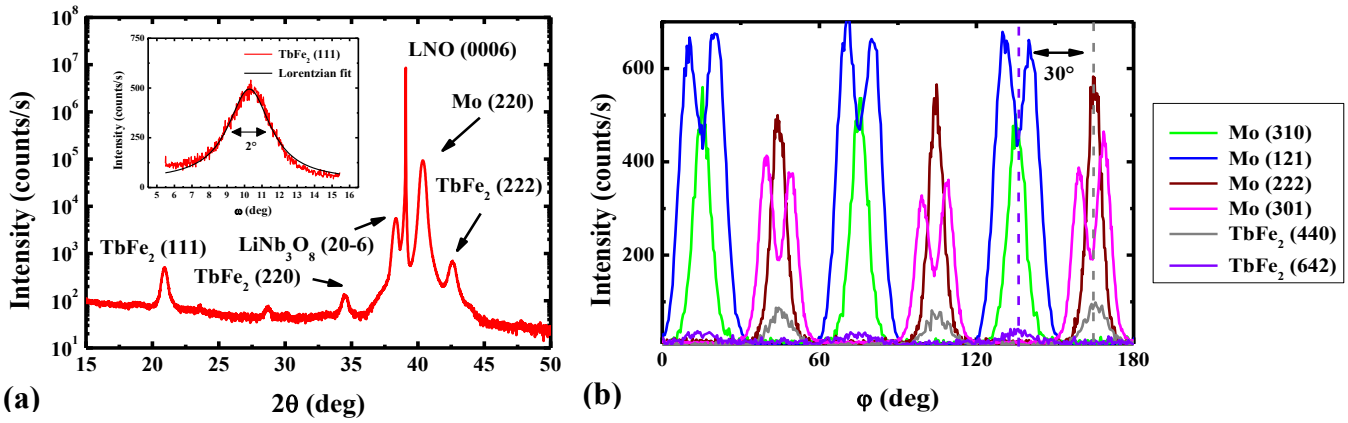

Figure 34. Specular X-ray scattering scan measured for a 50 nm thick $TbFe_2$ layer deposited on LNOZ/Mo (rocking curve across the (111) $TbFe_2$ Bragg peak is shown in inset) (a) and φ scans for Mo and $TbFe_2$ asymmetrical reflections (b).

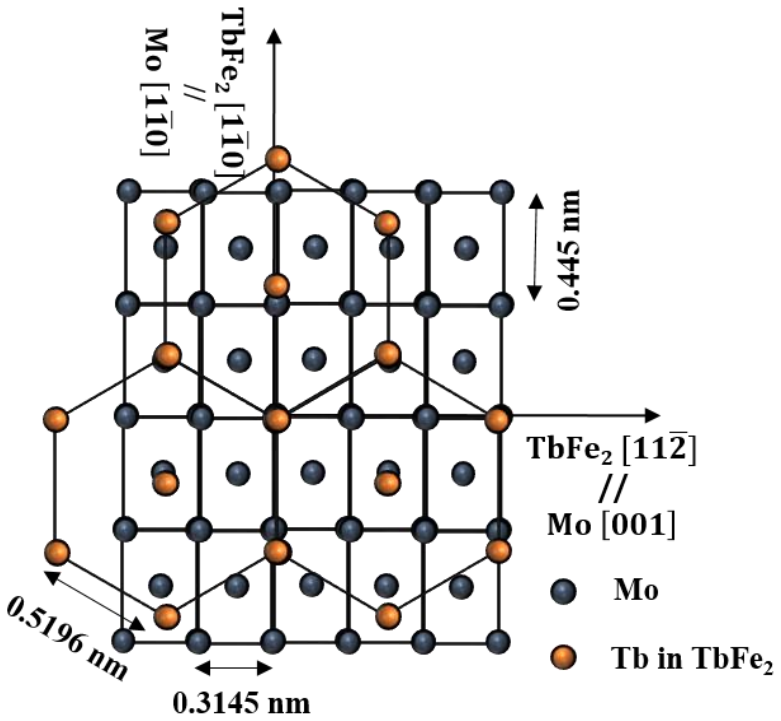

Figure 35. Superimposition of the (111) Tb in $TbFe_2$ (gold) and (110) Mo (blue) surface lattices.

This R30-OR is consistent with previous results reported for the (111) $TbFe_2$ growth on (110) Mo on sapphire substrates [HUT98a]. The ratio between in-plane nearest neighbor distances (bcc/fcc) is 0.52 and doesn't really fit to the ideal values calculated for this OR (appendix D); the 1 fcc : 3 bcc match between atomic rows perpendicular to Mo [001] however leads to an ideal ratio of 0.5 then very close to our experimental case.
The corresponding lattice mismatches are thus:

$\frac{3a_{Mo}-\frac{\sqrt{6}}{2}a_{TbFe_2}}{\frac{\sqrt{6}}{2}a_{TbFe_2}} = 4.95\,\%$ along Mo [001], for a 1 $TbFe_2$: 3 Mo coincidence between atomic rows.

$\frac{\sqrt{2}a_{Mo}-\frac{\sqrt{2}}{2}a_{TbFe_2}}{\frac{\sqrt{2}}{2}a_{TbFe_2}} = -14.4\,\%$ along Mo [1$\bar{1}$0], for a 1 $TbFe_2$: 1 Mo coincidence between atomic rows.

One can finally underline that only one in-plane orientation is obtained for this (111) $TbFe_2$ layer despite the occurrence of three (110) Mo domains, since those latter are rotated by 60°, which is suitable for the (111) symmetry.

2.2. $TbFe_2$ on double buffer layers

The RHEED patterns collected along two azimuths rotated by 90° after the $TbFe_2$ deposition on LNOZ/Ti/Nb (c and d) and on LNOZ/Ti/Mo (g and h) are presented in Figure 36. The RHEED for underlying Ti/Nb (a and b) and Ti/Mo (e and f) are recalled as well.

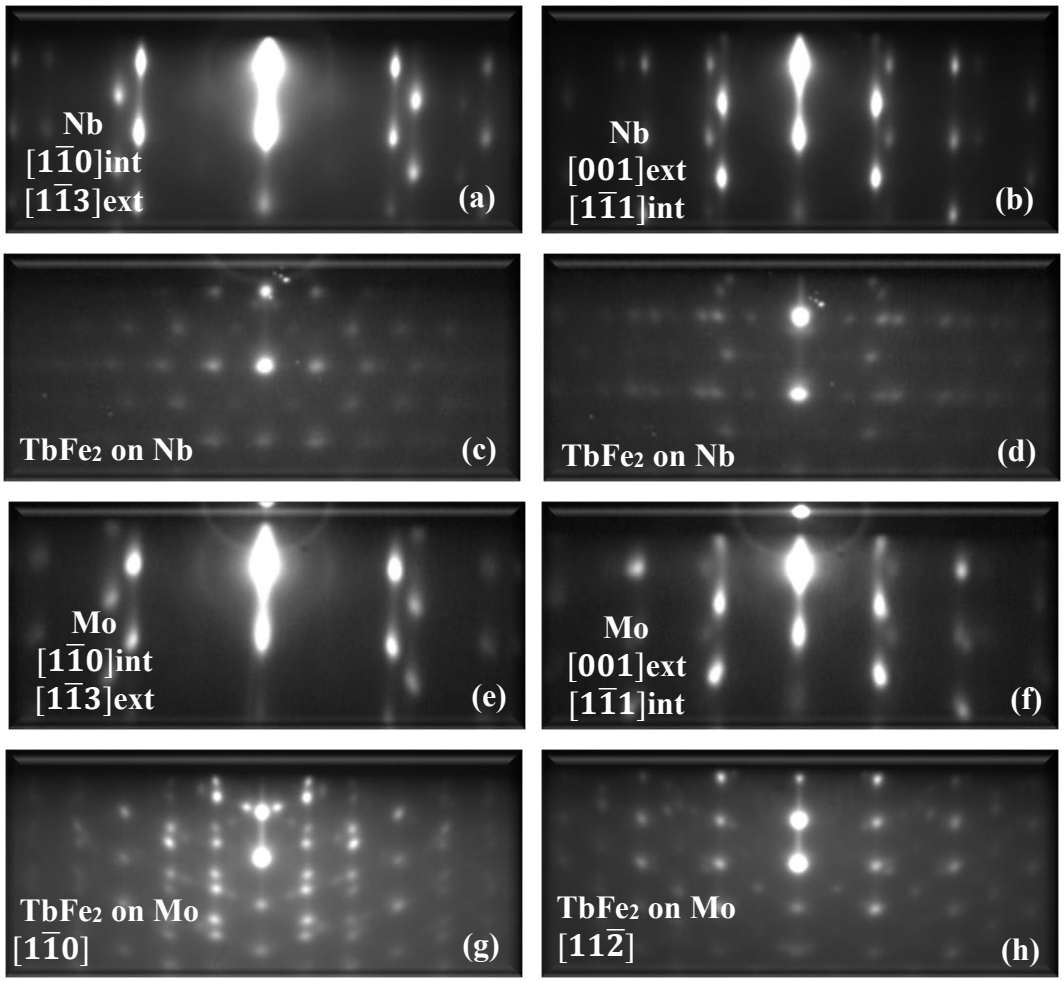

Figure 36. RHEED patterns collected along two azimuths rotated by 90° for 50 nm thick Nb deposited at 450°C on LNOZ/Ti (a and b), 50 nm thick $TbFe_2$ deposited on Ti/Nb at 650 °C (c and d), 50 nm thick of Mo deposited at 450 °C on LNOZ/Ti (e and f) and 50 nm thick $TbFe_2$ deposited on Ti/Mo at 650 °C (g and h).

On both Ti/Nb and Ti/Mo templates, the $TbFe_2$ RHEED patterns are relatively diffuse with a marked spotty character. Once again, extra spots and tilted streaks appear (especially on Ti/Mo). The presence of crystalline facets at the surface is once again suspected.
On the Ti/Mo buffer, the azimuthal succession of patterns (separated by 30° and each pattern recovered every 60°) and relative distances between main diffraction streaks are again consistent with (111) $TbFe_2$ growth planes, confirmed by specular X-ray scattering experiments (Figure 37 (b)). The indexation of the RHEED patterns obtained on the Ti/Nb buffer is still impossible, even after complementary X-ray analysis (Figure 37 (a)) that shows a [110] growth direction. The FWHM of the rocking curve across the $TbFe_2$ (111) Bragg peak is 2° on Ti/Mo while it is 3.6° on Ti/Nb, a sign of poor crystallographic quality in this latter case.

When $TbFe_2$ is deposited on Ti/Mo, it appears from the φ scans that in-plane $TbFe_2 < 11\bar{2} >$ directions are parallel to "some" Mo $< 1\bar{1}1 >$ directions. These latter are the ones rotated by 60°, belonging to different (110) Mo domains and parallel to $< 11\bar{2}0 >$ Ti directions (see Figure 38 (b)). Similarly, in-plane $TbFe_2 < 1\bar{1}0 >$ directions are parallel to "some" Mo $< 1\bar{1}3 >$ directions, those rotated by 60°, belonging to different (110) Mo domains and parallel to $< 1\bar{1}00 >$ Ti directions. This peculiar OR most likely results from the above described R30-OR for (111) $TbFe_2$ on (110) Mo. In the present case where six KS (110) Mo domains are present, their relative orientation should give rise to two (111) $TbFe_2$ domains, rotated by 10.52 ° [HEL98]. These are not separated in the φ scans that rather suggest the merge into a single median domain with large in-plane dispersion.

Despite the poor quality of the $TbFe_2$ deposit on Ti/Nb, the φ scans (see Figure 38 (a)) for AR suggest the alignment of main in-plane directions for (110) $TbFe_2$ and (110) Nb lattices, thus giving rise to three (110) $TbFe_2$ domains rotated by 60° on the three (110) Nb domains with:

$$TbFe_2\ [1\bar{1}0]\ //\ Nb\ [1\bar{1}0]$$
$$TbFe_2\ [001]\ //\ Nb\ [001]$$

One can recall here that the growth of $TbFe_2$ could not be achieved on Al_2O_3/Nb either. A supplementary thin Fe seed layer is necessary to form a NbFe-α surface alloy with suitable in-plane lattice constants to initiate the compound growth. The deposition of an Fe layer at 680 °C was attempted, but this could not initiate a proper $TbFe_2$ growth.

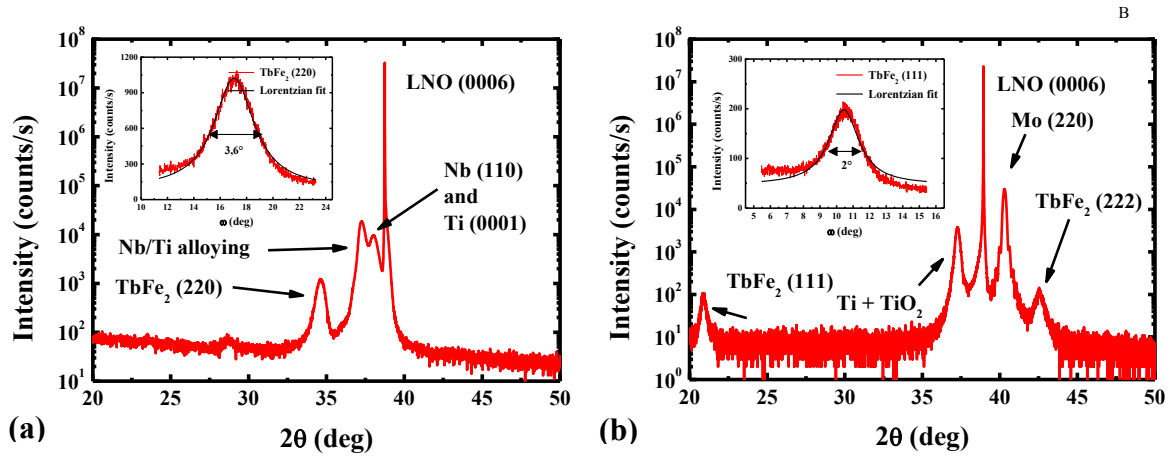

Figure 37. Specular X-ray scans performed for a 50 nm thick $TbFe_2$ layer deposited on LNOZ/Ti/Nb (a) and LNOZ/Ti/Mo (b). Rocking curves across the $TbFe_2$ Bragg peaks are shown in inset.

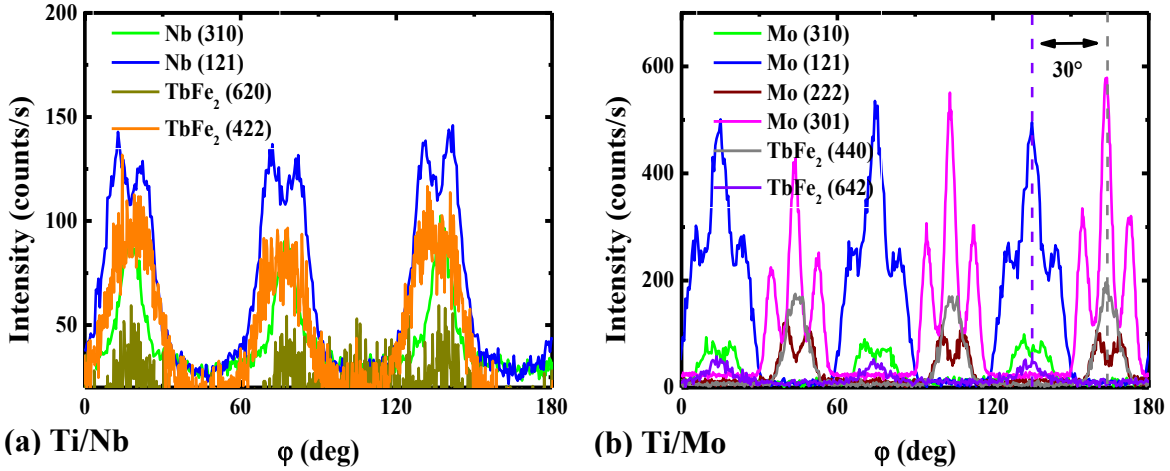

Figure 38. φ scans for Nb/Mo and $TbFe_2$ asymmetrical reflections in the case of $TbFe_2$ deposited on Ti/Nb (a) and Ti/Mo (b).

In-plane OR for the Nb/$TbFe_2$ growth are sketched in Figure 39 (one domain).
The corresponding lattice mismatches are thus:
$\frac{2\sqrt{2}a_{Nb}-\sqrt{2}a_{TbFe_2}}{\sqrt{2}a_{TbFe_2}} = -10.45$ % along Nb $[1\bar{1}0]$, where there is a 1 $TbFe_2$: 1 Nb coincidence between atomic rows.
$\frac{2a_{Nb}-a_{TbFe_2}}{a_{TbFe_2}} = -10.01$ % along Nb [001], where there is a 1 $TbFe_2$: 4 Nb coincidence between atomic rows.

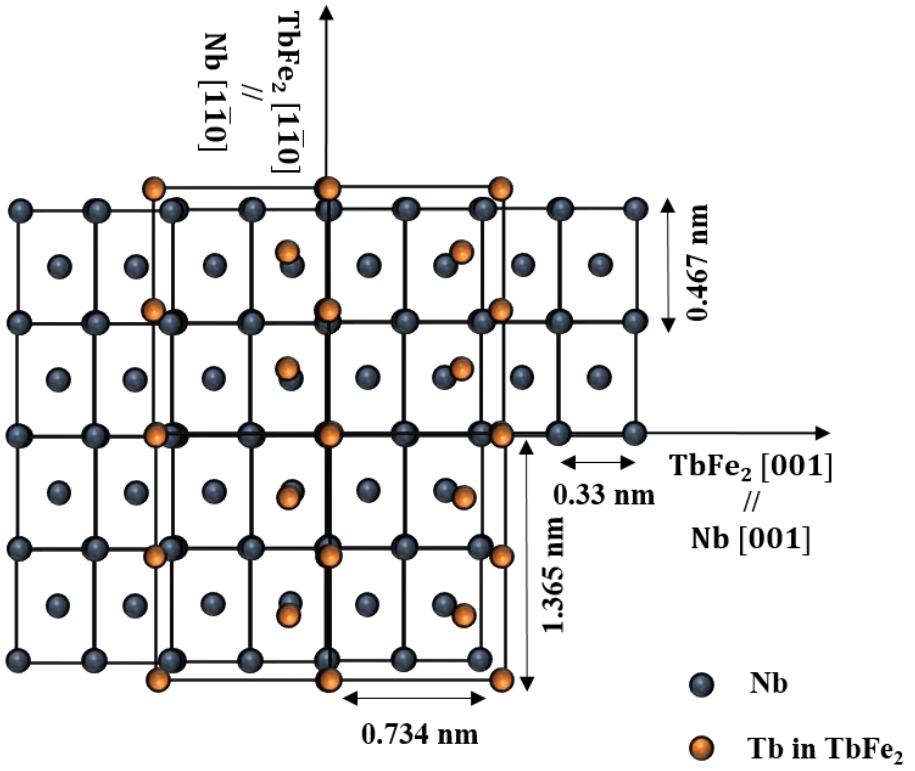

Figure 39. Superimposition of the (111) Tb in $TbFe_2$ (gold) and (110) Nb (blue) surface lattices.

2.3. Summary of the growth and structural properties for the $TbFe_2$ films deposited on LNOZ-cut

Table 4 summarizes the results from the growth of $TbFe_2$ films on LNOZ. Structural characteristics deduced from the X-ray analysis are gathered in Table 5.

Buffer layers	Structure in the growth direction	In-plane orientation relationships	$TbFe_2$ growth type

Ti	$TbFe_2$ (111)
	// Ti (0001)
	// LNO (0001)
		$TbFe_2$ [11$\bar{2}$] // Ti [11$\bar{2}$0] // LNO [1$\bar{1}$00]
		$TbFe_2$ [1$\bar{1}$0] // Ti [1$\bar{1}$00] // LNO [11$\bar{2}$0]
			1 domain
			2 variants

Nb	Polycrystalline $TbFe_2$
	// Nb (110)
	// LNO (0001)
		Nb [001] // LNO [1$\bar{1}$00]
		Nb [1$\bar{1}$0] // LNO [11$\bar{2}$0]
			--- 	

Mo	$TbFe_2$ (111)
	// Mo (110)
	// LNO (0001)
		$TbFe_2$ [11$\bar{2}$] // Mo [001] // LNO [1$\bar{1}$00]
		$TbFe_2$ [1$\bar{1}$0] // Mo [1$\bar{1}$0] // LNO [11$\bar{2}$0]
			R30 growth
			1 domain
			2 variants

Ti / Nb	$TbFe_2$ (110)
	// Nb (110)
	// Ti (0001)
	// LNO (0001)
		$TbFe_2$ [001] // Nb [001] // Ti [11$\bar{2}$0] // LNO [1$\bar{1}$00]
		$TbFe_2$ [1$\bar{1}$0] // Nb [1$\bar{1}$0] // Ti[1$\bar{1}$00] // LNO [11$\bar{2}$0]
			3 domains

Ti / Mo	$TbFe_2$ (111)
	// Mo (110)
	// Ti (0001)
	// LNO (0001)
		$TbFe_2$ [11$\bar{2}$] // Mo [001] (±5°) // Ti [11$\bar{2}$0] // LNO [1$\bar{1}$00]
		$TbFe_2$ [1$\bar{1}$0] // Mo [1$\bar{1}$0] (±5°) // Ti [1$\bar{1}$00] // LNO [11$\bar{2}$0]
			R30 growth
			1 domain
			2 variants

Table 4. Summary of growth directions, in-plane orientation relationships and $TbFe_2$ growth types obtained for 50 nm thick $TbFe_2$ films deposited on various buffer layers on LNOZ.

Buffer layers	FWHM of RC (°)	$\varepsilon_\perp$ (%)	⊥ coherence length (nm)	(440) IP dispersion at half maximum (°)
Ti	1.5	+0.159	30.3	6
Mo	2	+0.157	19.2	11
Ti / Nb	3	-0.139	11.3	---
Ti / Mo	2	+0.242	19.3	11.5

Table 5. Summary of the structural characteristics deduced from X-ray experiments for 50 nm thick $TbFe_2$ films deposited on various buffer layers on LNOZ.

The $TbFe_2$ crystalline growth was achieved on the different single and double buffer layers, except on the single Nb buffer, directly deposited on the LNOZ substrate. The Ti/Nb template enables the (110) growth, probably due to a slightly better quality of the Nb buffer on Ti, although the film crystalline characteristics (FWHM of the rocking curve, coherence length…) still reveal a poor quality on Ti/Nb. One can by the way recall that the $TbFe_2$ growth on sapphire/Nb was not possible without the deposition of an extra thin Fe layer [ODE96b].
The crystalline growth is obviously improved on Ti, Mo and Ti/Mo templates on which (111) $TbFe_2$ films is obtained. The best structural characteristics being measured for the single Ti buffer layer. The R30-OR between (111) $TbFe_2$ and (110) Mo is consistent with previous results on sapphire/Mo, both in the case of 3 NW-Mo domains (LNOZ/Mo) and in the case of 6 KS-Mo domains (LNOZ/Ti/Mo). Because of the relative orientations of these Mo domains, the $TbFe_2$ growth interestingly leads to one (111) $TbFe_2$ domain, even on Ti/Mo where 10.52 ° rotated lattices apparently merge. The $TbFe_2$ in-plane dispersion observed from φ scans, FWHM of the rocking curve and coherence length along the growth direction are namely similar for Mo and Ti/Mo templates.
One can finally notice that whatever the template, the same OR are observed between the (111) $TbFe_2$ and LNO (0001) lattices.

Let's now discuss the strain state of the $TbFe_2$ films along the growth direction, as deduced from the specular Bragg peak position. It appears that the films are under tensile strain on Ti, Mo and Ti/Mo, while they are under compressive strain on Ti/Nb.
Because of the large thickness of the deposited films and of the relatively complex OR with significant lattice mismatches, the strain cannot be related to the accommodation of the $TbFe_2$ lattice to the underlying buffer layers. The most probable source of strains likely arises from the different thermal expansion coefficients of the deposited layers and the substrate, as it has been previously reported [WAN96, MOU99a].
In this hypothesis, the lattice is supposed to be relaxed at the deposition temperature. The strains are induced during the cooling process because the deposited layer and the substrate exhibit different thermal expansion coefficients. This simple approach leads to a RT in-plane strain $\varepsilon_{//}$ that doesn't depend on the film thickness, on the growth direction, but only on the thermal expansion coefficients α and on the deposition temperature T_d:

$$\varepsilon_{//} = -\left(\alpha_{TbFe_2} - \alpha_{LNO}\right).(20°C - T_d°C)$$

The resulting perpendicular strain along the growth direction can be calculated from the elastic response [AVI06].
For a [110] growth direction:

$$\varepsilon_\perp = \frac{2C_{44} - 3C_{12} - C_{11}}{2C_{44} + C_{12} + C_{11}}.\varepsilon_{//}$$

For a [111] growth direction:

$$\varepsilon_\perp = \frac{4C_{44} - 4C_{12} - 2C_{11}}{4C_{44} + 2C_{12} + C_{11}}.\varepsilon_{//}$$

Given the thermal expansion coefficients of LNO (approximately 21×10^{-6} °C^{-1} at RT [VYA13]) and $TbFe_2$ (approximately 12×10^{-6} °C^{-1} at RT [MOU99a]) and the elastic coefficients C_{ij} of $TbFe_2$

(see Table 6), one can calculate the expected lattice strains at room temperature after the deposition at 650 °C:
For a [110] growth direction: $\varepsilon_{//} = -0.57\%$ and $\varepsilon_{\perp} = +0.43\%$.
For a [111] growth direction: $\varepsilon_{//} = -0.57\%$ and $\varepsilon_{\perp} = +0.40\%$.
Those can be compared to the experimentally measured perpendicular strains and corresponding calculated in-plane strains (Table 7).

Compound	C_{11} (GPa)	C_{12} (GPa)	C_{44} (GPa)
$TbFe_2$	143	66	48

Table 6. Elastic constants of $TbFe_2$ at RT.

Buffer layer	$\varepsilon_{\perp}$ (%)	$\varepsilon_{//}$ (%)
Ti	+0.159	-0.122
Mo	+0.157	-0.121
Ti / Nb	-0.139	+0.111
Ti / Mo	+0.242	-0.186

Table 7. $TbFe_2$ experimental perpendicular and calculated corresponding in-plane strains (assuming an elastic response) for the different buffer layers.

For Ti, Mo and Ti/Mo templates, the measured perpendicular tensile strains are consistent with the larger LNO expansion coefficient, although significantly smaller than expected. One can recall the -0.4% in-plane compression reported by Huth [HUT99] as deduced form their perpendicular measurements for a deposition temperature of 550 °C. In our case, the smaller strain while the deposition temperature is higher would reveal a limited clamping effect of the substrate.
The perpendicular compressive strain measured for a Ti/Nb template can obviously not be explained in the framework of this simple model. The improbable hypothesis of a matching between (110) Nb and (110) $TbFe_2$ lattices cannot be invoked either since this would also yield an in-plane $TbFe_2$ compression and thus a perpendicular tensile strain. Up to now, the only possibility is to consider that the buffer with a small thermal expansion coefficient (approximately 7×10^{-6} °C^{-1} at RT for Nb [ODE96a]) would be dominant over the effect of the substrate. This may be related to a bad adhesion to the substrate but remains surprising given the similar thicknesses for buffer and $TbFe_2$ layers.

2.4. Magnetic properties of the $TbFe_2$ layers deposited on LNO Z-cut

Magnetic hysteresis loops have been measured at room temperature with magnetic fields applied in the plane (IP) along different directions, and out of the plane (OOP) of the $TbFe_2$ layers deposited on the various buffer layers. Figure 40 presents the comparison between IP (H // $[1\bar{1}0]$ $TbFe_2$ // LNO $[11\bar{2}0]$) and OOP loops, and Figure 41 presents the IP measurements along two orthogonal directions. The field range is reduced to [-2T/+2T] for the latter because this is the maximum field available in the VSM instrument that enables in-plane measurements in varying the field orientation respect to the sample. It must be noticed that no demagnetization corrections were performed for OOP loops in order to show the magnetic field actually needed to magnetically saturate the film. The diamagnetic contributions from the sample holder and substrate have been however subtracted.

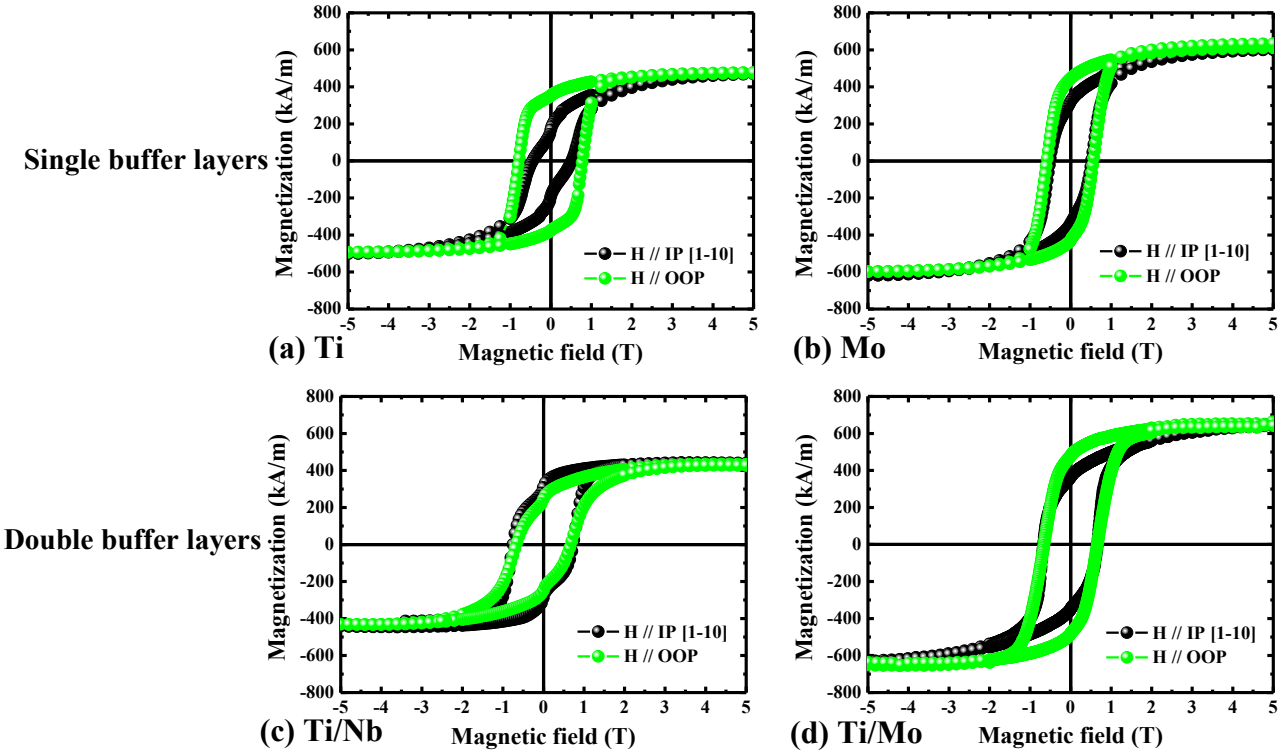

Figure 40. Hysteresis loops measured at room temperature with the magnetic field applied IP along [1$\bar{1}$0] $TbFe_2$ (black) and OOP (green) for 50 nm thick $TbFe_2$ layers deposited on different templates (single buffer layers (Ti (a) and Mo (b)) and double buffer layers (Ti/Nb (c) and Ti/Mo (d)).

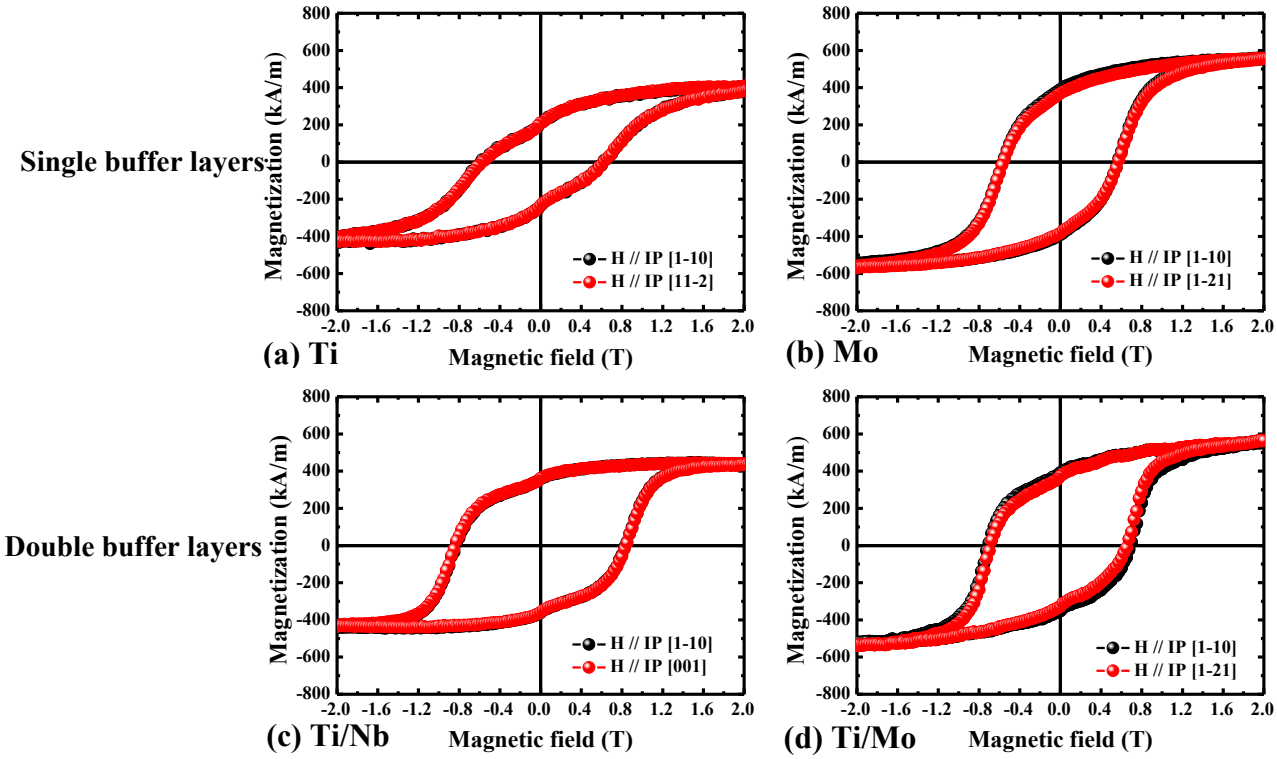

Figure 41. Hysteresis loops measured at room temperature with the magnetic field applied IP along two orthogonal $TbFe_2$ directions for 50 nm thick $TbFe_2$ layers deposited on different templates (single buffer layers (Ti (a) and Mo (b)) and double buffer layers (Ti/Nb (c) and Ti/Mo (d)).

The analysis of these different curves allows to extract magnetic parameters such as the saturation magnetization, the coercivity and the magnetic anisotropy (gathered in Table 8).

Buffer layer	M_s (kA.m^{-1})	$\mu_0 H_C$ (T)	Anisotropy
Ti	480	0.64	OOP
Mo	616	0.56	OOP
Ti / Nb	435	0.85	IP
Ti / Mo	646	0.7	OOP

Table 8. Saturation magnetization, coercive field and anisotropy for the 50 nm thick $TbFe_2$ layers deposited on various buffer layers.

(i) For all these $TbFe_2$ films, one can first observe that the saturation magnetization is significantly smaller than the value expected from the bulk (800 kA.m^{-1}). This is obviously a sign of limited quality of the films and could be attributed to different factors: poor crystalline order, chemical contamination by neighbor elements and/or elements diffusing from the substrate, oxidation … The Ti buffer layer alone may constitute an inefficient chemical barrier and lead to a small saturation magnetization despite a better crystalline quality of the deposited film. Mo and Ti/Mo buffers on which the $TbFe_2$ structural properties are similar also lead to close saturation magnetization, without a clear improvement brought by the supplementary Ti layer.
Further investigations would require detailed chemical analysis and surface analysis that have not been performed during this work. One can mention that (111) $TbFe_2$ films synthetized in the study by Huth *et al.* [HUT99] apparently don't exhibit this low saturation magnetization since the authors report a value close to 800 kA.m^{-1}.

(ii) The coercive fields measured for these various buffer layers are close to each other and close to 0.6 T, which is consistent with the values reported by Huth *et al.* on LNOZ [HUT99] and on Al_2O_3 [HUT98a, HUT98b]. The dispersion can come from different reasons but we can mention mainly the morphology of the film [MOU99a].

(iii) The comparison of IP and OOP measurements (Figure 40) shows that $TbFe_2$ films deposited on Ti, Mo and Ti/Mo exhibit a tendency to perpendicular magnetization (larger remanent magnetization, less rounded shape of the hysteresis loop), especially in the case of the single Ti buffer. On the contrary, the easy magnetization axis would rather lie in the plane for the film deposited on Ti/Nb.
These IP or OOP characters of the magnetic anisotropy are consistent with the expected influence of the magnetoelastic contribution when taking the measured lattice strain into account (appendix B): for both [110] and [111] growth directions, a perpendicular tensile strain favors an OOP magnetization, while a perpendicular compressive strain favors an IP magnetization. These are also consistent with previously reported results for $REFe_2$ and $REAl_2$ films deposited on various substrates with either smaller or larger thermal expansion coefficients, thus leading to either compressive or tensile perpendicular strains [HUT99, WAN96, MOU99a, AVI08].
Despite this qualitative agreement, the $TbFe_2$ film under larger tensile strain (on Ti/Mo) doesn't exhibit a stronger OOP anisotropy. The single Ti buffer promotes a stronger OOP anisotropy, likely connected to the smaller magnetization value, *i.e.* the smaller contribution of the demagnetizing field.

(iv) The comparison of IP measurements with the field applied along different directions (Figure 41) shows that the IP magnetic behavior is isotropic for all $TbFe_2$ films, whatever the buffer layers. In the case of the [111] growth direction, the presence of two variants leads to six $< 1\bar{1}1 >$ directions (easy direction in the bulk compound), rotated by 60° in azimuthal angle from each other, and tilted by 20° from the sample plane. The angle between any in-plane direction and an out-of-plane $< 1\bar{1}1 >$ direction is therefore in the [20°-35°] range (20° for $< 11\bar{2} >$ directions and 35° for $< 1\bar{1}0 >$ directions). Given the structural dispersion, this difference is obviously not large enough to induce an in-plane magnetic anisotropy. In the case of the [110] growth direction, $< 1\bar{1}1 >$ directions lie in the sample plane and despite the occurrence of three rotated domains, one could have expected an easier magnetization along

$< 001 >$ directions that are closer to $< 1\bar{1}1 >$ (see Figure 116 in appendix D). The large dispersion associated to a poor crystal quality likely smears this anisotropy out.
One can finally mention that the morphology can also have a significant influence on the IP anisotropy, as this has been shown in the case of $DyFe_2$ grown on sapphire [MOU00]. Further investigations would require detailed AFM analysis.

3. Summary of $TbFe_2$ growth on LNO Z-cut

In summary of this chapter on the $TbFe_2$ films grown on LNO Z-cut, one can first mention that the growth process revealed to be more difficult than expected, since we never could reproduce the results published by Huth *et al.* [HUT99]. Despite the use of a double Ti/Mo buffer, the Mo buffer always exhibits three (110) domains and the $TbFe_2$ saturation magnetization remains at a disappointing low value since we could only reach 81% of the bulk value. Given the difficulties related to this process, a large number of parameters may have an influence on the final film's characteristics. The time spent at high temperature can especially matter since the thermal stability of LNO is a key issue and Huth *et al.* by the way mention the time between Ti and Mo deposition (15 minutes) and the time between Mo and $TbFe_2$ deposition (10 minutes). Our setup doesn't enable us to change temperature in such short delays and these were in our case typically of the order of minimum 50 minutes between Ti and Mo and 40 minutes between Mo and $TbFe_2$. One can however notice that the structural characteristics obtained for these $TbFe_2$ films are satisfactory.
The use of a single buffer (Mo) and possibly a single buffer deposited at lower temperature (Ti) didn't permit to get a higher magnetization value, although the structural quality is significantly improved on the Ti buffer. Nb-based buffers, although efficient for the $TbFe_2$ growth on other substrates, are obviously not suitable for the growth on LNOZ. However, bilayer buffer (Ti/Nb) gives (110) $TbFe_2$ growth with an in-plane anisotropy but without enough good crystallographic and magnetic properties. Mo and Ti/Mo templates thus appear to be the best choices for the (111) $TbFe_2$ growth on LNOZ. In this study, the extra underlying Ti layer permits to slightly increase the saturation magnetization while keeping reasonable structural characteristics compared to the single Mo buffer. One can however notice that increasing the total buffer thickness is probably not a good idea for the magnetoelastic coupling between the piezoelectric substrate and the magnetostrictive material.

Chapter 4: Growth of $TbFe_2$ on LNO 128 and 41 Y-cut

As explained in chapter 2, these substrates are obtained by cutting a LNO crystal after specific rotations. The resulting physical surfaces do not correspond to high symmetry planes usually chosen for epitaxial growth, as (0001) or $(11\bar{2}0)$ sapphire planes for instance. The surface plane of a LNO 128 Y-cut substrate is a $(10\bar{1}4)$ crystalline plane, while the surface plane of a LNO 41 Y-cut substrate is tilted by 8.26 ° respect to $(01\bar{1}2)$ planes. One can notice that the $[11\bar{2}0]$ crystal axis belongs in both cases to the surface plane. This direction is generally called a X-direction among people working with such substrates; this denomination is therefore also used in the following.
The growth of $TbFe_2$ on these specific surfaces has been undertaken in this work because these substrates are commonly used for SAW devices. Given the results obtained on LNOZ substrates and the complexity related to the crystalline growth on such unconventional surfaces, only the growth of $TbFe_2$ on a Mo single buffer layer has been investigated, this combination leading to one of the highest saturation magnetization on LNOZ. This chapter simultaneously presents the results obtained on LNO 128Y- and LNO 41 Y-cut substrates, first for the buffer layer and then for the $TbFe_2$ film.

1. Molybdenum growth on LNO 128Y and 41Y-cut substrates

The Molybdenum growth on LNO 128Y and 41Y-cut substrates has been performed for deposition temperatures in the [500 °C – 800 °C] range. Trials for lower deposition temperatures were unsuccessful with the appearance of rings during RHEED analysis, sign of a polycrystalline order. A post-deposition annealing could not drive the formation of specific diffraction patterns.
Deposition rates have been varied in the [0.02 $nm.s^{-1}$ – 0.1 $nm.s^{-1}$] range and 20 nm to 100 nm thick films have been synthetized without a clear incidence of these parameters on the crystalline quality. As in the previous chapter, the results presented in the following correspond to 50 nm thick Mo films.

Figure 42 gathers the RHEED images obtained for Mo films deposited at 650 °C on LNO 128 Y-cut (a-b) and LNO 41 Y-cut (c-d) for several azimuthal angles labeled respect to the substrate surface X direction.

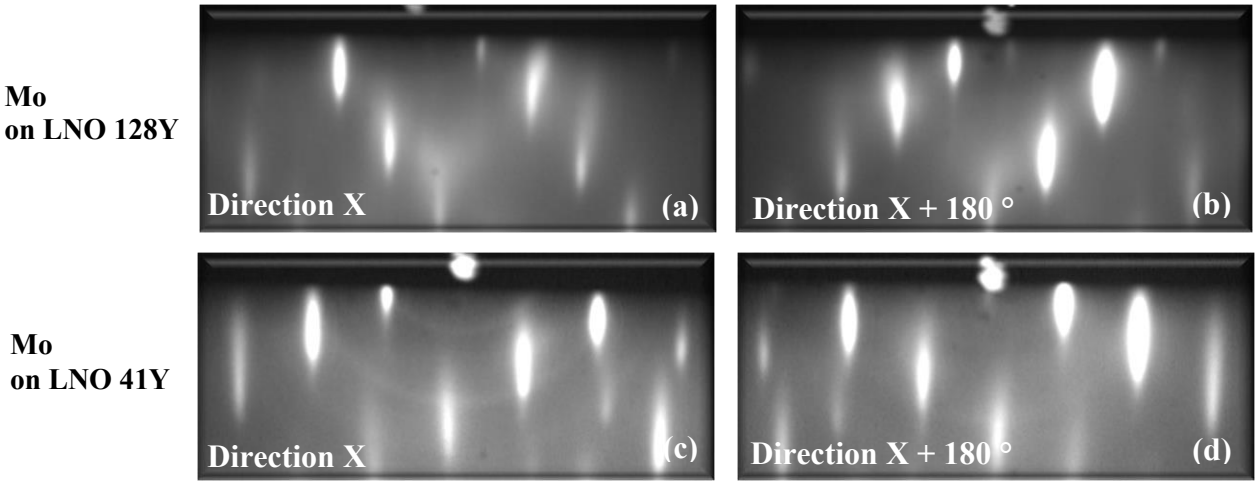

Figure 42. RHEED patterns obtained for 50 nm thick Molybdenum films deposited at 650 °C on LNO 128 Y-cut (a and b) and LNO 41 Y-cut (c and d). The direction X refers to the $< 11\bar{2}0 >$ *crystalline direction of the substrate.*

When changing the azimuthal angle, the RHEED images obtained after the Mo deposition are constituted of elongated dots and obviously do not form conventional diffraction patterns. It is moreover impossible to identify a specific surface symmetry from the succession of azimuthal angles. Finally, the images collected for a given azimuthal angle and when rotating by 180° from this angle are systematically different, as it can be seen on the Figure 42. All those observations indicate a relatively complex crystal orientation and the absence of Mo high symmetry growth planes parallel to the substrate surface.
One can nevertheless notice an interesting point: the images collected along LNO X and LNO X+180° directions reveal inclined broad lines formed by the vertically elongated features; the lines are tilted by approximately ± 38° with respect to the surface normal for Mo on LNO128Y and by ± 49° for Mo on LNO41Y. Those patterns are consistent with the presence of inclined crystalline planes, the intersection of which with the film surface is parallel to the LNO X direction (see appendix E). We can notice that the tilt angles of these lines are opposite between the two substrates.

In order to unravel these Mo films 3D orientations, pole figures have been measured via the X-ray scattering from (110) Mo planes for φ angles varying in the [0°-360°] range and χ angles varying in the [0°-80°] range (see appendix C). The results for Mo deposition on both substrates are presented in Figure 43 ((a) for LNO128 and (b) for LNO41). It should be noted that the sample is initially placed with the LNO X-axis along 270-90° axis. The LNO 0001 poles thus appear for φ angles of 0° or 180° (on the vertical direction) and for χ angles of 38° (resp. 49°) for the LNO 128Y (resp. LNO 41Y), as it is shown by a star symbol, and as it has been verified by experiments (not reported here).

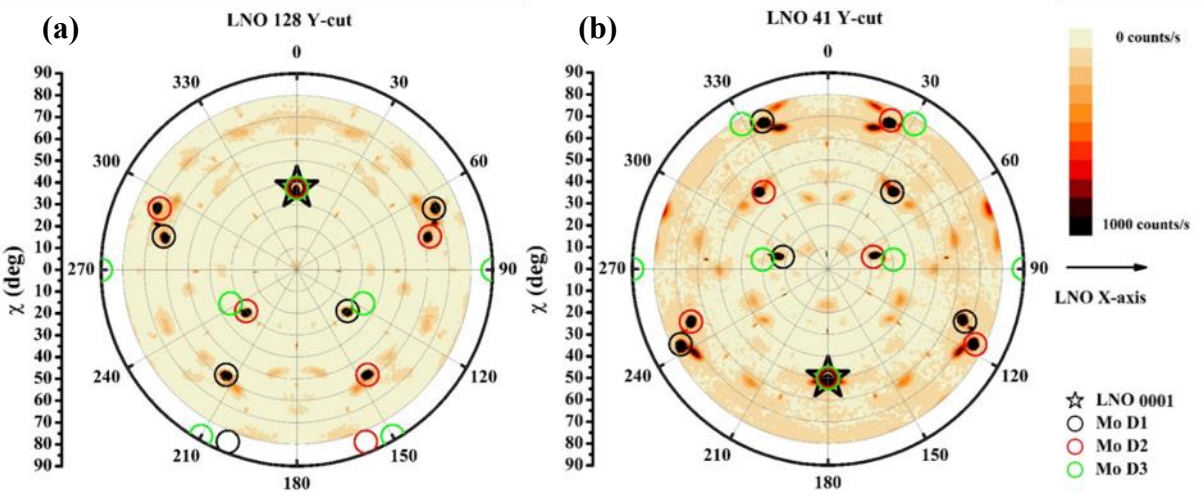

Figure 43. 110 Mo pole figures for Mo deposited on LNO 128 Y (a) and LNO 41 Y-cuts (b). Empty circles correspond to theoretical positions obtained from stereographic projections for OR described in the text. The star symbol refers to the LNO 0001 pole. The LNO X direction lies along the horizontal axis.

Both figures obviously reveal more 110 poles than expected from the cubic structure (12), which strongly suggests the presence of several crystalline domains. One can also notice that these figures are symmetrical with respect to the vertical 180-0° axis and that, for both substrates, one of the 110 Mo poles is superimposed with the 0001 LNO pole. This latter point reveals the following first relation between LNO and Mo lattices:

$$(110)\ Mo\ //\ (0001)\ LNO$$

Those tilted (110) Mo planes that intercept the LNO surface plane along the LNO X direction are consistent with the specific RHEED images (inclined planes with opposite angles between both substrates) observed when the electron beam is parallel to LNO X-axis.

Beyond the superimposed 110 Mo and 0001 LNO poles, the experimental positions of other 110 Mo poles ((Figure 43) have been compared to those expected from the R30 in-plane OR reported for (110) Mo deposited on (0001) LNO (cf. previous chapter)):

$$Mo < 001 > // LNO \ < 1\bar{1}00 > \text{ and } Mo < 1\bar{1}0 > // LNO \ < 11\bar{2}0 >$$

The theoretical positions of the poles (determined from the three theoretical stereographic projections associated with the three Mo domains following this R30-OR) are presented with empty circles (one color for each domain) in the Figure 43. The agreement between experimental and theoretical poles is very good for two domains D1 and D2, while experimental poles related to the third one (D3 in green) are obviously absent.

One can conclude to the occurrence of a three dimensional orientation relationship between Mo and LNO lattices, as this has already been reported in other system: Nb or Mo on sapphire [OST05].
The absence of the third Mo domain is relatively surprising given the symmetry of the (0001) LNO plane and must be related to a symmetry breaking issue linked to the surface. As shown by stereograms, some of these missing 110 poles (green circles in Figure 43) would be expected for large χ angles. Since (110) Mo planes are known to exhibit a very low surface free energy, (110) Mo surfaces are particularly stable, which most likely favors Mo domains the orientation of which gives rise to close-to-the-normal (110) poles. This is the case for D1 and D2 domains for which 110 poles are observed at 30° (resp. 21.5°) from the normal on LNO128Y (resp. on LNO41Y). The energy of the D3 domain with 110 poles at 34.1° (resp. at 30.3°) and especially one pole at 90° from the normal is likely larger than for other domains, and the D3 domain is consequently not favored during the growth process.

Figure 44 summarizes these results with: (a-b) the occurrence of (110) Mo planes parallel to (0001) LNO, thus significantly tilted from the surface normal and (c) the development of two Mo domains following the R30-OR in these parallel (110) Mo and (0001) LNO planes.

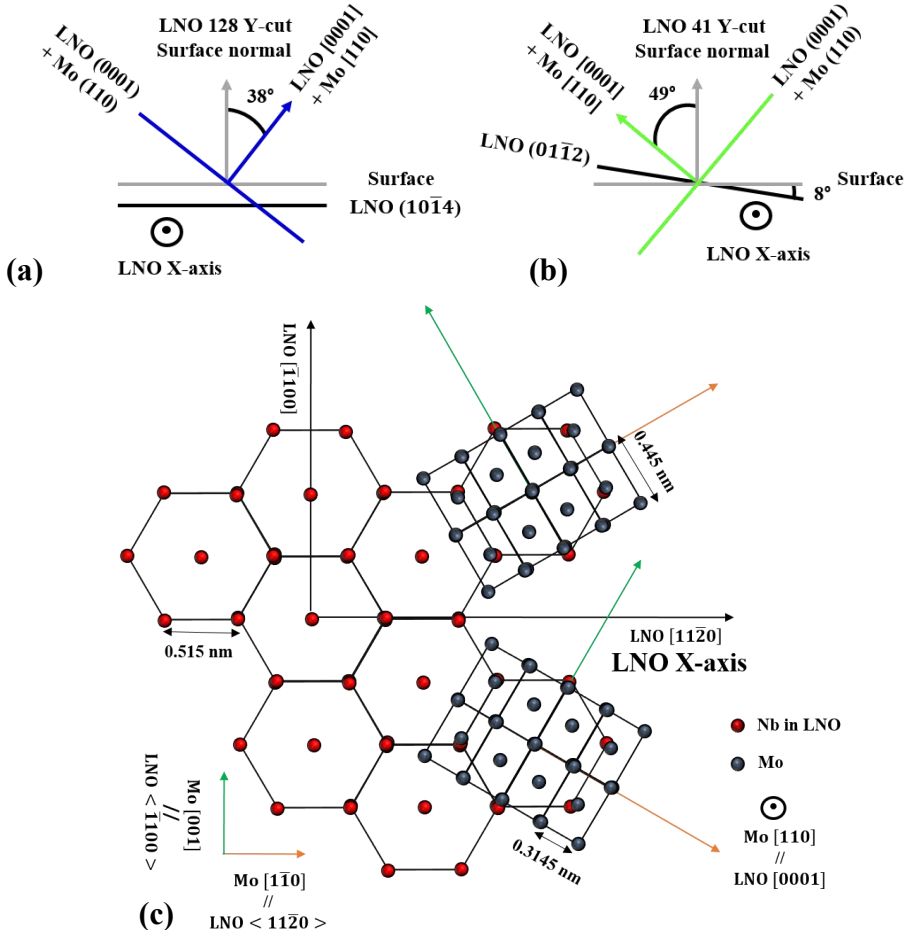

Figure 44. Schematic representation of the orientation of parallel (110) Mo and (0001) LNO planes in the case of LNO 128Y-cut (a) and LNO 41 Y-cut (b). Orientation relationships between the parallel (110) Mo (two domains in blue) and (0001) LNO (red) planes (c).

2. Growth of $TbFe_2$

The $TbFe_2$ growth on LNO128Y/Mo and LNO41Y/Mo has been performed in the [500 °C – 800 °C] temperature range without a clear incidence of this parameter on the crystalline quality. Results reported in this paragraph corresponds to 50 nm thick $TbFe_2$ films obtained for a deposition temperature of 650 °C.

Figure 45 gathers the RHEED images obtained for the $TbFe_2$ layers deposited on LNO 128 Y-cut (c and d) and LNO 41 Y-cut (g and h) along two azimuths labeled with respect to the substrate orientation (X and X+180°). The corresponding Mo images collected prior the $TbFe_2$ deposition are also recalled ((a-b) and (e-f)).

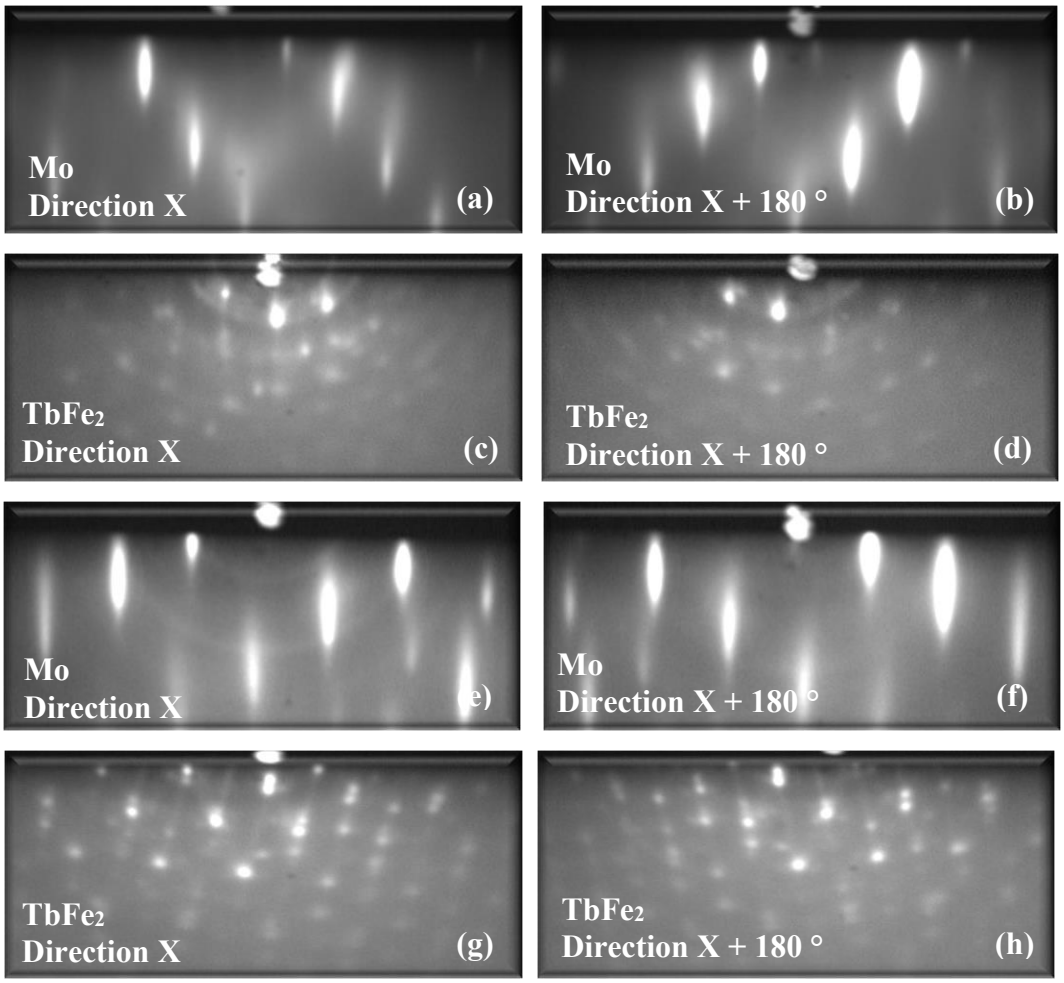

Figure 45. RHEED patterns of 50 nm thick $TbFe_2$ (c,d,g and h) deposited at 650 °C on LNO 128 Y/Mo (a and b) and LNO 41 Y/Mo (e and f). The direction X refers to the $< 11\bar{2}0 >$ crystalline direction of the substrate.

For both substrates, RHEED images obtained after the $TbFe_2$ deposition exhibit multiple dots, a high diffuse background and even sometimes a slight tendency to form rings (on LNO128Y). They are characteristics of a poor crystal order and most likely of the occurrence of multiple domains. One can also mention the occurrence of tilted features respect to the surface normal, as it is observed after the Mo deposition. For each azimuths, these lines are inclined in the same direction as Mo features but not with the same angle. Reasons of such behavior are still unknown.
It was not possible to properly analyze and extract relevant information from these RHEED measurements. As in the case of the Mo deposits, measurements of pole figures have been however undertaken to try to unravel the 3D orientation of the $TbFe_2$ films on these unconventional substrates.

Figure 46 presents the 111 and 220 $TbFe_2$ pole figures measured for $TbFe_2$ deposited on LNO 128Y/Mo and LNO 41Y/Mo.

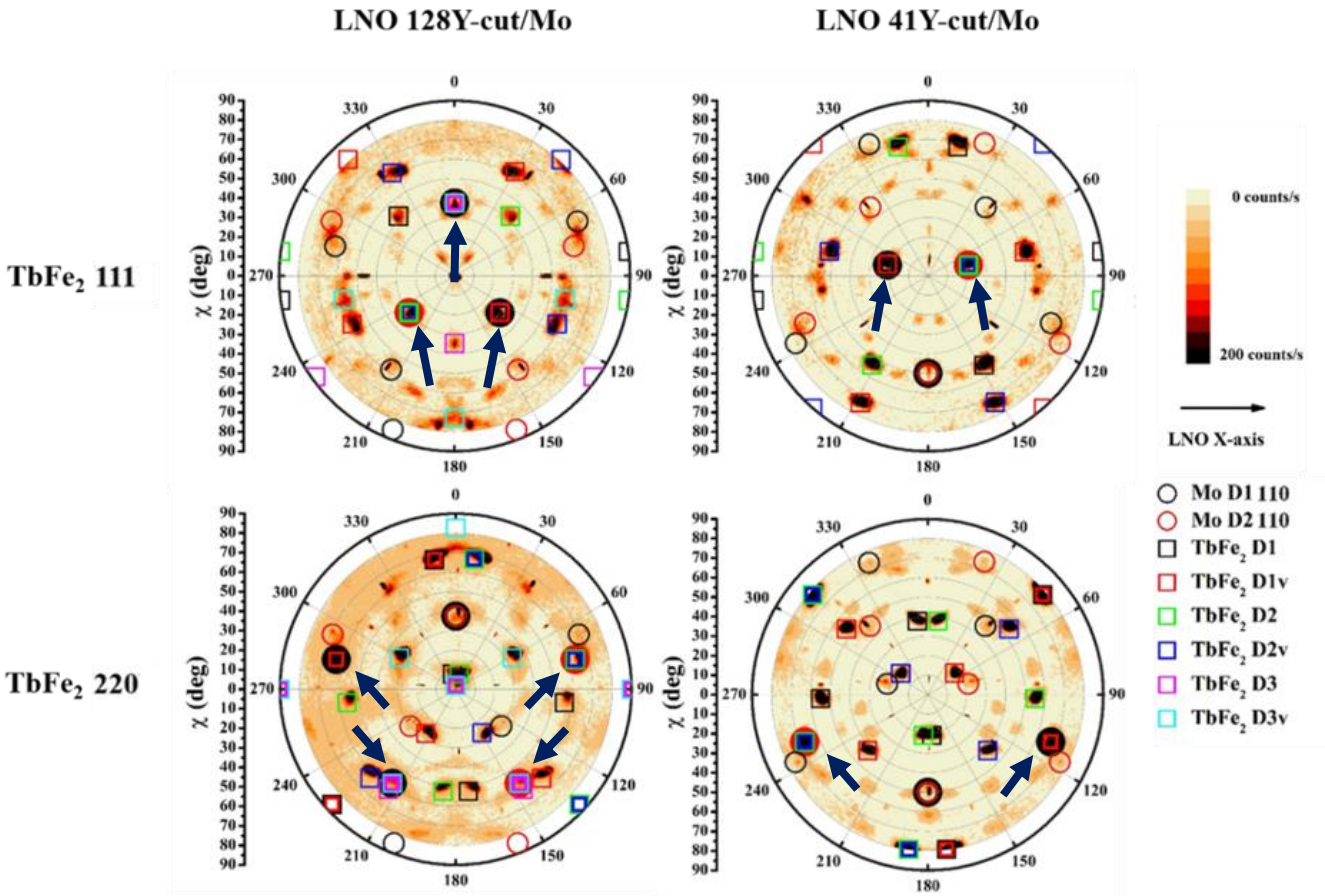

Figure 46. 111 and 220 $TbFe_2$ pole figures for deposition on LNO 128Y/Mo and LNO 41Y/Mo. Empty squares correspond to theoretical positions obtained from stereographical projections for various $TbFe_2$ domains and their variants, as described in the text. Empty circles correspond to theoretical positions for D1 and D2 Mo domains (see previous paragraph). The LNO X direction lies along the horizontal axis.

As expected from the RHEED results, these pole figures are complex with the observation of multiple poles. The measurements of both 111 and 220 pole figures were necessary to get a reasonable confidence in our interpretation. The analysis is by the way made harder by the fact that the poles appearing at low χ angles are systematically less intense than those appearing at larger χ, which is most likely related to the difference in sample volume probed in the different configurations. Poles at larger χ are also more dispersed, which is due to beam spreading. Intrinsic problems related to the X-ray source also make that the incident beam is not perfectly monochromatic and can lead to supplementary diffraction spots corresponding to different Bragg angles.

Beyond the occurrence of multiple poles, one can first underline two important points: (i) the pole figures are symmetrical respect to the vertical 180-0° φ axis (ii) there are several positions (indicated by arrows in Figure 46) where $TbFe_2$ experimental poles (111 or 220) are superimposed to the measured 110 Mo poles (recalled by empty circles).
The figures have been simultaneously and carefully analyzed, in comparison with theoretical stereograms calculated for possible ORs between Mo and $TbFe_2$ lattices. The best result yielding a reasonable agreement with experimental data is presented by empty squares in Figure 46. Each color refers to a given domain (D) or a variant (labeled "v").
The deduced OR between Mo and $TbFe_2$ lattices are the same for both LNO128Y and LNO41Y substrates:

(111) $TbFe_2$ // (110) Mo — with a selection for "less-tilted" planes respect to the sample surface (close-to-the-normal poles), as discussed in the following.

$TbFe_2 < 1\bar{1}0 > // Mo < 1\bar{1}0 >$
$TbFe_2 < 11\bar{2} > // Mo < 001 >$ — In the planes of coincidence.

The first relation with a selection for "less-tilted" planes respect to the sample surface is confirmed by off-specular large angle X-ray scattering experiments (Figure 47 (a)) where the scattering vector is tilted with respect to the surface normal, as sketched in Figure 47 (b).

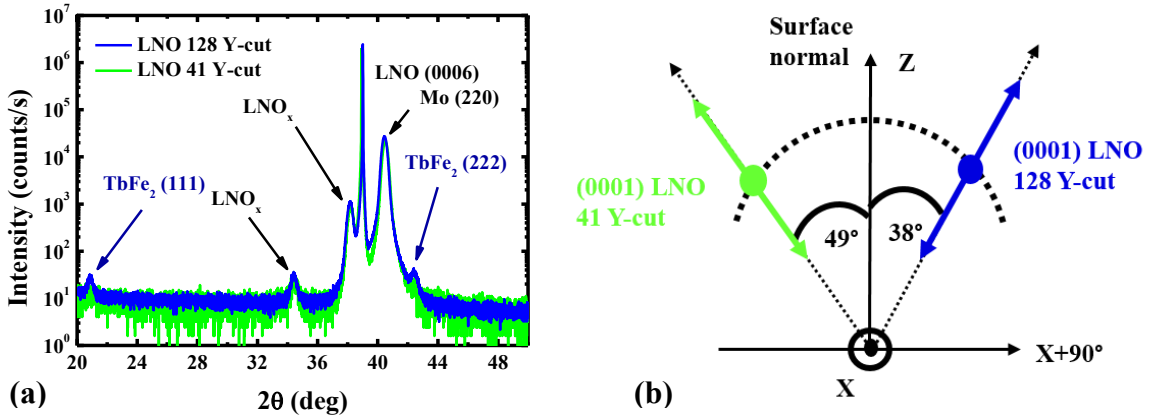

Figure 47. Off specular θ-2θ experiment performed on a 50 nm thick $TbFe_2$ film deposited on LNO128Y/Mo and LNO41Y/Mo at 650 °C (a). The measurements are carried out with scattering vectors along the [0001] LNO direction (38° and 49° with respect to the sample surface for LNO128Y and LNO41Y respectively) (b).

Despite a low $TbFe_2$ intensity, the measurements reveal parallel (0001) LNO, (110) Mo and (111) $TbFe_2$ planes as expected from pole figures. It has been verified that the Mo and $TbFe_2$ Bragg reflections disappear for scattering vectors shifting from tle LNO [0001] direction.

These OR correspond to the R30-OR observed between (111) $TbFe_2$ and (110) Mo planes on LNOZ substrates, pointing out the 3D character of this OR, as between Mo and LNO lattices. However, in contrast to the LNOZ case where the surface symmetry strongly favors (110) Mo and (111) $TbFe_2$ planes parallel to the surface, the occurrence of several tilted Mo domains gives rise here to multiple $TbFe_2$ domains and their associated variants (60° rotated around < 111 > directions). Those are however not fully equivalent, as this can be noticed in the poles figures: on LNO128Y, 111 $TbFe_2$ poles are observed on the three 110 Mo poles tilted by 30° and 38° from the normal (indicated by arrows), leading to 3×2 (variants) domains; on LNO41Y, 111 $TbFe_2$ poles are only observed on the two 110 Mo poles tilted by 21.5° from the normal (indicated by arrows), leading to 2x2 (variants) domains. No 111 $TbFe_2$ pole is observed on the 110 Mo poles tilted by 49° from the normal. As mentioned for the Mo growth on LNO128Y and LNO41Y, this non-equivalence of domains most likely originates from surface energy considerations. The (111) $TbFe_2$ planes with a low surface free energy are all the more favored than they lie close to the surface plane.
These $TbFe_2$ multidomains structures lead to a reasonable agreement between experimental poles and the expected stereographic projections for both substrates.

2. Magnetic properties of $TbFe_2$ deposited on LNO128Y and LNO41Y

The hysteresis loops measured for the $TbFe_2$ films deposited on LNO128Y/Mo and LNO41Y/Mo, with the magnetic field applied out of the plane and along the in-plane LNO X + 90° direction are presented

in Figure 48 (a and b). Figure 48 (c) and (d) present the measurements with the field applied along several in-plane directions between LNO X and X + 90° for these two substrates.

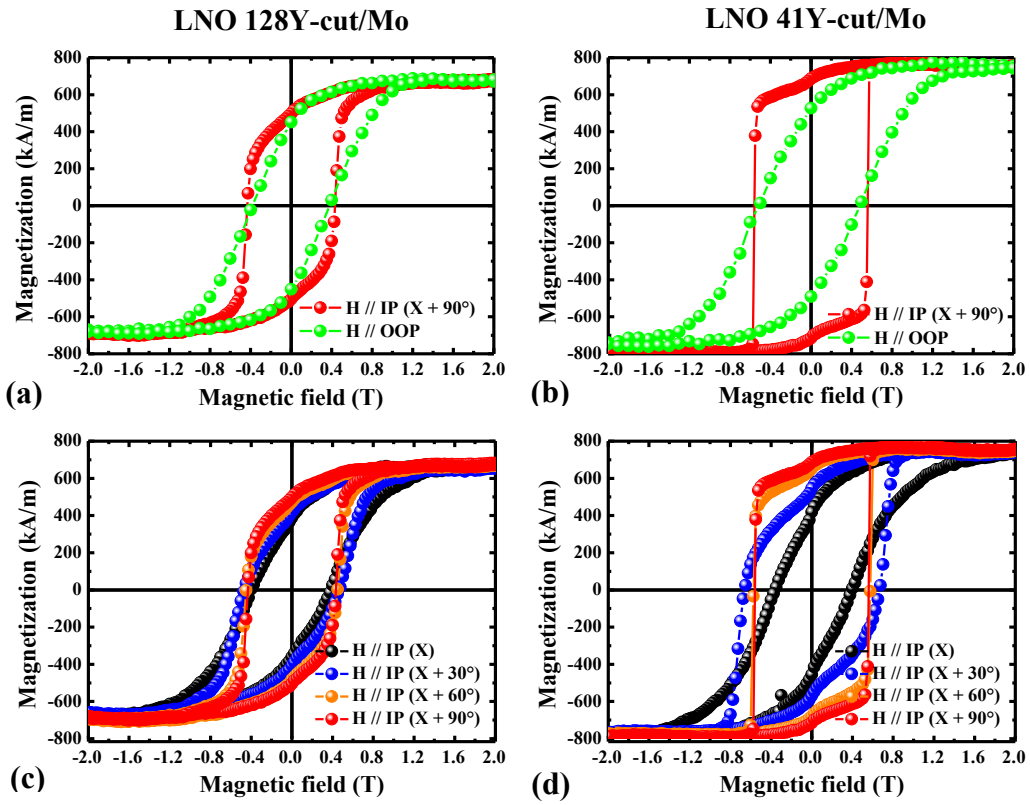

Figure 48. Room temperature hysteresis loops measured for 50 nm thick $TbFe_2$ films deposited on LNO128Y/Mo (a and c) and LNO41Y/Mo (b and d) with the magnetic field applied out of the plane (green), and in the plane along several directions from LNO X (black) to LNO X+90° (red).

The first point to underline here is the larger saturation magnetization compared to the one reported in the case of deposition on LNOZ. It reaches approximately 700 $kA.m^{-1}$ on LNO128/Mo and 800 $kA.m^{-1}$ on LNO41/Mo, this latter value being close to the saturation reported in the bulk compound. This higher saturation is relatively surprising given the moderate quality of the crystal order, the occurrence of multiple domains, and the use of a single Mo buffer layer; the supplementary Ti buffer is namely supposed to limit the interdiffusion with the LNO substrate. This would mean that these specific LNO cuts are more stable upon heating and that the high temperature chemical interaction with the $TbFe_2$ layer is reduced compared to the case of deposition on LNOZ. Further investigations are however required to sustain this interpretation.

The second point is the in-plane anisotropy, with the occurrence of an in-plane easy magnetization axis along the LNO X+90° direction for both substrates. It is especially clear on LNO41Y/Mo where the remanence is high and the magnetization reversal is sharp for the magnetic field applied along LNO X+90°. The OOP anisotropy observed for the films deposited on LNOZ disappears on these substrates, where different $TbFe_2$ crystal orientations are present and where the multidomain nature of the films most likely contribute to strain relaxation.
The in-plane anisotropic behavior, also different from the in-plane isotropy observed on LNOZ, is not easily understood from the complex $TbFe_2$ orientation. If induced strains, and thus magnetoelastic contributions, related to the growth process might not be relevant in this case, one can try to link the observed anisotropy to the magnetocrystalline and shape contributions. The shape anisotropy favors an in-plane magnetization but not a specific in-plane axis, except for an elongated microstructure that was not explored. The magnetocrystalline anisotropy should favor $< 111 >$ directions. From the measured poles figures and associated stereographic projections (see Figure 46), the different $TbFe_2$ domains lead

to several in-plane and close-to-the plane $< 111 >$ directions (for χ angles close to 90°) that should thus be favored by the combination of shape and magnetocrystalline anisotropy. These are obviously not responsible for the observed in-plane anisotropy with an easy axis along X+90° ; two of them are on the contrary close to 90° and 270° φ angles, *i.e.* close to the LNO X direction which appears as a magnetic hard axis.
The observed significant in-plane anisotropy thus remains up to now unexplained. Further investigation are required to analyze the domain morphology and films microstructure, and explore their possible influence. It could be also interesting to measure if the $TbFe_2$ lattice is strained and if it is strained differently in the different domains.

4. Summary of the $TbFe_2$ growth on LNO 128 and 41 Y-cut

In summary of this chapter on the $TbFe_2$ deposition on LNO128Y and LNO41Y-cut substrates, one can first underline that the crystalline growth of $TbFe_2$ on these unconventional and challenging substrates can be achieved in using a Mo buffer layer. The films do not exhibit a single crystalline character but are multidomains, as a consequence of the 3D orientation relationships between LNO, Mo and $TbFe_2$ lattices. Similar OR are namely observed for the crystalline growth on the three different LNO cuts:

$TbFe_2$ (111) // Mo (110) // LNO (0001)

with:

$$TbFe_2 < 1\bar{1}0 > // Mo < 1\bar{1}0 > // LNO < 11\bar{2}0 >$$
$$TbFe_2 < 11\bar{2} > // Mo < 001 > // LNO < 1\bar{1}00 >$$

i.e. R30-OR between Mo and LNO and R30-OR between $TbFe_2$ and Mo in these parallel planes.

Despite common 3D OR between various lattices, the surface free energy associated to different crystalline planes appears to play an important role since this will select specific domains among those that are equivalent from the OR point of view. A single domain is stabilized on LNOZ where the substrate's surface and OR drive low energy (110) Mo and (111) $TbFe_2$ growth planes; two or three domains with their associated variants develop on LNO128Y and LNO41Y where the substrate's orientation leads to Mo domains with significantly tilted $< 110 >$ directions. One has by the way to underline that the quality of the $TbFe_2$ crystal order is limited on these substrates, as revealed by the spatial extension of the diffracted intensity in pole figures.
These films however exhibit satisfactory magnetic characteristics with especially a large saturation magnetization in agreement with the expected bulk value. The easy magnetization axis lies in the sample plane and along the X+90° LNO direction, which still remains to be explained.

As mentioned at the beginning of this chapter, only Mo buffers have been used up to now. Complementary experiments are now planned to investigate whether 3D OR could also be observed with a single Ti buffer, which would possibly give rise to a single $TbFe_2$ domain if surface free energy considerations do not prohibit this growth process with a 38° or 49° tilted $< 111 >$ $TbFe_2$.

Chapter 5: Ni and [Co/IrMn] growth on LNO substrates

Ni-based and [Co/IrMn]-based SAW devices have been also synthetized and investigated for different reasons. First of all, Nickel has been used as a starting point since results on MSAW using this material can be found in literature and in a second step, [Co/IrMn] multilayers have been chosen to induce a in-plane first order anisotropy (appendix F) that helps controling the magnetization reversal for fields applied perpendicular to the sample plane (detailed in Part 3). For those materials, the samples have been fabricated with the sputtering technique described in appendix A.
This chapter summarizes the results obtained from the structural and magnetic characterization performed on these Ni films and [Co/IrMn] multilayers deposited on various LNO substrates.

1. Nickel films

For the various LNO substrates, a 5 nm thick Tantalum buffer layer is first deposited in order to improve the adhesion of the Nickel layer and also to promote a (111) Ni texture. It is well known that, in standard conditions, sputtered Ta with thickness less than 5 nm is amorphous and can be used to promote closed packed (111) fcc plane film deposition. Then, 50 nm or 200 nm thick Ni layers are deposited and capped with a 5 nm thick Pt layer to protect the Ni from contamination and oxidation. Ni is deposited using an RF Ar plasma with a power of 90 W and an Ar pressure of 7×10^{-3} Torr. In those conditions, the deposition rate is 0.1 $nm.s^{-1}$. The sample-holder is moved on top of the Ni target, forth and back along one axis during the process, to insure a good homogeneity of the deposition. The target configuration and the movement of the sample insure an in-plane magnetic anisotropy that has been chosen to be oriented along the LNO X-axis during deposition. The induction of an easy magnetization axis in a sputtering machine with respect to geometrical effects and/or stray field of the target material is well known and reported for example in [TEN86].

1.1. Structural characterization

Large angle X-ray scattering measurements performed for Ni films deposited on LNO Z, 128 Y and 41 Y-cuts are presented in Figure 49 ((a) for 50 nm and (b) for 200 nm). Since the alignment is performed with respect to the sample surface, the LNO 41 Y-cut substrate doesn't give rise to any specific Bragg peak in this configuration.

Beyond the substrate diffraction peak, these measurements mainly reveal the occurrence of a Bragg peak associated to Ni (111) planes. Since no other Bragg peaks were found on φ scans for AR**,** we conclude to a polycrystalline layer with a texture along [111]. The rocking curves measured across these Bragg peaks always present a FWHM of approximately 3-4°, whatever the Ni thickness and the LNO cut. The fcc Pt layer is also (111) textured as revealed by the peak at 40°. As expected, no evidence of texture could be found for the Ta layer.
In contrary to 200 nm thick Ni films, the quality of the 50 nm films does not depend on the substrate as evidenced by the intensity of the (111) Bragg peak. We have not explored in further details this effect.
All Nickel films are under compressive strain along the growth direction ($\varepsilon_\perp$): approximatively -0.06 % for all 50 nm thick Ni and -0.17 / -0.23 / -0.26 % for 200 nm thick Ni deposited on LNO Z/128Y/41Y respectively.

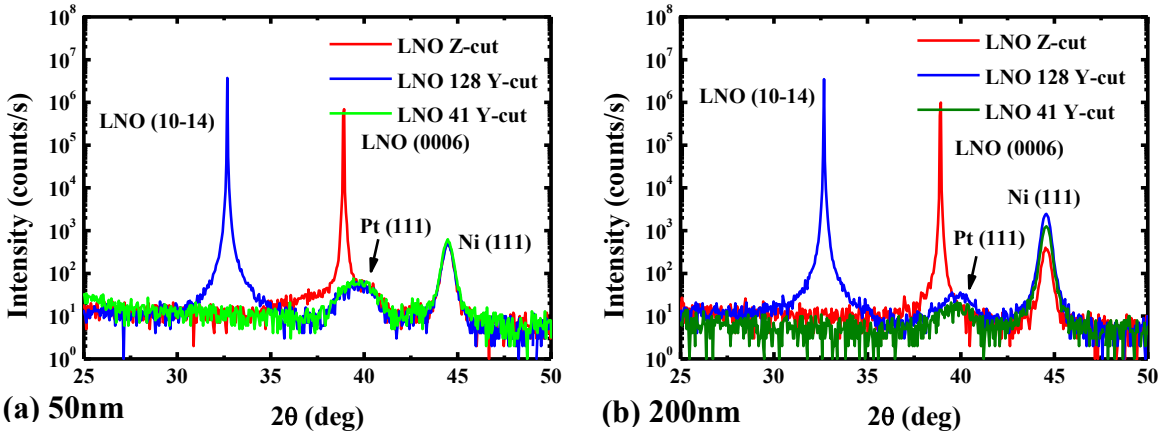

Figure 49. Large angle specular X-ray measurements performed for 50 nm (a) and 200 nm (b) thick Ni films deposited on different LNO substrates (Z/128Y/41Y-cuts).

1.2. Magnetic characterization for 50 and 200 nm thick Nickel films

Figure 50 (a, d, g for 50 nm thick Ni and b,e,h for 200 nm thick Ni) shows the hysteresis loops measured when the magnetic field is along two perpendicular in-plane directions of the various LNO substrates (H // IP (X (black) and X + 90° (red))). Figure 50 (c, f and i) present the results obtained when the magnetic field is applied perpendicular to the plane (OOP) for both Nickel thicknesses deposited on various LNO substrates.

Nickel 50 nm thick

The comparison of IP and OOP curves reveals that the easy magnetization axis lies in the plane whatever the LNO substrate. For LNO Z and LNO 41Y, a clear IP uniaxial anisotropy axis along LNOX is observed, as expected from previous deposition on Si and glass substrates (not reported here). Surprisingly, the films on LNO128Y have however isotropic characteristics, which remains unclear.
The main parameters deduced from these measurements are gathered in Table 9: the saturation magnetization, the in-plane coercive field measured along the EA, the in-plane and perpendicular to the sample plane saturation magnetic fields.

Substrate	Saturation magnetization (kA.m^{-1})	IP coercive field along EA (T)	IP saturation magnetic field along HA (T)	OOP saturation magnetic field (T)
LNO Z-cut	480	0.0025	0.0052	0.57
LNO 128 Y-cut	490	0.002	0.003	0.56
LNO 41 Y-cut	505	0.004	0.009	0.56

Table 9. Saturation magnetization, IP coercive field measured along EA, in-plane and perpendicular to the sample plane saturation magnetic field for 50 nm thick Nickel layers deposited on various LNO substrates.

One can first notice that, for the three substrates, the Ni saturation magnetization is consistent with the value expected from bulk Ni at room temperature (490 kA.m^{-1} [DAN68]). The OOP saturation field, equal to 0.56 T, is in accordance with the value extracted from $\mu_0 M_s = 0.61$ T (using M_s = 490 kA.m^{-1}). The in-plane saturation field is low, less than 9 mT. The easy magnetization axis in such soft materials strongly depends on shadowing effects (deposit with a deposition angle) [CHO14], residual strains [GHI15] or shape effects.

Nickel 200 nm thick

The results for the 200 nm thick Ni film reveal strong differences compared to the 50 nm film. The IP behavior is isotropic with a large remanence. The OOP curves for the films deposited on LNO 128Y

and LNO 41Y are typical of a perpendicular magnetic anisotropy with strong stripes domains configurations (see appendix F); one can namely notice the characteristic opening of small hysteresis loops close to the saturation. The IP and OOP hysteresis loops for the film deposited on LNO Z are closer to the response expected for weak stripe domains [HEH97].
The main parameters deduced from the magnetic measurements are gathered in Table 10: the saturation magnetization, the in-plane coercive field, the in-plane and perpendicular to the plane saturation magnetic fields and the perpendicular nucleation magnetic field (see appendix F).

Substrates	Saturation magnetization ($kA.m^{-1}$)	IP coercive field (T)	IP saturation field (T)	OOP saturation field (T)	OOP nucleation field (T)
LNO Z-cut	350	0.015	≈ 0.1	0.57	---
LNO 128 Y-cut	450	0.02	≈ 0.1	0.46	0.41
LNO 41 Y-cut	430	0.02	≈ 0.1	0.43	0.37

Table 10. Saturation magnetization, IP coercive field, IP and OOP saturation magnetic fields and OOP nucleation magnetic field for 200 nm thick Nickel layers deposited on various LNO substrates.

The saturation magnetization values are lower than expected from bulk Ni, especially for the deposit on LNO Z-cut. This could be related to the weak (111) Ni Bragg peak intensity measured in this case.
The perpendicular saturation and nucleation fields for Ni deposit on LNO 41 Y-cut are smaller than those obtained on LNO 128 Y-cut. In Thiele's theory [THI71] (appendix F), these fields depend on the set of exchange and anisotropy constants. The higher these constants, the lower the saturation and nucleation fields.

The stripes domains configuration in magnetic materials with perpendicular magnetic anisotropy is supposed to occur above a critical thickness h_1 with a transition from weak to strong stripes above a second thickness h_2 (see appendix F). Those thicknesses depend on saturation magnetization, exchange and anisotropy constants. From the expression of the OOP saturation field calculated by Thiele ($H_{s,OOP} = 4\pi M_s \left(1 - 1.596\sqrt{\frac{\sigma_w}{4\pi {M_s}^2 h}}\right)$ [THI71]), one can extract a value of the anisotropy constant of 3.3×10^4 J.m^{-3} (M_s = 490 kA.m^{-1}, A = 0.9×10^{-11} J.m^{-1} [YOU12] and $H_{s,OOP}$ = 0.43 T). The resulting values of h_1 and h_2 are 213 nm and 313 nm respectively.
Weak or strong stripes can thus be reasonably expected in the 200 nm thick Ni films, depending on the real values of K and saturation magnetization.

Let's now discuss the possible origin for the observed perpendicular anisotropy.
K_1 of Nickel, which leads to $< 111 >$ easy magnetization axis, *i.e.* the growth texture, is too weak (-5.7×10^3 J.m^{-3} at RT) to explain itself the perpendicular anisotropy constant found previously. The strains may however play a role as observed in literature for (001) BTO / polycrystalline Nickel (50 nm) [GHI15] or epitaxial (111) Si/Ag/Ni stack [NAI02]. In the case of the polycrystalline Ni films (strong stripes), the uniaxial OOP anisotropy arises from isotropic IP tensile stress generated at the grain boundaries during Volmer-Weber growth. In the case of the epitaxial layers (strong stripes above 50 nm), the uniaxial perpendicular magnetic anisotropy energy density is reported to be 3×10^4 J.m^{-3}, *i.e.* 5 times smaller than the demagnetizing field energy. According to these authors, the origin of K could be due to a growth induced residual stress.
The magnetoelastic energy in the case of a uniaxial stress on an isotropic thin layer can be written:

$$E_{m.e} \approx \frac{3}{2}\lambda_s \varepsilon_\perp {\alpha_z}^2$$

where λ_s is the magnetostriction coefficient at saturation, $\varepsilon_\perp$ is the perpendicular strain and α_z is the magnetization direction cosine along the perpendicular to the surface.
For a negative magnetostrictive material ($\lambda_s < 0$), the magnetic moments tend to align parallel to the compression. A compressive perpendicular strain ($\varepsilon_\perp < 0$) will generate a perpendicular easy axis and thus lead, above a critical thickness, to the nucleation of stripe domains [HUB98].

Knowing the tensile strain along the growth direction observed in the X-ray diffraction experiments and because polycrystalline Nickel posses a negative magnetostriction of -33×10^{-6} at RT [CLA80], a supplementary magnetoelastic energy contribution to the anisotropy can thus explained the observed perpendicular magnetization. The smaller compression on LNOZ could explain the weak stripes configuration, while the larger compression on LNO41Y could explain the smaller OOP saturation and nucleation fields.

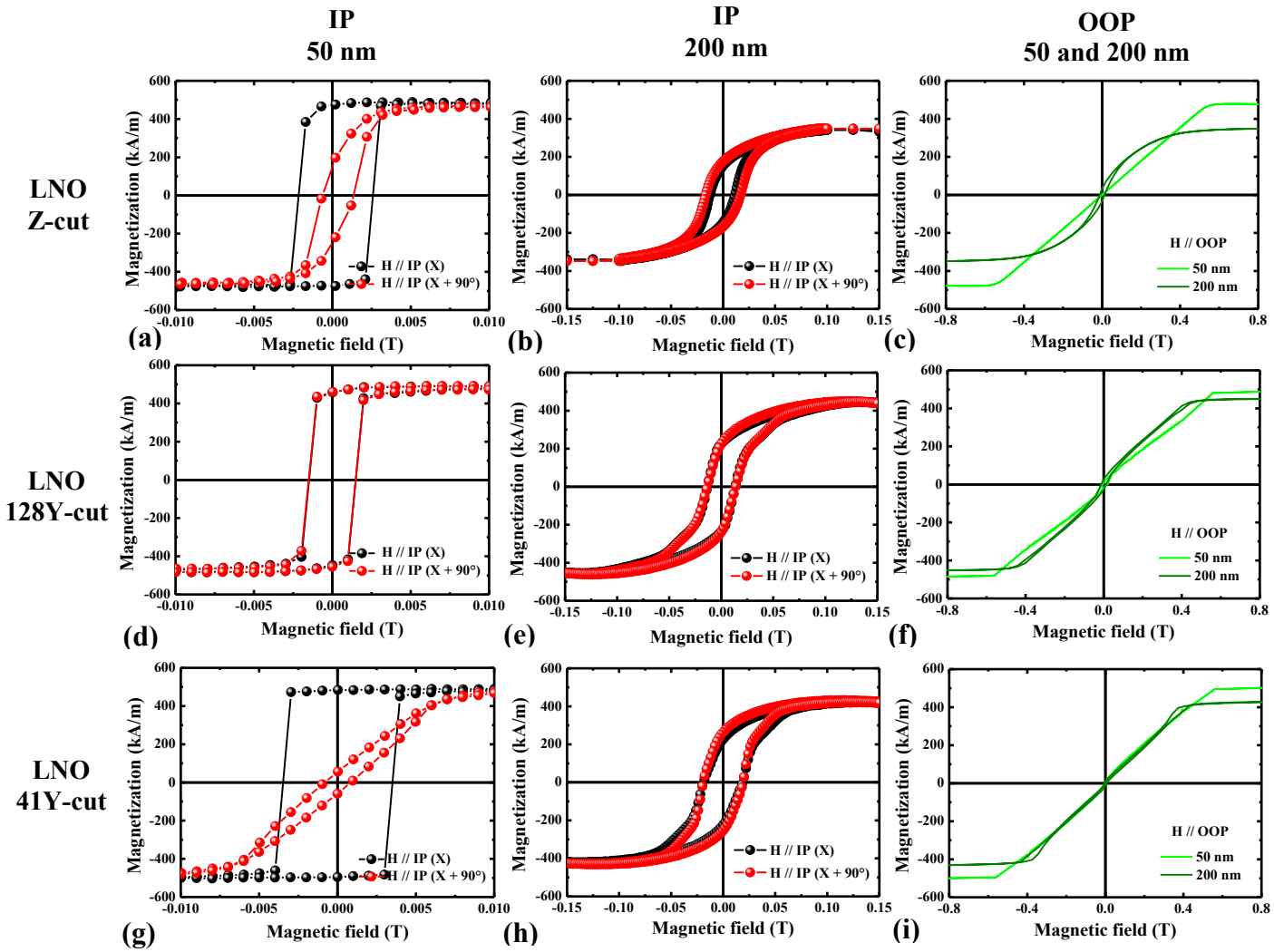

Figure 50. Room temperature hysteresis loops measured for 50 nm and 200 nm thick Ni films deposited on LNOZ (a-b-c), LNO128Y (d-e-f) and LNO41Y (g-h-i) substrates with the magnetic field applied along two in-plane directions (H//LNO X in black and H//LNO X+90 in red) and perpendicular to the sample plane (light green and dark green for 50 nm and 200 nm respectively).

2. [Co/IrMn] multilayers

As mentioned at the beginning of this chapter, the purpose of depositing [Co/IrMn] multilayers is to synthetize a magnetic material with a unidirectional in-plane anisotropy. A well-known possibility to achieve this is to combine a ferromagnetic and an antiferromagnetic material, to benefit from the interface exchange coupling giving rise to the exchange bias phenomenon, as explained in details in the appendix F.

[Co/IrMn] multilayers have been deposited on the LNO 41 Y-cut that exhibits the largest electromechanical coupling in comparison with LNO Z and LNO 128 Y-cuts. A 5 nm thick Ta layer is

used as an amorphous buffer layer to promote a (111) textured film and a 5 nm thick Pt layer protects the sample. The magnetic multilayer is composed of $[Co(5nm)/Ir_{0.2}Mn_{0.8}(5nm)]_{15}$. This $Ir_{0.2}Mn_{0.8}$ composition is commonly used in spintronics devices like in tunnel junctions to pin the reference magnetic layer [LIU08]. Co is deposited with a power of 100 W under an RF plasma (working pressure of 5×10^{-3} Torr) and with a deposition rate of 0.01 $nm.s^{-1}$. IrMn is deposited with a power of 10 W under a DC plasma (working pressure of 5×10^{-3} Torr) and with a deposition rate of 0.1 $nm.s^{-1}$. The sample-holder is moved forth and back along one axis during the process to insure a good homogeneity of the deposition. The multilayer stack is eventually annealed under an in-plane magnetic field (0.06 T) for 1 h at 200 °C to set the exchange-bias direction (along the X + 90° crystallographic direction of the substrate) as it is already reported in previous studies [NOZ00].

3.1. Structural characterization

Large angle specular X-ray diffraction measurement is presented in Figure 51 (green curve) for $[Co(5nm)/Ir_{0.2}Mn_{0.8}(5nm)]_{15}$ deposited on LNO 41 Y-cut. As mentioned previously, no Bragg peak from the LNO 41 Y-cut substrate is measured in this configuration. We have simulated the diffraction curve by considering that the multilayer diffracts coherently *i.e.* taking the multiple X-ray reflections on each atomic plane of the multilayer into account. The final result is the product of the interference function characteristic of the periodicity of the multilayer, and the structure factor of the bilayer. The development of the calculations can be found in [MAL04]. The simulated diffraction curve from this multilayer stack is presented in black.

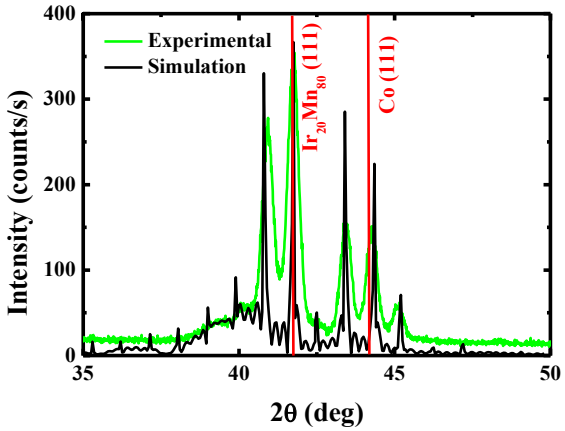

Figure 51. Large angle specular X-ray diffraction measurement (green) from a $[Co(5nm)/Ir_{0.2}Mn_{0.8}(5nm)]_{15}$ multilayers deposited on LNO41 Y-cut. Simulated curve is presented in black.

The measurements reveal a [111] textured multilayers, in agreement with previous results obtained with a Ta buffer layer [MAL03, MAL04]. Surstructure peaks can be well reproduced by the simulation with a $[Co(4.9nm)/Ir_{0.2}Mn_{0.8}(5.1nm)]_{15}$ multilayers stack with a slight in-plane contraction of the Co lattice.

3.2. Magnetic characterization

The magnetic hysteresis loops measured with the magnetic field applied in the plane along two perpendicular directions (LNO X and LNO X + 90° (a)) and OOP (b) are presented in Figure 52.

These results reveal an in-plane easy magnetization direction, parallel to the LNO X+90° direction, with an exchange bias field of the order of 33 mT (as expected from [MAL04]) and an opening of the loop of 7 mT. The in-plane saturation magnetic field is 0.1 T. The saturation magnetization is 1289 $kA.m^{-1}$, slightly smaller than the expected value of 1420 $kA.m^{-1}$. The saturation field along the OOP direction is 1.6 T.

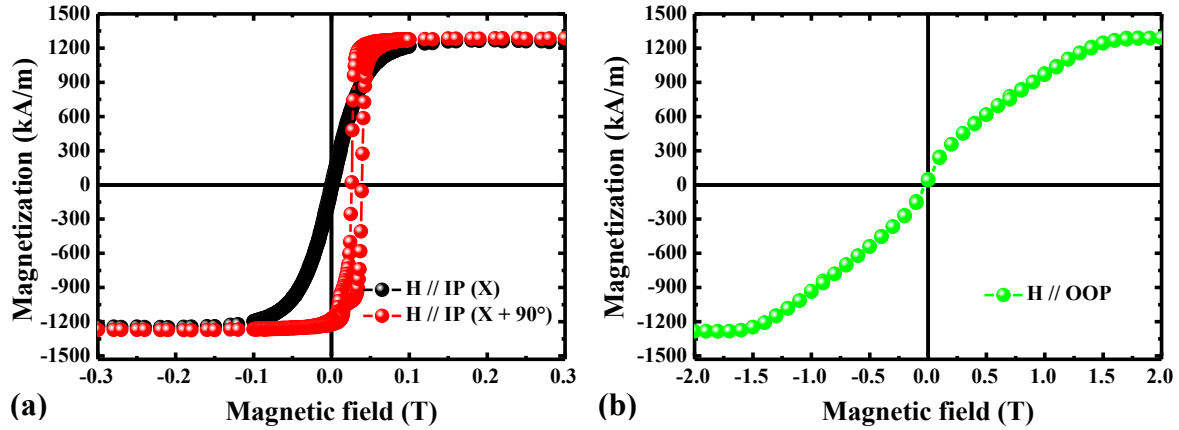

Figure 52. Room temperature hysteresis loops measured for a [Co(5nm)/$Ir_{0.2}Mn_{0.8}$(5nm)]$_{15}$ multilayers deposited on LNO 41Y-cut with the magnetic field applied along two in-plane directions (LNO X and X + 90° (a)) and along the perpendicular to the sample plane (b).

References

[AND05] S. Andrieu and P. Muller, *Les surfaces solides: Concepts et méthodes*, EDP Sciences, Savoirs actuels, (2005).

[AVI06] A. Avisou, *Croissance épitaxiale et propriétés magnétiques de films de $Sm_{1-x}Gd_xAl_2$: un ferromagnétique sans moment*, PhD dissertation, Université H. Poincaré, Nancy, (2006).

[AVI08] A. Avisou, C. Dufour and K. Dumesnil, *Control of magnetic anisotropy in (111) $SmAl_2$ films*, J. Appl. Phys. **103**, 07E135, (2008).

[CHO14] N. Chowdhury and S. Bedanta, *Controlling the anisotropy and domain structure with oblique deposition and substrate rotation*, AIP Advances**. 4**, 027104, (2014).

[CLA80] A. E. Clark, *Magnetostrictive RFe_2 intermetallic compounds*, Chap. 15, in Handbook on the physics and chemistry of rare earths, North Holland Publishing Company, (1980).

[DAN68] H. Danan, A. Herr and A. J. P. Meyer, *New determinations of the saturation magnetization of nickel and iron*, J. Appl. Phys**. 39**, 669, (1968).

[ELH16] M. Elhosni, O. Elmazria, S. Petit-Watelot, L. Bouvot, S. Zhgoon, A. Talbi, M. Hehn, K. Ait Aissa, S. Hage-Ali, D. Lacour, F. Sarry and O. Boumatar, *Magnetic field SAW sensors based on magnetostrictive-piezoelectric layered structures: FEM modeling and experimental validation,* Sensors and Actuators A: Physical**. 240**, 41-49, (2016).

[GAN76] A. K. Ganguly, K. L. Davis, D. C. Webb and C. Vittoria, *Magnetic control of surface elastic waves in a novel layered structure,* J. Appl. Phys. **47**, 2696, (1976).

[GHI15] M. Ghidini, F. Maccherozzi, X. Moya, L. C. Phillips, W. Yan, J. Soussi, N. Métallier, M. E. Vickers, N. J. Steinke, R. Mansell, C. H .W. Barnes, S. S. Dhesi and N. D. Mathur, *Perpendicular local magnetization under voltage control in Ni films on ferroelectric $BaTiO_3$ substrates*, Advanced Materials**. 27**, 1460-1465, (2015).

[HAS00] K. Y. Hashimoto, *Surface Acoustic Wave Devices in Telecommunications: Modeling and simulation*, Springer, (2000).

[HEH97] M. Hehn, *Elaboration, étude des propriétés structurales et magnétiques de couches et réseaux de plots submicroniques à base de Cobalt*, PhD dissertation, Université Louis Pasteur, Strasbourg, (1997).

[HEL98] 0. Hellwig, K. Theis-Briihl, G. Wilhelmi, A. Stierle and H. Zabel, *Growth of fcc (111) on bcc (110): new type of epitaxial transition observed for Pd on Cr*, Surface Science. **398**, 379-385, (1998).

[HOM87] H. Homma, K. Y. Yang and I. K. Schuller, *Role of lattice matching in epitaxy: Novel Ce Phase and new fcc-bcc epitaxial relationship*, Phys. Rev. B**. 36**, 18 (1987).

[HUB98] A. Hubert and R. R. Schafer, *Magnetic domains: The analysis of magnetic microstructure*, Springer, p 450, (1998).

[HUT98a] M. Huth and C. P. Flynn, *Magnetism and microstructure in epitaxial $TbFe_2$ (111) thin films*, Phys. Rev. B. **58**, 17, (1998).

[HUT98b] M. Huth and C. P. Flynn, *Effect of heteroepitaxial strain on Laves phases $TbFe_2$ and $DyFe_2$*, J. Appl. Phys. **83**, 7261, (1998).
[HUT99] M. Huth and C. P. Flynn, *Strain-induced perpendicular magnetization in $TbFe_2$ (111) thin films on $LiNbO_3$*, J. Mag. and Magn. Mat. **204**, 204-208, (1999).
[KWO86] J. Kwo, M. Hong and S. Nakahara, *Growth of rare-earth single crystals by molecular beam epitaxy: the epitaxial relationship between hcp rare earth and bcc niobium*, Appl. Phys. Lett. **49**, 319, (1986).
[LIU08] Y. F. Liu, J. W. Cai, W. Y. Lai and G. H. Yu, *Effect of Ir-Mn composition on exchange bias and thermal stability of spin valves with nano-oxide layers*, J. Appl. Phys**. 103**, 093908, (2008).
[MAL03] G. Malinowski, M. Hehn, O. Lenoble and A. Schuhl, *Magnetic origin of enhanced top exchange biasing in Py/IrMn/Py multilayers,* Phys. Rev. B**. 68**, 184404, (2003).
[MAL04] G. Malinowski, *Transport dépendant du spin et couplage d'échange: de la jonction tunnel au capteur magnétique intégré*, PhD dissertation, Université H. Poincaré, Nancy, (2004).
[MAT99] K. Matsubara, P. Fons, A. Yamada, M. Watanabe and S. Niki, *Epitaxial growth of ZnO thin films on $LiNbO_3$ substrates*, Thin Solid Films**. 347**, 238-240, (1999).
[MCC94] M. A. McCoy, S. A. Dregia and W. E. Lee, *Crystallography of surface nucleation and epitaxial growth of lithium triniobate on congruent lithium niobate,* J. Matter. Res. **9**, 2029-39, (1994).
[MOU99a] A. Mougin, *Nanosystèmes magnétostrictifs de $TRFe_2$ (110) (TR=terre rare): croissance, morphologie et propriétés magnétiques*, PhD dissertation, Université H. Poincaré, Nancy, (1999).
[MOU99b] A. Mougin, C. Dufour, K. Dumesnil, N. Maloufi and Ph. Mangin, *Strain in single-crystal RFe_2* (110) thin films (R=Y, Sm, Gd, Tb, $Dy_{0,7}Tb_{0,3}$, Dy, Er, Lu), Phys. Rev. B. **59**, 8, (1999).
[MOU00] A. Mougin, C. Dufour, K. Dumesnil, N. Maloufi and Ph. Mangin, *$DyFe_2$ (110) nanostructures: Morphology and magnetic anisotropy*, Appl. Phys. Lett**. 76**, 11, (2000).
[MOU01] A. Mougin, C. Dufour, N. Maloufi, K. Dumesnil and Ph. Mangin, *From anisotropic dots to smooth RFe_2 (110) single crystal layers (R= rare earth)*, Eur. Phys. J. B.**19**, 289-296, (2001).
[NAG97] H. Nagata, K. Shima and J. Ichikawa, *Effect of hydroxyl content on thermally induced change in surface morphology of Lithium Niobate (0001) substrates,* J. Am. Ceram. Soc. **80**, 1203-207, (1997).
[NAI02] R. Naik, S. Hameed, P. Talagala, L. E. Wenger and V. M. Naik, *Comparative study of stripe magnetic domains in epitaxial Ni(111) and Co(0001) films*, J. Appl. Phys**. 91**, 10, (2002).
[NAM05] G. Namkoong, K. K. Lee, S. M. Madison, W. Henderson, S. E. Ralph and W. A. Doolittle, *III-nitride integration on ferroelectric materials of lithium Niobate by molecular beam epitaxy,* Appl. Phys. Lett. **87**, 171107, (2005).
[NAM11] M. H. Nam, W. Yang, M. D. Kim and I. S. Park, *Epitaxial growth of GaN films on atomically stepped (0001) Lithium-Niobate ($LiNbO_3$) substrates*, Journal of the Korean Physical Society**. 58**, 5, (2011).
[NOZ00] J. P. Nozières, S. Jaren, Y. B. Zhang, K. Pentek, A. Zeltser, P. Wills and V. S. Speriosu, *Correlation between lifetime and blocking temperature distribution in spin-valve structures*, American Institute of Physics**. 87**, 6609, (2000).
[ODE96a] V. Oderno, *Croissance de couches minces épitaxiées de phases de Laves TR-Fe_2 (TR=Y, Tb, Dy et Er). Influence des déformations épitaxiales sur l'anisotropie magnétique*, PhD dissertation, INPL, Ecole des mines de Nancy, (1996).
[ODE96b] V. Oderno, C. Dufour, D. Dumesnil, Ph. Mangin and G. Marchal, *Epitaxial growth of (110) $DyFe_2$, $TbFe_2$ and $Dy_{0,7}Tb_{0,3}Fe_2$ thin films by molecular beam epitaxy*, Journal of Crystal Growth. **165**, 175-178, (1996).
[OST05] J. Otser, L. Wiehl, H. Adrian and M. Huth, *Magnetic and magnetoelastic properties of epitaxial (211)-oriented RFe_2 (R=Tb or Dy) thin films*, J. Mag. and Magn. Mat**. 292**, 164-177, (2005).
[STA98] E. M. Standifer, D. H. Jundt, R. G. Norwood and P. F. Bordui, *Chemically reduced Lithium Niobate single crystals: Processing, properties and improvements in SAW device fabrication and performance,* IEEE. Frequency control. **87**, 470-472, (1998).
[TEN86] E. Teng and N. Ballard, *Anisotropy induced signal waveform modulation of DC magnetron sputtered thin film disks*, IEEE**.** Trans. Magn**. 22**, 579, (1986).
[THI71] A. A. Thiele, A. H. Bobeck, E. Della Torre and U. F. Gianola, *The energy and general translation of cylindrical magnetic domains*, Bell Syst. Tech. Journal**. 50**, 711, (1971).
[VYA13] J. C. Vyas and S. G. Singh, *The negative thermal expansion coefficient in lithium niobate single crystals*, AIP Advances. **1512**, 912, (2013).

[WAN96] C. T. Wang, B. M. Clemens and R. L. White, *Effects of substrate on the magnetic properties of epitaxial $TbFe_2$ (111) films*, IEEE. Trans. Magn. **32**, 4752, (1996).
[YAM79] H. Yamamoto, M. Naoe, S. Yamanaka, M. Yamaguchi and H. Kogo, *Variable surface acoustic wave delay line consisting of a magnetic thin film on a $LiNbO_3$ substrate,* Jap. J. of Appl. Phys**.** **18**, 209-213, (1979).
[YAM80] M. Yamaguchi, K. Y. Hashimoto, H. Kogo and M. Naoe, *Variable saw delay line using amorphous $TbFe_2$ film,* IEEE. Trans. Magn**. 16**, (1980).
[YOU12] C. Y. You, *Dependence of the spin transfer torque switching current density on the exchange stiffness constant*, App. Phys. Express**. 5**, 10, (2012).
[ZHO14] H. Zhou, *Etude théorique et expérimentale de systèmes à ondes de surface dans des structures multicouches piézomagnétiques pour des applications en contrôle santé intégré de MEMS par imagerie acoustique non linéaire*, PhD dissertation, IEMN, Lille, (2014).

Third part: Magnetic Surface Acoustic Wave (MSAW) devices

This part reports on the study of magnetic surface acoustic waves devices patterned from the hybrid piezoelectric/magnetostrictive stacks presented previously. The first chapter will give a general introduction on acoustic waves and surface acoustic wave devices. After describing the two main geometries (delay line and resonator), we see how magnetic devices can be created. State of the art concerning such devices is then presented, which permits to underline the objective of this work. The chapter 2 describes the nano-fabrication steps, basic characterizations and measurements configurations of our resonator devices. The chapter 3 is specifically devoted to the 50 nm thick Nickel-based devices on various LNO cuts. A piezomagnetic equivalent model developed by Zhou *et al.* [ZHO14] is used to understand the role of the magnetic anisotropy for the in-plane magneto acoustic responses. A wireless remote interrogation is presented. The following chapter (chapter 4) presents how the MSAW responses can be controlled and designed in controlling the magnetic properties. Finally, the last chapter (chapter 5) summarizes additional effects observed in non-conventional geometries.

Chapter 1: Acoustic waves and devices

The aim of this first chapter is to express the various acoustic waves propagating in materials and to present the devices that can generate and detect those specific waves. So-called surface acoustic waves will be distinguished from bulk acoustic waves. All these waves can be generated by inverse piezoelectric effect in devices whose geometries are presented further. A state of the art of magnetic surface acoustic wave devices is given at the end of the chapter.

1. Different acoustic waves

1.1. Bulk acoustic waves

Bulk acoustic waves are defined as waves that penetrate and propagate in the host material with a penetration depth equal to the thickness of the material. Two types of bulk waves are distinguished: longitudinal waves and transverse waves. Usually, acoustic waves in materials are a linear combination of these two types of waves. For longitudinal waves, the displacement of the atoms is collinear to the direction of propagation (Figure 53 (a)). The atoms move back and forth with respect to their equilibrium position with a succession of compressions and expansions of the lattice. These waves do not exhibit a polarization (parameter that describes the geometrical orientation of oscillations) and have the highest speed since the move is linear. For a cubic/hexagonal crystal, a longitudinal wave propagating along [100]/[$1\bar{1}00$] or [010]/[$11\bar{2}0$] travels with the velocity (found with Christoffel equation [NEW04]):

$$v_L = \sqrt{\frac{C_{11}}{\rho}}$$

where C_{ij} is the elastic constant and ρ is the material's density.

For transverse waves, the displacement of the atoms is perpendicular to the direction of propagation. Two kinds of polarization of transverse waves are distinguished: Shear Horizontal (SH) or Shear Vertical (SV (Figure 53 (b))). Transverse waves propagating in a cubic/hexagonal crystal along [100]/ [$1\bar{1}00$] or [010]/[$11\bar{2}0$] travel with the following velocities (found with Christoffel equation [NEW04]):

$$v_{SH} = v_{SV} = \sqrt{\frac{C_{44}}{\rho}} \text{ (cubic)}$$

$$v_{SH} = \sqrt{\frac{C_{66}}{\rho}} = \sqrt{\frac{(C_{11}-C_{12})}{2\rho}} \text{ (hexagonal)}$$

$$v_{SV} = \sqrt{\frac{C_{44}}{\rho}} \text{ (hexagonal)}$$

Depending on the cut and the direction of wave propagation in Lithium Niobate, a transverse wave and a longitudinal wave have velocities close to 4000 m.s^{-1} and 6500 m.s^{-1} respectively [CAM98]. It is well-known that transverse waves propagate with a speed about half the speed of longitudinal waves.

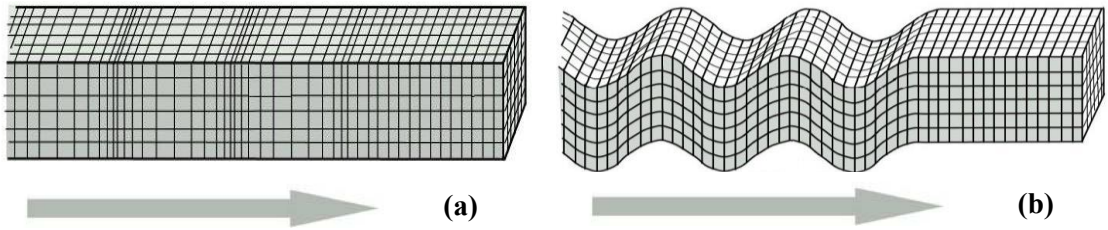

Figure 53. Longitudinal wave (a) and shear vertical wave (b) propagating in a material. Arrows represent the direction of wave propagation.

1.2. Surface acoustic waves (Rayleigh and quasi SH/SV surface acoustic waves)

Surface acoustic waves arise from the interaction of acoustic waves with the interface (rough surface, covered with a layer…), and are defined as waves that penetrate the host material in a depth less than a few acoustic wavelengths [NAZ17]. Among the various surface acoustic waves, one can mention:
(i) Rayleigh Waves (RW) were named in reference to Lord Rayleigh who predicted mathematically the existence of this type of wave in 1885 [RAY85]. Rayleigh waves result from the superposition of vertical and horizontal atomic displacements that defines a complex movement. It results actually from the combination of a shear vertical and a longitudinal wave and has an elliptical polarization (Figure 54). However, the main displacement is essentially longitudinal. The velocity of this kind of wave can be approximated by using the following formula [BER48]:

$$v_R \approx \frac{0.87 + 1.12\nu}{1 + \nu} . v_{SH/SV}$$

with $v_{SH/SV}$ the Shear Horizontal/Vertical velocity and ν the Poisson ratio (Roditi : 0.25 for LNO) of the material. The propagation velocity of this surface acoustic wave is thus smaller than longitudinal or transverse waves. Depending on the cut and the direction of wave propagation in Lithium Niobate, a Rayleigh wave has a velocity close to 3500 $m.s^{-1}$ [CAM98].

(ii) Transverse waves propagating close to the surface may exhibit multiple polarizations with vertical and horizontal displacements of the atoms. These waves are named by their strong displacement field: Quasi Shear Horizontal Surface Acoustic Wave (QSHSAW) or Quasi Shear Vertical Surface Acoustic Wave (QSVSAW). Velocities of these surface waves are close to their respective transverse volume wave velocities. The penetration depth of these waves is usually larger than for Rayleigh waves [PAR87].

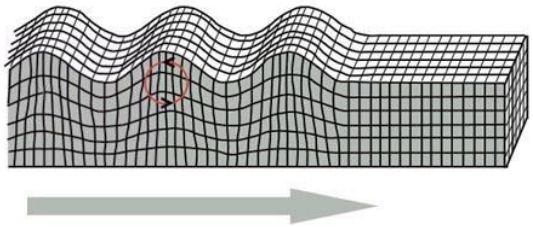

Figure 54. Rayleigh wave propagating in a material. The arrow represents the direction of wave propagation.

2. SAW devices

The first surface acoustic wave transducers were manufactured by White and Voltmer in 1965 [WHI65]. When an electric voltage is applied to an InterDigitated Transducer (IDT) designed on the top of a piezoelectric material (Figure 55), a strain is induced by the electric field through the inverse piezoelectric effect. By the use of an alternative electric voltage, compression and expansion of the

piezoelectric layer occur and a surface acoustic wave is generated. In a SAW device, either the substrate itself or a deposited layer can be piezoelectric.

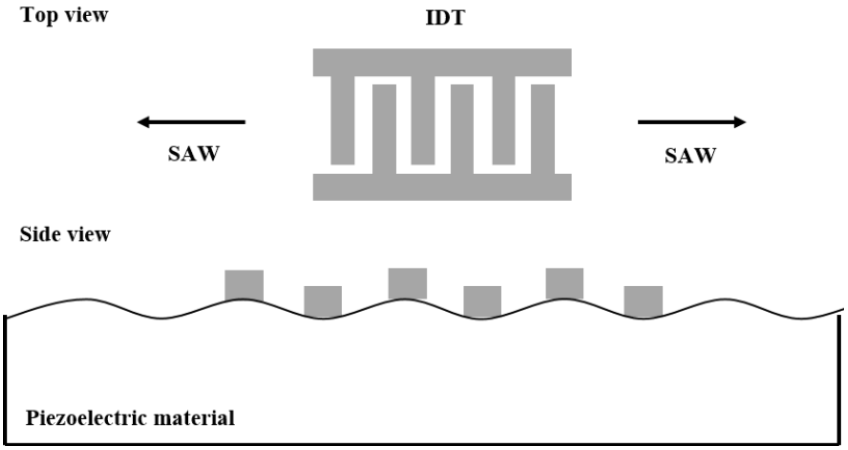

Figure 55. Generation of surface acoustic waves using voltage applied to IDT deposited on the surface of a piezoelectric material. Arrows represent the direction of wave propagation.

Reciprocally, when a surface acoustic wave propagates under an IDT, an AC electric voltage can be induced by piezoelectric effect. The association of emitter and receiver IDTs on the same substrate permits to build up acoustic devices as will be shown in the following. Considering a given acoustic velocity, the frequency of the device can be modulated as a function of the wavelength. For a given wavelength, the frequency of the device can be modified by an external stimulus that changes the wave velocity. As a result, many applications can be prospected, such as the use of SAW devices as filters, oscillators, transducers or sensors.
SAW sensors offer some interesting advantages. They are easy to manufacture, they do not require embedded power and they can be remotely addressed. Acoustic waves in a material are moreover sensitive to temperature, pressure, mass loading and since they are located at the surface, they can be modified by humidity or molecules adsorbed at the surface allowing for instance gas analysis [BO16]. As a result, SAW devices are used as cheap physical and chemical sensors.

As it is extensively detailed in [CAM98], two main geometries are used in SAW devices: the delay line and the resonator geometries.

2.1. Delay line devices

Such devices contain two separate IDTs: one is the emitter, which generates an acoustic wave through inverse piezoelectric effect and the second one is the receiver, which converts the acoustic wave into an alternating voltage (Figure 56). Since, in the case of unidirectional IDT, the acoustic waves are emitted on both sides of the emitter IDT, only half of the injected power reaches the receiver IDT and is reconverted into electrical energy. The device frequency can be modified by an external stimulus that changes the wave velocity and thus the time spent to travel between IDTs. A test layer can be inserted between IDTs, on the trajectory of the acoustic wave, to study its properties. Delay lines devices are often employed for oscillators, clock recovery filters for fiber optics communications repeater stages, IF (Intermediate Frequency, which is a fixed frequency where a wave is shifted as an intermediate step during transmission) filters for mobile receivers [CAM98]. Moreover, when combined with reflectors, delay line devices coud also be used as wireless SAW sensor including RF tag for identification.

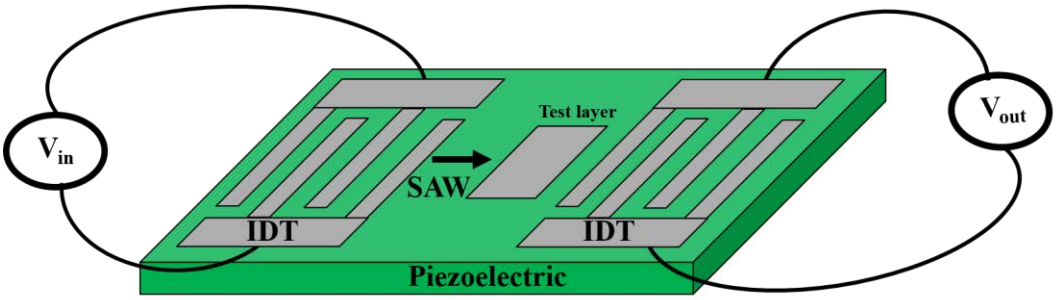

Figure 56. Delay line geometry. The arrow represents the direction of wave propagation from the acoustic wave emitter towards the receiver (those are separated).

2.2. Resonator devices

A SAW resonator is composed of only one IDT and two Bragg reflectors located on each side of the IDT (Figure 57). The waves generated by the IDT towards the right and the left are reflected by the reflectors. The positions of the reflectors are such that constructive interferences of the reflected acoustic waves occur at the IDT position for a given frequency. At other frequencies, the waves get reflected out-of-phase and consequently die out. The reflected waves form a stationary wave which is fundamental to device operation. Resonator filters are often used in automotive keyless entry, medical alert transmitter circuits or communication systems, where the combination of several resonators leads to achieve very low oss filter [CAM98].

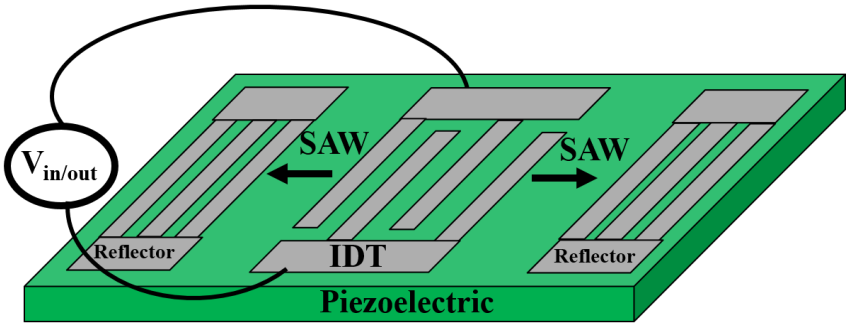

Figure 57. Resonator geometry for SAW devices. The arrows represent the directions of wave propagation. A single IDT constitutes the acoustic wave emitter and receiver.

3. MSAW devices

In order to get the capability to sense magnetic fields, magnetic materials have to be added to the SAW device. As it will be presented in the paragraph devoted to the state of the art, such systems combining magnetic and piezoelectric materials are designed to investigate the influence of the SAW propagation on the magnetic properties, especially the magnetization dynamics or to tune the operating frequency of SAW devices.

3.1. Geometries for MSAW devices

The main geometries usually proposed for MSAW devices (Figure 58 (a, b and c)) are similar to those presented in the previous paragraphs.

In delay line devices, a magnetic layer is deposited between the two IDTs, on the trajectory of the acoustic wave (Figure 58 (a)). In the resonator geometry, the sensitivity to an external magnetic field is achieved either in using a magnetostrictive material to pattern the IDT and reflectors (Figure 58 (b)) or

in separating IDT and magnetic material (Figure 58 (c)). In the latter case, the piezoelectric layer must be thin (thickness < penetration depth) enough for the SAW to probe the magnetic material.

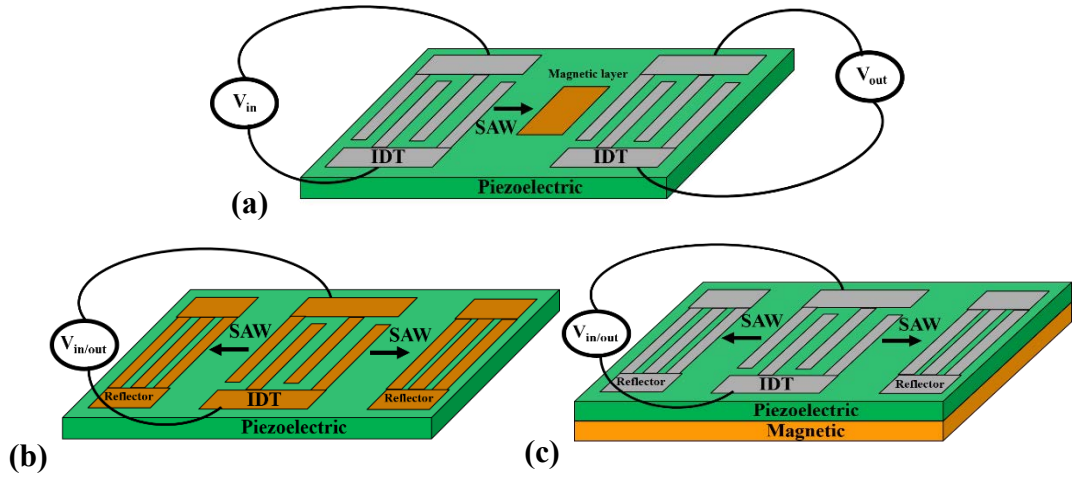

Figure 58. MSAW devices in delay line geometry (a) and resonator geometry (b and c). The magnetic material is presented here in gold. The arrows represent the direction of acoustic wave propagation.

3.2. State of the art

MSAW devices are complex coupled systems due to the interaction, mainly mediated by interface lattice strains, that is likely to occur between the magnetization and the surface acoustic wave. A complete description of such systems could be achieved in considering coupled equations that govern the magnetization dynamics (Landau-Lifshitz-Gilbert (LLG)) and the wave propagation (equation of motion). To give first basic ideas on the underlying physics involved in the MSAW behavior, one can distinguish static and dynamical contributions, although those could be of course intimately mixed.
Static contributions arise from the change in magnetic configurations that can be induced by an external magnetic field before reaching the saturation. The associated magnetostrictive strains and changes in elastic constants would influence the SAW characteristics.
Dynamical contributions arise from the SAW propagation that induces an interface time-dependent strain and thus a time-dependent magnetoelastic contribution to the magnetic free energy density. A corresponding dynamical internal magnetoelastic field thus adds to the external applied static field and anisotropy field. The resulting total effective field can drive the magnetization dynamics. Such a magnetoelastically induced magnetization dynamics can have a backaction on the SAW characteristics, both on the velocity and the attenuation, as it has been shown by several authors.

Most of the research activities related to MSAW devices appear to focus on two main aspects of these systems: (i) the modification of the SAW characteristics by an external static magnetic field (ii) and the elastic excitation of the magnetization dynamics. The major studies published on these topics are summarized in the following paragraphs.

3.2.1. MSAW devices as possible magnetic field sensors

In these studies, the authors mostly focus on the changes in the SAW characteristics related to the field induced changes in the magnetic configuration. These changes are generally observed for small field amplitude before reaching the magnetic saturation and a clear understanding of the correlation between magnetic and magneto acoustic responses is thus required. Less attention is generally paid to the possible induced magnetization dynamics although, as mentioned previously, both static and dynamical contributions can simultaneously play a role if the conditions (frequency, geometry…) are fulfilled. A strong motivation to these various studies is the possible development of magnetic field sensors.

In the early 1980's, MSAW devices in a delay line geometry have been studied with Nickel, or with amorphous $TbFe_2$ [YAM79, YAM80, WEB79] deposited on LNO substrates.
The authors present the dependence of the SAW resonance frequency (the type of SAW is not reported) on the applied field intensity and direction with respect to the wave propagation direction (see Figure 59). They do not correlate these responses to the magnetic properties (not reported), but mention a deltaE-effect and a dynamic magnetoelastic coupling related to magnetostrictive properties, SAW-induced strains, field direction. Without providing a formal approach to this coupling, the explanation remains relatively unclear. They obtained however a maximum amplitude of frequency variation of approximatively 2800 ppm when the magnetic field is applied along the wave propagation direction.

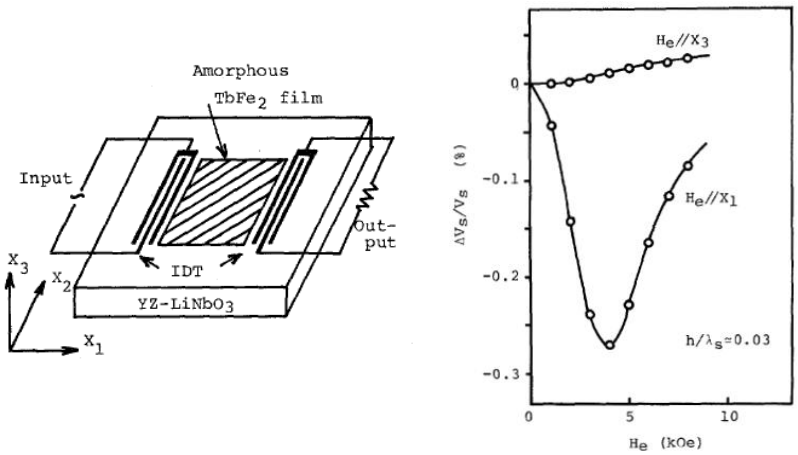

Figure 59. Variation of the SAW frequency as a function of the applied magnetic field along the wave propagation direction and perpendicular to the device surface. Results are measured on an amorphous LNOY/$TbFe_2$ device in the delay line geometry with a wave propagation direction along LNO Z crystallographic axis [YAM80].

In the 2010's, a comprehensive work has been published by Zhou *et al*. [ZHO14]. Using a LNO Y-cut substrate and $[TbCo_2(5nm)/FeCo(5nm)]_{20}$ magnetic multilayers (Aluminum IDTs with a wavelength of 16 µm in the delay line geometry), they showed that the direction of magnetic anisotropy and the direction of the applied magnetic field play a significant impact on the SAW response for the Rayleigh wave as well as for the surface shear horizontal wave. In-plane measurements proved the hysteretic signature of the magnetic multilayer without going further into the details. They did not investigate the OOP case.
The authors developed an interesting equivalent piezomagnetic model that permitted to simulate the experimental SAW responses. This model is inspired from previous work by Ganguly *et al.* [GAN76] and is used in the low frequency regime, which allows to write the evolution of elastic constants versus static field without frequency dependence. They explain the resonance frequency variations mainly by a change of the elastic constants combined to small dynamical magnetoelastic effects but didn't look in further details on the latter effect. The Figure 60 presents an example of agreement between their experiments and calculation for fields applied along the magnetic HA (⊥ Q). They correlate the saturation of the MSAW response with the magnetic saturation. Finally, it must be noticed that they obtained a maximum amplitude of frequency variation of approximatively 400, 2000 and 6000 ppm when the magnetic field is applied along the wave propagation direction for Rayleigh, first and third harmonics of surface shear horizontal wave. The third harmonic appears at three times the resonance frequency of the first harmonic. The penetration depth, proportional to the acoustic wavelength, is therefore smaller and the wave, more confined in the magnetic material, is more sensitive to magnetic/elastic changes.

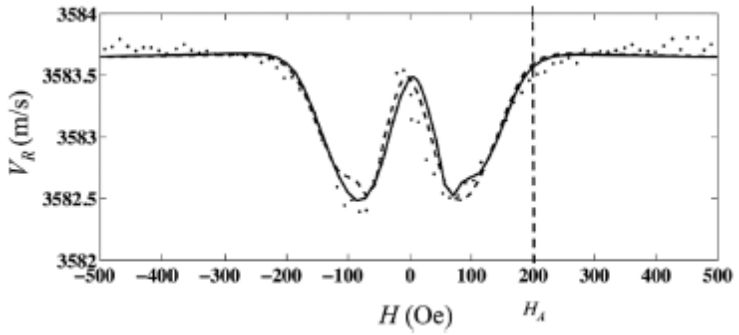

Figure 60. Comparison between theoretical calculation (solid line) and experimental results (dots) for the variations of the Rayleigh wave's velocity as a function of the amplitude of the magnetic field applied along the hard axis (⊥ Q) [ZHO14].

Elhosni *et al.* [ELH15] showed quite recently that changing the magnetic material enables to change the sensitivity of the SAW device. Indeed, by replacing the Nickel layer by a CoFeB softer layer on LNO 128 Y-cut, the SAW frequency exhibits a stronger variation with applied field, a consequence of the lower magnetization saturation field of the CoFeB layer, *i.e.* of the lower magneto acoustic saturation field. Their devices are patterned in the delay line geometry, the wavelength is 4.8 µm and the waves propagate along the LNO X-axis.

The resonator geometry has been used in only few studies, the most complete one being undertaken by Kadota *et al.* [KAD11a, KAD11b]. The IDT and reflectors are made of Ni (wavelength of 14.6 µm) and deposited on a quartz substrate. The easy magnetization direction is perpendicular to the plane but no magnetic characterization is presented.
The authors report on the field dependence of the surface shear horizontal wave frequency for different directions of the applied magnetic field but only for positive fields (Figure 61). A surprisingly small frequency shift is observed for a magnetic field applied out of the device plane. The MSAW response is not directly correlated to the magnetic response of the Ni IDT, but the interpretation mentions the combination of both the dynamic magnetoelastic coupling and the deltaE-effect. They claim that for Ni with negative magnetostriction and for a SH wave with a displacement along By, the dynamical magnetoelastic coupling is only efficient for fields applied along Bx and maximum when the angle between applied field and magnetization is 45°. This would give rise to the maximum variation measured along Bx. The variation measured for field along By would be only due to the deltaE-effect. However, as in the previous works by [YAM79, YAM80, WEB79], the authors don't provide a formal approach to this coupling and the proposed explanation of the coupling efficiency remains unclear.

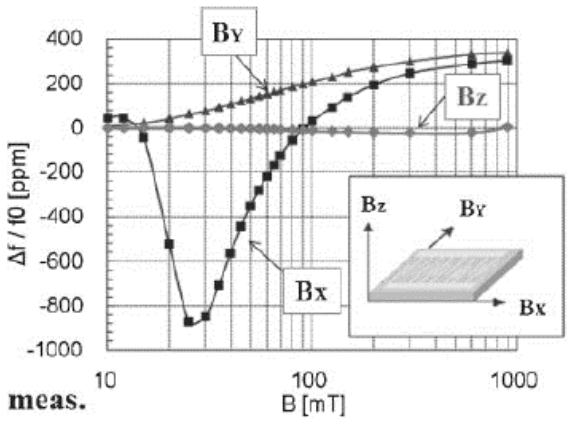

Figure 61. Variation of the SAW frequency (SHSAW) as a function of the applied magnetic field along three different directions. Results are measured on a ST-90°X quartz/Ni device in the resonator geometry [KAD11a, KAD11b].

Nan *et al.* [NAN13] finally investigated an unconventional device structure (the same as Figure 58 (c)): Pt electrodes are patterned on a Si substrate and the system is covered by 250 nm thick AlN piezoelectric layer on which a 250 nm thick magnetic $[FeGaB/Al_2O_3]_{10}$ multilayer is deposited. The Si substrate is removed at the end of the manufacturing process. The authors do not provide information on the magnetic properties of the multilayer but report on a SAW frequency response versus field similar to Kadota's results and invoke only a change in Young's modulus (deltaE-effect). The maximum amplitude of frequency variation along the wave propagation direction is huge, *i.e.* 10000 ppm. Since the wavelength of the device is 11 µm, the acoustic wave probes the whole stack. Therefore, the volume ratio of magnetic material over piezoelectric material probed is much more important than in the other cases expressed previously. The impact of magnetic/elastic changes on acoustic propagation is thus huge.

3.2.2. Elastically driven magnetization dynamics

The possibility to elastically drive the magnetization dynamics constitutes a new alternative for the excitation of magnetic resonance, in addition to an externally applied Radio Frequency (RF) magnetic field or to spin torque effects. These studies mostly focus on the SAW magneto acoustic response for external magnetic field of magnitude larger than the one required to saturate the magnetic material.

In the early 2000's, German researchers [WEI11, DRE12] have investigated LNOY-cut/polycrystalline Ni (50 nm) MSAW devices in a delay line geometry. The direction of wave propagation is along the LNO Z-axis. No magnetic characterization of the thick Nickel layer is presented but the experimental MSAW responses suggest a magnetic hard axis along this LNO Z-axis.
They have studied the SAW characteristics (Rayleigh wave) versus the intensity of an external magnetic field applied along different directions. They measured the S_{21} signal (transmission of the losses suffered by the propagating wave between the input and the output – attenuation variations). The Figure 62 reports their results for an in-plane magnetic field applied at 30° from the direction of wave propagation and for different harmonics.

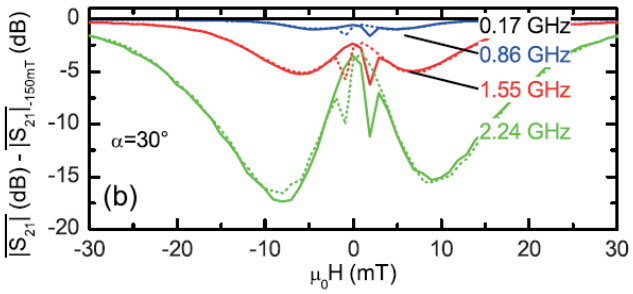

Figure 62. Attenuation variation as a function of the in-plane applied magnetic field at 30° from the direction of wave propagation and for different harmonics of Rayleigh wave (solid lines: upsweep, dashed lines: downsweep) [WEI11].

Their analysis and interpretation underlines:
(i) The occurrence of sharp variations and an hysteretic behavior in the low field region. These are related to the field-induced changes of the magnetic configuration. This is a non-resonant interaction between the SAW and the ferromagnet.
(ii) The occurrence of two symmetrical minima, observed after the magnetic saturation and shifted towards higher field when increasing the wave's frequency. These dips are attributed to the maximum coupling between the acoustic and spin waves, *i.e.* when the SAW frequency and the material ferromagnetic resonance match.
While the variations related to the magnetization reversal are observed for any in-plane directions of the applied field, the features associated to the dynamical coupling strongly depend on the field orientation.

As explained by the authors and confirmed by their calculation (free energy approach and LLG calculation), this angular dependence is specific to the elastically driven dynamics: The magnitude of the "acoustic" RF magnetic field (the component of the effective field perpendicular to M) strongly depends on the magnetization orientation, *i.e.* on the external static magnetic field orientation, in contrast to conventional ferromagnetic resonance. Let's underline that the in-plane dependence of this "acoustic" RF field also depends on the strain field generated by the SAW, thus on the type of SAW.

The authors solve then the equation of motion (coupled to LLG) to analyze the mechanical backaction of the magnetization dynamics on the SAW. They especially calculate the wave number of the perturbated SAW in the case of purely longitudinal strains. Beyond the effect due to the standard mass loading of the SAW, the analytical results allow a quantitative analysis of the phase shift and attenuation of the SAW upon FMR.
In these studies, the authors have also measured and simulated the case where an applied magnetic field is perpendicular to the sample plane [DRE12]. The dynamical magnetoelastic field is inefficient to drive the magnetization dynamics for a fully out of plane static field/magnetization. A slight tilt away from the perpendicular however enables the elastically induced dynamics.

Thevenard *et al.* [THE14] focused on a rather similar topic but for a significantly different system: a 50 nm thick $(Ga_{0.97},Mn_{0.03})(As_{0.94},P_{0.04})$ magnetostrictive layer is grown on a GaAs substrate and covered by a sputtered SiO_2(70nm)/ZnO(250nm) bilayer. The system possesses a perpendicular anisotropy but no magnetic characterizations are shown.
These authors measure two parameters versus the magnitude of the in-plane magnetic field applied along the direction of wave propagation (thus along a magnetic hard axis): the signal attenuation and the frequency resonance. The data reveal a maximum of attenuation and of relative change in velocity for close magnetic fields associated to a resonance process. The experimental resonance fields correspond indeed to a crossing between the magnetic precession frequency and the SAW (Rayleigh wave) frequency.
As performed in the above mentioned studies, the authors calculate the magnetization and acoustic dynamics in solving the LLG and motion equations. They could simulate the attenuation and velocity variations resonance fields, which interestingly confirm the experimental observation (Figure 63): their non-monotonous temperature variation and a slightly lower resonance field for the velocity variations than for the acoustic attenuation variations.

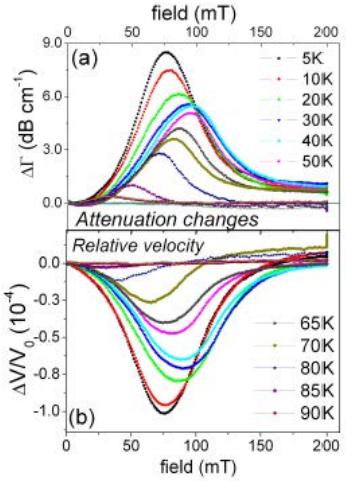

Figure 63. Variation of acoustic attenuation (a) and relative velocity change (b) of the RW between 5K and 90K. The magnetic field is applied in-plane along the direction of propagation wave (//HA) [THE14].

One can underline that the authors report here a resonant interaction between the SAW and the magnetization for an external static magnetic field applied along the wave propagation direction, whereas the efficiency of the dynamic magnetoelastic field calculated by Dreher [DRE12] is zero for this field orientation. This apparent inconsistency comes from the fact that the calculation by Dreher is

performed for a saturated magnetization (M//H) while the magnetization is not fully aligned with the field in the experiments by Thevenard *et al.*. Their formal approach also points out a vanishing resonance when the magnetization is collinear or normal to the SAW wave vector.

More recently, studies by Li [LI17], Sasaki [SAS17] and Gowtham [GOW15, GOW16] showed similar results on MSAW responses in different systems. Physical explanations and theoretical model are similar to those previously reported.

3.3. Our objectives in this topic

This PhD work is mainly focused on the effect of the applied magnetic field on the SAW characteristics. It has been previously shown that the SAW frequency in a MSAW device depends on the magnetic field applied to the system. However, in the large majority of cases, magnetic and structural characterizations of the devices are not provided. If the field dependence of the SAW frequency is indubitably related to the field dependence of the magnetic state in the magnetostrictive material, there is no precise correlation between the SAW response and the magnetic response of the device, which prevents building devices with optimized behavior. The objective of the third part is to address the following issues:

- What is the impact of the hysteretic response of the magnetic material on the SAW response? Is there a direct connection between these? In the case where the SAW response itself is hysteretic, how can it be suppressed to make a reliable magnetic sensor?
- Is it possible to exploit the out of plane magneto acoustic response to envision the development of out of plane magnetic sensors? Are there specific issues related to this geometry that is rarely considered both in experimental and theoretical works?
- Can we go further in the understanding of the role of magnetic anisotropy in the SAW response? How can it be used and controlled to tailor and optimize MSAW sensors?
- Can MSAW devices properties and performances be significantly modified/improved in turning to highly magnetostrictive crystalline materials? The magnetic materials used up to now are indeed amorphous, polycrystalline or textured, while a much larger magnetostrictive response is expected from single crystalline $TbFe_2$ for example. Despite the difficulties associated to the $TbFe_2$ growth on LNO substrates (as presented in the previous part), can these systems bring valuable input to the fundamental understanding and/or development of SAW based magnetic devices? What are the bottleneck towards the use of such materials?

We will address these points in the following chapters by considering various MSAW devices in a resonator geometry, *i.e.* the geometry that easily enables wireless measurements for future applications. These are based on different magnetic materials grown by sputtering or molecular beam epitaxy on different LNO cuts (see part 2). On the basis of their crystalline structure and magnetic properties and by the use of the equivalent piezomagnetic model developed by Zhou *et al.* [ZHO14], we will give a comprehensive picture of the MSAW behavior and propose new magnetic geometries/functionalities for sensor applications.

Chapter 2: Device nano-fabrication and basic characterizations

This chapter summarizes the nano-fabrication process and the design of the devices. Informations are also given on the intrinsic characteristics of the resonators, a first step towards the study of the device response as function of the applied magnetic field.

1. MSAW design parameters

The resonance frequency (F_r) of a SAW device is determined by two parameters: (i) the wavelength (λ) related to the geometry of the IDT and (ii) the considered wave velocity (v) related to the nature of the piezoelectric material and the IDT material:

$$F_r = \frac{v}{\lambda}$$

1.1. IDT

Figure 64 is a sketch of the designed IDT. P_I is the pitch, also called spatial period or wavelength (λ), that fixes the acoustic wavelength of the acoustic wave, W is the length between alternately fingers that gives the aperture width of the device and N is the number of finger pairs. One important parameter is the Metallization Ratio (MR) of the device. It represents the percentage of overlap by an IDT over a wavelength. For a metallization ratio of 50 %, the width of a finger is equal to the width separating it from the next finger, *i.e.* the width of one IDT finger is in this case equal to $P_I/4$.

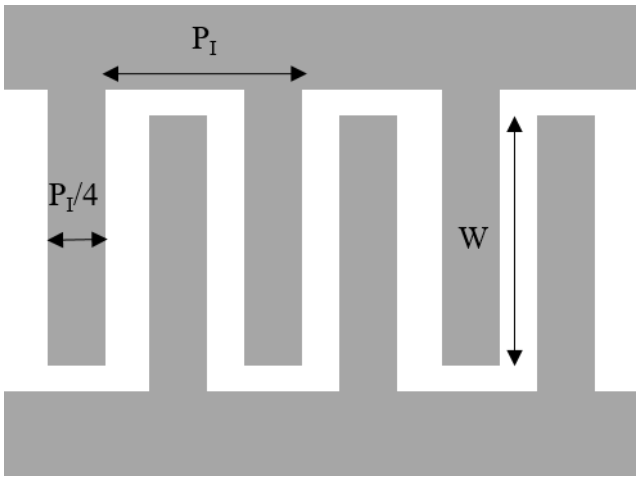

Figure 64. Sketch of the IDT structure with its characteristic lengths.

1.2. Resonator

A resonator is based on the use of an IDT inserted between two Bragg reflectors, as sketched in Figure 65. The distance between the end of the IDT and one Bragg reflector equals L_G. As far as the Bragg reflectors are concerned, the pitch of their fingers equals P_M and the number of fingers per Bragg reflector equals N_M.

Figure 65. Resonator structure with its characteristic lengths.

1.3. Design parameters

For all the devices fabricated in this PhD work, N has been fixed to 100 and N_M has been fixed to 200. P_M is set to λ/2 and L_G is set to λ/4. We have chosen to work with wavelengths equal to 6.5 µm and 13 µm which allows resonance frequencies of RW/QSHSAW/QSVSAW in the 300 MHz – 1 GHz range (Ultra High Frequency (UHF) band [IEE02]). The thickness of the IDT has been varied depending on the magnetic material and the desired magnetic response with values between 0.007 λ and 0.04 λ. Metallization ratios of 40%, 50% and 60% have been tested. The aperture width of the device is equal to 250 µm (respectively 500 µm) for wavelength of 6.5 µm (respectively 13 µm). These values arise from the adaptation of the electrical resistance of the device the closest as possible to 50 Ω, which is the electronic reference. It thus reduces electrical losses for wireless interrogation. The electrical resistance of the device is approximatively given by:

$$R_s \approx \frac{\Delta v}{v_0} . \frac{1}{2\pi v_0 (\frac{W}{\lambda})(\kappa_0 + \kappa)}$$

where R_s is the device electrical resistance, $\frac{W}{\lambda}$ is the relative aperture and κ_0 (respectively κ $(= \kappa_r \kappa_0)$) is the permittivity of free space (respectively dielectric constant of the piezoelectric). Δv is the difference between the free surface velocity (piezoelectric material (v_0)) and the metalized surface velocity (piezoelectric and IDT materials (v_m)) [MOR85].

Finally, devices have been designed to generate and propagate acoustic waves in two orthogonal directions. A single lithographic process provides devices with a wave propagation direction along LNO X-axis and others with a wave propagation direction along LNO X + 90°-axis. This enables testing whether the propagation direction has an influence on the MSAW response and check if the magnetism of the IDT is influenced by the lithographic process.

2. Nano-fabrication process

Several fabrication processes and lithography techniques can be used to fabricate SAW devices. Since several materials involved in this study are grown at high temperatures, lift off shaping of the IDT is not possible. The transfer of the IDT shape to the deposited film is therefore performed by Ar dry etching. As far as the lithographic process is concerned, electronic or optical lithography are mostly used. Optical lithography has been used to shape the devices. In our photolithography equipment, reliable structures can be obtained with lateral dimensions above 1 µm and the technique is faster than electronic lithography. The clean room process has been made in the Minalor center at Institut Jean Lamour.

2.1. Optical lithography

In a first step, the S1813 resist is spread on the surface by spincoating (10000 turns/mn during 1 mn). After spincoating, the resist is backed at 115 °C during 1 mn to evaporate the solvents. Profilometry measurements show that in these conditions, a resist thickness of 1 µm is obtained. This thickness is sufficient to protect the underlying magnetic layer during the total etching of the part that is not covered by the resist.
The positive S1813 resist is irradiated by UV light through the optical mask. The optical mask is composed of glass and UV absorbing material (Cr) that define the shape to be transferred to the resist. The irradiation causes a photochemical reaction: for a positive resist, the long carbon chains are cut into smaller carbon chains. As a result, the part of the resist irradiated by the UV light dissolves faster than the part of the resist that has not been irradiated. After development using the chemical "developer" (MF319), a rinse with deionized water and a nitrogen drying are immediately performed to block the chemical dissolution of the resist. The Figure 66 presents some pictures of a resonator device with various magnifications.

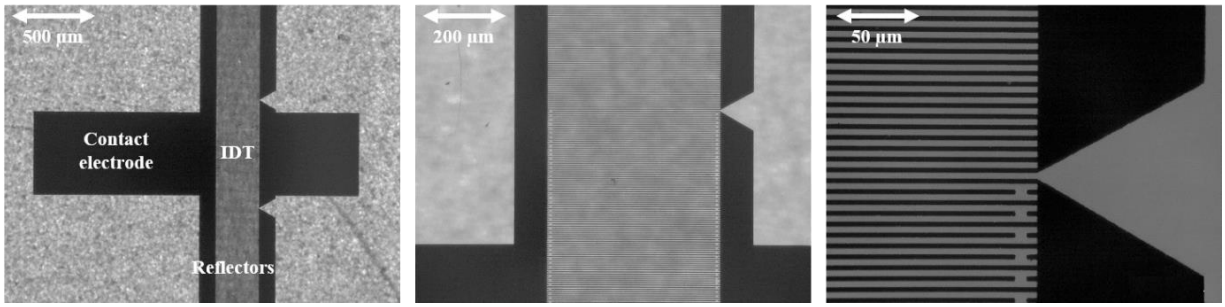

Figure 66. Optical microscope images (multiple zoom) of a SAW device. The device has a metallization ratio of 40% and a wavelength of 13 µm.

2.2. Ar physical dry etching

The shapes defined in the resist are then transferred to the magnetic layer using Ar physical dry etching. Ar^+ ions are accelerated towards the surface with energy of 200 eV and electrically neutralized before reaching the sample surface to avoid positive charges accumulation (especially important when insulating substrates are used as it is in our case). If the energy of the ions is sufficient, the surface of the sample is sputtered. In the region covered by the resist, the resist is sputtered; in the unprotected regions, the magnetic material is sputtered. The Ar pressure was chosen equal to 3×10^{-3} Torr and the beam current to 50 mA. In order to prevent deposition on the side of the resist and so to avoid the formation of collars, the Ar ion beam incidence angle is generally taken equal to 10 degrees with respect to the sample normal and the sample is rotated during etching. The etching depth is controlled in situ by SIMS. A mass spectrometer analyzes the chemical composition of sputtered elements during the etching. The etching can be stopped when the substrate is reached. Figure 67 gives an example for SIMS spectra measured during etching of a LNO41/Ta(5nm)/$[Co(5nm)/Ir_{0.2}Mn_{0.8}(5nm)]_{15}$/Pt(5nm) multilayer. The alternation of Co and IrMn is clearly seen.

At the end of the etching process, the sample is kept 4 hours in an acetone bath to promote the lift off of the resist (the resist is hardened during etching making it more difficult to remove). Finally, an ultrasonic bath with acetone for 5 minutes followed by an ultrasonic bath with isopropanol for 5 minutes are used to ensure a clean SAW surface.

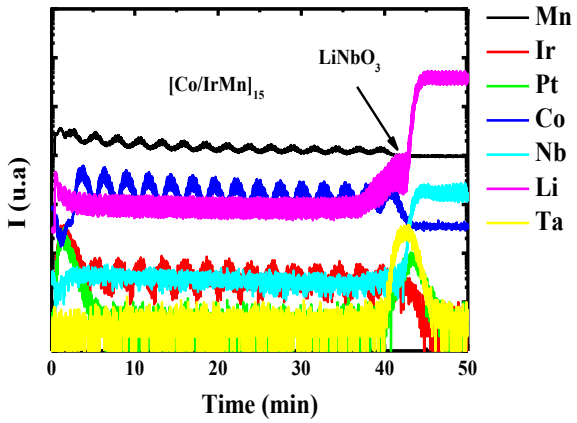

Figure 67. SIMS spectra measured during etching of a LNO41/Ta(5nm)/[Co(5nm)/$Ir_{0.2}Mn_{0.8}$(5nm)]$_{15}$/Pt(5nm).

3. Equivalent electrical circuit of resonator geometry

A SAW device can be modeled by an equivalent electrical circuit [IEE87]. The Butterworth Van-Dyke (BVD) equivalent circuit for a resonator geometry is shown in Figure 68. This model is basic and can be improved with additional resistance and capacitance but it is sufficient to describe the system. It mainly allows to describe the behavior of a resonator and to express all the important parameters during its characterization.

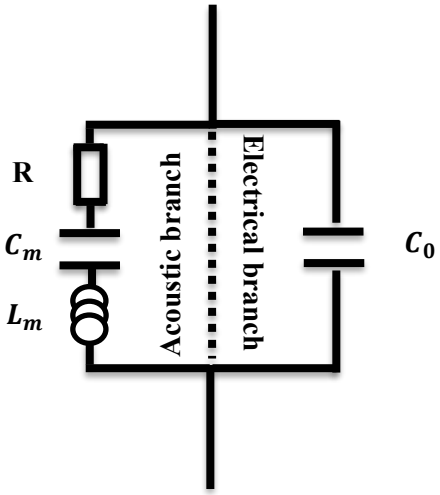

Figure 68. Butterworth Van-Dyke equivalent circuit for a SAW resonator.

The BVD model consists in a RLC branch in series with a capacitance C_0 in parallel, which models the piezoelectric conversion and the static capacitance (directly linked to the IDT) respectively. The inductance L_m and the capacitance C_m are motional components associated to the surface wave resonance, representing the exchange of mechanical energy between kinetic energy and elastic potential energy of particle motion respectively. C_m is usually weaker than C_0. The resistance R represents the losses through the whole device.

The admittance (Y) function of the BVD equivalent circuit is given by:

$$Y = i2\pi FC_0 + \frac{1}{R + i(2\pi FL_m - \frac{1}{2\pi FC_m})} = A + iB$$

The impedance (Z), which is the inverse of the admittance (Y^{-1}) can be obtained with:

$$Z = \frac{A - iB}{A^2 + B^2}$$

From these two expressions, it is possible to define all parameters of the experimental SAW measurements.
The interplay of the static capacitance and the RLC branch gives rise to two characteristic frequencies.

The first is the series frequency and corresponds to the maximum of the real part of the admittance:

$$F_s = \frac{1}{2\pi\sqrt{L_m C_m}}$$

The second is the parallel frequency and corresponds to the maximum of the real part of the impedance:

$$F_p = F_s\sqrt{1 + \frac{C_m}{C_0} - \frac{R^2}{2{L_m}^2(2\pi F_s)^2}}$$

A first important factor can be extracted from the BVD model, the so-called quality factor (Q_{ual}). This dimensionless factor is defined as the ratio of the energy carried by a wave to the dissipated energy. The stored energy in the motional branch is $(1/2\pi F_s C_m).I^2$ and the dissipated energy is $R.I^2$, where I^2 is the current in the branch. The quality factor can therefore be calculated at the series resonance as:

$$Q_{ual} = \frac{1}{2\pi F_s R C_m} = \frac{2\pi F_s L_m}{R}$$

and the parallel frequency can be rewritten as:

$$F_p = F_s\sqrt{1 + \frac{C_m}{C_0} - \frac{1}{2{Q_{ual}}^2}}$$

If Q_{ual} >> 1, the parallel frequency is approximate to:

$$F_p \approx F_s\sqrt{1 + \frac{C_m}{C_0}}$$

At maximum, when C_m is equal to C_0, $F_p = F_s\sqrt{2}$.

The relative difference in the frequencies F_s and F_p depends on both the material electromechanical coupling factor (described in the first part) and the resonator geometry [ERH17].
For this reason, a second critical factor is used for a resonator device whatever the direction of stress or strain induced by inverse piezoelectric effect: the effective electromechanical coupling factor ${K_{eff}}^2$. This dimensionless factor is the ratio of mechanical energy (U_m) stored in the volume of the resonator and capable of conversion to the total energy (electrical + mechanical) supplied to the entire system ($U_o + U_m$):

$${K_{eff}}^2 = \frac{U_m}{U_o + U_m} = \frac{\frac{1}{2}C_m V^2}{\frac{1}{2}C_0 V^2 + \frac{1}{2}C_m V^2} = \frac{C_m}{C_o + C_m} \approx \frac{C_m}{C_o}$$

where V is the AC electric voltage applied to the IDT.

Since F_p can be expressed as a function of F_s and knowing that C_0 >> C_m:

$${K_{eff}}^2 \approx \frac{C_m}{C_o} \approx \left(\frac{{F_p}^2 - {F_s}^2}{{F_s}^2}\right) + \frac{1}{2{Q_{ual}}^2} \approx (\frac{{F_p}^2 - {F_s}^2}{{F_s}^2})$$

If Q_{ual} increases, ${K_{eff}}^2$ decreases. Furthermore, the higher the effective electromechanical coupling factor, the higher the relative difference between parallel and series frequency.

Finally, some publications [VAR12] go further and knowing that $C_0 >> C_m$, they express the parallel frequency as:

$$F_p \approx F_s(1 + \frac{C_m}{2C_0})$$

In that case, the effective electromechanical coupling is thus:

$${K_{eff}}^2 = \frac{C_m}{C_o} \approx 2.(\frac{F_p - F_s}{F_s})$$

4. Basic characterizations

In a first step, basic characterizations of the SAW devices have been performed in order to identify the acoustic waves that can be generated and propagated. The frequency response of the resonators was measured using a Vector Network Analyzer (VNA) (Agilent PNA 5230A) and a RF probe station (PM5 Süss Micro-tech). The resonance frequencies have been measured using the entrance reflection coefficient when output is adapted (S_{11}). For all the measurements presented in this PhD work, the intensity of the VNA was fixed to 0 dBm. It was previously checked that the shape of the response does not evolve as a function of intensity (between -20 dBm and 10 dBm), *i.e.* that the device is working in its linear regime. Indeed, when the power is sufficiently high, SAW devices start operating in a non-linear mode. One sign of non-linear phenomena is the shift of the resonance frequency as a function of the amplitude of the acoustic excitations [LEG14].

4.1. Relevant parameters

4.1.1. Impedance Z

Figure 69 proposes a sketch of a Device Under Test (DUT) probed by a VNA and connected by a coax wire on one port.

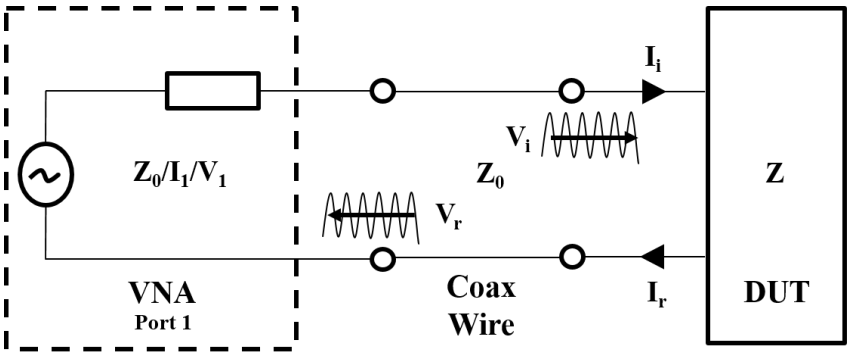

Figure 69. Equivalent system for a one port measurement with VNA.

The VNA sends an RF signal (characterized by the voltage V_i and current I_i) propagating through the coax wire towards the DUT. At the DUT entrance, a part of the power is transmitted to the DUT and absorbed by the latter, whereas another part is reflected and travel back to the VNA (characterized by the voltage V_r and current I_r). The voltage along the coax wire is the sum of the two waves (V_1) while the current (I_1) is the difference of the two waves, divided by its characteristic impedance Z_0 (50 Ohms), since the waves are travelling in opposite direction. This impedance can only be measured by a VNA

which is able to dissociate the incident and reflected waves and cannot be measured with a classical ohmmeter.

$$V_1 = V_i + V_r$$
$$I_1 = I_i - I_r = \frac{V_i - V_r}{Z_0}$$

Into the DUT, the impedance is:

$$Z = \frac{V_1}{I_1} = \frac{V_i + V_r}{\frac{V_i - V_r}{Z_0}} = Z_0 . \frac{V_i + V_r}{V_i - V_r}$$

where Z, the complex impedance can be written as: $Z = Re + iIm = R + iX$.

The real part of the impedance is the resistance (R) and the imaginary part is the reactance (X). Resistance and reactance are expressed in Ohms (Ω).

4.1.2. Reflection coefficient S_{11}

A measurement obtained with a VNA does not give direct access to the impedance, but to dimensionless parameters S expressed in decibels (dB). In this study, the measurement is performed in reflection and the parameter S_{11} is studied.
When an RF signal is applied to the DUT, the reflection coefficient S_{11} is given by:

$$S_{11} = \frac{V_r}{V_i}$$

the impedance can be rewritten as:

$$Z = Z_0 . \frac{1 + S_{11}}{1 - S_{11}}$$

and the reflection coefficient:

$$S_{11} = \frac{Z - Z_0}{Z + Z_0}$$

A typical variation of S_{11} versus frequency is given in Figure 70. A clear signature of a resonance frequency (F_r) is observed when the reactance (the imaginary part of Z) is zero and the impedance is thus purely resistive. The resonance peak increases in amplitude when the dissipation and thus the absorption of the system increases.
The measurement of S_{11} is helpful to identify the nature of the generated acoustic waves since the resonance frequency is connected to the wavelength and the velocity of the acoustic wave.

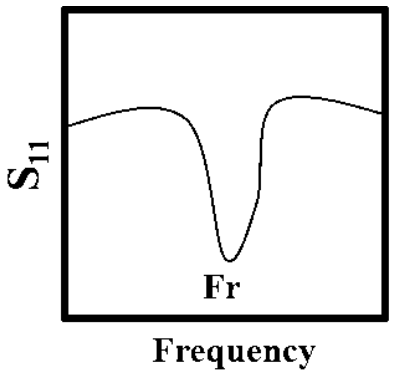

Figure 70. Schematic of a S_{11} signal. Fr corresponds to the resonance frequency.

4.1.3. Admittance

The admittance (Y) is also a complex number that can be written as: $Y = Re + iIm = G + iB$.
The real part of the admittance is the conductance (G) and the imaginary part is the susceptance (B). Conductance and susceptance are expressed in Siemens (S).
The admittance modulus is given by: $|Y| = \sqrt{G^2 + B^2}$.

We can get the admittance from the reflection coefficient through:

$$Y = \frac{1}{Z_0} \cdot \frac{1 - S_{11}}{1 + S_{11}}$$

and then:

$$S_{11} = \frac{Y_0 - Y}{Y_0 + Y}$$

with the characteristic admittance Y_0, which is the inverse of the characteristic impedance.
Figure 71 reports a schematic of the admittance modulus extracted from the S_{11} signal shown in Figure 70.

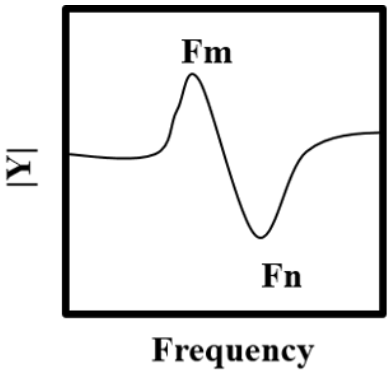

Figure 71. Admittance modulus extracted from the S_{11} signal shown in Figure 70.

The maximum of the admittance modulus is obtained at the frequency F_m, the minimum, F_n.

4.1.4. Quality factor

The quality factor is calculated from the real part of the admittance signal by:

$$Q_{ual} = \frac{F_s}{FWHM}$$

Figure 72 shows the real part of the admittance extracted from the S_{11} signal shown in Figure 70.

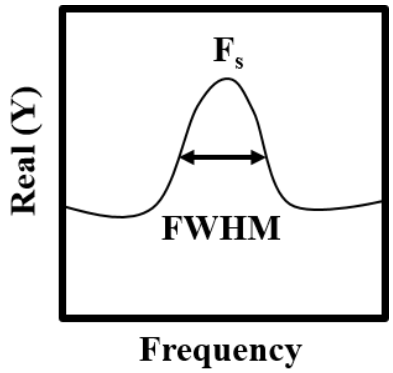

Figure 72. Real part of the admittance extracted from the S_{11} signal shown in Figure 70.

4.1.5. Effective electromechanical coupling factor

As it has be presented in paragraph 3, if $Q_{ual} >> 1$:

$$K_{eff}{}^2 \approx \frac{C_m}{C_o} \approx 2.(\frac{F_p - F_s}{F_s})$$

When $Q_{ual}.K_{eff}{}^2 > 50$, F_m and F_n become respectively F_s and F_p [IEE87, HAF69]. In this PhD work, this condition is true and we will thus use this approximation:

$$K_{eff}{}^2 \approx 2.(\frac{F_n - F_m}{F_m})$$

4.2. Gathered results

The Table 11 summarizes the results of the basic characterizations performed on the MSAW devices fabricated in this PhD work. Using S_{11} and the admittance, F_r, Q_{ual} and K_{eff}^2 were determined. From the value of F_r, we could deduce the nature of the propagating wave, either from the literature [CAM98] or from Comsol simulations. For $TbFe_2$ and [Co/IrMn]-based devices, the nature of the wave was essentially confirmed by the shape of the magneto acoustic response described further in this part.
The [100 MHz - 1 GHz] frequency range is investigated and thus, only the main resonances are present. Harmonics peaks are too poorly resolved to extract relevant data.
As already mentioned, different combinations of various magnetic materials and LNO substrates have been investigated. For each combination, devices have been patterned for two wavelengths and two orthogonal directions of wave propagation. Only the results for SAW propagating along the LNO X-axis are gathered in Table 11 since the observations are rather similar for the orthogonal direction. The devices presented in the table may exhibit different metallization ratios (40, 50 and 60 %) but the distinction is not made here because its effect on resonance frequency and critical factors is weak due to poor resolution on lithography steps and etching.

Some physical parameters are still missing in the Table 11 (replaced by question marks). In these cases, relevant values could not be extracted maybe because of second-order effects, including:

- Mass-loading by IDT, causing SAW velocity changes.
- Bulk acoustic wave emissions accompanying SAW emissions, causing passband distortion.
- Finite source and load impedances, causing frequency-dependent voltages across IDTs.
- IDT diffraction similar to optical systems, causing changes in transition band and shape.
- Poor quality of the IDT processing (different width from finger to finger, roughness, re-deposit) that can generate weak resolution and then bandpass distortion.

A RW could be measured for all combinations of magnetic material/LNO substrate. The existence of QSVSAW or QSHSAW depends on the substrate cuts: a QSVSAW is present for LNO Z and LNO 128Y, while a QSHSAW is observed for LNO 41Y. No explanations of this phenomenon could be found in literature.
Several points can be underlined from the Table 11:
(i) The first remark concerns the wavelength effect. As expected from $F_r=v/\lambda$, if the wavelength is two times higher, the resonance frequency is two times lower.
(ii) The second remark concerns the thickness effect (observed for Ni-based devices). As the thickness increases, the resonance frequency of accoustic waves decreases. This is expected and also confirmed by Comsol simulations, since the larger the thickness, the more the wave propagates in the IDT and is sensitive to its properties. Since the bulk longitudinal velocity in Nickel and LNO (depending of LNO cuts and wave propagation direction) are approximatively 5000 $m.s^{-1}$ [LID03] and 6500 $m.s^{-1}$ [CAM98] respectively, the decrease in acoustic velocity, *i.e.* resonance frequency, is expected for RW and QSHSAW/QSVSAW, which exhibit longitudinal components (observed on numerical results for QSHSAW/QSVSAW).
(iii) The third remark concerns the resonance frequencies obtained with $TbFe_2$-based devices. For both waves, the resonance frequencies values are close to those obtained with Ni-based devices. However,

elastic constants are significantly lower in $TbFe_2$ than in Ni (Nickel: $C_{11} = 224\ GPa$, $C_{44} = 120\ GPa$, $\rho = 8.9\ g.cm^{-3}$ [LUO11] and $TbFe_2$: $C_{11} = 143\ GPa$, $C_{44} = 48\ GPa$, $\rho = 9.1\ g.cm^{-3}$ [CLA80] at RT), which usually leads to a decrease in resonance frequency ($v = \sqrt{C/\rho}$). A possible explanation is to consider both buffer layer and $TbFe_2$ properties in effective elastic properties. In fact, Mo elastic constants are: $C_{11} = 441\ GPa$, $C_{44} = 122\ GPa$ and $\rho = 10.1\ g.cm^{-3}$ at RT [FEA63].
(iv) A last remark concerns the effective electromechanical coupling and the quality factors. The K_{eff}^2 factor is larger for a QSHSAW or a QSVSAW than for a RW. This is the opposite for Q_{ual}. Comsol simulations and theoretical predictions [CAM98] are consistent with this effect. We can nevertheless mention that these values could not be compared with literature because they are directly linked to the geometry and are thus specific to our experiments

Substrate / Material	Wavelength (µm)	Acoustic wave	F_r (MHz)	Q_{ual}	${K_{eff}}^2$ (%)
LNO Z-cut / Ni (50nm)	6.5	RW QSVSAW	578 667	840 ???	0.32 ???
	13	RW QSVSAW	289 331	??? ???	??? ???
LNO 128Y-cut / Ni (50nm)	6.5	RW QSVSAW	598 618	1111 820	0.14 0.28
	13	RW QSVSAW	300 306	850 830	0.23 0.33
LNO 41 Y-cut / Ni (50nm)	6.5	RW QSHSAW	556 717	1100 714	0.23 0.46
	13	RW QSHSAW	279 350	550 ???	0.75 ???
LNO Z-cut / Ni (200nm)	6.5	RW QSVSAW	569 645	740 63	0.42 6.7
	13	RW QSVSAW	289 331	480 46	0.78 7.8
LNO 128Y-cut / Ni (200nm)	6.5	QSVSAW	608	1117	0.21
	13	RW QSVSAW	301 309	1101 588	0.2 0.68
LNO 41 Y-cut / Ni (200nm)	6.5	RW QSHSAW	552 710	1215 800	0.19 0.37
	13	RW QSHSAW	278 348	870 87	0.29 5.1
LNO Z-cut / Ti (20nm) / Mo (20nm) / $TbFe_2$ (50nm)	6.5	RW QSVSAW	574 648	500 52	0.7 6.9
	13	RW QSVSAW	288 335	515 71	0.66 5.9
LNO 128Y-cut / Mo (15nm) / $TbFe_2$ (50nm)	6.5	RW QSVSAW	583 612	879 720	0.29 0.45
	13	RW	305	1211	0.19
LNO 41 Y-cut / Mo (20nm) / $TbFe_2$ (50nm)	6.5	RW QSHSAW	552 718	392 276	0.88 1.14
	13	RW QSHSAW	277 360	720 301	0.46 1.06
LNO 41 Y-cut / $[Co(5nm)/Ir_{0.2}Mn_{0.8}(5nm)]_{15}$	6.5	RW QSHSAW	536 663	1101 782	0.23 0.39
	13	RW QSHSAW	265 334	800 740	0.37 0.42

Table 11. Characteristics of the various MSAW devices (wavelength, type of wave, F_r, Q and K_{eff}^2). RW : Rayleigh Wave, QSHSAW : Quasi Shear Horizontal Surface Acoustic Wave and QSVSAW : Quasi Shear Vertical Surface Acoustic Wave. Those results are obtained for waves propagating along the LNO X-axis.

5. Temperature coefficient of frequency (TCF)

The temperature coefficient of frequency is a parameter that determines the thermal stability of the resonator device. It indicates how much the resonance frequency drifts with a change in temperature. The origin of TCF is mainly related to the expansion coefficient of the entire resonator and to the dielectric constant variation with temperature of the pyroelectric material.
In order to get this coefficient, the resonance frequency variation is plotted as a function of temperature. The TCF (expressed as parts per million per degree Celsius (ppm.°C^{-1})) is calculated as:

$$TCF = \frac{1}{F_r} \cdot \frac{\Delta F_r}{\Delta T} \cdot 10^6$$

In electronic devices, the best results are obtained for a TCF as close to zero as possible since it is important that the frequency of the device does not drift (exept for temperature sensors). In this PhD work, optimize TCF is not the aim. This coefficient is however calculated to estimate the experimental error.
It has been measured under probe station, which is equipped of a thermal chuck, through the Rayleigh wave resonance peak close to 600 MHz for a 50 nm thick Nickel-based device deposited on LNO 128 Y-cut with a direction of wave propagation along LNO X-axis. The wavelength is 6.5 µm and the metallization ratio is 60%. Experimental results are given in Figure 73.

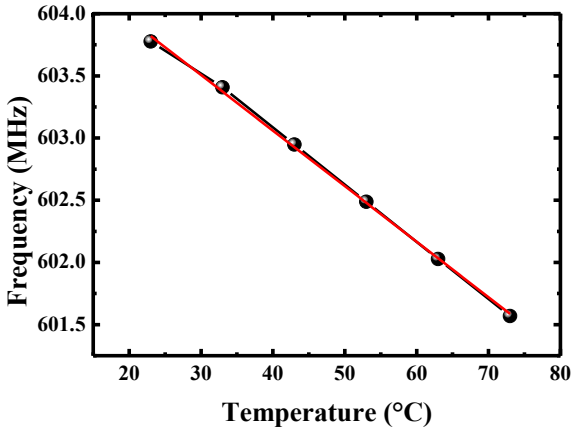

Figure 73. Frequency resonance variation as a function of temperature for a 50 nm thick Nickel-based device deposited on LNO 128 Y-cut with a direction of wave propagation along LNO X-axis. Wavelength equals 6.5 µm and metallization ratio is 60 %. The red line corresponds to a linear fit.

The TCF value extracted from this curve is approximatively -80 ppm.°C^{-1} in the [23 °C – 75 °C] tempterature range. This value is close to the value given in literature [MAY11] for LNO 128Y-cut with a direction of wave propagation along LNO X-axis.
TCF values can be mainly affected by the direction of wave propagation and the piezoelectric cut, but they can also depend on the wavelength, the temperature range, the metallization ratio, the IDT material and the nature of the wave. The values measured in our other MSAW devices (not reported here) are however of the same order of magnitude.
The change in temperature during the measurements presented in the following (essentially produced by the electromagnet) is measured close to the IDT surface with temperature sensor and is of approximatively 0.05 °C. The measurement error related to TCF can thus be estimated to only ± 2 ppm.

6. Measurements under applied magnetic field

6.1. Measurement configuration under applied field

In order to measure the magneto acoustic response of the MSAW device, *i.e.* the resonance frequency variation as a function of the applied magnetic field, samples are bonded to a copper-coated Printed

Circuit Board (PCB), suitable for micro-electronics applications. The connections are established between the PCB and the SAW device using a bounded 20 µm diameter Gold wire. Finally, a SubMiniature version A (SMA) connector is used to connect the PCB at the VNA through a coax wire. The resonance frequency as a function of the applied magnetic field is tracked via the measurement of S_{11} versus frequency for different magnetic fields (Figure 74).

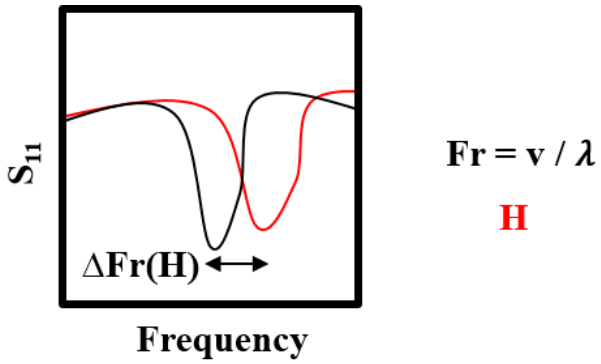

Figure 74. Resonance frequency variations under the application of an external magnetic field (in red), as observed in the output signal S_{11}.

The normalized frequency shift is then calculated and plotted as a function of applied field:

$$\Delta F_r/F_r = \frac{F_r(H) - F_r(0)}{F_r(0)}$$

By convention, $F_r(0)$ denotes the frequency resonance without magnetic field.
All measurements presented in the following have been performed in starting from a positive saturation field.

6.2. Color code for the measurement configuration under applied field

A common color code convention has been chosen for all the presented measurements, in order to help the reader follow the measurement geometry (Figure 75). The black color is used for a magnetic field applied in-plane and parallel to the direction Q of wave propagation (*i.e.* perpendicular to the IDT fingers). The red color is used for a magnetic field applied in-plane and perpendicular to the direction Q of wave propagation (*i.e.* along the IDT fingers). Finally, the green color is used for a magnetic field applied perpendicular to the plane of the layer. These colors are used, whatever the crystallographic directions and the anisotropy of the magnetic layer.

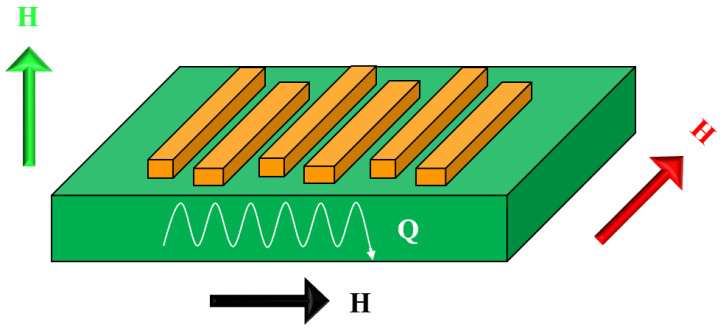

Figure 75. Color code used to present the experimental results corresponding to the three measurement configurations: with the applied magnetic field in the device plane along (black) or perpendicular (red) to the wave propagation, or perpendicular to the device plane (green).

Chapter 3: 50 nm Nickel-based devices

The starting point of this PhD work is the study of MSAW devices composed of Ni. Several results using Ni as IDT have been previously reported in literature, including in resonator geometries with a wireless response [KAD11a, KAD11b]. The current experiments can thus be interestingly compared to these, and Ni-based devices by the way constitute a relatively simple case to present and explain the main characteristics of these systems.
More precisely, we report here first and extensively on the MSAW response obtained for 50 nm thick Ni IDT patterned on a Lithium Niobate 41 Y-cut substrate and for a wave propagation direction along the LNO X-axis (the device wavelength is 6.5 µm). A piezomagnetic equivalent model and associated simulations are compared with the experimental results and used to understand the role of magnetic anisotropy. Some results obtained for Ni deposited on another LNO cut, with another wavelength and for another direction of wave propagation with respect to the LNO substrate, are also summarized at the end of the chapter.

1. Experimental results on device on LNO 41Y-cut

All the measurements presented in this section have been performed on resonator devices based on the following initial stack: LNO41Y/Ta(5nm)/Ni(50nm)/Pt(5nm). The device patterning yields a wavelength of 6.5 µm, a metallization ratio of 60% or 50%, and a wave propagation direction along the LNO X-axis.
As explained in the previous chapter, the measurements are performed in measuring the S_{11} signal versus frequency for different applied magnetic fields. Typical examples are given in Figure 76 where the panel (a) presents the signal over an extended frequency range for zero applied field (metallization ratio of 60 %) and the panel (b) presents the curves obtained close to 558 MHz for three different values of the external field applied along the wave propagation direction (metallization ratio of 50 %). Considering the wavelength, the panel (a) reveals the presence of a RW at a frequency close to 556 MHz and of a QSHSAW close to 717 MHz.

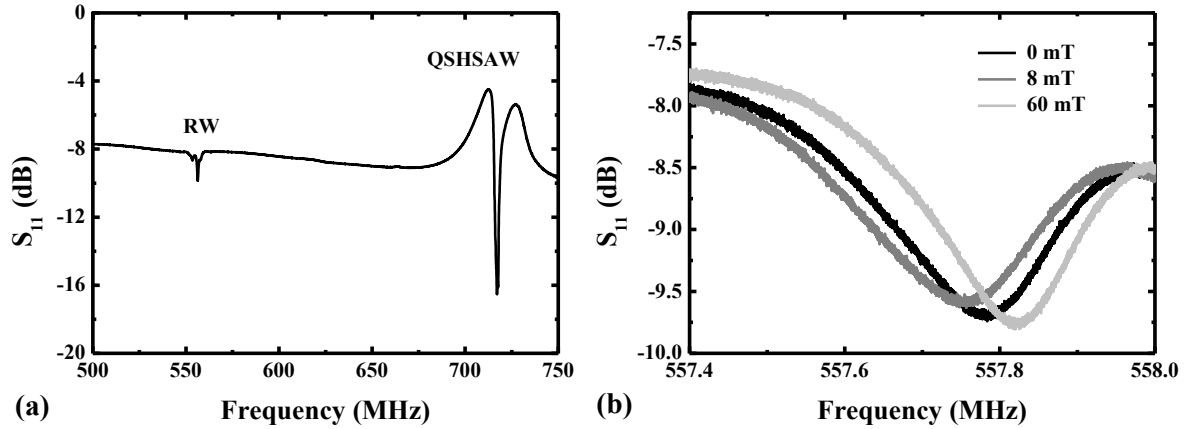

Figure 76. S_{11} signal versus frequency for a 50 nm thick Ni-based resonator device (on LNO 41Y) under zero applied field. The device has a metallization ratio of 60% (a). S_{11} signal versus frequency (around the RW resonance) for a 50 nm thick Ni-based resonator device (on LNO 41Y) for three different fields applied along the direction of wave propagation. The device has a metallization ratio of 50% (b). In both cases, the direction of wave propagation is along LNO X-axis and the wavelength equals 6.5 µm.

The panel (b) first shows that the device is indeed sensitive to the application of an external magnetic field.

(i) The frequency corresponding to the S_{11} minimum varies with the field intensity. This non monotonous dependence is extensively analyzed and discussed in the following.

(ii) The amplitude and the shape of the signal varies with the field, which has to be related to a variation of dissipation/absorption.

The amplitude follows the resonance frequency variations. A decrease in amplitude is observed when the resonance frequency decreases and vice versa (the base line far from the Rayleigh resonance peak is identical for these different applied fields).

1.1. Field dependence of the SAW frequency

Figure 77 presents a set of measurements performed with the field applied along three different directions (IP//X, IP//X+90° and OOP) on the initial plain stack (LNO41Y/Ta(5nm)/Ni(50nm)/Pt(5nm) before any patterning) and on the corresponding patterned device (with 60% metallization ratio). Figure 77 (a) and (b) show the field-dependent magnetization of the plain stack, while (c) and (d) (respectively (e) and (f)) correspond to the field-dependent frequency of the RW (respectively QSHSAW).

The Figure 77 (a and b) reveal the Ni in-plane easy magnetization axis along the LNO X direction in the plain stack, as it has already been reported and discussed in part two.
The Figure 77 (c and e) reveal that both the RW and the QSHSAW identified in the patterned device exhibit a clear dependence on the applied magnetic field's amplitude and direction, most likely in close connection with the IDT magnetic response to the external field. As mentioned previously, we mainly focus here on the field dependence of the resonance frequency. Beyond this field sensitivity, several observations can be interestingly made:
(i) For both acoustic waves, the frequency exhibits an hysteretic field-dependence for fields applied along the LNO X+90° direction (red) and a reversible field-dependence for fields applied along the LNO X direction (black). Along LNO X+90°, the shapes are qualitatively similar with a monotonous decrease of frequency when the field is reduced from saturation, an abrupt upwards jump for a negative field of approximately -5 mT and finally a slow monotonous increase when the negative field increases back in amplitude. A symmetric behavior is observed when the field is swept from negative to positive values. Along LNO X, the frequency variation is reversible for both RW and QSHSAW waves but the curves exhibit significantly different shapes, especially in the low field region (d and f). Those responses versus field are rather similar to those previously reported on magnetic SAW delay lines [ZHO14].
One can however notice that the irreversible and reversible characters of these variations with field are exchanged for the magnetization in the plain stack (irreversible along X and reversible along X+90°) and for the SAW frequency in the device (reversible along X and irreversible along X+90°). The present results are also different from those reported in devices with a delay line geometry where the easy magnetization axis lies along the LNO X-axis [ZHO14] (irreversible frequency variation along X and reversible along X+90°). These observations suggest a change in the easy magnetization axis in the patterned device compared to the plain stack, as it is discussed in further details in the following chapter.
(ii) In the high field region, the frequency of the RW measured for a magnetic field parallel to X seems to saturate while it continues to increase with the magnetic field when this latter is parallel to X+90°. For the QSHSAW, no saturation of the frequency is observed whatever the direction of applied field. Since these effects are anisotropic, they cannot be only related to the forced magnetostriction.
(iii) More quantitatively, the frequency relative variation observed for the QSHSAW is much larger than that observed for the RW, by a factor of almost 7. As reported in the literature and observed in our devices, QSHSAW has a higher electromechanical coupling factor and is related to the elastic coefficient (C_{66}) whose variation with field is larger than for C_{11} (the RW is related to the elastic coefficient C_{11} because the displacement is essentially longitudinal) [ZHO14]. A larger variation of resonance frequency is therefore expected and observed in the case of the QSHSAW.
(iv) When the magnetic field is applied perpendicular to the device plane, the measured frequencies are also clearly sensitive to the field value. The magneto acoustic responses for both waves are qualitatively similar and exhibit an hysteretic behavior with a coercive field close to 80 mT, *i.e.* much larger than the

one observed for in-plane applied fields. One can notice that this hysteresis occurs while the magnetization reversal of the plain stack is perfectly reversible for this field orientation.
This geometry is rarely reported in previous studies. We recall that Kadota studies [KAD11a, KAD11b] report a small magneto acoustic response, but without hysteresis (only positive fields are measured).
The observations reported above are discussed and analyzed in further details in the following paragraphs and chapter.

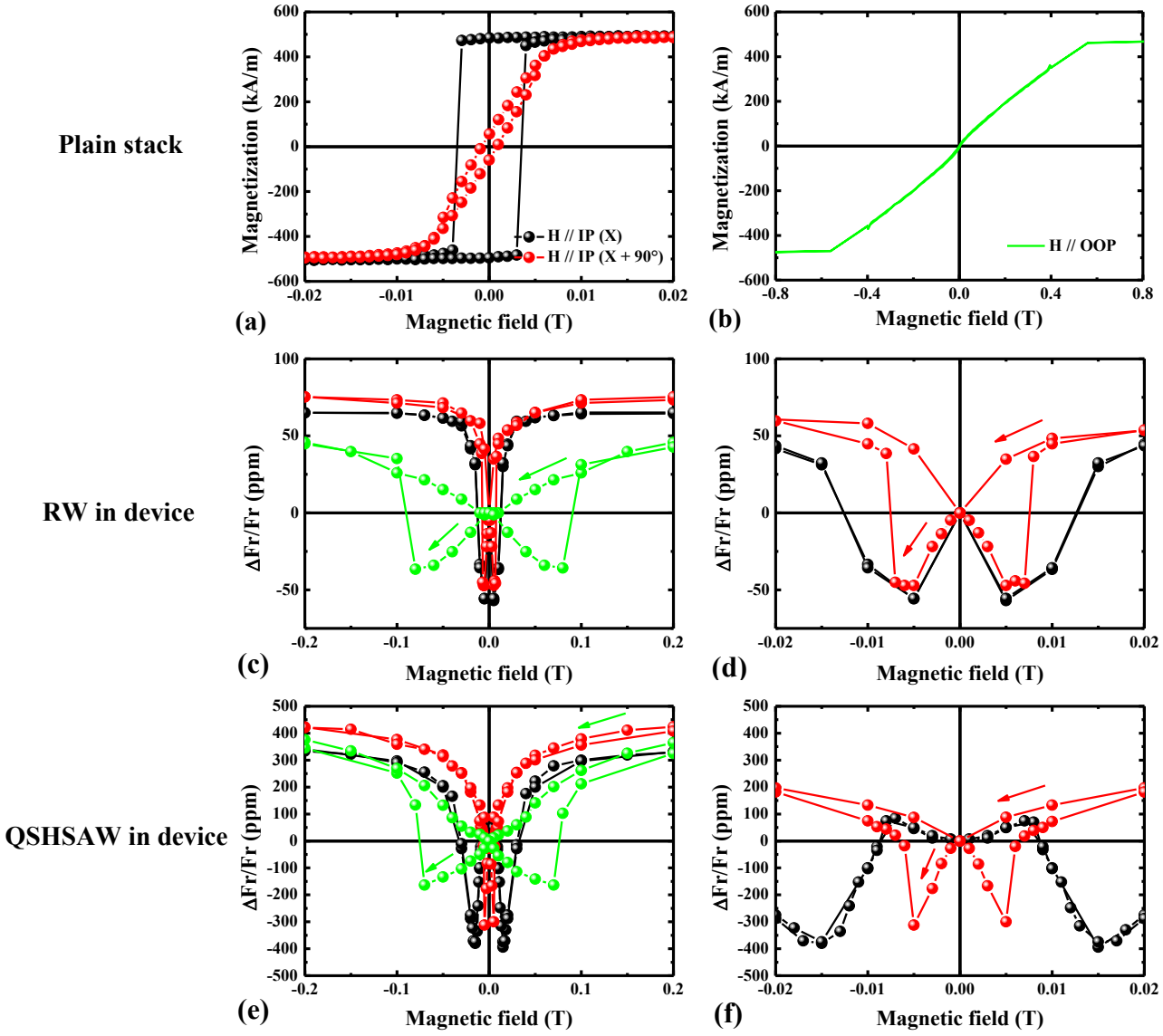

Figure 77. Magnetization measured for the LNO41Y/Ta(5nm)/Ni(50nm)/Pt(5nm) plain stack for a magnetic field applied along LNO X (black), LNO X+90° (red) and OOP (green) directions (a and b). Normalized resonance frequencies measured in the corresponding SAW device with the external field applied along the same directions (same color code) for the RW (c and d (zoom)) and the QSHSAW (e and f (zoom))). On (c-d-e-f), green and red arrows represent the magneto acoustic responses sense obtained from positive to negative saturation field.

1.2. Reversibility range for the SAW frequency

As shown previously, the response of the MSAW device is hysteretic for both waves when the field is applied along the LNO X+90° direction. Although this aspect is not presented and discussed in most of the previous studies [KAD11a, WEB79, …], it could be a strong limitation for the development of

magnetic field sensors since a measured resonance frequency cannot be unambiguously attributed to a single value of magnetic field.
The magnetic field range where this type of device can nevertheless exhibit a reversible behavior has been studied. The Figure 78 presents the RW (a) and QSHSAW (b) frequencies field dependence for fields applied along the LNO X+90° direction, when the magnetic field is swept from +50 mT to -50 mT (in red) and when it is swept back and forth before reaching the coercive value where the abrupt increase in frequency occurs (minor loops, in other colors). For both waves, the results show that the magneto acoustic response is indeed perfectly reversible from high field to approximately -5 mT, when the negative magnetic field doesn't exceed the coercivity, which is likely related to a reversible magnetic behavior of the Ni IDT in this field range. As a result, a bipolar response, *i.e.* a sensor that can measure not only the intensity of the field but also the fact that the field is positive or negative, can be obtained for applied fields swept in a suitable range provided that the coercivity is not reached.

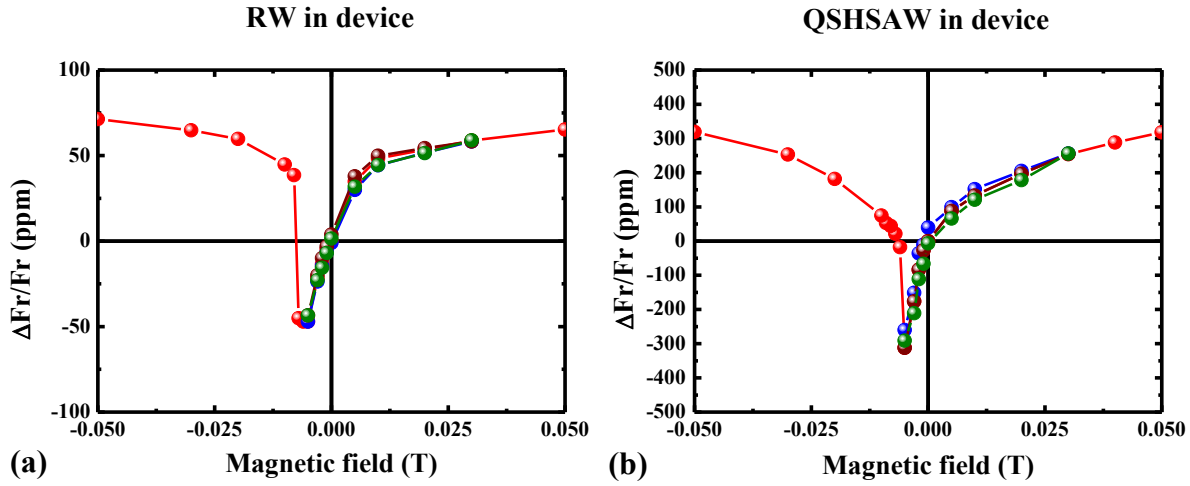

Figure 78. Normalized RW (a) and QSHSAW (b) frequencies variation versus magnetic field applied along LNO X+90° for the LNO41Y/Ta(5nm)/Ni(50nm)/Pt(5nm) SAW device patterned with a wave propagation direction along LNO X. The red curve corresponds to a full field sweep from positive to negative fields, other colors correspond to the measurements of minor loops.

1.3. Angular variation for the RW frequency

Since the MSAW response is highly dependent on the direction of the applied field with respect to the substrate crystalline direction/IDTs orientation, the RW frequency field variation has been measured for several in-plane field directions lying between the main LNO X and LNO X+90° directions. The Figure 79 gathers the results (magnetization for the plain stack in (a) and RW frequency for the patterned device in (b) and (c)) for magnetic fields applied along LNO X, X+30°, X+60° and X+90° directions. Measurements of the device have been also performed for fields along X-30° and X-60° (not reported here), which lead to similar results to X+30° and X+60°.

For the plain stack magnetization, the measurements are consistent with an evolution from a magnetic hard axis (along X+90° in red) to a magnetic easy axis (along X in black): the hysteresis loop opens and become more and more square with an increase of both the remanence and the coercive field.
Concerning the RW frequency in the patterned device, one can make several observations:

(i) As mentioned previously, the shape and more specifically the non hysteretic/hysteretic character of the curves measured along X and X+90° are reversed compared to the plain stack magnetization.
(ii) As observed in Figure 79 (c), the abrupt change and associated hysteresis are always present at approximatively the same field value except for an applied magnetic field along the HA. This is consistent with coercive field values obtained on hysteresis loops in Figure 79 (a).
(iii) The evolution observed from the black to the red curve is not monotonous since the two dips (occurring between 5 mT and 15 mT) first decrease in amplitude and shift to higher fields, even

larger than magnetization saturation field, before reaching the case H//X+90° where the sharp reversal is approximately at the same amplitude and position as dips for H//X.

(iv) The variations measured for high fields, *i.e.* above 15 mT, exhibit a significantly larger slope for the fields applied at 30° or 60° from X, than for fields applied along X and at 90° from X.

These various remarks confirm that the variation in magnetization alone cannot fully explain the observed field dependence of the RW frequency. The variations of elastic constants as well as dynamical effects should be likely taken into account.
The experiments and calculation in [DRE12] namely conclude to possible dynamical effects above the saturation when the field is applied between EA and HA, as attested by a strong amplitude variation versus field. It is thus consistent with our experimental results. Finally, the last two observations (points (iii) and (iv)) are by the way in agreement with numerical simulations reported by Zhou *et al.* [ZHO14].

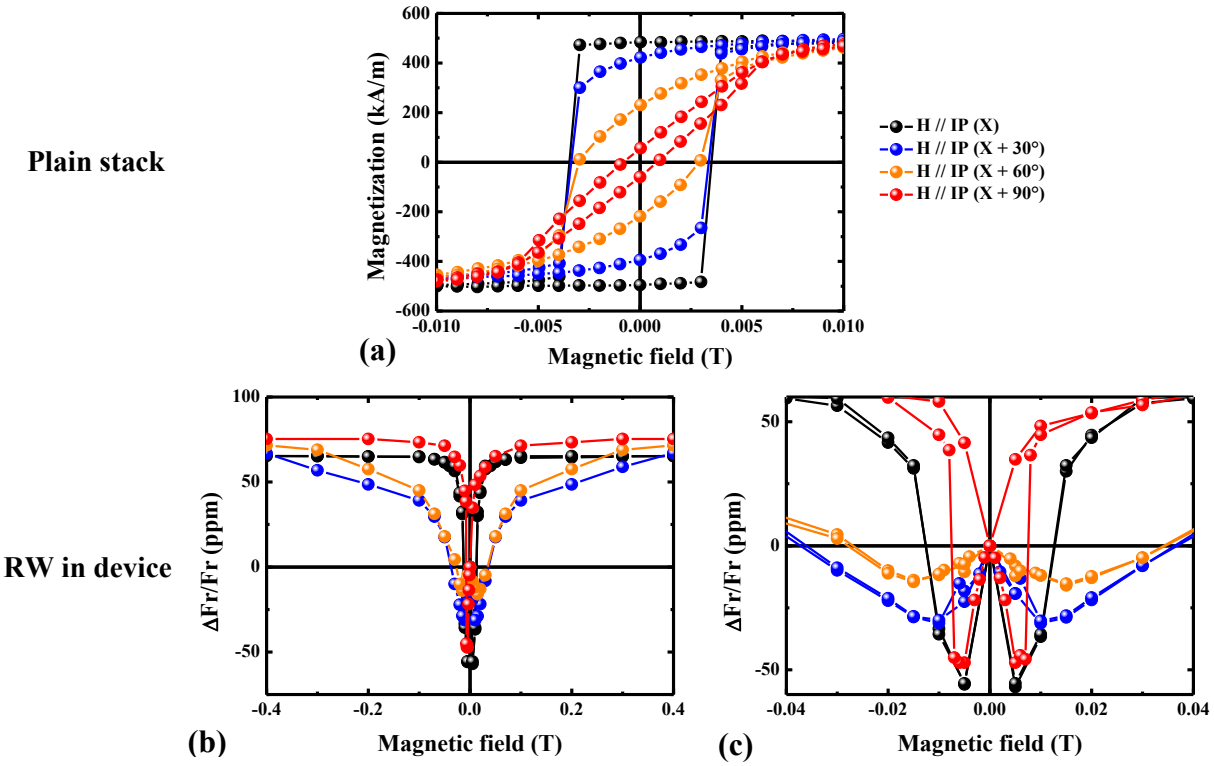

Figure 79. Magnetization measured for the LNO41Y/Ta(5nm)/Ni(50nm)/Pt(5nm) plain stack for a magnetic field applied along four in-plane directions (a). Normalized RW frequency measured in the corresponding SAW device (Q//X and MR=60%) with the external field applied along the same in-plane directions (b). Zoom of normalized RW frequency with back and forth swept field with the external field applied along the same in-plane directions (c).

1.4. Variation of the quality and effective electromechanical coupling factors

Let's first recall the aim of getting high quality and high effective electromechanical coupling factors in SAW devices:
(i) The interest of high-Q_{ual} consists in obtaining wireless devices where the signal can be detected for up to several tens of microseconds after switching off the exciting RF signal. High-Q_{ual} devices are characterized by a Q_{ual} factor of several thousands [POH00].
(ii) High-K_{eff}^2 devices are required for broader bandwidth (difference between admittance maximum and minimum) and high sensitivity in imaging or filter applications [CAM98].

In literature, previous experiments report on the huge variation of the quality factor versus field, which follows the same shape as the normalized frequency resonance variations [KAD11a, NAN13] but

without providing a clear explanation. This paragraph reports the field variation of these factors in our device.
Experimentally, these critical factors are determined from the admittance curve and its real part thanks to the formula given in the previous chapter:

$$Q_{ual} = \frac{F_s}{FWHM}$$
$$K_{eff}{}^2 \approx 2.\left(\frac{F_n - F_m}{F_m}\right)$$

Figure 80 reports, for the three directions of the applied field (IP // X (black), IP // X+90° (red) and OOP (green)), the normalized resonance frequency variations (a), the variations of the quality factor (b) and of the effective electromechanical coupling factor (b) for the RW measured in a device with 60% metallization ratio. For the sake of clarity, only the field sweep from maximum positive field to maximum negative field is reported. Similar observations (not reported here) have been made for the QSHSAW.

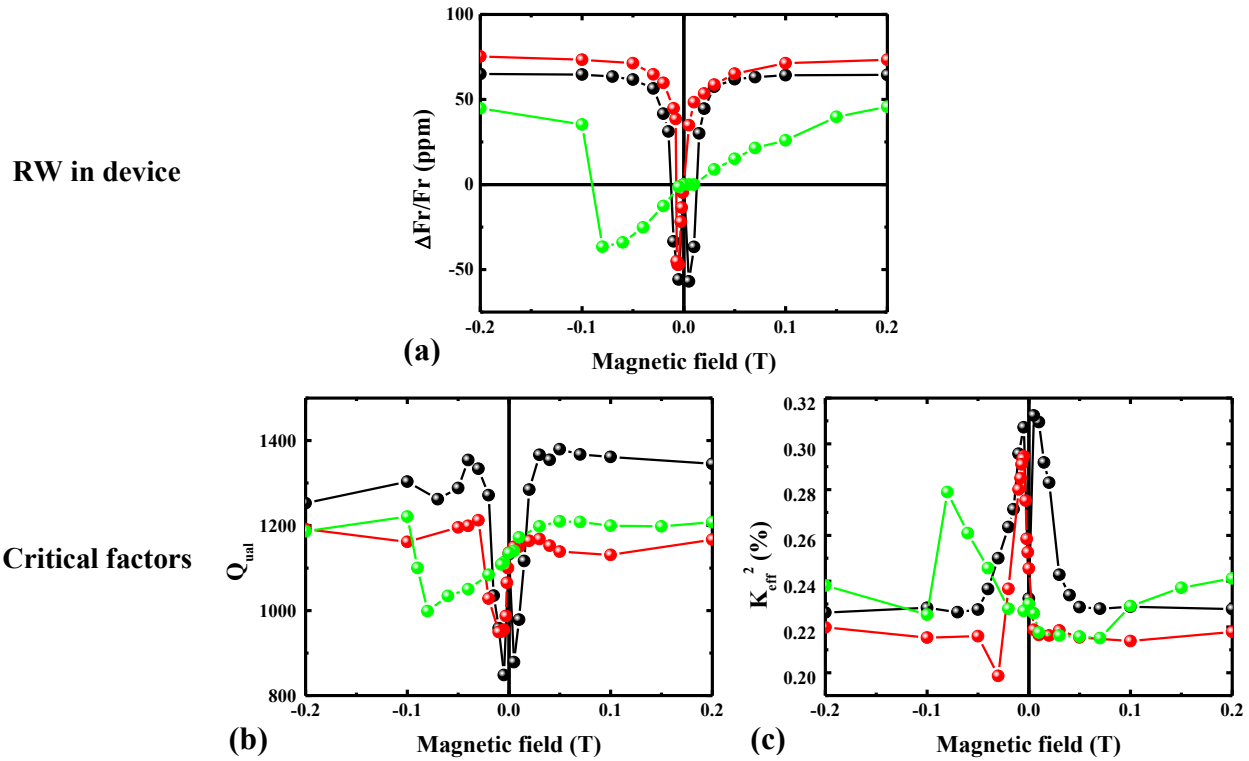

Figure 80. Normalized resonance frequency variations (a) and variations versus the applied magnetic field of the quality factor Q_{ual} (b) and the effective electromechanical coupling factor K_{eff}^2 (c) for the SAW device patterned from the LNO41Y/Ta(5nm)/Ni(50nm)/Pt(5nm) stack (metallization ratio of 60%) and with a direction of wave propagation along X. Three directions of the applied magnetic field are presented: IP// X (black), IP// X+90° (red) and OOP (green).

It appears clearly that the quality factor Q_{ual} (Figure 80 (b)) follows the same trend as the variation of frequency resonance during the field sweep (Figure 80 (a)), while the effective electromechanical coupling factor K_{eff}^2 (Figure 80 (c)) exhibits opposite variations. Quality factor values are reasonable to undertake wireless measurements.

To go further, values of R, L_m, C_m and C_o (the latter is constant with field) have been extracted for a field applied along X by fitting the admittance curve and its real part for three magnetic field values (0 T, 0.005 T (minimum (maximum) of resonance frequency and Q_{ual} (K_{eff}^2) variations during field sweep) and 0.04 T (saturated point of resonance frequency, Q_{ual} and K_{eff}^2 during field sweep) (following the

procedure in [VAR12]). Values of Q_{ual} and K_{eff}^2 have been calculated from the BVD model formulas, which are already expressed in the previous chapter:

$$Q_{ual} = \frac{1}{2\pi F_s R C_m} = \frac{2\pi F_s L_m}{R}$$

$$K_{eff}{}^2 \approx \frac{C_m}{C_o}$$

with $F_s = \frac{1}{2\pi\sqrt{L_m C_m}}$. These values are gathered in Table 12.

Magnetic field	C_0 (pF)	R (Ω)	L_m (µH)	C_m (fF)	Q_{ual}	$K_{eff}{}^2$(%)
0 T	11	10.7	3.38	24.5	1098	0.223
0.005 T	11	12.4	3.08	31.1	803	0.282
0.04 T	11	9.3	3.70	22.8	1370	0.208

Table 12. RLC components of the BVD model extracted from the admittance curve and its real part for different magnetic fields (0T/0.005T/0.04T) applied along the wave propagation direction. Critical factors are calculated from BVD model formulas.

Since critical factor values calculated are consistent with experimental results, BVD model is justified to describe a resonator SAW device. However, the BVD model is just an equivalent model that does not explain the underlying physics. We can nevertheless notice that the decrease in Q_{ual} and increase in K_{eff}^2 are accompagnied by an increase of the resistance R. The maximum effective electromechanical coupling is thus obtained for maximum losses.
In Nan's study [NAN13], a more complex BVD model leads to R = 53 Ω, C_m = 18.9 fF, L_m = 28.7 µH and C_0 = 1.52 pF at zero applied magnetic field. Since these values are highly dependent on the geometry, a direct comparaison with the values reported in Table 12 would be hazardous but the order of magnitude is similar.

2. Simulation of the magneto acoustic responses

An equivalent piezomagnetic model for MSAW devices has been developed by Zhou *et al.* [ZHO14]. The piezomagnetic equivalent model aims in studying the impact of the strains generated by a magnetostrictive material under applied magnetic field and by the acoustic wave propagation at the interface of a piezoelectric/magnetostrictive system.
In the following, we recall the main ingredients of this model and then use it to compute the expected MSAW responses under magnetic field, in the specific case of the 50 nm Ni-based devices described in the previous paragraphs.
The fundamental equations governing the system are given in a first step. In a second step, the piezomagnetic equations and the constants of the system are expressed. Then, the equilibrium states for an in-plane magnetic field applied parallel or perpendicular to the in-plane easy axis are described. It thus allows to write presicely the effective elastic, piezomagnetic and magnetic permeability constants as function of the applied magnetic field. Variations of some elastic constants will be studied. In a last step, we will present how these constants inside constitutive piezomagnetic equations can impact the dynamic response of a MSAW device by resolving the equation of motion on Comsol Multiphysics.

2.1. Basic equations

The basics equations governing the system are (i) the equation that links the displacement to the stress (equation of motion) and (ii) the equation that gives the time dependence of the magnetization, the LLG equation [AHA96]:

$$\rho \frac{\partial^2 u_i}{\partial t^2} = \frac{\partial \sigma_{ij}}{\partial x_j}$$

$$\frac{\partial \vec{M}}{\partial t} = -\frac{1}{1+\eta^2}(\gamma\mu_0.[\vec{M} \times \overrightarrow{H_{eff}}] - \frac{\gamma\mu_0\eta}{M_s}.[\vec{M} \times \vec{M} \times \overrightarrow{H_{eff}}])$$

The effective magnetic field and the stress tensor σ_{ij} are calculated using: $\overrightarrow{H_{eff}} = \vec{H} - \frac{1}{\mu_0}.\frac{\partial U^{int}}{\partial \vec{M}}$ with $\sigma_{ij} = \frac{\partial U^{int}}{\partial \varepsilon_{ij}}$ where U^{int} is the internal energy density of the material, H is the applied field and ε_{kl} is the strain tensor.

The total energy density U of a ferromagnetic film is given by:

$$U = E_{m.a} + E_{m.e} + E_{el} + E_D + E_Z = U^{int} + E_D + E_Z$$

with:
(i) The uniaxial magnetocrystalline energy density: $E_{m.a} = -K\alpha^2$ with α the cosine director of M along the easy axis of magnetization (OX in the case described after) and K the anisotropy constant.
(ii) The magnetoelastic energy density: $E_{m.e} = b_{ijkl}\alpha_i\alpha_j\varepsilon_{kl}$ where b_{ijk} are the magnetoelastic constants and α are the director cosines of magnetization.
(iii) The elastic energy density: $E_{el} = \frac{1}{2}C_{ijkl}\varepsilon_{ij}\varepsilon_{kl}$ where C_{ijkl} are the elastic constants.
(iv) The demagnetizing field energy density: $E_D = -\frac{\mu_0}{2}\vec{M}.\overrightarrow{H_D}$ where $\overrightarrow{H_D}$ corresponds to the dipolar field.
(v) The Zeeman energy density: $E_Z = -\mu_0\vec{M}.\vec{H}$.

In the case of acoustic wave propagation, only small dynamic perturbations around the equilibrium state are considered. The field, the magnetization, the mechanical stress and the strain are given by:

$$\vec{H} = \overrightarrow{H_0} + \vec{h},\ \vec{M} = \overrightarrow{M_0} + \vec{m},\ \vec{\sigma} = \overrightarrow{\sigma_0} + \overrightarrow{\sigma^m},\ \vec{\varepsilon} = \overrightarrow{\varepsilon_0} + \overrightarrow{\varepsilon^m}$$

where $\overrightarrow{H_0}$ is the static applied field, $\overrightarrow{M_0}$ is the static magnetization, $\overrightarrow{\sigma_0}$ is the stress at equilibrium and $\overrightarrow{\varepsilon_0}$ is the spontaneous strain induced by magnetostriction. The quantities $\vec{h}$, $\vec{m}$, $\overrightarrow{\sigma^m}$ and $\overrightarrow{\varepsilon^m}$ are dynamical contributions which are due to lattice perturbations under propagation of an acoustic wave and could give a backaction on the SAW characteristics.
$\vec{h}$ satisfies the magneto static equation: $\vec{\nabla} \cdot \vec{b} = \vec{\nabla} \cdot (\mu_0(\vec{h} + \vec{m})) = 0$, where $\vec{b}$ is the dynamical magnetic induction.

2.2. Piezomagnetic problem

In this section, we solve the piezomagnetic problem in the low frequency regime for which the damping term is neglected. The high frequency regime is not studied because magneto acoustic simulated results with low frequency regime will be satisfactory. LLG equations are first written in spherical coordinates as:

$$\frac{\partial \theta}{\partial t} = -\frac{\gamma}{M_s.sin\theta}.\frac{\partial U^{int}}{\partial \varphi} + \gamma\mu_0 H_\varphi = \gamma\mu_0 H_{\varphi,eff}$$

$$\frac{\partial \varphi}{\partial t} = \frac{\gamma}{M_s.sin\theta}.\frac{\partial U^{int}}{\partial \theta} - \frac{\gamma\mu_0}{sin\theta}H_\theta = -\frac{\gamma\mu_0}{sin\theta}H_{\theta,eff}$$

with $H_\varphi = -H_x sin\varphi + H_y cos\varphi$ and $H_\theta = H_x cos\theta cos\varphi + H_y cos\theta sin\varphi - H_z sin\theta$.

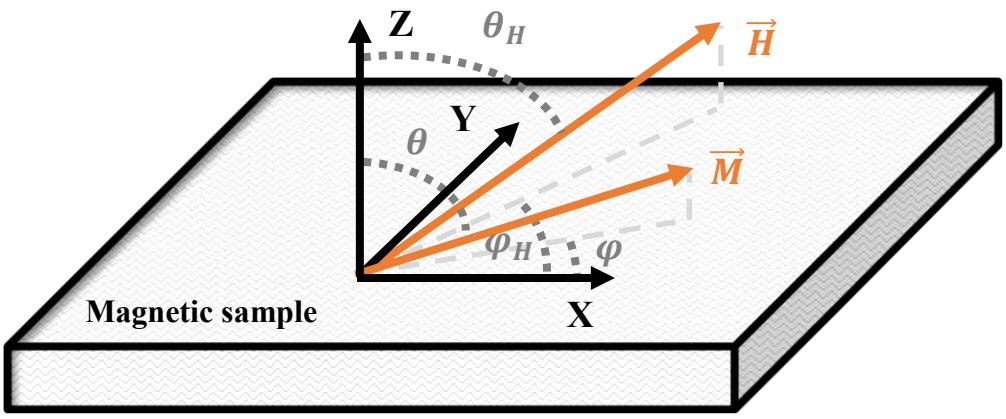

Figure 81. Schematic and associated coordinates of the magnetic system. θ (respectively θ_H) is the angle between the Z direction and the magnetization (respectively applied field), φ (respectively φ_H) is the angle between the X axis and the projection of magnetization (respectively applied field) in the (XY) plane.

Under the acoustic excitation, the magnetization evolves from its equilibrium (θ_0,φ_0) position towards a new (θ,φ) position that can be expressed as:

$$\theta = \theta_0 + \delta_\theta \text{ and } \varphi = \varphi_0 + \delta_\varphi \text{ with } \delta_\theta, \delta_\varphi \ll 1.$$

The internal energy density can thus be developed at first order in δ_θ and δ_φ:

$$U^{int} = {U_0}^{int} + {U_\theta}^{int}\delta_\theta + {U_\varphi}^{int}\delta_\varphi + \frac{{U_{\theta\theta}}^{int}}{2}{\delta_\theta}^2 + \frac{{U_{\varphi\varphi}}^{int}}{2}{\delta_\varphi}^2 + {U_{\theta\varphi}}^{int}\delta_\theta\delta_\varphi + {U_{\theta\varepsilon^m}}^{int}\delta_\theta\frac{\partial u_i}{\partial x_j} + {U_{\varphi\varepsilon^m}}^{int}\delta_\varphi\frac{\partial u_i}{\partial x_j}$$

where ${U_{ij}}^{int}$ are the second order derivatives.

Zhou *et al.* [ZHO14] assume that the magnetic sub-system has enough time to adjust to the elastic sub-system and linearize the system of equations (motion and LLG equations) around a ground state position, dependent on the direction and intensity of the external applied magnetic field. After long calculations, the following piezomagnetic equations are obtained:

$${\sigma^m}_{ij} = \left(C_{ijkl} + \Delta C_{ijkl}\right)\frac{\partial u_k}{\partial x_l} - q_{lij}h_l$$

$$\frac{\partial b_i}{\partial x_i} = \frac{\partial(\mu_0(h_i + m_i))}{\partial x_i} = 0$$

the piezomagnetic constants (q), the effective elastic constants (C'), the magnetic permeability (μ), the dynamical magnetization (m) and the dynamical magnetic induction (b) are given by:

$$q_{lij} = -\frac{b_{ijmn}}{M_s^2}.(M_m^0\chi_{nl} + M_n^0\chi_{ml})$$

$$C'_{ijkl} = C_{ijkl} + \Delta C_{ijkl} = C_{ijkl} + \frac{b_{ijmn}}{M_s^2}.(M_n^0 q_{mkl} + M_m^0 q_{nkl})$$

$$\mu_{il} = \mu_0(\delta_{il} + \chi_{il})$$

$$m_i = q_{ikl}.\frac{\partial u_k}{\partial x_l} + \chi_{il}h_l$$

$$b_i = \mu_0 q_{ikl}.\frac{\partial u_k}{\partial x_l} + \mu_{il}h_l$$

χ_{il} is the susceptibilty tensor which is only composed of a real part in the low frequency regime approximation. The expressions of χ_{il} can be found in [ZHO14].

Three important remarks must be made:
(i) The equation ($\sigma^m{}_{ij}$) is similar to the piezoelectric equation expressed in first part, first chapter. The magnetic field and the piezomagnetic constants replace the electric field and the piezoelectric constants respectively.
(ii) The different component of ($\sigma^m{}_{ij}$) are also given by:

$$\sigma^m{}_{ij} = \frac{\partial U^{int}}{\partial \varepsilon_{ij}} = \frac{\partial E_{el}}{\partial \varepsilon_{ij}} + \frac{\partial E_{m.e}}{\partial \varepsilon_{ij}} = C_{ijkl}\frac{\partial u_k}{\partial x_l} + \frac{\partial E_{m.e}}{\partial(\frac{\partial u_k}{\partial x_l})}$$

By analogy with the piezomagnetic equations, the dynamical magnetic field results from the variation of the magnetoelastic energy density under the lattice perturbation associated to the wave propagation.
(iii) Express the magnetic field dependence of the elastic constant is equivalent to the so-called deltaE-effect. In fact, Young modulus and elastic constant are commonly used for isotropic and anisotropic material respectively. Both parameters described the elastic behavior between stress and strain.

2.3. Case of a film with uniaxial magnetic anisotropy, for in-plane applied magnetic field and in-plane magnetization ($\theta = \theta_H = \pi / 2$)

The magnetization equilibrium state is obtained by the minimization of the energy with respect to the magnetization direction:

$$\frac{\partial(E_Z + E_{m.a})}{\partial \varphi_0} = 0$$

with: $E_Z = -\mu_0 M_s H\, cos(\varphi_0 - \varphi_H)$ and $E_{m.a} = -K\, cos^2(\varphi_0)$ for an easy axis along X and with $K = \frac{\mu_0 M_s H_s}{2}$. As done in [ZHO14], the static strains, *i.e.* ε_0, are considered negligible.

For an in-plane field applied perpendicular to the easy axis ($\theta_H = \frac{\pi}{2}$ and $\varphi_H = \frac{\pi}{2}$), the minimum of energy is obtained when:
$sin\varphi_0 = \frac{H}{H_s}$ below saturation ($H < H_s$).
$\varphi_0 = \pm\frac{\pi}{2}$ above saturation ($H > H_s$).

For an in-plane field applied parallel to the easy axis ($\theta_H = \frac{\pi}{2}$ and $\varphi_H = 0$), the minimum of energy is obtained when:
$\varphi_0 = 0$ or $\varphi_0 = \pi$.

When the in-plane applied field lies neither along the easy nor along the hard axis, $\varphi_0(H, \varphi_H, \theta_H)$ can be calculated numerically but there are no analytical solutions.

In the next paragraphs, the magnetic properties injected in the calculation are described by the hysteresis loops calculated in the macrospin approximation. The M_x (along the field) and M_y (perpendicular to the field) components are shown in Figure 82 for the field applied along the easy axis (EA in red) and along the hard axis (HA in black). M_y is simply calculated using: $M_y = \sqrt{M_S - M_x}$.

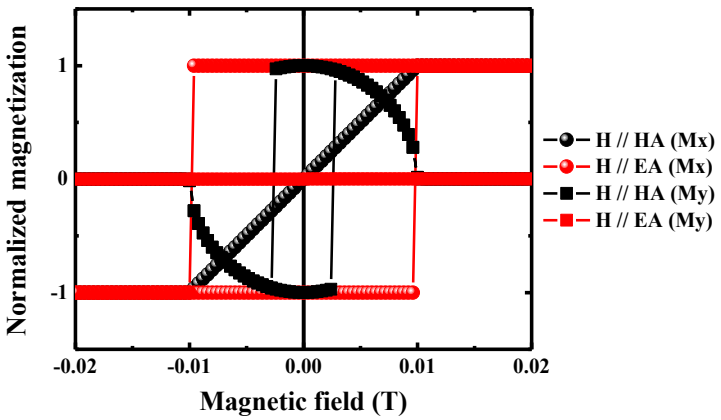

Figure 82. (Mx,My) simulated in a macrospin approach versus applied field in the case of a uniaxial anisotropy (H // HA (Mx (black spheres), My (black squares)) and // EA (Mx (red spheres), My (red squares))). The coercive and the in-plane saturation fields are equal to 0.01 T.

In real samples, the magnetization reversal can be inhomogeneous and lead to coercive field values smaller than expected from the macrospin model. In this case, $\varphi_0(H, \varphi_H, \theta_H)$ extracted from magnetic measurements can be used when vectorial VSM is performed.

2.3.1. Static magneto acoustic response

The calculations by Zhou *et al.* [ZHO14] show that the frequency variation of the propagating waves are essentially related to variations of the elastic constants.
For a thin film with a cubic symmetry and a uniaxial magnetic anisotropy, the matrix giving the corrections to the elastic constants (Voigt notation) is written as:

$$\Delta C = \begin{bmatrix} \Delta C_{11} & \Delta C_{11} & 0 & 0 & 0 & \Delta C_{16} \\ \Delta C_{11} & \Delta C_{11} & 0 & 0 & 0 & -\Delta C_{16} \\ 0 & 0 & 0 & 0 & 0 & 0 \\ 0 & 0 & 0 & \Delta C_{44} & \Delta C_{45} & 0 \\ 0 & 0 & 0 & \Delta C_{45} & \Delta C_{55} & 0 \\ \Delta C_{16} & -\Delta C_{16} & 0 & 0 & 0 & \Delta C_{66} \end{bmatrix}$$

where:

$$\Delta C_{11} = -\frac{\mu_0 b_2^2}{U_{\varphi\varphi}} cos^2\varphi_0 sin^2\varphi_0$$

$$\Delta C_{16} = \frac{\mu_0 b_2^2}{8U_{\varphi\varphi}} sin4\varphi_0$$

$$\Delta C_{44} = -\frac{\mu_0 b_2^2}{4U_{\theta\theta}} sin^2\varphi_0$$

$$\Delta C_{45} = -\frac{\mu_0 b_2^2}{U_{\theta\theta}} sin\varphi_0 cos\varphi_0$$

$$\Delta C_{55} = -\frac{\mu_0 b_2^2}{4U_{\theta\theta}} cos^2\varphi_0$$

$$\Delta C_{66} = -\frac{\mu_0 b_2^2}{4U_{\varphi\varphi}} cos^2 2\varphi_0$$

In these expressions, the second order derivatives of U_{ij} are:

$$U_{\theta\theta} = \mu_0 M_s(H_s(1 - sin^2\varphi_0) + Hcos(\varphi_0 - \varphi_H))$$
$$U_{\varphi\varphi} = \mu_0 M_s(H_s(1 - 2sin^2\varphi_0) + Hcos(\varphi_0 - \varphi_H))$$

Since the magnetization is in-plane, the demagnetizing field is zero. The elastic energy does not appear since it does not depend on the magnetization direction cosines. Finally, the magnetoelastic energy is neglected because it does not change significantly the results for this case.

The variations of the effective elastic constants related to the different waves (C_{11} for RW and C_{66} (= C_{44}) for QSHSAW in cubic material) can be calculated using the magnetic responses computed in Figure 82.

For an in-plane field applied perpendicular to the easy axis, the effective elastic constants are:

$$\begin{cases} C'_{11} = C_{11} - \frac{b_2^2 H^2}{M_s(H_s{}^3)} \\ C'_{66} = C_{44} - \frac{b_2^2(1-2\frac{H^2}{H_s{}^2})^2}{4M_s(H_s(1-\frac{H^2}{H_s{}^2}))} \end{cases}$$ below saturation ($\theta_0 = \frac{\pi}{2}$ and $sin\varphi_0 = \frac{H}{H_s}$).

$$\begin{cases} C'_{11} = C_{11} \\ C'_{66} = C_{44} - \frac{b_2^2}{4M_s(\pm H - H_s)} \end{cases}$$ above saturation ($\theta_0 = \frac{\pi}{2}$ and $\varphi_0 = \pm\frac{\pi}{2}$).

For an in-plane field applied parallel to the easy axis, the effective elastic constants are:

$$\begin{cases} C'_{11} = C_{11} \\ C'_{66} = C_{44} - \frac{b_2^2}{4M_s(\pm H + H_s)} \end{cases}$$ in the entire field range ($\theta_0 = \frac{\pi}{2}$ and $sin\varphi_0 = 0$).

The calculated variations of the effective elastic constants C'$_{11}$ and C'$_{66}$ as a function of the intensity of the applied magnetic field are shown in Figure 83 (a and b respectively) for a Ni film with an in-plane magnetization. The following constants are used: $C_{11} = 224\ GPa$, $C_{44} = 120\ GPa$ [LUO11], $b_2 = 1 \times 10^7\ J.m^{-3}$ and $M_s = 490\ kA.m^{-1}$ [SAN99].

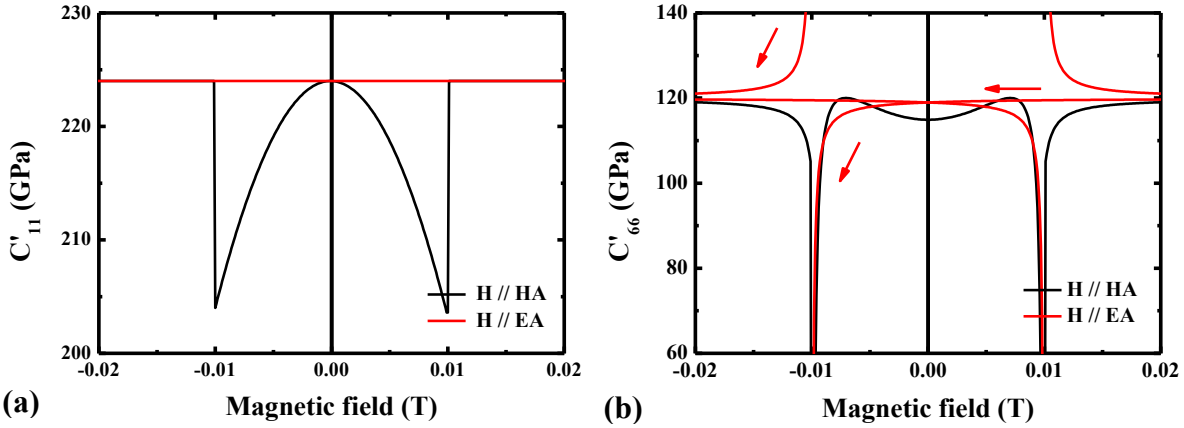

Figure 83. Calculated variations of the effective elastic constants C'$_{11}$ (a) and C'$_{66}$ (b) as a function of the magnetic field applied along and perpendicular to the easy axis for a thin Ni film. On (b), red arrows represent the effective elastic constant variation sense obtained from positive to negative saturation field for a field applied along the EA.

When the field is applied perpendicular to the easy axis (black curves), C'_{11} and C'_{66} variations have a typical "w" and "double w" shape. For both waves, two huge troughs are present at saturation field. Above saturation, C'_{11} is constant while it is not the case for C'_{66}.
When the field is applied along the easy axis (red curves), C'_{11} doesn't depend on the field, while C'_{66} exhibits a huge variation in the vicinity of the saturation field. The divergence of the C'_{66} variation has no physical meaning but just comes from mathematical singularity of the formula expressed above.

Finally, we can note that these huge variation are just theoretical and did not explained small frequency resonance variations observed experimentally. In fact, the elastic constants of LNO, which exhibit no dependence on magnetic field, impact also the final MSAW response.

2.3.2. Dynamic magneto acoustic response

Considering the effective elastic constant variations, the Comsol Multiphysics software is used to solve the equation of motion. The geometry (direction of propagation wave, metallization ratio…), the physical properties of each elements, the mesh and the physics (piezoelectric device module) are then introduced in the software.
Even if the Comsol Multiphysics setup in [ZHO14] is developed for a delay line device where there is only one magnetic material, numerical simulations are used in resonator geometry by considering that all fingers act as an assembly of independent material. This geometry is shown in Figure 84.

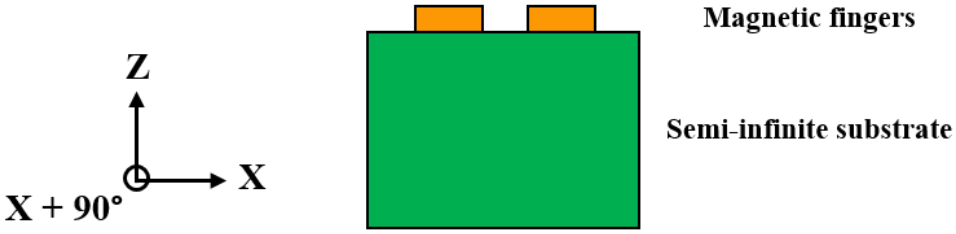

Figure 84. Schematic view of the 2D model implemented on Comsol Multiphysics.

The substrate is considered as semi-infinite (LNO 41Y-cut with a direction of wave propagation along LNO X-axis, a metallization ratio of 50 % and a 6.5 µm wavelength). The gold area corresponds to Nickel fingers (50 nm thick). Two fingers are used since the simulation of the whole real device would be extremely long.

The dynamic response of the SAW resonator when a wave is propagating in the device is obtained by introducing, for each field value, a set of consants of the thin film, *i.e.* magnetic fingers (effective elastic constants, piezomagnetic constants and magnetic permeability constants), and by calculating the resonance frequencies. In the following case, $\varphi_0(H, \varphi_H, \theta_H)$ is calculated numerically by taking the magnetoelastic energy into account.

The MSAW responses have been calculated for the RW (Figure 85 (c)) and for the QSHSAW (Figure 85 (d)) when the in-plane magnetic field is applied parallel (red) or perpendicular (black) to the easy axis of magnetization. For this simulation, the EA is chosen perpendicular to the direction of wave propagation.
The experimental curves and the field variations of the effective elastic constants extracted from the equivalent piezomagnetic model are recalled in Figure 85 (e), (f), (a) and (b) for an easier comparison.

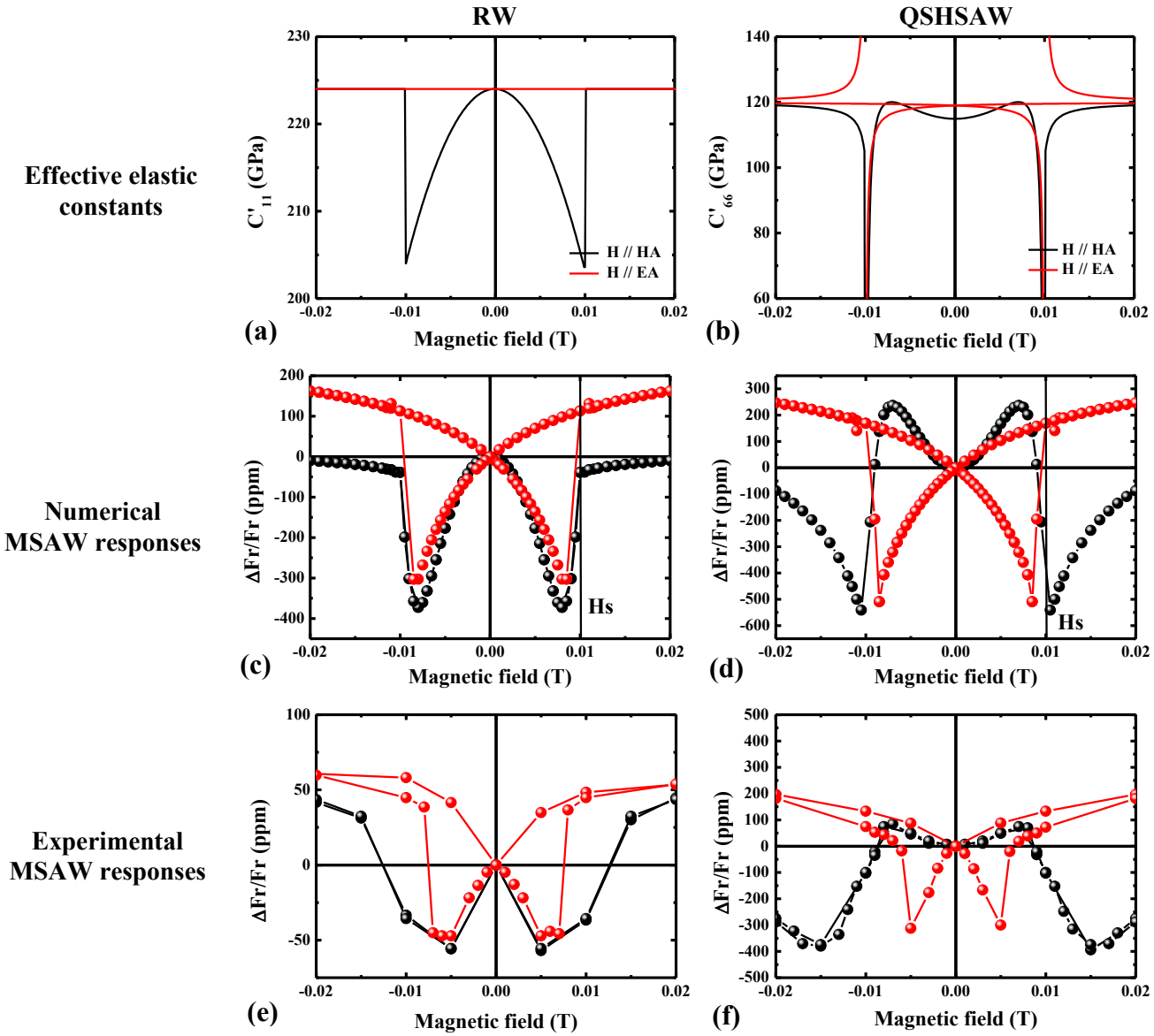

Figure 85. Calculated (c and d) and experimental (e and f) variations of the resonance frequency as a function of applied field for the RW (left) and the QSHSAW (right) when the in-plane magnetic field is applied parallel (red) or perpendicular (black) to the magnetization easy axis. (a) and (b) present the corresponding field variations of the effective elastic constants C'_{11} and C'_{66} as calculated from the piezomagnetic model (a-d) have been obtained using theoretical magnetization curves presented in Figure 82. Device wavelength is 6.5 µm, MR is 50 %, the wave propagation direction is LNO X and the EA axis is choose perpendicular to LNO X.

The experimental and calculated curves can be interestingly compared and discussed, together with the corresponding variations of the effective C'_{11} and C'_{66} elastic constants versus field, as obtained from the equivalent piezomagnetic model.

(i) The first noticeable point is the relative good qualitative agreement between calculated and experimental curves. The simulated frequency variation is reversible for fields applied along the hard axis with slightly different shapes for RW and QSHSAW; they both exhibit important field sensitivity in the vicinity of the saturation field. For fields applied along the easy axis, the normalized frequency variations for RW and QSHSAW exhibit similar shapes with an hysteresic behavior and a strong field sensitivity in the vicinity of the saturation field. This good qualitative agreement strongly suggests that the black (resp. red) experimental curve is obtained for fields applied along the hard (resp. easy) magnetization axis as mentioned in the paragraph 1.1. These observations suggest that the magnetic

anisotropy would thus be modified between the plain stack and the patterned IDT, as this is eventually discussed in the following chapter.
(ii) Some discrepancies can nevertheless be underlined between calculated and experimental curves: the experimental curves exhibit less sharp field dependences, especially along the hard axis, with frequency variations expanding over more than 10 mT while calculated variations occur in less than 5 mT. Even if the saturation field is smaller in the experimental full film magnetic, the experimental extrema are also shifted towards high fields compared to calculated ones. These features can be related to the fact that the calculated curves are obtained from theoretical magnetization curves that can be significantly different from the magnetization curves describing the magnetic behavior of the IDT. Nonetheless, the RW MSAW saturation field, *i.e.* the field above which the resonance frequency varies little with field, is obviously linked to the magnetization saturation field (Figure 85 (c)). The quantitative variation is also significantly smaller in the experimental case since it is reduced by approximately 35 % for the QSHSAW and by more than 75 % for the RW. One should recall here that the simulation only considers 2 fingers and doesn't take account of the leaky component of the wave, electric losses and experimental roughness. The overall experimental sensitivity is however larger for the QSHSAW than for the RW, as in the calculation.
(iii) Let's now discuss those calculated and experimental curves in comparison with the effective elastic constants variations obtained from the piezomagnetic model (a and b). One can recall here that the real IDT magnetization curves are likely different from the ideal case presented in Figure 82, but that both calculated effective elastic constants and calculated frequency variations are obtained using the same theoretical magnetization curves.
Important features from the frequency variation obviously originate from the field dependence of the effective elastic constants, especially the overall shapes obtained for fields applied along the hard axis.
Several points observed in both calculated and experimental frequency variations however cannot be explained by the field dependence of the effective elastic constants. The first difference is the apparition of an hysteretic MSAW response for fields applied along the EA. The second difference are the slopes observed for fields larger than the saturation field. The RW frequencies calculated for both field directions indeed still increase when increasing the field above saturation, with slightly different slopes for EA and HA, while the effective C'_{11} value is constant. For the QSHSAW, the resonance frequency increases also for both field directions, with a larger slope for a field applied along the HA and after the saturation field.
These observations point out the influence of a dynamical contribution on the propagating wave characteristics. Such a contribution might be explained by the occurrence of a dynamical stress field of magnetoelastic origin, related to the magnetization dynamics, which is itself induced by the acoustic wave. The impact of this dynamical magnetoelastic field would depend on the static magnetization orientation and on the the type of SAW (see next paragraph). This contribution is most likely the analogous of what has been introduced in various studies as [GOW16, DRE12].

2.4. High field behavior

To study the impact of the dynamic magnetoelastic field at high fields on MSAW responses, we have compared its value for fields larger than the saturation field, *i.e.* when the magnetization lies along the applied magnetic field, for the two field directions respect to the direction of wave propagation.
During simulations that give MSAW results (Figure 85 (c and d)), we have extracted the in-plane components values of the dynamic magnetoelastic field perpendicular to the DC field direction and for 20 mT DC magnetic field applied along and perpendicular to Q. Values are gathered in Table 13 for RW and QSHSAW.

These values are more or less consistent with values that can be obtained in usual VNA-FMR experiments (0.011 mT for 9.5 GHz with an injected power of 200 mW in Co/Pt bilayers [ROJ14]).
For the Rayleigh wave whose stress displacement field is essentially along the direction of wave propagation, the h component is larger for a magnetic field perpendicular to Q. For the QSHSAW, with a transverse polarization, the h component is three times higher for a magnetic field parallel to Q than for a magnetic field perpendicular to Q.

Experimentally (see Figure 77 (d and f)), a larger high field slope is observed for a Rayleigh wave when the magnetic field lies perpendicular to Q, while the slope is larger when the field lies along Q for QSHSAW (only if we consider the frequency variation obtained just after the dip). These results suggest that the high field slope observed on MSAW responses is indeed related to the dynamic magnetoelastic field.

Acoustic wave	H (// Q)	H (⊥ Q)
RW	0.0888	0.1274
QSHSAW	0.2218	0.0718

Table 13. In-plane perpendicular to the 20 mT DC field component of the dynamic magnetoelastic field (h) for a magnetic field applied along and perpendicular to the direction of wave propagation (RW and QSHSAW).

3. Experimental results obtained for other Ni-based devices

The results presented up to now were obtained for Ni-based devices grown on Lithium Niobate 41Y-cut, with a wavelength of 6.5 µm and a wave propagation direction along the LNO X-axis.
Similar experiments have been performed for devices with a 13 µm wavelength, for acoustic waves propagating along the LNO X+90° direction and for devices patterned from a stack grown on different LNO surfaces (LNO Z- and LNO 128Y- cuts).
The following paragraphs summarize the most relevant results that can be interestingly compared to those previously presented: (i) MSAW device on LNO 41 Y-cut (Q//X) with a wavelength of 13 µm, (ii) MSAW device on LNO 41 Y-cut (6.5 µm) with Q//X+90° and (iii) MSAW device on LNO 128 Y-cut.

3.1. MSAW devices on LNO 41 Y-cut (Q // X) with a wavelength of 13 µm

The Figure 86 (b) gathers the magneto acoustic responses (RW) collected for 50 nm thick Ni-based devices on LNO 41 Y-cut with Q // X, MR of 50 % and H // X for two different wavelengths, *i.e.* 6.5 µm and 13 µm. The associated S_{11} signals are presented in Figure 86 (a). These devices have been patterned from the same initial plain stack.

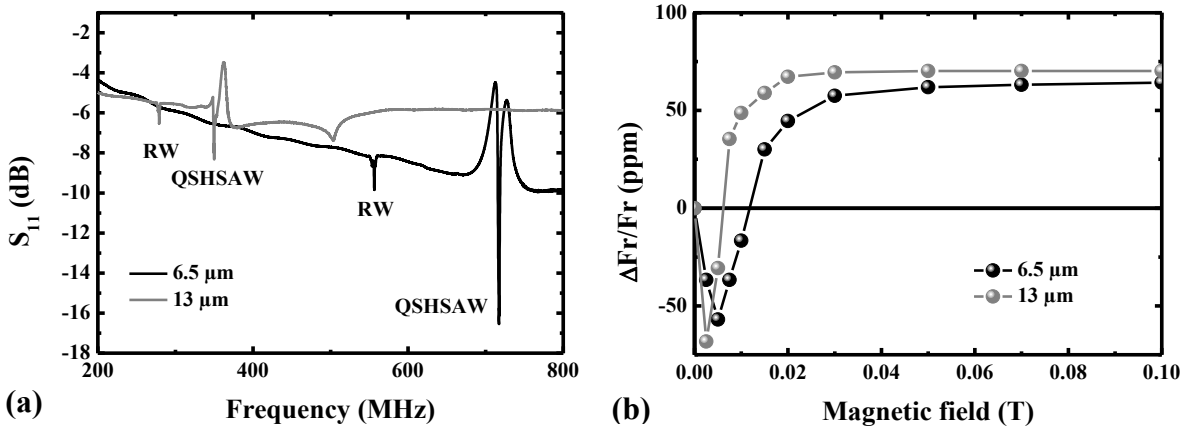

Figure 86. S_{11} signals for 50 nm thick Ni-based devices deposited on LNO 41 Y-cut with a direction of wave propagation along LNO X-axis and two different wavelengths (6.5 µm in black and 13 µm in grey) (a). Associated normalized resonance frequency variations of RW for a magnetic field applied along the wave propagation direction (b). Only positive fields are presented.

The first point that can be observed in (a) is the difference in the resonance frequencies for both RW and QSHSAW, which is expected from $F_r=v/\lambda$ and already discussed in Table 11.

The variations of the RW frequency versus applied field along X exhibit similar shapes, although the minimum and the saturation appear for smaller fields when the wavelength increases. This is most likely related to a change in the IDTs magnetic behavior since, as mentioned in chapter 2, the change in the finger periodicity is accompanied by a change in the finger's width. One can however notice that despite a larger width for 13 µm periodicity, this curve obtained for field along X suggests again a magnetization hard axis along X, as for the smaller periodicity, and contrary to the plain stack before patterning. This shape effect is detailed in the following section.
Similar results were obtained for these two wavelengths but for MSAW devices on LNO Z-cut and 128 Y-cut (not shown here).

3.2. MSAW devices on LNO 41 Y-cut (6.5 µm) with Q // X + 90°

The point is to explore here the incidence of the wave propagation direction in comparing two Ni-based devices on LNO 41Y-cut, both patterned with a 6.5 µm wavelength from the same initial plain stack, but with two perpendicular IDTs orientations yielding two perpendicular wave propagation directions: LNO X and LNO X+90°.
Figure 87 (a) shows the output S_{11} signals for Q // X (MR of 60 %) and Q // X + 90° (MR of 50 %), while the RW frequency variation versus the magnetic field applied along three different directions are presented in Figure 87 (b) and (c) for Q // X and (d) and (e) for Q // X + 90°. (c) and (e) are simply zoomed from (b) and (d). Let's recall here that the color code used for the different field directions is the one presented in chapter 2: the black curves are collected for H // Q (thus // X or // X + 90 ° depending on the device), the red curves are collected for H // Q + 90 ° (thus // X + 90 ° or // X depending on the device) and the green curves are collected for H // OOP.

First of all, when the wave propagation direction is along X + 90°, the S_{11} signal (Figure 87 (a)) doesn't show the presence of QSHSAW and the RW is shifted in frequency in comparison with the Q // X device. The RW resonance frequencies are different between the two directions due to different metallization ratios and wave velocities. The absence of QSHSAW most likely means that the set of constants (elastic, dielectric and piezoelectric) gives an electromechanical coupling factor close to zero. Numerical simulations on Comsol have confirmed the presence and the nature of these waves thanks to their resonance frequencies and motion fields respectively.

Concerning the in-plane magneto acoustic responses (b, c, d and e), similar curves are observed for both devices, whatever the wave propagation direction with respect to the LNO crystalline axis. The main parameter governing the frequency variation versus field appears to be the direction of the applied magnetic field with respect to the wave propagation direction Q. Similar hysteretic responses are namely measured for magnetic fields applied perpendicular to Q (red), *i.e.* along the IDTs; and similar reversible responses are measured for magnetic fields applied parallel to Q (black), *i.e.* perpendicular to the IDTs. This strongly suggests that the key factor here is the direction of the applied field respect to the magnetic anisotropy that is itself governed by the IDTs shape. The underlying LNO crystal structure doesn't affect the shape of frequency responses to an external field.
Despite very similar behaviors for the two devices, one can however notice slight differences, in particular when the field is parallel to Q: the minima and the maxima (when the resonance frequency becomes constant or vary little with field) values observed on the black curves are shifted to higher fields by approximately 10 mT for the device with wave propagating along X+90°. Such features are most likely due to slightly different magnetic behaviors of the IDTs.
One can finally notice that the magneto acoustic responses obtained for fields applied perpendicular to the device plane (green curves) are also similar. They especially both exhibit a strong hysteretic behavior, although this direction is supposed to be a hard magnetization axis for the IDT, as it is the case in the original plain stack (see Figure 50 (i)).

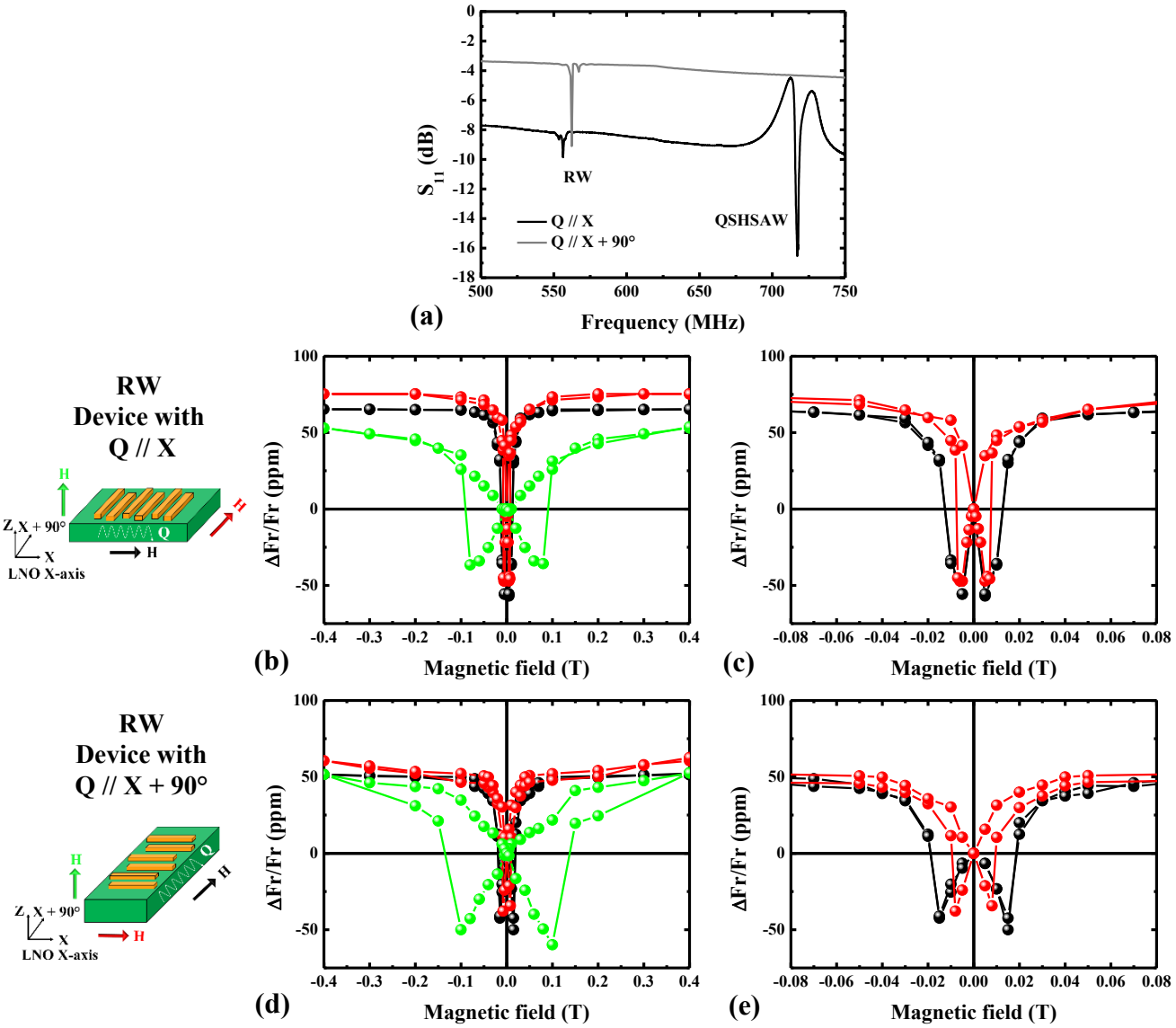

Figure 87. S_{11} signals for 50 nm thick Ni-based devices on LNO 41Y with two different directions of wave propagation (a) and variation of the RW frequency versus field for the two devices with Q // X (b and c) and Q // X + 90° (d and e) for different directions of applied magnetic fields (black: along Q; red: along Q+90°; green: perpendicular to the surface).

3.2. MSAW device on LNO 128 Y-cut

In this last paragraph concerning other Ni-based devices, we present the results obtained for a device patterned from the LNO128Y/Ta(5nm)/Ni(50nm)/Pt(5nm) plain stack, the magnetization curves of which are recalled in Figure 88 (b) and (c), for magnetic fields applied in the plane and perpendicular to the plane respectively. The device has been patterned for a wave propagation direction along LNO X-axis, a wavelength of 6.5 µm and a metallization ratio of 40%.
Figure 88 (a) shows the output signal S_{11} obtained for the device. The RW and QSVSAW normalized frequency variations versus field are presented in (d-e) and (f-g) respectively for the three directions of applied field (X, X+90° and OOP).

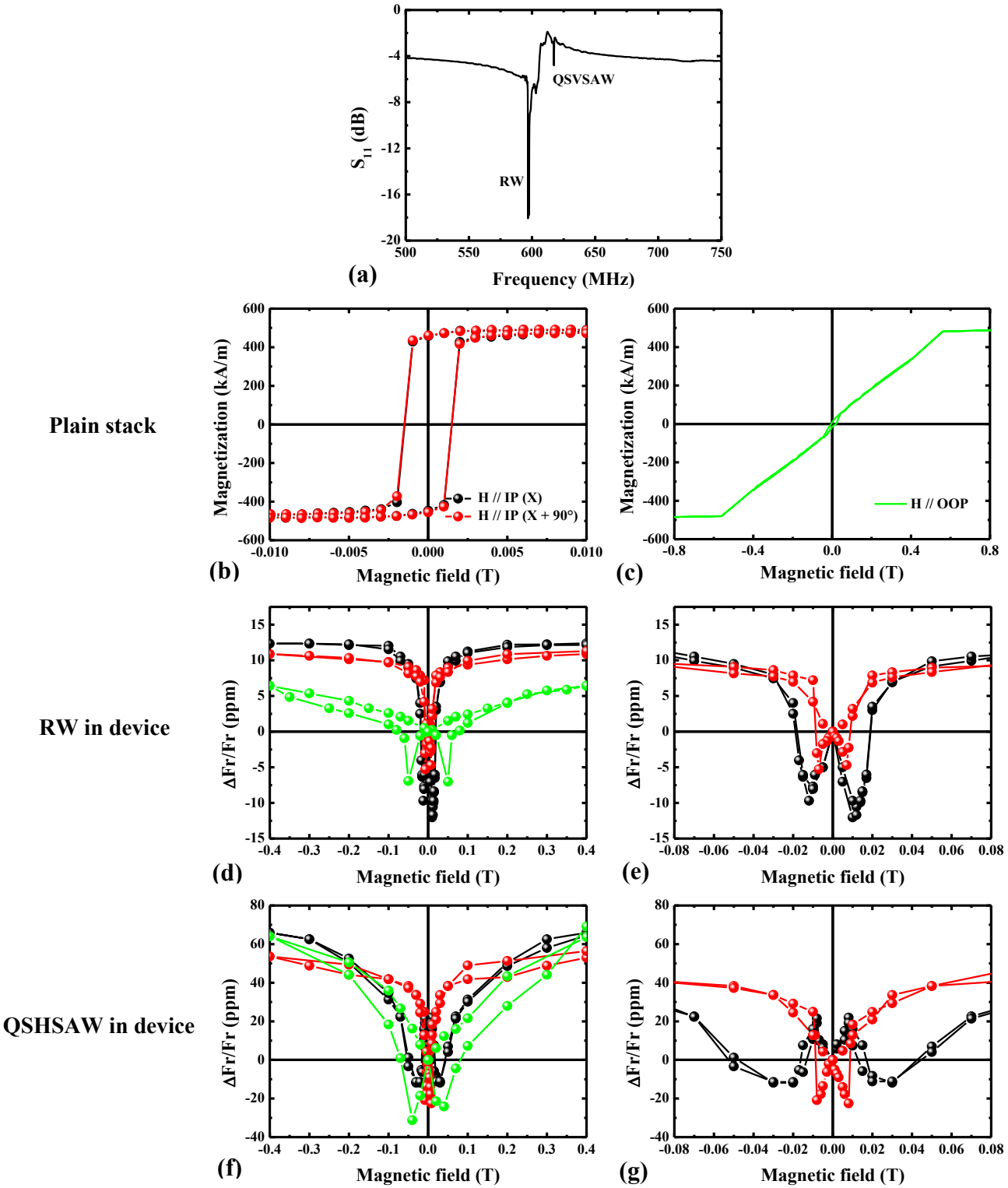

Figure 88. S_{11} signal for the MSAW device patterned from a LNO128Y/Ta(5nm)/Ni(50nm)/Pt(5nm) plain stack (Q//X, 6.5µm and MR of 40%) (a). Hysteresis loops before patterning when the field is applied along in-plane X and X+90° (b) and perpendicular to the plane (c). Variation of the resonance frequencies for RW (d and e) and QSVSAW (f and g) for the different directions of the applied magnetic field.

As mentioned in Figure 50 (d and f), and as recalled by the results presented in Figure 88 (b and c), the Ni film obtained on this LNO cut doesn't exhibit a specific in-plane anisotropy since both magnetization curves obtained for fields along X or X+90° are typical of easy magnetization directions with high remanence and a square shape. The OOP curve however reveals a hard magnetization axis. Those

characteristics are significantly different from those reported for the Ni film deposited on the LNO 41Y-cut.
The magneto acoustic responses measured for both the RW and QSVSAW (d, e, f and g) however exhibit the same shapes and main characteristics as those obtained for the device patterned from Ni on LNO41Y (Figure 77): hysteretic when the magnetic field is applied perpendicular to the device and when it is perpendicular to the direction of wave propagation, *i.e.* along the IDT, and reversible when the field is applied parallel to the wave propagation direction, *i.e.* perpendicular to the IDT. Following our previous interpretations, this would be related to the occurrence of an in-plane easy magnetization axis along the IDT's length and a hard axis along the in-plane perpendicular direction. In this case where the plain stack exhibits an in-plane isotropic behavior, the shape effect in the IDTs would induce a supplementary term that lowers the energy associated to the magnetization lying along the fingers.
As for all other Ni-based devices, the OOP magneto acoustic response is hysteretic while this perpendicular direction is not supposed to become an easy axis in the patterned system.
The differences that can still be underlined between the devices are the specific field values where the frequencies are minima and/or vary more abruptly. These are significantly smaller in this device on LNO128Y which is likely related to the lower coercivity measured in the initial full stack.

Finally, the amplitude of the SAW frequency variation is larger for QSVSAW than for RW, as it has been observed for QSHSAW compared to RW on LNO 41Y. It is however smaller than for QSHSAW on LNO 41Y-cut, in agreement with effective electromechanical coupling factor values obtained from Table 11.

4. Wireless measurements

As introduced at the beginning of this work, one main advantages of MSAW devices patterned in the resonator geometry is the possibility to envision relatively simple wireless measurements in using a single antenna connected to the single IDT' system.
Such measurements can be achieved in the frequency domain with the setup that is schematized in Figure 89.

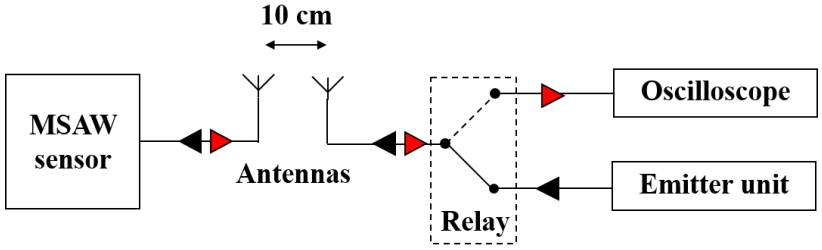

Figure 89. Sketch of the setup used for wireless measurement. Black arrows symbolize the signal traveling from the emitter unit to the device while red arrows symbolize the signal traveling from the device to the oscilloscope.

1. An emitter unit generates a RF pulse signal close to the resonance frequency of the device that is transmitted to the first antenna. This unit is composed of a generator (continuous sinusoidal signal expressed in dBm (Agilent HP8657D)), a trigger that cuts the signal into short pulses, and an operational power amplifier. The power sent in our case is 10 dBm and the frequency is 699 MHz.
2. The first antenna emits the RF pulse to the second antenna, which is connected to the device through a probe station (Signatone 1160 series probe station). Antennas are made of Copper and spaced by 10 cm. It may be necessary to adapt the device impedance to 50 Ohms with RLC components, since this is the electronic reference of the entire system. Otherwise, some additional losses can occur.
3. IDT patterned on the piezoelectric substrate receive the RF pulse which generates a SAW by inverse piezoelectric effect.
4. SAW travels on the surface and experiences a change in velocity due to the application of an external magnetic field.

5. Reflectors reflect the propagating SAW back to the IDT that convert it back to an RF signal. The expected signal is a decreasing wave that becomes zero in a certain time corresponding to the attenuation and thus losses (related to the quality factor). This signal is emitted by the antenna.
6. The back RF signal is received by the first antenna, which is also connected to an operational power amplifier and an oscilloscope (Teledyne LeCroy 760ZI) thanks to an electronic relay.
7. A Fourier transform is used to get a Gaussian signal and extract the resonance frequency from the maximum position.

A MSAW device patterned from a 50 nm thick Ni film deposited on LNO 41Y (Q//X, 6.5 µm and MR= 40%) has been addressed close to the QSHSAW resonance frequency, both with and without wires. The measured attenuation as well as the Fourier transform are presented in Figure 90 (a and b). In Figure 90 (c), the resonance frequency for an applied magnetic field perpendicular to the wave propagation direction was tracked, both with and without wires, as a function of the field intensitiy. Contrary to wired measurements using an electromagnet, wireless measurements were performed using a permanent magnet positioned at different distances from the setup.

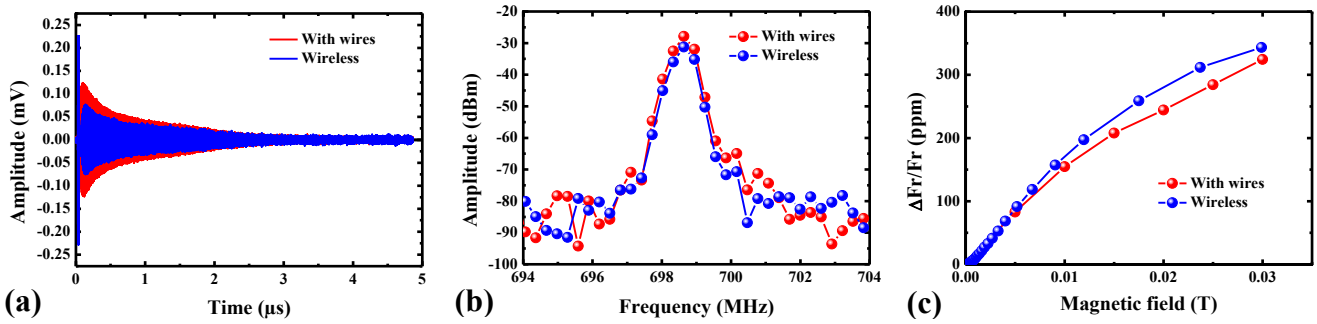

Figure 90. Measurements performed with wires (red) and in a wireless configuration (blue) for a 50 nm thick Ni-based MSAW device on LNO41Y (Q//X, 6.5 µm and MR=40%). Amplitude of the signal generated by the propagation of QSHSAW (a). Fourier transforms of these signals (b). Normalized resonance frequency variation as a function of the in-plane magnetic field applied perpendicular to the wave propagation direction (c).

The generated signals are properly obtained in both measurement geometries and exhibit an attenuation time of approximatively 5 µs. The Fourier transforms reveal clear resonance peaks at the same frequency of 699 MHz.
In Figure 90 (c), the MSAW responses show that wired and wireless measurements lead to very similar field dependences. As expected from this SAW geometry, we have thus confirmed the possibility of making wireless measurements, a promising result for possible industrial applications.

5. Summary of the 50 nm thick Nickel-based devices results

The goal of this chapter was to extensively present and analyze the variations of the resonance frequency versus magnetic field for acoustic waves traveling in 50 nm thick Ni-based MSAW devices. This has been achieved in a large variety of systems, starting from different full stacks to test several LNO cuts and playing with the geometry to explore the incidence of wave propagation direction, wavelength … The objective was also to provide a complete set of information collected if possible for several acoustic waves (RW and QSHSAW/QSVSAW) and several directions of the applied magnetic field, both in the plane and perpendicular to the plane of the devices. The results have been discussed in connection with the full stack magnetic properties and in following the formal and numerical approaches previously proposed by Zhou *et al.* [ZHO14].

Several points can be highlighted at this stage:

(i) All the investigated Ni-based MSAW devices, independently of the magnetic properties of the initial plain stack, exhibit similar magneto acoustic responses: (i) hysteretic behavior when the magnetic field is applied perpendicular to the direction of the wave propagation. (ii) Reversible behavior when the magnetic field is applied parallel to the direction of the wave propagation. Typical "w" or "double w" shapes are measured for RW and QSHSAW/QSVSAW respectively. As suggested by the simulated results, these behaviors would result from similar magnetic anisotropy in all those patterned devices, with an in-plane easy axis along the IDT's fingers (perpendicular to Q) and an in-plane hard axis perpendicular to the IDT's fingers (parallel to Q). This point is discussed in further details in the following chapter.

(ii) The formal and numerical approach permits to satisfactorily reproduce the experimental results with a good qualitative agreement between experimental and simulated shapes of the curves. This applies for both the RW and QSHSAW, provided that the in-plane easy and hard magnetization axis are assumed parallel and perpendicular to the IDT fingers respectively. This approach has confirmed the role of both static and dynamic contributions in the magneto acoustic response. The former mainly contributes in the field range where the external magnetic field drives the magnetization direction, *i.e.* for fields smaller than the saturation field. The latter contributes in a wider field range, both below and above saturation.

(iii) The reversible response of the MSAW has been checked both for in-plane fields parallel to Q (over the entire range) and for fields perpendicular to Q (in the range limited by the opening of hysteresis related to magnetization reversal). A bipolar sensor can be thus envisioned for H perpendicular to Q provided that the negative field doesn't exceed the coercivity.

(iv) The magneto acoustic responses for fields applied perpendicular to the device plane exhibit a clear hysteretic behavior for all the investigated devices. Although the numerical approach has not been adapted for this specific configuration, the first idea would be to attribute this observation to the occurrence of an hysteresis in the magnetization behavior as well. This could not be checked in the patterned devices; the original full stacks however do not exhibit such hysteresis for fields applied perpendicular to the surface and up to now, we could not find any relevant contribution that could explain a change between the plain stack and the patterned system in this direction. Complementary investigations have been undertaken to clarify this point and they are presented in the next chapter.

(v) Finally, it has been successfully verified that the resonator geometry enables an efficient wireless remote interrogation.

Chapter 4: Control of the MSAW response via tailored IDT magnetic properties

The previous chapter has shown how the MSAW response is closely related to the magnetic properties of the IDT, although some discrepancies remain to be clarified, especially concerning the role of in-plane magnetic anisotropy and the magneto acoustic response obtained for fields applied perpendicular to the device plane.
The goal of this chapter is to analyze these points in further details and to show how tailoring the IDTs' magnetic properties (in playing with either the IDTs design or the IDTs magnetic material) can help designing MSAW devices with suitable and better controlled responses.
The first part is devoted to the role of shape anisotropy that is carefully analyzed in combining Anisotropic Magneto-Resistance (AMR) measurements with magnetostatic calculations and micromagnetic simulations. The second part deals with the origin of the hysteretic MSAW response along the perpendicular to the device direction and the possible solution that can be implemented to achieve a reversible behavior in this configuration. The third part finally addresses the reversibility for fields applied along the in-plane easy axis, and especially how the field range where the device response is reversible can be extended despite the IDTs' magnetization reversal.

1. Shape anisotropy in the IDT

1.1. AMR response

Anisotropic magneto-resistance measurements [CAM70] have been performed in order to determine the magnetic properties of the fingers (or reflectors (same size)) after patterning of the plain stack.
The resistivity (ρ) of a magnetic material namely depends on the angle (φ) between the magnetization and the applied current direction with a squared sine variation:

$$\rho(\varphi) = \rho_{//} - \Delta\rho sin^2(\varphi)$$

where $\rho_{//}$ and $\rho_{\perp}$ are the electrical resistivities when the magnetization is either parallel or perpendicular to the current direction and $\Delta\rho = \rho_{//} - \rho_{\perp} > 0$.
The origin of the AMR effect lies in spin-orbit coupling, which causes an aspherical charge distribution within the ferromagnetic layer. The electron cloud around each nucleus slightly deforms as the direction of the magnetization rotates, and this deformation changes the amount of scattering cross section undergone by the conduction electrons when traveling though the lattice. The scattering cross section is higher when the magnetization is oriented parallel to the current than perpendicular. It gives a high and low resistant state respectively [MCG75].
The AMR response measured on Bragg reflectors for a 50 nm thick Ni-based device patterned on LNO Z-cut (wavelength of 6.5 µm and metallization ratio of 50%) is reported in Figure 91 when the field is applied along the direction of wave propagation (LNO X-axis, which is also the easy magnetization axis before patterning as presented in Figure 50 (a)).

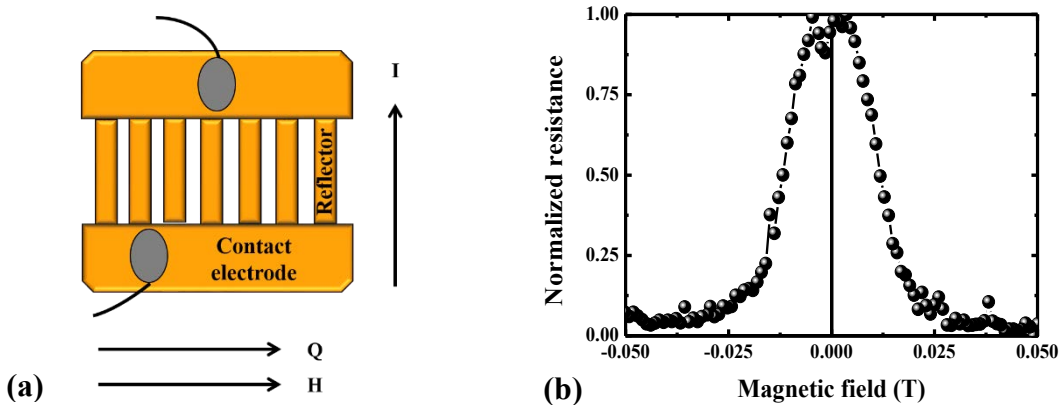

Figure 91. Sketch of the AMR measurements configuration with Q, H and I the directions of wave propagation, applied magnetic field and applied current respectively. The applied current is of few mA (a). Normalized resistance measured on the 50 nm thick Ni reflector on LNOZ, when the in-plane field is applied parallel to Q (wavelength of 6.5 µm and metallization ratio of 50%) (b).

These results show that the resistance is maximum for low fields and smoothly decreases when the field increases to reach the minimum value for field's values close to ±25 mT. This indicates that the magnetization initially lies along the current direction (*i.e.* along the finger/reflector) for small fields and progressively rotates towards the field direction (*i.e.* perpendicular to the finger/reflector), revealing a hard magnetization axis along Q with a saturation field of 25 mT.
This hard axis being perpendicular to the initial hard axis in the plain stack before patterning (see Figure 50 (a)), a supplementary anisotropy contribution associated with the shape of the IDT most likely counterbalance the initial anisotropy term measured in the thin layer. Etching the film into wires induces the reorientation of the easy axis from LNO X towards LNO X + 90° direction.
Magnetostatic calculations and micromagnetic simulations have been undertaken to confirm the role of shape anisotropy in this reorientation process.

1.2. Magnetostatic calculations

As already mentioned in the first part (chapter 2), the magnetization inside a ferromagnetic system is responsible for the appearance of magnetic charges that create a demagnetizing field. For an homogeneous magnetization ($\vec{M}$), demagnetizing field ($\overrightarrow{H_D}$) equals: $\overrightarrow{H_D} = -\bar{\bar{N}}\vec{M}$, where $\vec{M}$ is the magnetization and $\bar{\bar{N}}$ is the positive demagnetizing field tensor.

One can calculate the components of the demagnetizing field tensor, also called demagnetizing factor, in order to compare this contribution with the in-plane saturation field of the plain stack. Starting from the ideal case of a monodomain parallelepiped [HEH97], the components of the demagnetizing tensor (N_{ij}) are calculated along each direction perpendicular to the volume faces. Different aspect ratios can be easily used to reproduce real systems.
Figure 92 (a) and (b) presents the components of the demagnetizing tensor, along the three directions of the space for a finger and for a contact electrode as a function of the finger width and contact electrode length, *i.e.* parallel to the wave propagation direction, in a 6.5 µm wavelength device. N_{xx} is the component perpendicular to the finger length / parallel to the contact electrode length, N_{yy} is along the finger length / perpendicular to the contact electrode length and N_{zz} is the OOP component.

In Figure 92 (a), one can first observe that the demagnetizing factor along Z is close to 1 for large widths, leading to an in-plane magnetization. In this case, the other components are close to 0, which means no preferential in-plane directions induced by this energy term. However, when the width of the finger is reduced, the Z component decreases and the component along the width increases, *i.e.* N_{xx}. The

demagnetizing energy consequently favors the alignment of the magnetization along the length and induces an in-plane anisotropy.
For a typical Ni finger in a 6.5 µm wavelength device (Ms = 490 kA.m^{-1}, 50 nm thick, 1.625 µm wide, 250 µm long), the calculated demagnetizing field along the width is 28 mT, *i.e.* larger than the experimental in-plane saturation field measured for the Nickel film on LNO41Y for instance (9 mT, see Figure 77 (g)). The shape anisotropy thus counterbalances the initial anisotropy and can induce the observed magnetization reorientation along the finger length. One can by the way notice that this calculated value is in relatively good agreement with the experimental saturation field due to shape anisotropy and measured by AMR (Figure 91).
Concerning the contact electrode, the Figure 92 (b) shows that for a 700 µm length (6.5 µm wavelength device), the demagnetizing factor is much smaller, leading to a demagnetizing field of 0.8 mT perpendicular to the width. This contribution can thus be neglected.

For a typical Ni finger in a 13 µm wavelength device (Ms = 490 kA.m^{-1}, 50 nm thick, 3.25 µm wide, 500 µm long), the components of the demagnetizing tensor are not presented but varying only the length doesn't change significantly the results and we can reasonably estimate them from Figure 92 (a). The calculated demagnetizing field along the width is 17 mT, *i.e.* still larger than the experimental in-plane saturation field measured for the Nickel film on LNO41Y (see Figure 77 (g)).
In the previous chapter, we have shown that minimum and maximum of magneto acoustic measurement for an applied magnetic field along the direction of wave propagation decrease by a factor of 2 by changing the wavelength from 6.5 µm to 13 µm (see Figure 86). This is consistent with the results presented in Figure 92 (a).

One can finally conclude that the magnetic responses expected in the Ni fingers by taking the shape anisotropy into account are then consistent with the measured MSAW magneto acoustic responses.

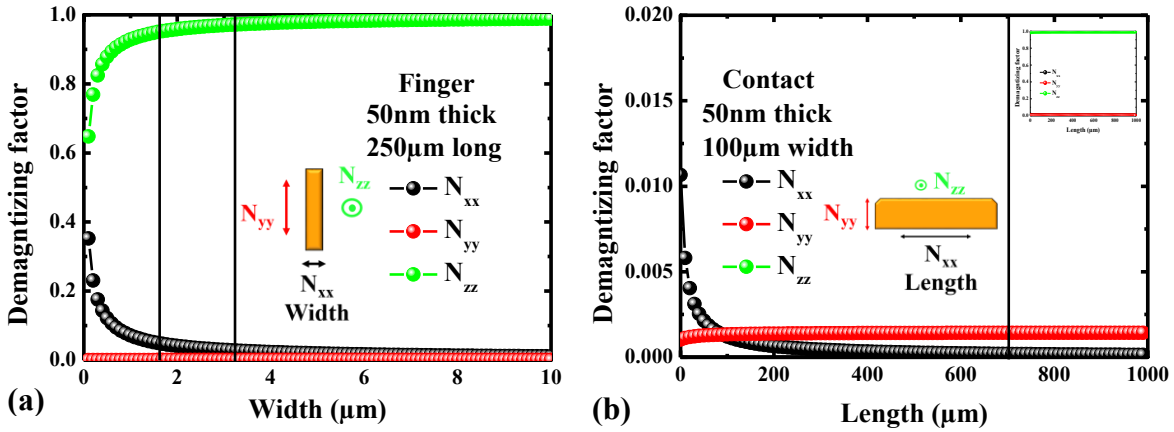

Figure 92. Components of the demagnetizing field tensor as a function of the finger width and contact electrode length for a 50 nm thick finger (a) and contact electrode (b).

1.3. Micromagnetic simulations

Micromagnetic simulations have been performed for a 10 µm long, 1 µm wide and 50 nm thick Ni finger using Object Oriented MicroMagnetic Framework (OOMMF) simulator [DON99] with cell sizes of 5 nm. Our computing power prohibits the use of real finger dimensions. However, the chosen aspect ratio is correct to compare to the experimental case. The magnetic parameters were exacted from VSM measurements and the exchange constant A is chosen at 0.9×10^{-11} J.m^{-1} [YOU12]. The simulated magnetization curve for fields applied along the direction of wave propagation, *i.e.* perpendicular to the finger length, is given in Figure 93 (a), together with the magnetic configurations corresponding to four different field values (b,c,d and e). The results are obtained in first applying a large field of 0.2 T and then decreasing the field towards 0.

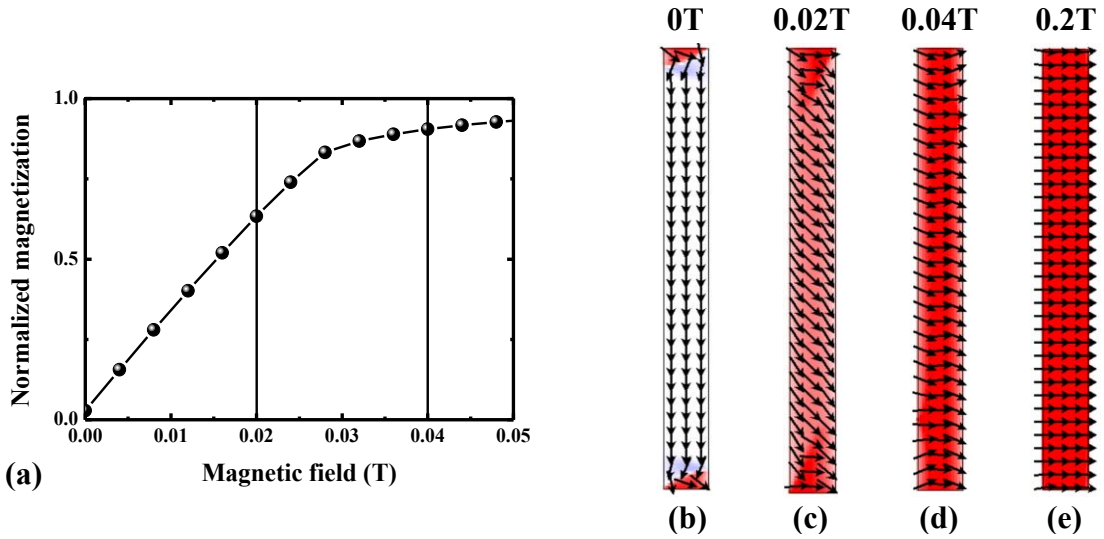

Figure 93. Normalized magnetization in a Ni finger (10µm long, 1µm wide and 50nm thick) versus magnetic field applied along the width (OOMMF simulations) (a). Micromagnetic configurations calculated using OOMMF for applied fields of 0T (b), 0.02T (c), 0.04T (d) and 0.2T (e).

The micromagnetic simulation confirms that starting from a saturated state along the field direction, the magnetization reorients towards the finger length when the field decreases. This reorientation happens mainly through magnetization rotation, but more complex magnetic domain configurations most likely occur in the real case (for example 180° domain walls). The saturation field extracted from the OOMMF simulation (28 mT) is in good agreement with the value determined from the AMR measurements or magnetostatic calculations.
Moreover, one can notice that this value is consistent with the experimental MSAW response (see Figure 77): the resonance frequency varies very little with field for fields larger than approximately 30 mT, which is expected from the equivalent piezomagnetic model above the saturation field and it is perfectly corroborates Zhou *et al.* study [ZHO14].

As confirmed by these different calculations and simulations, the shape anisotropy gives the opportunity to control the IDTs' magnetization behavior when the in-plane magnetic field is applied perpendicular to the fingers. Changing the aspect ratio of the fingers directly leads to a change in the saturation field. This is of course possible when the shape anisotropy contribution can counterbalance other sources of anisotropy (growth induced anisotropy, magnetocrystalline anisotropy…), *i.e.* when the magnetic material is a reasonably soft magnetic material.
Using a resonator geometry where the IDT fingers are patterned from the magnetic material thus provides a supplementary and interesting lever to control the MSAW behavior and thus to design a device with specific and optimized responses.

2. Hysteretic MSAW response for fields perpendicular to the device plane

The results presented in the previous chapter have highlighted a strong hysteresis of the frequency variation measured for fields applied perpendicular to the device plane, even when the magnetization curves obtained in a similar configuration for the plain stack exhibit a reversible behavior. Although the magnetic properties are likely different in the patterned IDTs, as shown in the previous paragraph, the shape anisotropy is not supposed to induce such a magnetic hysteresis for OOP fields in the IDT fingers. The first goal is thus to identify the origin of this hysteretic MSAW response.

2.1. Origin of OOP magneto acoustic hysteresis

In order to look for possible sources of magnetic hysteresis in the specific configuration where the field is applied perpendicular to the plane (OOP), vectorial VSM experiments (Figure 94) were performed on a 50 nm thick Nickel film deposited on LNO 41Y-cut (LNO41/Ta(5nm)/Ni(50nm)/Pt(5nm) plain stack). The external magnetic field is applied OOP and two components of magnetization are measured: the longitudinal component parallel to the field direction (green) and the transverse component parallel to the in-plane LNO X direction (black).
A macrospin model has also been used to calculate those magnetization components (solid lines) for magnetic parameters extracted from the experimental curves (anisotropy field, saturation magnetization, demagnetizing field). In the model, the field is applied at 5° from Z with the in-plane field projection lying at 5° from X. Similar results are obtained for -5° from Z and from X. The agreement is however no longer accurate (shape and coercive field value) if the tilt changes or becomes zero.

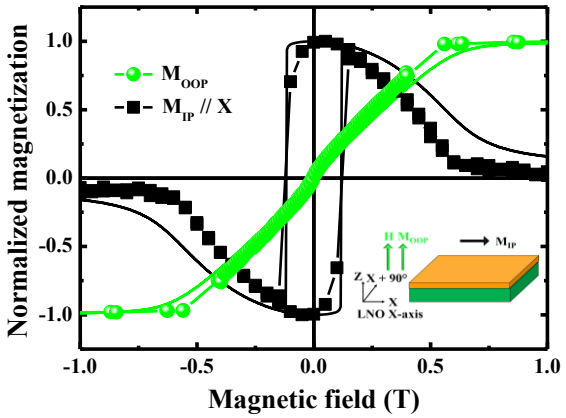

Figure 94. VSM measurements of a 50 nm thick Nickel film deposited on LNO41 with the magnetic field applied perpendicular to the plane. Both longitudinal (M_{OOP}, green dots) and transverse (M_{IP}, black squares) magnetization components are measured. The sketch presents the measurement configuration. The solid lines correspond to calculated longitudinal (green) and transverse (black) magnetization components using a macrospin model (see text).

As previously mentioned, the field variation of the OOP magnetization component (green) is consistent with the occurrence of a perpendicular hard axis. The in-plane magnetization component (black) tends naturally towards zero for large applied fields. When the OOP field decreases, the in-plane magnetization component however smoothly increases till the magnetization mainly aligns along the in-plane LNO X easy axis at zero field. The in-plane M_{IP} component eventually presents a steep reversal towards –X before decreasing back to zero when the film gets saturated along the –Z direction.
The calculation performed with the macrospin model nicely reproduces this behavior, provided that the applied field is slightly tilted respect to Z. An in-plane symmetry breaking is namely required to lower the energy of +X respect to –X and induce a non-zero net in-plane component. Such a symmetry breaking obviously also exists in the experimental case.
From these experimental and calculated curves, one can interestingly notice that the coercive field associated to the in-plane component reversal corresponds approximatively to the field where an abrupt variation of frequency is observed in the OOP configuration (Figure 77 (c and e)).
Similar results were obtained for 50 nm thick Ni-based devices deposited on LNO 128Y and LNO Z.

The hysteresis of the in-plane magnetization component thus appears to be a likely possible source of hysteresis for the OOP MSAW response. Since such an hysteresis would limit the use of this geometry to build up an OOP field sensor, a strategy has to be developed to avoid the in-plane magnetization flip. A possible option is to use magnetic materials in which the control of the in-plane magnetization can be envisioned, which is typically the case when a supplementary exchange energy contribution would bias the in-plane anisotropy and induce a first order anisotropy term.

2.2. MSAW device based on ferromagnetic/antiferromagnetic exchange biased system

A system combining ferromagnetic and antiferromagnetic materials, where the exchange field is known to induce an in-plane first order anisotropy in the ferromagnetic material, could be an interesting alternative to try forcing a smooth magnetization reversal in the perpendicular configuration. This kind of magnetic system has not been used up to now in SAW structures, neither in the delay line nor in the resonator geometry configurations.
Our choice fell on [Co/IrMn] multilayers deposited on LNO 41 Y-cut. As presented in part two (chapter five), this stack grows with a [111] texture and exhibits an in-plane exchange bias field of 33 mT along LNO X+90°.

The hysteresis loops before patterning when the in-plane field is applied along (//X+90°) (red) and perpendicular (//X) (black) to the exchange axis induced by thermal annealing are recalled in Figure 95 (a). Figure 95 (b) presents, for the OOP applied field, the longitudinal (green) and the two in-plane transverse magnetization components along X (black) and along X+90° (red). The solid lines correspond to the three magnetization components calculated using a macrospin model; the magnetic parameters (anisotropy field, saturation magnetization, demagnetizing field, exchange field) are extracted from the experimental magnetization curves.
After patterning (device with wave propagation direction along LNOX, with 6.5 µm wavelength and metallization ratio of 50 %), the output signal S_{11} is given in Figure 95 (c) and (e), where both the RW (536.5 MHz) and the QSHSAW (663 MHz) can be identified. Two resonance peaks are in fact visible for the RW, due to parasitic interferences with Bragg reflectors. It has been checked that the field variations are however identical for both peaks.
Figure 95 (d) and (f) present the magneto acoustic responses for RW and QSHSAW respectively for the magnetic field applied along three directions (X, X+90° and OOP).

The measurement of the transverse in-plane magnetization components when the field is perpendicular to the plane (red and black in Figure 95 (b)) confirms that the magnetization reversal occurs in this case smoothly, without any abrupt switch, neither for longitudinal, nor for in-plane components. The main trends are well reproduced by macrospin simulation that confirms the absence of in-plane abrupt switch for perpendicular applied field, even if a tilt of 5° from Z, whatever the in-plane field projection direction, is applied.

The RW and QSHSAW magneto acoustic responses measured in the perpendicular direction (green curves in Figure 95 (d) and (f)) reveal a smooth and reversible field dependence, and confirm that controlling the in-plane magnetization properties enables us to achieve the proposed goal, *i.e.* the suppression of the perpendicular hysteresis observed in the Ni-based devices. It was also checked that the MSAW responses are similar by tilting the applied field by 5° from Z [POL17].
In-plane magneto acoustic responses measured for both waves exhibit the same characteristics and features as those reported and described in Ni-based devices. The only noticeable difference is the shift towards positive fields of the curves measured along the easy magnetization axis (red), in perfect agreement with magnetization measurements and with the effect of the exchange bias field. One can also underline that in this case where the initial easy axis lies along X+90°, the shape anisotropy induced in patterning the fingers along this same direction (Q//X) doesn't compete but reinforce the in-plane anisotropy.
Complementary measurements have been performed to check the reversibility of the RW and QSHSAW magnetoacoustic response for these [Co/IrMn]-based devices. As in the case of 50 nm thick Nickel-based devices, the MSAW responses are perfectly reversible when measuring minor loops along the easy magnetization axis, provided that the applied field doesn't exceed the magnetic coercivity.

One can finally notice that all MSAW responses in [Co/IrMn]-based device exhibit lower amplitude than in Ni-based devices. The magnetostriction at saturation value in polycrystalline Co is approximatively the same as in Ni (approximatively -30×10^{-6} at RT) [SAN99] but no data could be found for IrMn, whatever its stoichiometry. Several reasons could be thus invoked at this stage: (i) the possibly low magnetostriction of IrMn but specific measurements are needed to affirm this point, (ii)

the possibly interface roughness and (iii) the acoustic impedance mismatch occurring at the interfaces (at surface discontinuities between two materials, acoustic impedance changes and thus, one part of the wave is reflected, and the other one is transmitted [CAM98]).

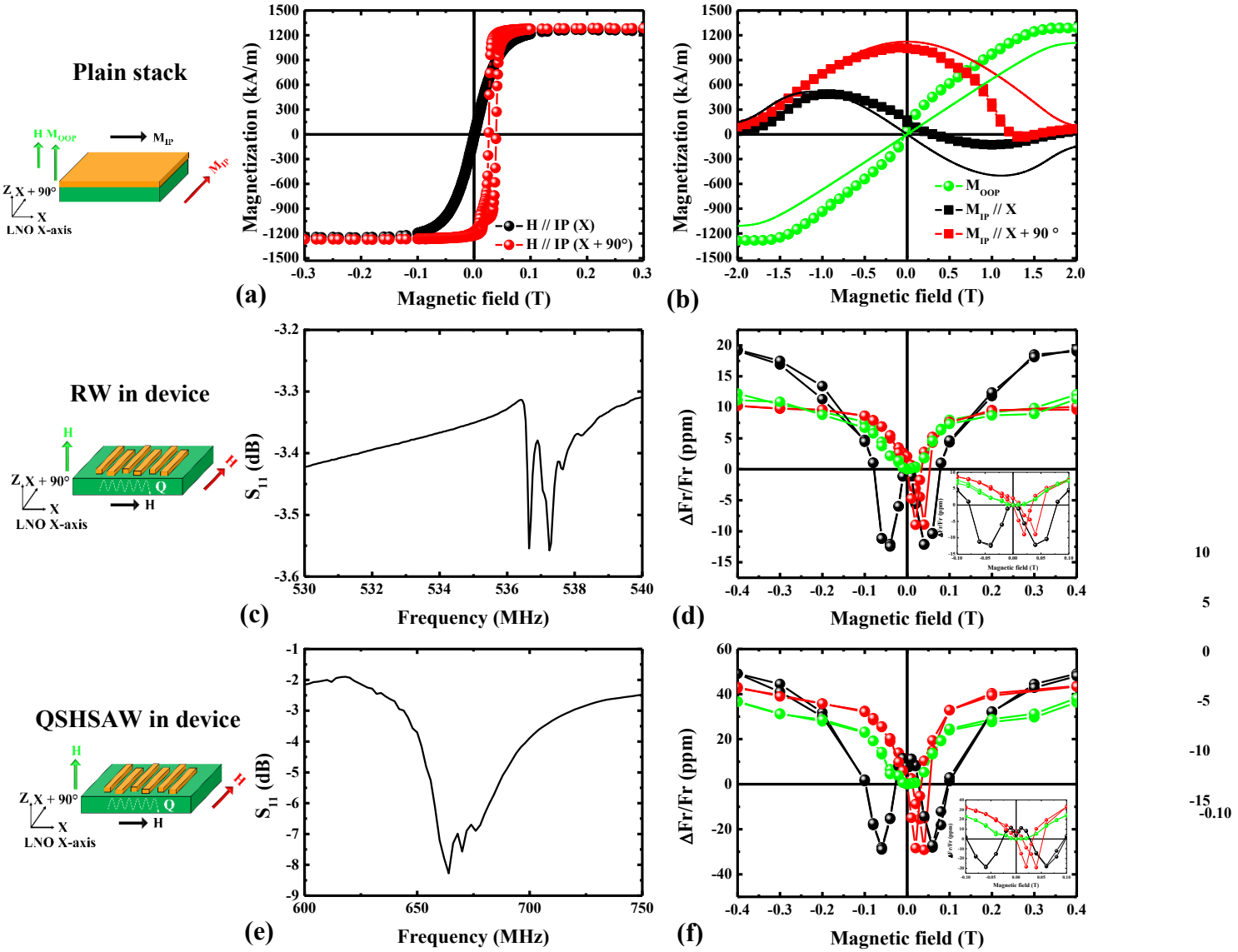

Figure 95. Hysteresis loops measured for the LNO41/Ta(5nm)/[Co(5nm)/$Ir_{0.2}Mn_{0.8}$(5nm)]$_{15}$/Pt(5nm) plain stack and for magnetic fields applied along LNO X (black) and LNO X+90° (red) (a) and perpendicular to the plane (green) (b). Black and red squares in (b) correspond to transverse in-plane components along LNO X and LNO X+90°, while the continuous lines are the result of a macrospin simulation (see text). S_{11} signal versus frequency for the corresponding patterned device (Q//X, 6.5µm wavelength and MR=50%) (c and e). Field dependence of the resonance frequencies for RW and QSHSAW for the different directions of magnetic field (d and f).

3. $TbFe_2$-based devices

Epitaxial $TbFe_2$-based devices are new in the field of MSAW. As explained previously, one aim is to increase the amplitude of the magneto acoustic responses through the strong room temperature magnetostriction of this compound. Another goal consists in using the high coercive field to obtain a reversible response over a wide range of magnetic fields. Finally, we also want to check the low impact of the shape anisotropy versus the strong magnetocrystalline anisotropy of this materials. We expect no reorientation of magnetization in the patterned devices, and thus reversed in-plane magneto acoustic responses for orthogonal directions of wave propagation.

In order to address these points, two devices with different directions of wave propagation (LNO X and LNO X+90°) have been patterned from the same initial full stack : LNO 41Y/Mo(20nm)/$TbFe_2$(50nm)/Au(5nm) (part two, chapter four). Both devices have a wavelength of 6.5 µm and a metallization ratio of 50 %.
$TbFe_2$-based devices on LNO Z (LNOZ/Ti(20nm)/Mo(20nm)/$TbFe_2$(50nm)/Au(5nm)) and LNO 128Y (LNO128/Mo(15nm)/$TbFe_2$(50nm)/Au(5nm)) are not reported here since they lead to similar results.
The output signals S_{11} measured for the devices on LNO 41Y (Figure 96 for Q // X (black) and Q // X + 90° (grey)) both exhibit a resonance close to 550-560 MHz attributed to the propagation of RW. As in Ni-based devices, the RW resonance peak for the device with Q // X + 90° appears at higher frequency.

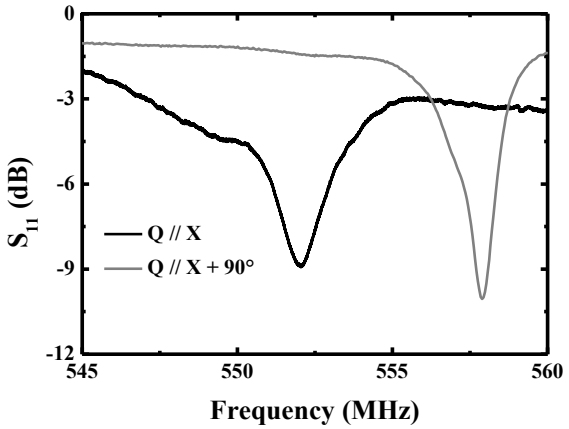

Figure 96. S_{11} signal versus frequency for $TbFe_2$-based devices on LNO 41Y (6.5 µm and MR = 50 %) with wave propagation directions along X (black) and X+90° (grey).

3.1. Field dependence of the SAW frequency

The resonance frequency variations versus field are presented for both devices, *i.e.* both directions of wave propagation in Figure 97 (c, d, e and f). As for magnetization measurements performed on the initial full stack (recalled in Figure 97 (a and b)), the field is applied along in-plane X and X+90° directions and along the perpendicular to the plane.

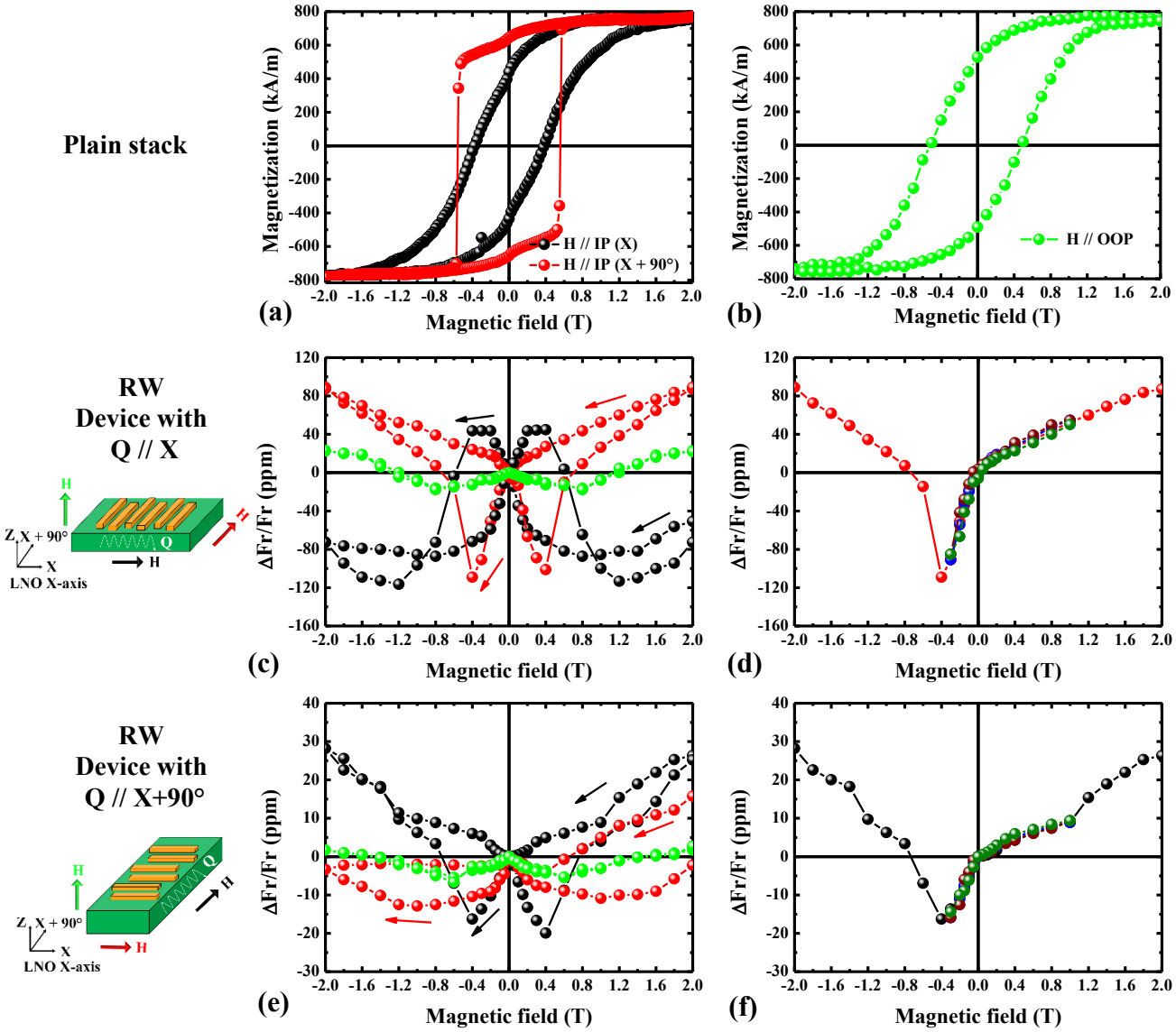

Figure 97. Hysteresis loops for a 50 nm thick $TbFe_2$ film deposited on LNO41Y (LNO41/Mo(20nm)/$TbFe_2$(50nm)/Au(5nm)) when the magnetic field is applied in-plane along LNO X (black) and LNO X + 90° (red), and perpendicular to the plane (green) (a and b). Normalized resonance frequency variation of RW versus field for two corresponding patterned devices (wavelength of 6.5 µm and MR=50%) with Q//X (c and d) and Q//X+90° (e and f). The magnetic field is applied in-plane along Q (black) and Q+90° (red), and perpendicular to the plane (green). On (c and e), black and red arrows represent the magneto acoustic responses sense obtained from positive to negative saturation field. Measurements in (d and f) correspond to successive minor loops performed in the [-0.3 – 1 T] field range for H//Q+90°.

Several points can be underlined from these results:
(i) Concerning the magneto acoustic responses obtained when the magnetic field is applied in the device plane (black and red curves), one can first notice that they are both hysteretic. This is different from the Ni-based devices presented previously (Figure 77), but consistent with the magnetization curves measured on the plain stack where opened hysteretic loops are observed both for the easier (X+90°) and harder (X) axis.
(ii) A second point to be noticed is now the predominant contribution of intrinsic anisotropy compared to the shape anisotropy associated to the fingers' geometry. While similar reversible (resp. hysteretic) curves are obtained for H//Q (resp. H//Q+90°) whatever the Q direction respect to LNO in Ni-based devices, in the present case, different shapes are observed for H//Q//X and H//Q//X+90° (black curves in Figure 97 (c) and (e)). The responses are however similar when the field is applied along X+90° (red

curve in Figure 97 (c) and black curve in Figure 97 (e)), independently of the Q direction. This simply reveals that the magnetic anisotropy with respect to the LNO substrate is similar in both devices, *i.e.* that the shape anisotropy in this case is not strong enough to counterbalance the intrinsic anisotropy, much larger in this intermetallic compound than in Ni. The shape of magneto acoustic responses measured for fields along the easy magnetization axis of the plain stack (X+90°) are by the way similar to those obtained in Ni-based devices for fields applied along the easy magnetization axis of the IDT fingers (along the fingers).
One can also underline that the SAW response is reversible during the measurements of successive minor field loops for an applied field along the EA (//X+90°) (Figure 97 (d and f)), as far as the magnetic field is reversed before the abrupt variation of resonance frequency. Despite an irreversible behavior, the increased coercive field compared with Ni-based devices leads to a significant extension of the magnetic field range where a bipolar response can be obtained.
(iii) The magneto acoustic responses obtained along the in-plane harder magnetization axis (black curve in Figure 97 (c) and red curve in Figure 97 (e)) present variations that cannot be easily linked to the field variations of elastic constants, as calculated in the equivalent piezomagnetic model.
(iv) For fields applied perpendicular to the device plane (green curves), the magneto acoustic responses are surprisingly perfectly reversible despite the hysteretic magnetization curve obtained in this configuration.
Complementary simulations and experiments have definitely to be undertaken for these devices in order to unravel to influence of the in-plane magnetic hysteresis along the harder axis and to explore the magnetization reversal process (longitudinal and transverse magnetization components) in the perpendicular configuration.
(v) A last important remark is the disappointing low amplitude of frequency variation achieved in these devices based on a crystalline highly magnetostrictive compound, whatever the direction of wave propagation. The largest amplitude of frequency variation is approximatively 200 ppm (similar to Ni-based devices), which is lower than what we could expect, since the magnetostriction at saturation increases from -33×10^{-6} in polycristalline Ni to 1753×10^{-6} in $TbFe_2$ [CLA80]. A maximum amplitude of frequency variation of approximatively 2000 ppm was by the way measured with amorphous $TbFe_2$ [YAM80] that presents a magnetostriction at saturation of 600×10^{-6} [CLA80].
This point is specifically discussed in the following paragraph.

3.2. Possible origins for the limited reponse in epitaxial devices

Different reasons could be invoked to try to explain the low amplitude of frequency variation achieved in these systems:
(i) *The poor crystal order of the $TbFe_2$ films* deposited on the LNO substrates. As explained in second part (chapter four), the deposition of $TbFe_2$ on LNO41Y and LNO128Y substrates lead to multidomains structures. The $TbFe_2$ order on LNO Z-cut is more satisfactory with the occurrence of only two variants around a common [111] growth direction, but doesn't provide a larger amplitude of frequency variation under applied magnetic field. The crystalline order and structure should thus not be the main reason to this low amplitude of frequency variation.
(ii) *The presence of single or multiple buffer layers*. The buffer layers required to enable the crystalline growth of the compound can reduce the amplitude of frequency variation in different ways: acoustic impedance mismatch, interdiffusion at high temperature during deposition, increase of the roughness at the interfaces and variation of the effective electromechanical coupling factor. On this latter point, the difference of K_{eff}^2 values observed in Table 11 between for instance 50 nm thick Ni-based devices and $TbFe_2$-based devices is not significant. However, the variation of K_{eff}^2 as a function of the applied field could be different due to the presence of buffer layers. Several simulations and experimental measurements are currently in progress to unravel this point.
(iii) *The poor quality of the LNO/buffer interface*. Due to the high temperature required to enable the crystalline growth of the compound, the LNO surface experiences a significant degradation, as shown in Figure 19, that can maybe influence the elastic coupling.

4. Summary of MSAW with tailored IDT magnetic properties results

The goal of this chapter was to address specific issues of the physics in MSAW devices, in particular the role of shape anisotropy, the link between reversible/irreversible behaviors in the magnetic and magneto acoustic systems, and to show how the device properties could be tailored in playing with materials and geometry.

Calculations and micromagnetic simulations have definitely proven that the shape anisotropy can become predominant in the resonator geometry when a soft magnetic material is used for the IDTs. This contribution to magnetic anisotropy permits to explain our experimental results in Ni-based devices, in agreement with previous results reported on similar systems. Shape anisotropy can thus be used as an interesting supplementary lever to control the IDTs magnetization and consequently to control the MSAW response. The use of a much harder magnetic material such as $TbFe_2$ on the contrary underlines the role of intrinsic anisotropy that in this case governs the magneto acoustic behavior.

The reversibility under magnetic field, an important point for sensors applications, appears to depend both on the magnetization reversal process and on the measurement configuration. For in-plane applied fields, the different investigated systems show that irreversibility in the magneto acoustic response are directly linked to irreversibility in the IDT's magnetization reversal. Reversible magnetization variations consequently lead to reversible frequency variations. This can be the case for fields applied along the magnetic hard axis but also along the easy axis when measuring minor loops in a field range avoiding coercivity. Working with hard magnetic materials such as $TbFe_2$ is then a good way to increase the coercivity and thus to extend the field range of reversible magneto acoustic response where sensor applications could be envisioned.

For perpendicularly applied fields, the different investigated systems show that the situation is more complex. Irreversible MSAW response can be observed while magnetization reversal is reversible (Ni-based devices) and reversible MSAW response can be observed while magnetization reversal is hysteretic ($TbFe_2$-based devices). The detailed magnetization reversal process obviously matters, especially the possible occurrence of irreversibility in the in-plane (transverse) magnetization components' reversal. Controlling those in-plane components in an exchange-biased magnetic multilayer permits to suppress the source of irreversibility and to achieve a reversible MSAW response in the perpendicular configuration. The recent observation of a reversible OOP MSAW response in $TbFe_2$-based systems with a strong magnetic hysteresis in a similar configuration is however puzzling at this stage. Complementary experiments and simulation are now highly required to unravel the intricate link between magnetization and magneto acoustic irreversibilities in this OOP geometry.

If the use of crystalline $TbFe_2$ as IDTs unambiguously enables a gain in coercivity, it remains very disappointing when considering the sensitivity of the SAW characteristics to an external magnetic field. The specific conditions of the $TbFe_2$ crystalline growth on LNO substrates (high temperature, presence of buffer layer(s)) most likely contribute to the reduction of the elastic coupling and thus to the low field sensitivity of the devices. The development of other growth conditions would thus be required to try to increase the response of the devices, but this constitutes a challenging task and could not be undertaken during this work.

Chapter 5: Non-conventional geometries in MSAW devices

This chapter reports magnetic responses of MSAW devices in non-conventional geometries. In a first part, we present the MSAW response of a Nickel-based device where the Ni thickness is such that the magnetic IDT host magnetic stripe domains with magnetization perpendicular to the acoustic wave propagation plane. In a second part, we report a magnetic response associated to a bulk acoustic wave which appears to be independent on the applied field direction.

1. 200 nm thick Nickel-based devices

As reported in the second part of this manuscript, 200 nm thick Nickel layers deposited on LNO 41Y or LNO 128Y-cuts exhibit perpendicular to the plane magnetization. The hysteresis loop measured with the field applied perpendicular to film plane (Figure 50 (f and i)) is consistent with a layer hosting magnetic stripe domains (see appendix F).

1.1. Stripe domains in the IDT

While the hysteresis loop gives a hint to extrapolate the existence of stripe domains, a direct measurement of the stripe domains state in the IDT after technological process is mandatory. Therefore, an Atomic Force Microscopy – Magnetic Force Microscopy (AFM-MFM) study was carried out. Figure 98 (a) provides the AFM image of the surface of fingers made from a 200 nm thick Nickel layer deposited on LNO 41Y with a wavelength of 6.5 µm and a metallization ratio of 50 %. A cross section along the red double arrows is also given in Figure 98 (b). The measurement of the MFM contrast is reported in Figure 98 (c) which shows the phase contrast for zero applied field after an in-plane saturating magnetic field has been applied along the finger's width (horizontal direction). A cross section along the red double arrows is given in Figure 98 (d).

As observed in the cross section of the AFM image (Figure 98 (b)), "rabbit ears" appear after the etching process to define the IDT's fingers. For a nominal lateral extension of 1.625 µm and a thickness of 200 nm, the finger has a lateral size of approximately 1.70 µm (by taking rabbit ears into account), a thickness of approximatively 200 nm and the rabbit ears are 60 nm height for a few nm width. These most likely form during the Ar dry etching, since atoms sputtered from the surface are redeposited on the side of the resist that protects the part of the Nickel layer to be transformed in the IDT. After dissolution of the resist, the redeposited material persists and gives rise to these thick edges. Since the redeposited atoms are magnetic, the ears should present some magnetic contrast and make the MFM observation more difficult.

In a first approximation, the MFM signal is a measurement of the second derivative of the stray field along the direction perpendicular to film plane. While this contrast is mainly located close to areas where magnetization is strongly inhomogeneous (domain wall for example), in the case of a domain structure with perpendicular to film plane magnetization with domain size of the order of 100 nm, *i.e.* small, the contrast is centered on the domains [HEH97]. As a result, the MFM profile of Figure 98 (d) confirms the presence of magnetic domains with alternately up and down magnetic state since the period of the magnetic stripes is approximatively 300 nm. This magnetic state for zero applied field has been stabilized after applying an in-plane field, along the IDT's width. As previously observed in other materials, this field history leads to the appearance of a mixture of bubbles and stripes mainly oriented

along the applied field direction [HEH97]. The resulting configuration is here even more complex because of the reduced lateral width of the IDT and the presence of the rabbit ears. The MFM contrast in the rabbit ears is very difficult to understand. As these edges' thickness is larger than the thickness of the Nickel layer, we will admit that in this region, the magnetization is perpendicular. Since the period of the magnetic stripes varies as a square-root of film thickness [HEH97], the period should be around 340 nm in those regions. The rabbit ears, which measure approximatively few nm width (see Figure 98 (b)), should be magnetically saturated.

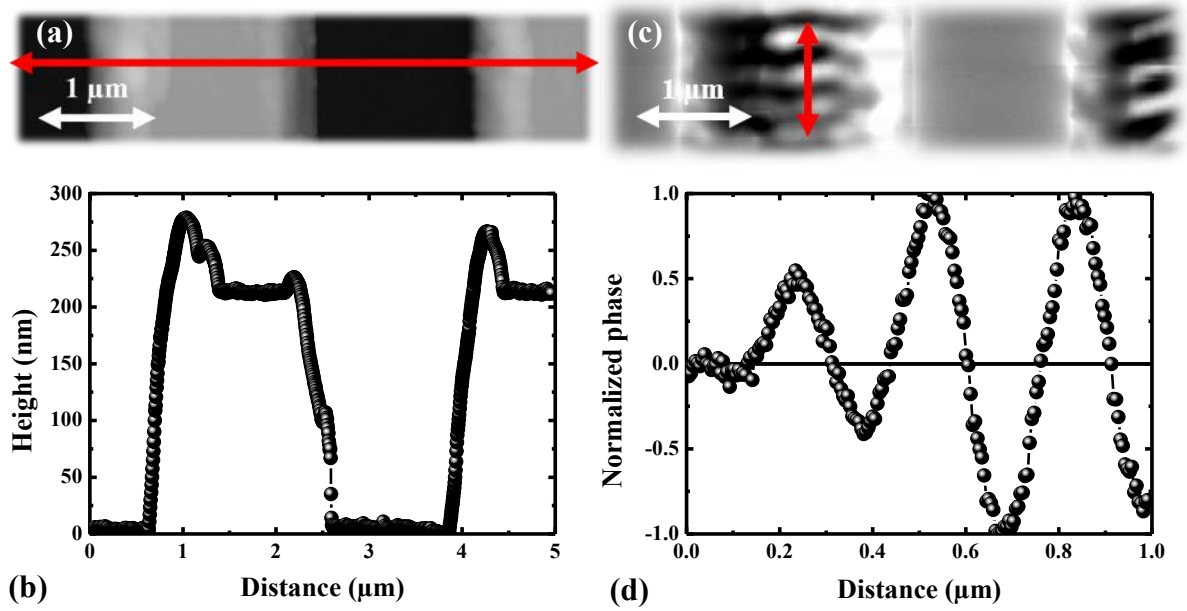

Figure 98. AFM image of fingers made of 200 nm thick Nickel film (on LNO 41Y) with a wavelength of 6.5 µm and a metallization ratio of 50 % (a). Associated cross section along the finger width (along the red double arrows in (a)) (b). MFM image for the same fingers and for zero applied field after an in-plane saturating magnetic field has been applied along the finger's width (c). Associated cross section (along the red double arrows in (c)) of the stripe domains structure to determine the period of the domains (d).

1.2. Field dependence of the RW frequency

The output S_{11} signal presented in Figure 99 was obtained for a device with Q // LNO X-axis, with a wavelength of 6.5 µm and a metallization ratio of 50 %. The resonance peak corresponds to a Rayleigh wave.

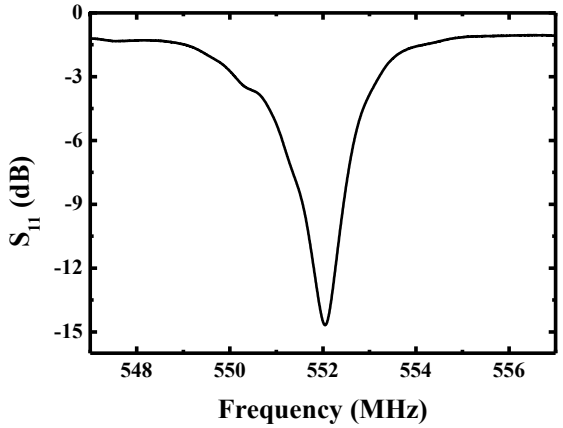

Figure 99. S_{11} signal versus frequency for a 200 nm thick Nickel-based device deposited on LNO 41 Y (wavelength of 6.5 µm and metallization ratio of 50 %). The direction of wave propagation is along LNO X-axis.

The RW frequency variations versus field are presented in Figure 100 (c and d). As for the magnetization measurements performed on the initial plain stack (recalled in Figure 100 (a and b)), the field is applied along in-plane X (black) and X+90° (red) directions and along the perpendicular to the plane (green).

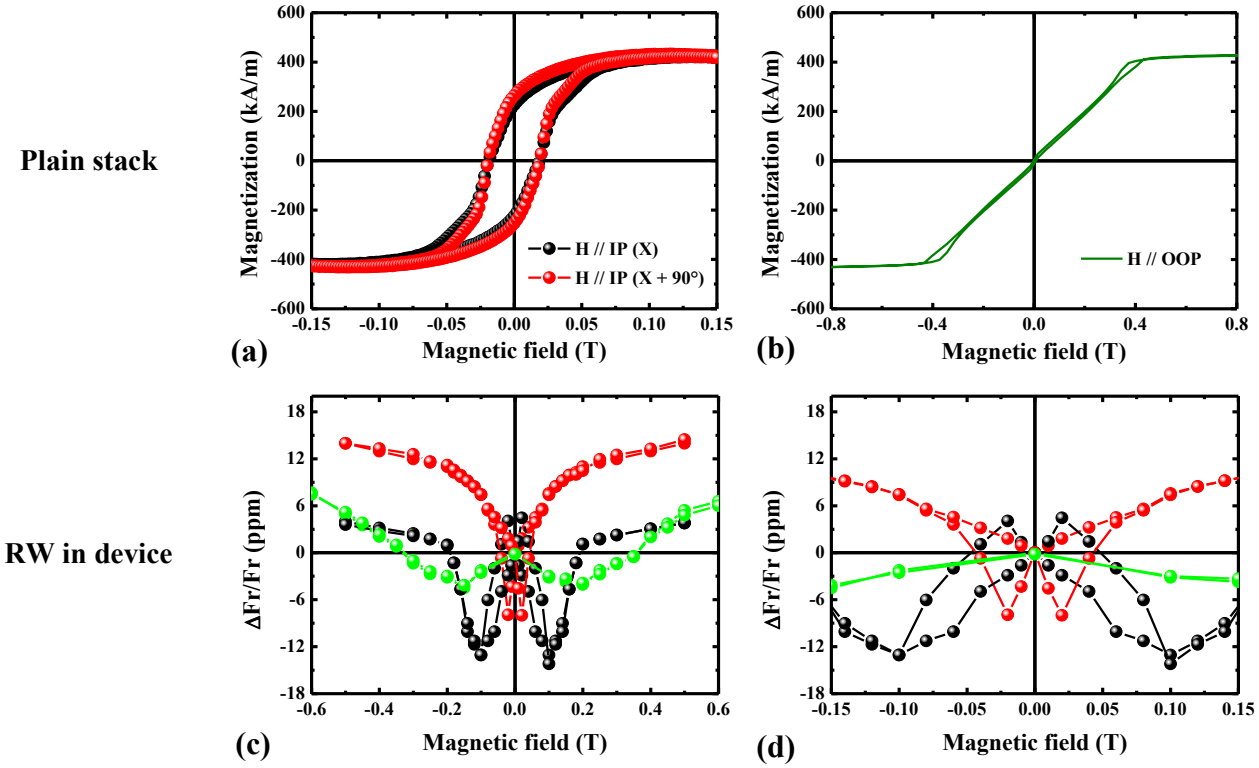

Figure 100. Hysteresis loops measured for LNO41Y/Ta(5nm)/Ni(200nm)/Pt(5nm) plain stack with the magnetic field applied in-plane, along LNO X (black) and LNO X + 90° (red) and OOP (green) (a and b). Variation of the RW frequency for the patterned device (Q//LNO X, 6.5 µm wavelength and MR= 50%) (c and d).

The reversal of the in-plane magnetization occurs at a field smaller than 0.05 T. As for the 50 nm thick Nickel patterned device, this reversal is likely modified by the shape of the IDT. On the contrary, the stripe domains structure is conserved after patterning and the hysteretic magnetization curve for an applied field perpendicular to the plane should be mainly conserved.
Whatever the direction of the in-plane applied magnetic field, the MSAW responses of the RW are very close to those of the 50 nm thick Ni-based device.
Along the IDT (red curve in Figure 100 (c)), the response is typical of the behavior expected along an EA with the occurrence of both dynamical effects and the hysteresis due to the reversal of the magnetization related to the shape of the fingers. The response can be understood by the micromagnetic configurations (thin black arrows) reported in Figure 101 (a), expected for a stripe domains structure that evolves in a nanostructure. When the in-plane field is perpendicular to the IDT (black curve in Figure 100 (c)), the response exhibits a "w" shape typical of the behavior expected along an HA and related to the C'_{11} elastic constant variation. In contrast to the 50 nm thick Nickel-based device, an hysteresis is observed, probably linked to the reversal of the expected inhomogeneous component of in-plane magnetization (thin black arrows in Figure 101 (b)). Close to the edges, and with some extension in the core of the IDT, the magnetization reorients parallel to the IDT length when the field is progressively brought from saturation to zero.

While the OOP magneto acoustic response is highly hysteretic for the 50 nm thick Nickel-based device (hysteretic reversal of the in-plane magnetization components), the response is reversible in the case of the 200 nm thick Nickel-based device, with a "w" shape generally encountered when the field is applied

along an in-plane HA. The reason is unknown and further investigations are needed to explain this shape. The OOP MSAW response moreover does not seem to saturate in the investigated field range.
In the current version of the piezomagnetic equivalent model, the component of magnetization perpendicular to film plane is not taken into account and the magnetic response with the field applied perpendicular to film plane cannot be calculated. Nevertheless, with our understanding of the 50 nm thick Nickel MSAW responses, a possible scenario can be proposed to account for the reversible OOP MSAW response in this 200 nm thick Nickel-based device (Figure 101 (c)). At saturation, the magnetization is fully aligned along the perpendicular direction. When the applied field decreases, the IDT hosts magnetic stripes or bubbles, a domains structure with up and down magnetization. At zero applied field, the sizes of up and down domains are equal and no remanence is expected. Up and down domains are separated by Bloch walls that have an in-plane component. In contrast to the cases in Figure 101 (a and b), the wall contributions are distributed in all the in-plane directions since the in-plane symmetry is not broken. As a result, an isotropic distribution of in-plane magnetization is expected and neither an easy axis nor an hard axis response is expected.

Finaly, it must be noticed that the amplitudes of all MSAW responses are smaller than those obtained with 50 nm thick Nickel-based devices, as expected from the decrease of the electromechanical coupling factor when the thickness increases [CAM98].

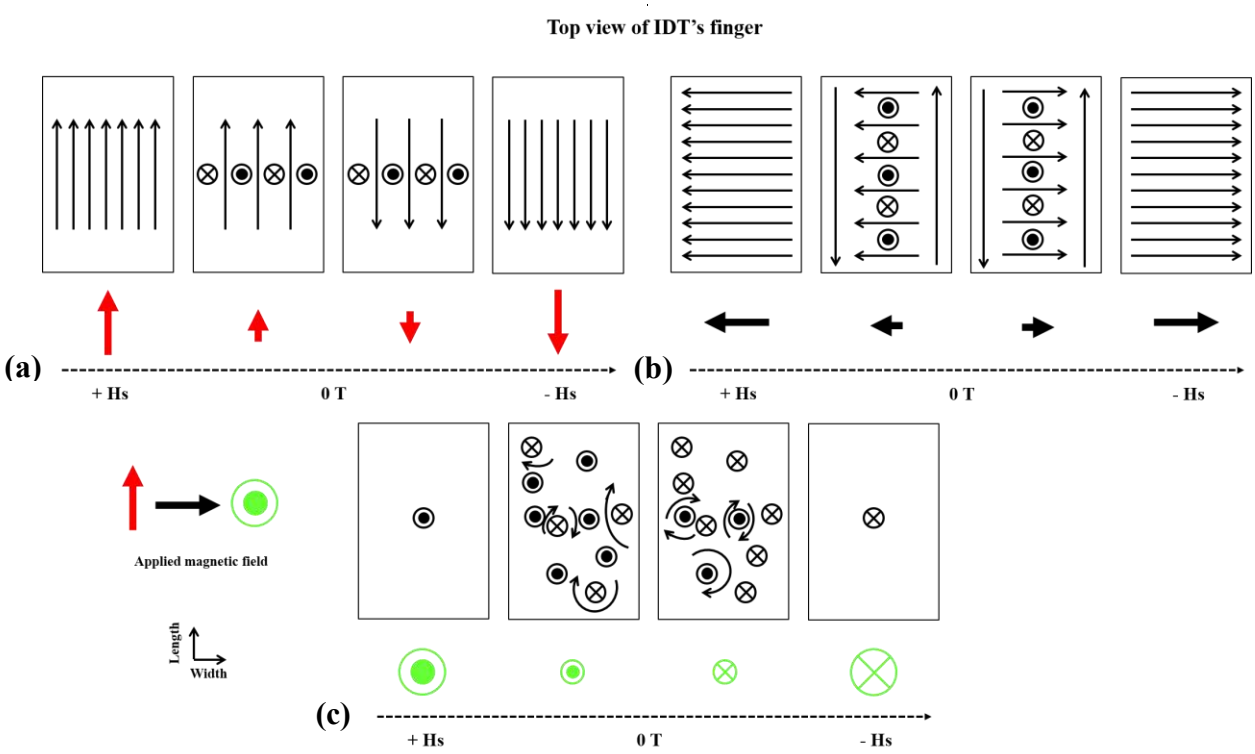

Figure 101. Sketch of the expected magnetic configurations as a function of the in-plane applied field along the IDT (a), perpendicular to the IDT (b) and of the field applied perpendicular to the IDT plane (c). Black and red arrows and green circles represents the direction of applied field. The size of circles and arrows are related to the field intensity. Black thin arrows represent the magnetization in the IDT finger.

2. MSAW devices towards Magnetic Bulk Acoustic Wave (MBAW) devices

The S_{11} signals have been reported up to now for frequencies between 100 MHz and 1 GHz. However, another resonance peak appears for frequencies close and above 1 GHz, for all 6.5 µm wavelength resonator devices.

For a LNO Z-cut with a wave propagation direction along X, the velocity expected for longitudinal bulk acoustic wave is 6470 m.s^{-1} ($v_L = \sqrt{C_{11}/\rho}$ with ρ = 4.85 g.cm^{-3} and $C_{11} = 203\ GPa$ for LNO), which corresponds to a resonance frequency at 995 MHz for a SAW device with 6.5 µm wavelength. This result lead us to investigate the motion fields of this wave to confirm the presence of a longitudinal bulk acoustic wave.

2.1. Motion fields of acoustic waves

For a given piezoelectric material and a given crystal cut, the motion fields of acoustic waves can be simulated by the use of the Comsol multiphysics software. We consider the case of IDT made from a 50 nm thick Nickel film deposited on LNO 41Y (Q//X+90°, wavelength of 6.5 µm and metallization ratio of 50 %). The width of the simulated substrate corresponds to half of the wavelength, which means that only one finger is required for the simulation.
The in-plane parallel to Q and perpendicular to the surface components of the motion fields are reported for a resonance frequency close to 560 MHz (Figure 102 (a and c)) and near 1 GHz (Figure 102 (b and d)).

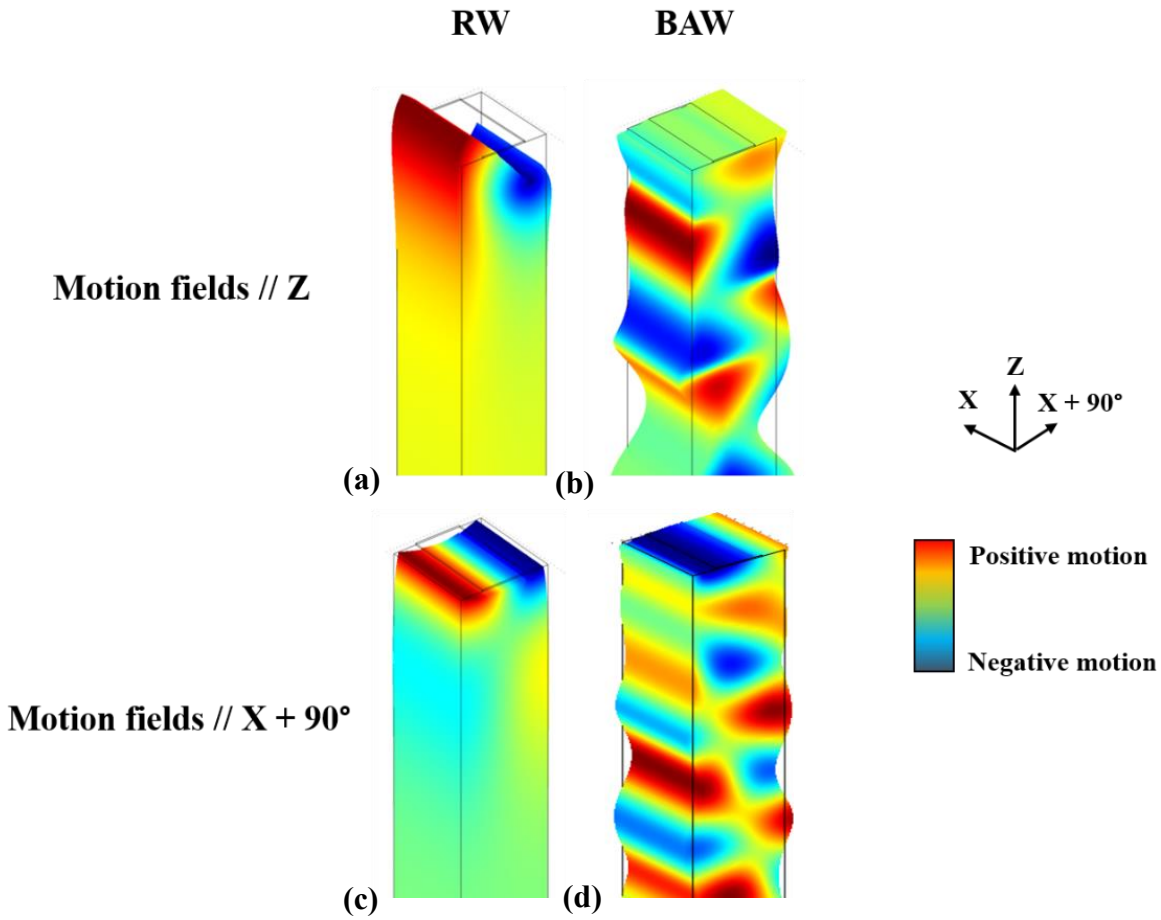

Figure 102. Perpendicular to the surface (a and b) and in-plane parallel to the wave propagation direction (c and d) components of the motion fields of a RW and BAW in a LNO41Y/Ni(50nm) MSAW device (Q//LNO X+90°, wavelength of 6.5 µm and MR of 50 %).

Motion fields at 560 MHz (Figure 102 (a and c)), exhibit longitudinal and vertical components that give rise to an elliptical polarization. This acoustic wave is attributed to a Rayleigh wave. Motion fields close to 1 GHz (Figure 102 (b and d)), are more complex. The penetration depth is much larger at this frequency, confirming the development of a BAW with a mix of vertical and longitudinal components.

2.2. Field dependence of the BAW frequency for different MSAW devices

The following results are obtained for two devices patterned from a 50 nm and a 200 nm thick Nickel film, both deposited on LNO 41Y (6.5 µm, MR of 50% and Q // X+ 90°). Figure 103 (a) shows the S_{11} signals and Figure 103 (b and c) show the relative variation of bulk acoustic wave frequency as a function of the magnetic field applied along different directions. Only downsweeps in field are shown here because the behaviors are perfectly reversible.

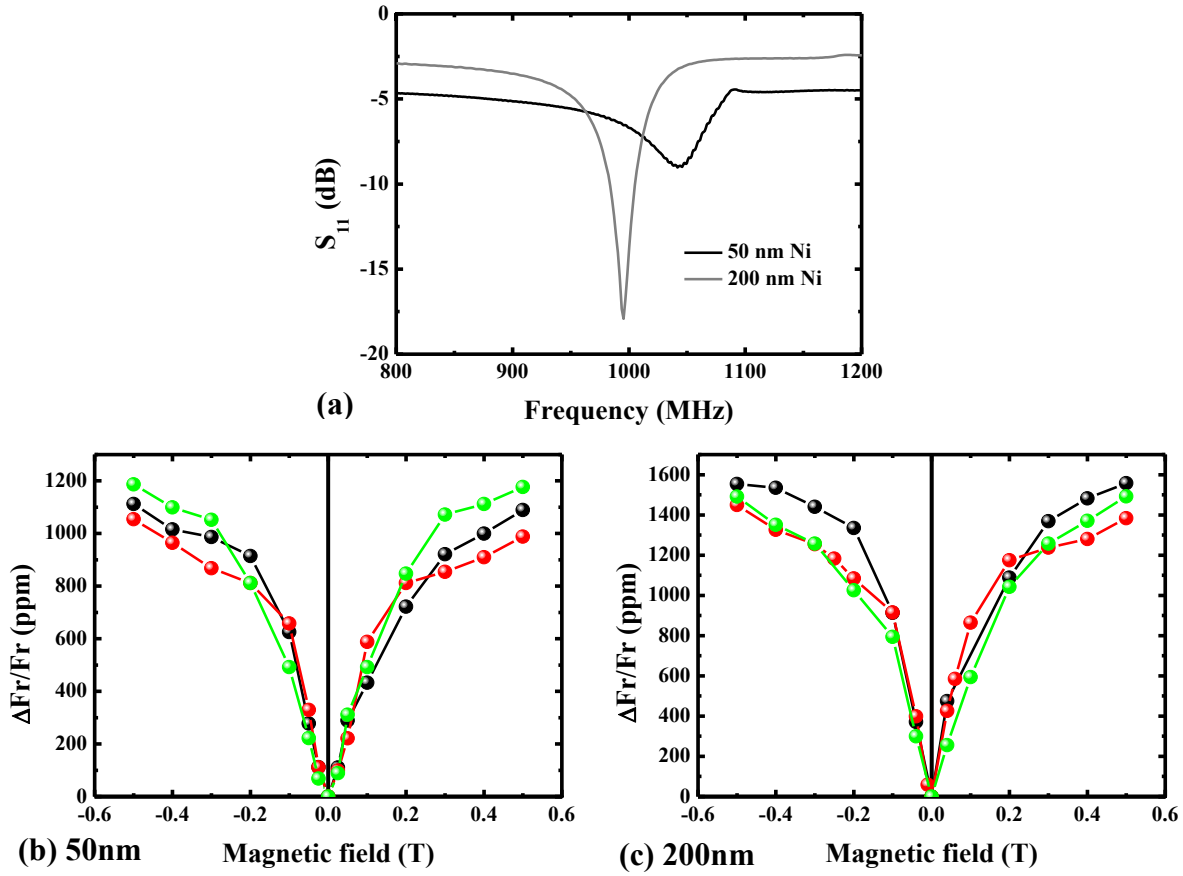

Figure 103. S_{11} signal versus frequency for 50 nm and 200 nm thick Ni-based devices deposited on LNO 41Y (a). Variation of the BAW frequency versus field applied along different directions (in-plane along LNO X + 90° (black) and LNO X (red) and OOP (green)) for the 50 nm thick (b) and 200 nm thick (c) Ni-based devices (6.5 µm wavelength, metallization ratio of 50 % and Q//LNOX+90°).

As discussed from Table 11, the resonance frequency decreases when increasing the Ni IDT thickness. The differences observed in the S_{11} output signal shape and amplitude are not discussed and explored in further details since they are extremely dependent on the device.
In contrast to the results reported up to now in this work, the magneto acoustic responses in this case do not depend on the direction of the applied magnetic field and exhibit a huge frequency variation. No sign of magnetic hysteresis are observed, neither for the in-plane (black and red curves) nor for the out of plane (green curves) magneto acoustic response. It should be noted that similar results are observed for other LNO substrates and for other magnetic materials ([Co/IrMn] or $TbFe_2$). Since all devices present the same isotropic MSAW responses, the sensitivity to the applied magnetic field should not arise from the magnetic layers.

2.3. Field dependence of the acoustic wave frequency for a non-magnetic device

A device was specifically patterned with the same resonator geometry but from a 50 nm thick Aluminum layer deposited on LNO 41Y. An RF-sputtering process was performed at a pressure of 2×10^{-3} Torr and a power of 250 W (on a 4 inch Al target). The deposition is carried out in rotation at a rate of 0.04 $nm.s^{-1}$. Neither a capping nor a buffer layer were used. After optical lithography, the shape defined in the resist was transferred in the Al layer by chemical etching using a bath of phosphoric and nitric acids during two minutes. After etching, the protecting resist was removed by standard cleaning procedure.

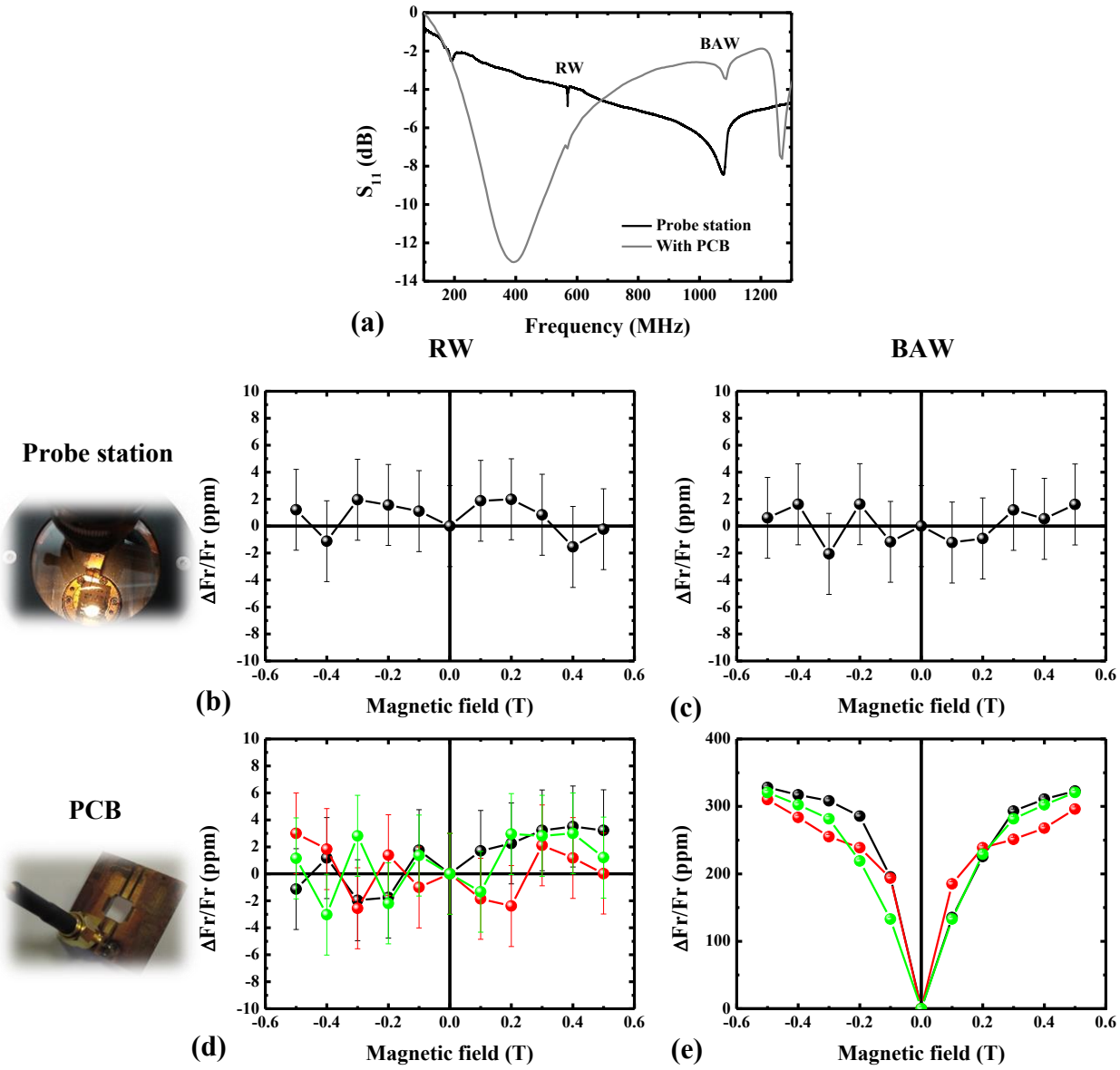

Figure 104. S_{11} signals versus frequency for a 50 nm thick Al-based device deposited on LNO 41Y (Q//LNOX+90°, 6.5 µm wavelength and metallization ratio of 50%) measured with a probe station (black) or PCB (grey) (a). Normalized frequency variations of RW (b and d) and of BAW (c and e) versus magnetic field with probe station and PCB (see text for the directions of the magnetic field).

The measured S_{11} output signals are shown in Figure 104 (a) for two different measurement setups: using wire bonding, a PCB and a SMA connector (grey curve) and using non-magnetic RF probes in a probe station (black curve). In this device, the wavelength is 6.5 µm, the metallization ratio is 50 % and the direction of wave propagation is LNO X + 90°-axis.

The normalized RW and BAW frequency variations were then extracted as a function of applied field (downsweep, Figure 104): in-plane parallel to Q (black curve) in the probe station (limited to this direction with respect to our probe station and device geometries), in-plane parallel and perpendicular to Q (black and red curves respectively) and OOP (green curve) on the PCB in the electromagnet. The error bars are estimated to ± 3 ppm. ± 2 ppm come from the heat variations produced by the electromagnet (see third part, second chapter) and ± 1 ppm come from the instrumental error (the experiments have been repeated a few times).

In Figure 104 (a), slight changes in frequency but huge changes in amplitude are observed when changing from a probe station to the PCB geometry. This variation can only be explained by the introduction of RLC components by PCB, wire bonding and SMA connectors. These additional components give also rise to an additional resonance close to 1.3 GHz.

When using the probe station (Figure 104 (b and c)), variations of RW and BAW resonance frequency are not significant considering the measurement errors. This conclusion also holds for RW with PCB and SMA connectors (Figure 104 (d)). However, a huge variation in the BAW frequency is observed when the PCB is used (Figure 104 (e)). This acoustic response does not exhibit any dependence on the magnetic field direction but is extremely sensitive to the field amplitude. This BAW frequency variation, observed for all resonator devices (magnetic or not) when the PCB is used, must originate from the measurement setup and especially from the PCB. This is studied in the next paragraph.

It must be noticed at this point that the same RW and QSHSAW/QSVSAW frequency variations versus field are obtained in magnetic devices whatever the setup, probe station or PCB connection.

2.4. Origin of setup magnetism dependence

In order to investigate the magnetic field-dependent responses when the PCB is used, even for non-magnetic IDT, we have first considered the magnetic response of the SMA connector (Figure 105 (a)). The room temperature hysteresis loop when the field is applied along an arbitrary direction is reported in Figure 105 (b).

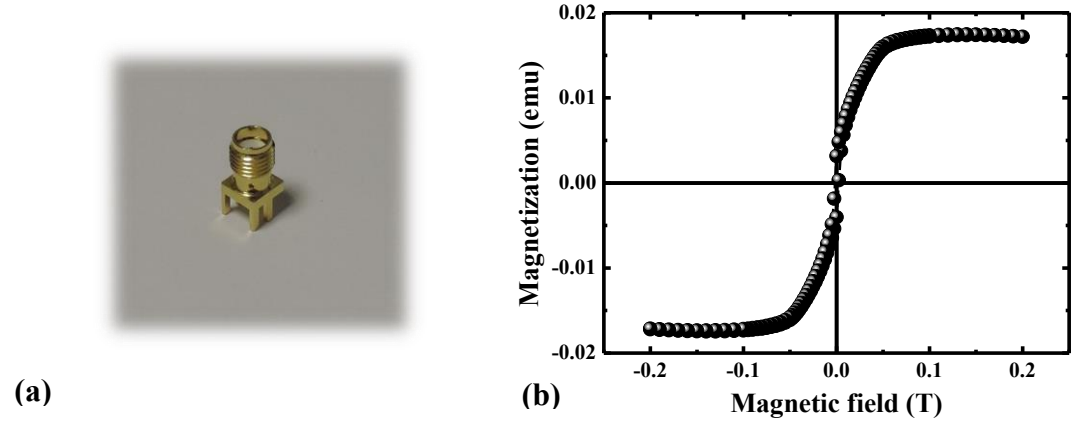

Figure 105. Picture of the SMA connector (a). Hysteresis loop of the SMA connector measured at room temperature with the magnetic field applied in an arbitrary direction (b).

As shown in Figure 105 (b), the SMA connector exhibits a reversible magnetic signal with a saturation field close to 0.05 T. This response is linked to the intrinsic composition of the connector, especially the brass body, composed mainly of Copper, Zinc and Nickel. The magnetism of the coax wire was also checked: an attraction is clearly felt on the whole wire when approaching a permanent magnet.

Considering that both magnetic pieces can disturb the magneto acoustic responses, we have investigated their impact. The S_{11} signals under applied field in an open circuit geometry composed of the PCB, the SMA connector and the coax wire (Figure 106 (a)) are reported in Figure 106 (b) for three different field values (0.3 T, 0 T and -0.3 T).

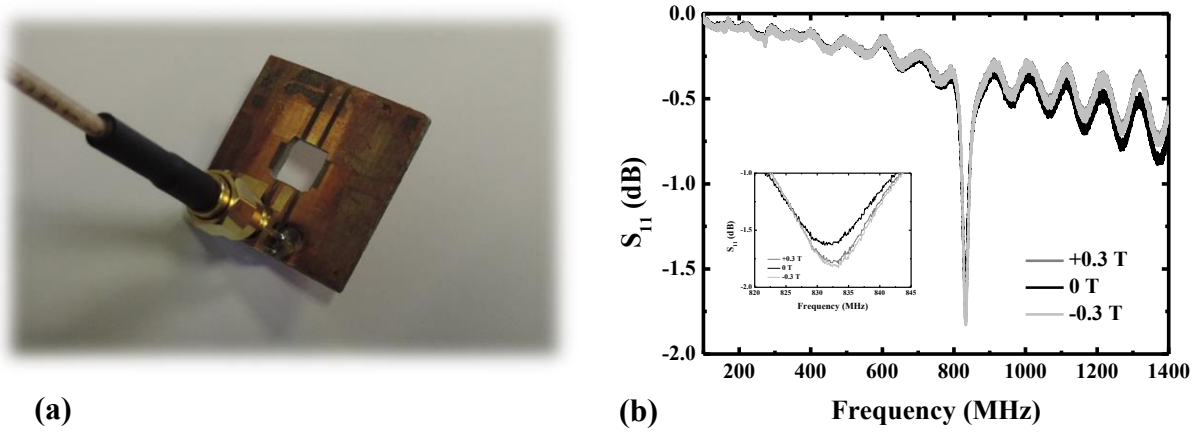

Figure 106. Picture of the PCB + SMA + coax wire setup used for the measurement under magnetic field. A SMA connector is welded to a PCB. On the transmission line, Gold pads are needed to operate the wire bonding (a). S_{11} variations for three different values of the magnetic field applied along an arbitrary direction (b).

Since no calibration steps are done before these measurements, many resonances can occur through defects along the transmission line, which generates dissipation at certain frequencies. Such a resonance occurs at approximatively 820 MHz (Figure 106 (b)) and is shifted towards higher frequency under positive or negative magnetic field. At ± 0.3 T, the variation is approximatively +1000 ppm.
The signal is thus sensitive to the magnetic field, especially at high frequency (small wavelength). We believe that the magnetic field leads to a mechanical strain (via magnetostrictive effect) of the PCB and connector system, which gives rise to changes in S_{11} signal, *i.e.* to a frequency variation under field. Since BAW is found at high frequency and its field dependence is close to +1000 ppm at ± 0.3 T (different PCB + SMA + coax wire setups are used for measurements), such an artifact can explain the observed BAW field sensitivity.

3. Summary of non-conventional geometries results

In this chapter, we have reported on the link between magnetic and magneto acoustic responses for MSAW devices in non-conventional geometries:
(i) In 200 nm thick Nickel-based devices, where the easy magnetization axis is perpendicular with strong stripes domains configurations. The OOP magneto acoustic response is in this case reversible, which is attributed to specific magnetic configurations and reversal processes when stripe domains are stabilized. In-plane MSAW variations are similar to those obtained in 50 nm thick Ni-based devices.
(ii) In magnetic and non-magnetic SAW devices, where a strong and isotropic field sensitivity has been observed for a high frequency BAW. The presence of this effect, also in non-magnetic SAW devices, proves the influence of the magnetic measurement setup (PCB + SMA + coax wire system). Although this only affects high frequency resonances, a non-magnetic measurement setup must be definitely used in the future.
Benefiting from a controlled magnetic field-sensitivity of a BAW would be however an interesting perspective. Both MSAW and MBAW responses could be interrogated in such devices to get more accuracy and/or complementary information in the magnetic field detection. This could be for example envisioned via implantation of ferromagnetic particles such as Cobalt into the piezoelectric substrate [SON06]. The incidence of such an implantation on piezoelectric properties, wave generation and propagation, would have to be checked carefully.

References

[AHA96] A. Aharoni, *Introduction to the theory of ferromagnetism*, International series of monographs on physics**. 109**, (1996).
[BER48] L. Bergmann, *Ultrasonics and their scientific and technical applications*, Wiley, New York, (1948).
[BO16] L. Bo, C. Xiao, C. Hualin, M. A. Mohammad, T. Xiangguang, T. Luqi, Y. Yi and R. Tianling, *Surface acoustic wave devices for sensor applications,* Journal of semiconductors**. 37**, 2, (2016).
[CAM70] I. A. Campbell, A. Fert and O. Jaoul, *The spontaneous resistivity anisotropy in Ni-based alloys*, J. Phys. C: Metal Phys., Suppl. No.1, S95, (1970).
[CAM98] C. K. Campbell, *Surface Acoustic Wave Devices for Mobile and Wireless Communications*, San Diego, California: Academic Press, (1998).
[CLA80] A. E. Clark, *Magnetostrictive rare earth – Fe_2 compounds*, Naval Surface Weapons Center, White Oak Laboratory, USA, (1977).
[DRE12] L. Dreher, M. Weiler, M. Pernpeinter, H. Huebl, R. Gross, M. S. Brandt and S. T. B. Goennenwein, *Surface acoustic wave driven ferromagnetic resonance in nickel thin films: Theory and experiment*, Phys. Rev. B. **86**, 134415, (2012).
[DON99] M. J. Donahue and D. G. Porter, OOMMF User's Guide Version 1.0, National Institute of Standards and Technology, Report No. NISTIR 6376, (1999).
[ELH15] M. Elhosni, *Capteurs à ondes élastiques de surface (SAW) pour des champs magnétiques à base de structures multicouches piézo-magnétiques*, PhD dissertation, Université de Lorraine, (2015).
[ERH17] J. Erhart, P. Pulpan and M. Pustka, *Piezoelectric ceramic resonators*, Book, Topics in mining, metallurgy and materials engineering, (2017).
[GAN76] A. K. Ganduly, K. L. Davis, D. C. Webb and C. Vittoria, *Magnetic control of surface elastic waves in a novel layered structure*, AIP Conference Proceedings. **34**, 259, (1976).
[GOW15] P. G. Gowtham, T. Moriyama, D. C. Ralph and R. A. Buhrman, *Traveling surface spin-wave resonance spectroscopy using surface acoustic waves,* J. Appl. Phys. **118**, 233910, (2015).
[GOW16] P. G. Gowtham, D. Labanowski and S. Salahuddin, *The mechanical back-action of a spin-wave resonance in a magnetoelastic thin film on a surface acoustic wave,* Phys. Rev. B. **94**, 014436, (2016).
[HAF69] E. Hafner, *The piezoelectric crystal unit: definitions and methods of measurement,* Proceedings of IEEE**. 57**, 179-201, (1969).
[HEH97] M. Hehn, *Elaboration, étude des propriétés structurales et magnétiques de couches et réseaux de plots submicroniques à base de Cobalt*, PhD dissertation, Université Louis Pasteur, Strasbourg, (1997).
[IEE87] American National Standards Institute, *Standard on piezoelectricity*, ANSI/IEEEStd. **176**, (1987).
[IEE02] American National Standards Institute, *IEEE standard letter designation for radar-frequency bands*, ANSI/IEEEStd. **521**, (2002).
[KAD11a] M. Kadota, S. Ito, Y. Ito, T. Hada and K. Okaguchi, *SAW magnetic sensors composed of various Ni electrode structures on quartz,* IEEE. International Ultrasonics Symposium Proceedings, (2011).
[KAD11b] M. Kadota, S. Ito, Y. Ito, T. Hada and K. Okaguchi, *Magnetic Sensor Based on Surface Acoustic Wave Resonators,* Jpn. J. Appl. Phys**. 50**, 07HD07, (2011).
[LI17] X. Li, D. Labanowski, S. Salahuddin and C. S. Lynch, *Spin wave generation by surface acoustic waves*, J. Appl. Phys. 122, 043904, (2017).
[LID03] D. R. Lide, *CRC Handbook of Chemistry and Physics*, CRC Press. Boca Raton, Florida, (2003).
[LEG14] J. B. Legland, *Caractérisation par acoustique non linéaire des effets de vieillissement dans les milieux granulaires non cohésifs et désordonnés*, PhD dissertation, Université du Maine, Le Mans, (2014).
[LUO11] F. Luo, X. R. Chen, L. C. Cai and Q. Wu, *Thermoelastic properties of nickel from molecular dynamic simulations*, J. Ar. Mol. Sci**. 2**, 10-19, (2011).
[MAY11] A. S. Mayorov, N. Hunter, W. Muchenje, C. D. Wood, M. Rosamond, E. H. Linfield, A. G. Davies and J. E. Cunningham, *Surface acoustic wave generation and detection using graphene interdigitated transducers on lithium niobate*, Appl. Phys. Lett**. 104**, 083509, (2011).

[MCG75] T. R. McGuire and R. I. Porter, *Anisotropic magnetoresistance in ferromagnetic 3d alloys*, IEEE. IEEE. Trans. Magn. **4**, 11, (1975).
[MOR85] D. P. Morgan, *Surface-Wave devices for signal processing*, Amsterdam, Elsevier (1985).
[NAN13] T. Nan, Y. Hui, M. Rinaldi and N. X. Sun, *Self-biased 215 MHz magnetoelectric NEMS resonator for ultra-sensitive DC magnetic field detection*, Scientific reports**. 10**, 1038, (2013).
[NAZ17] Z. Nazarchuk, V. Skalskyi and O. Serhiyenko, *Acoustic emission: Methodology and application*, Book, Foundations of engineering mechanics, (2017).
[NEW04] R. E. Newhnam, *Properties of materials: anisotropy, symmetry, structure*, Book, Oxford university press, (2004).
[PAR87] D. F. Parker and G. A. Maugin, *Recent developments in surface acoustic waves*, Book, Springer series on wave phenomena, (1987).
[POH00] A. Pohl, *A review of wireless SAW sensors,* IEEE. Trans. Ultra**. 47**, 2, (2000).
[POL17] V. Polewczyk, K. Dumesnil, D. Lacour, M. Moutaouekkil, H. Mjahed, N. Tiercelin, S. Petit Watelot, Y. Dusch, S. Hage-Ali, O. Elmazria, F. Montaigne, A. Talbi, O. Bou Matar and M. Hehn, *Unipolar and bipolar high-magnetic field sensors based on surface acoustic wave resonators*, Phys. Rev. App**. 8**, 024001, (2017).
[RAY85] L. Rayleigh, Proc. London Math. Soc, vol**. 17**, 4 (1885).
[ROJ14] J. C. Rojas-Sanchez, N. Reyren, P. Laczkowski, W. Savero, J. P. Attané, C. Deranlot, M. Jamet, J. M. George, L. Villa and H. Jaffrès, *Spin pumping and inverse spin hall effect in Platinum: The essential role of spin-memory loss at metallic interfaces*, Phys. Rev. Lett**. 112**, 106602, (2014).
[SAN99] D. Sander, *The correlation between mechanical stress and magnetic anisotropy in ultrathin films*, Rep. Prog. Phys**. 62**, 809-858, (1998).
[SAS17] R. Sasaki, Y. Nii, Y. Iguchi and Y. Onose, *Nonreciprocal propagation of surface acoustic wave in Ni/$LiNbO_3$*, Phys. Rev. B. **95**, 020407(R), (2017).
[SON06] C. Song, F. Zeng, Y. X. Shen, K. W. Geng, Y. N. Xie, Z. Y. Wu and F. Pan, *Local Co structure and ferromagnetism in ion-impanted Co-doped $LiNbO_3$*, Phys. Rev. B**. 73**, 172412, (2006).
[THE14] L. Thevenard, C. Gourdon, J. Y. Prieur, H. J. Von Bardeleben, S. Vincent, L. Becerra, L. Largeau and J. Y. Duquesne, *Surface acoustic wave driven ferromagnetic resonance in (Ga,Mn)(As,P) epilayers*, arXiv. 1406, 6483v1, (2014).
[VAR12] P. Varshney, B. S. Panwar, P. Rathore, S. Ballandras, B. Francois, G. Martin, J. M. Friedt and T. Rétornaz, *Theoretical and experimental analysis of high Q SAW resonator transient response in wireless sensor interrogation application,* IEEE Frequency control symposium, (2012).
[WEB79] D. C. Webb, D. W. Forester, A. K. Gangu1y and C. Vittoria, *Applications of amorphous magnetic-layers in surface-acoustic-wave devices*, IEEE. Trans. Magn**. 15**, (1979).
[WEI11] M. Weiler, L. Dreher, C. Heeg, H. Huebl, R. Gross, M. S. Brandt and S. T. B. Goennenwein, *Elastically driven ferromagnetic resonance in Nickel thin films*, Phys. Rev. Lett. **106**, 117601, (2011).
[WHI65] R. M. White and F. W. Voltmer, *Direct Piezoelectric Coupling to Surface Elastic Waves*, Appl. Phy. Lett**. 7**, p314, (1965).
[YAM79] H. Yamamoto, M. Naoe, S. Yamanaka, M. Yamaguchi and H. Kogo, *Variable surface acoustic weve delay line consisting of a magnetic thin film on a $LiNbO_3$ substrate,* Jap. J. of Appl. Phys**. 18**, 209-213 (1979).
[YAM80] M. Yamaguchi, K. Y. Hashimoto, H. Kogo and M. Naoe, *Variable saw delay line using amorphous $TbFe_2$ film,* IEEE. Trans. Magn**. 16**, (1980).
[YOU12] C. Y. You, *Dependence of the spin transfer torque switching current density on the exchange stiffness constant*, Applied Physics Express. **5**, 10, (2012).
[ZHO14] H. Zhou, *Etude théorique et expérimentale de systèmes à ondes de surface dans des structures multicouches piézomagnétiques pour des applications en contrôle santé intégré de MEMS par imagerie acoustique non linéaire*, PhD dissertation, IEMN, Lille, (2014).

Conclusion and future projects

The first aim of this PhD work was the growth of magnetostrictive materials on Lithium Niobate substrates with different cuts (Z / 128Y / 41Y) and the analysis of their magnetic properties. This concerns first the epitaxial growth by molecular beam epitaxy of the $TbFe_2$ magnetostrictive compound using different single or multiple buffer layers. Some basic structural and magnetic characterization have been also presented for magnetic layers deposited by sputtering: Ni films and [Co/IrMn] multilayers.

$TbFe_2$ on LNO Z-cut

The growth of $TbFe_2$ by co-evaporation was first performed on LNO Z-cut with hexagonal symmetry using different buffer layers of Ti, Mo, Ti/Mo, Ti/Nb.
Ti grows along [0001] with in-plane directions rotated by 30° with respect to the underlying (0001) substrate's plane. Nb and Mo on (0001) Ti grow along the [110] direction and form multiple domains following the Nishiyama-Wasserman (Nb [001] // Ti $[11\bar{2}0]$) or Kurdjumov-Sachs (Mo $[1\bar{1}1]$ // Ti $[11\bar{2}0]$) relations. When Mo or Nb are directly grown on the LNO Z-cut, the so-called R30 relationships (Mo-Nb [001] // LNO $[1\bar{1}00]$) are observed for both buffer layers.
On Ti, Mo and Ti/Mo, 50 nm thick (111) $TbFe_2$ could grow with the same final orientation with respect to the LNO (0001) surface: $[11\bar{2}]$ $TbFe_2$ // $[1\bar{1}00]$ LNO and $[1\bar{1}0]$ $TbFe_2$ // $[11\bar{2}0]$ LNO. $TbFe_2$ exhibits two variants rotated by 60° around the [111] growth direction. Growth over Mo or Ti/Mo exhibit R30 relationships in the plane while there is only 30° rotation between Ti and $TbFe_2$ basal planes lattices. The best crystallographic quality (coherence length, full width at half maximum of the rocking curve, in plane dispersion) is obtained with a Ti single buffer layer.
As far as magnetism is concerned, these magnetic thin films deposited on Ti, Mo and Ti/Mo exhibit an easy magnetization direction along the growth axis (perpendicular to the film plane), which is attributed to the magnetoelastic contribution associated to the lattice expansion measured along the growth direction. The in-plane magnetic response is isotropic and could be due to in-plane dispersion of easy magnetization directions.
Even if the epitaxial growth cannot be achieved with a single buffer layer of Niobium, $TbFe_2$ on Ti/Nb could grow as: [001] $TbFe_2$ // [001] Nb with three in-plane domains. This film however exhibits a poor crystallographic quality (large in plane dispersion, large full width at half maximum of rocking curve).
As far as magnetism is concerned, these $TbFe_2$ films deposited on Ti/Nb exhibit an in-plane magnetization, attributed to the lattice contraction measured along the growth direction.

This study of the epitaxial growth of $TbFe_2$ on LNOZ has revealed several issues related to the specific requirements for the crystalline growth.
The main problem is the degradation of the substrate, especially at its interface due to heating in ultra-high vacuum. This degradation likely occurs with ascend of Lithium and Oxygen, which is one possible explanation to the reduced saturation magnetization. Further investigations would require a detailed chemical analysis, both at the surface and in the depth of the samples, in order to check the efficiency of the buffer layers as a chemical barrier.
Such degradation and the presence of multiple (110) Mo domains are the blocking points to reproduce the experimental results reported in [HUT99].
In the future, different thicknesses of magnetic material could be analysed to see the evolution and connections between magnetic and structural properties. Mougin *et al.* [MOU99] have namely shown that the film morphology, which is extremely dependent on the deposition temperature and thickness, can play a drastic role in the magnetic reponses. These can thus also affect the magnetic and structural IDT quality in MSAW devices.

$TbFe_2$ on LNO 128 Y-cut and LNO 41 Y-cut

On LNO 128Y-cut ($(10\bar{1}4)$ planes with rectangular surface symmetry) or on LNO 41Y-cut ($(01\bar{1}2)$ planes at ± 8.26 ° from the macroscopic surface) substrates, the $TbFe_2$ growth was achieved on a Mo buffer layer. X-ray diffraction experiments and especially pole figures revealed the relative orientations of the various materials in the composite system. For both substrates, Mo (110) // LNO (0001) (tilted by ± 38 ° from the surface normal for LNO 128 Y and by ± 49 ° for LNO 41 Y), with the R30 orientation between (0001) LNO and (110) Mo planes. The (111) $TbFe_2$ are found to be parallel to (110) Mo, with the R30 orientation between $TbFe_2$ and Mo in these parallel planes.
It is possible to grow crystalline $TbFe_2$ on more exotic LNO 128Y and 41Y, with 3D orientation relationships similar to those obtained on LNO Z-cut, both between the Mo and the LNO lattices and between the $TbFe_2$ and the Mo lattices. However, one has to underline that specific orientations are selected among equivalent ones, which is most likely related to surface energies considerations.
From the magnetic point of view, these films present a planar anisotropy, with an easy axis perpendicular to the LNO $[11\bar{2}0]$ direction. The reason is still unknown. The saturation magnetization is close to the theoretical value (800 $kA.m^{-1}$), which means that the Oxygen diffusion from the substrate might be lower when LNO 128Y or LNO 41Y are used. This point could be specifically investigated in the future with detailed chemical analysis.
A next step for the growth on LNO 128Y and LNO 41Y substrates will be now to test other buffer layers, as it has been performed on LNO Z. The first experiments with a Ti buffer layer have revealed the alignement between Ti [0001] and LNO [0001] axis (both tilted by ± 38° or ± 49° from the surface normal depending on the substrate), as observed on LNO Z-cut. The orientation of the multidomains $TbFe_2$ deposit could however not be completely unraveled up to now. In parallel to the different buffer layers, in–situ Scanning Tunneling Microscope (STM) studies could be undertaken to observe the presence of the stepped surfaces and the morphology of the deposited layers. The recent connection of the MBE chamber to the DaVm instrument will indeed enable the UHV access to various surface analysis techniques.

Ni and [Co/IrMn] multilayers on various LNO cuts

Ni films and [Co/IrMn] magnetic multilayers have been deposited using the sputtering technique. Whatever the LNO cut, Ni films (50 and 200 nm thick) and [Co/IrMn] multilayers exhibit a polycrystalline structure with a marked [111] texture axis along the perpendicular to the film plane, due to the amorphous Tantalum buffer layer. Despite similar structures observed by X-ray diffraction for different Ni thicknesses, the magnetic properties are significantly different.
50 nm thick Ni films deposited on LNO Z and LNO 41Y present an in-plane uniaxial anisotropy most likely resulting from geometrical considerations during the sputtering process. The Ni deposit on LNO 128 Y however exhibits an in-plane isotropic magnetic response and the reason is still unknown. 200 nm thick Ni films deposited on LNO 128Y and LNO 41Y exhibit a perpendicular magnetic anisotropy, strong enough to stabilize magnetic strong stripes domains configurations. This phenomenon could not be observed for the deposit on LNO Z.
We have confirmed that [Co/IrMn] multilayers deposited on LNO 41Y exhibit an exchange biased hysteresis loop for in-plane applied fields, the exchange field being of 33 mT.

The second part of this PhD work aimed in using the hybrid piezoelectric/magnetostrictive systems to design and investigate magnetic surface acoustic wave devices in a resonator geometry.

After completing the optimization and processing steps to transform the plain stacks into MSAW devices, the dependence of the surface acoustic waves (RW or QSHSAW/QSVSAW) on the applied magnetic field direction (with respect to magnetic anisotropy and/or wave propagation direction) and intensity has been studied in details. Although the MSAW response to an external magnetic field has been previously considered in various studies [YAM79, GAN76 …], several aspects were still lacking

to get a comprehensive understanding of the underlying phenomena, especially a clear description of the magnetic component's structural and magnetic properties.

As a first step, 50 nm thick Ni-based devices have shown that a magneto acoustic hysteresis was clearly present for fields applied along the easy magnetization axis, a phenomenon that could be inferred from the Ni magnetic properties but hidden in most experiments published up to now in the SAW community. Along the hard axis, the magneto acoustic response for applied fields lower than the saturation field is mainly governed by the variation of the elastic constants. A variation of MSAW frequency however persists above the magnetic saturation, which should mainly be due to the dynamic magnetoelastic field created by the propagation of the acoustic wave. The in-plane responses can be simulated with a piezomagnetic equivalent model, initially developed by Zhou and his coworkers [ZHO14].
The response of the MSAW for in-plane fields can by the way be controlled by the shape anisotropy of the IDT's electrodes. For IDT widths close to the µm, the shape of the IDT namely imposes an anisotropy axis along the IDT length, especially for soft magnetic materials such as Nickel.
Rarely reported in the literature, the MSAW response for fields applied perpendicular to the device plane appears to be also hysteretic, while the magnetization field variation reveals an hysteresis free hard axis behavior. This apparent inconsistency is related to the sensitivity of the MSAW response to all magnetization components, both OOP and IP. In order to control the reversal of the in-plane magnetic components, an exchange-biased [Co/IrMn] multilayers was used to stabilize a unidirectional in plane anisotropy that induces a smooth in-plane magnetization reversal. The resulting suppression of hysteresis in the OOP MSAW response could let envision the development of OOP magnetic field sensor. A next step would be to replace IrMn by another antiferromagnetic material with high magnetostriction, as $KCoF_3$, NiO, $Mn_{42}Fe_{58,...}$ [GOM02, PEN06]. Another way to control the OOP magneto acoustic hysteresis was obtained with 200 nm thick Nickel MSAW devices that host stripe domains for a large window of OOP applied fields. Due to this magnetic configuration, the hysteresis of the magneto acoustic OOP response, observed for in-plane magnetized materials, is suppressed. The equivalent piezomagnetic model has now to be implemented to take the perpendicular to the film plane geometry into account. Another extension of this work will be the carefull analysis of the impact of different parameters via the equivalent piezomagnetic model, to possibly reach a larger frequency variation and thus optimize the MSAW devices. The IDT thickness, the wavelength, the metallization ratio, the different SAW harmonics, the architecture itself with the presence of intermediate layers between the magnetic and the piezoelectric materials… are many parameters that definitely play a role on the MSAW response.

MSAW based on $TbFe_2$ epitxial layers lead to complex magneto acoustic responses that could not be completely unraveled during this work. The particular shape of in-plane MSAW responses and the non-hysteretic OOP MSAW response remain difficult to understand on the basis of the magnetization response under field. The main motivation to the use of epitaxial $TbFe_2$ layers was the probable increase of the frequency variation due to the high magnetostriction in bulk $TbFe_2$, but the results were disappointing. The small MSAW field sensitivity is most likely linked to specific issues resulting from the $TbFe_2$ crystalline growth: degradation of LNO while heating in UHV, occurrence of buffer layer(s), crystallization in multidomains. The use of stoichiometric LNO substrates, more stable during a high temperature treatment, should be tested. A collaborative work with T. Aubert (LMOPS, Metz) was recently initiated: first X-ray diffraction experiments for stoichiometric LNO Z after annealing at 700 °C in air do not reveal the $LiNb_3O_8$ phase that was observed with the congruent LNO Z. Further investigations are in progress to confirm the stability of these stoichiometric substrates.
The measurement of the magnetostrictive properties in the specific systems including substrate, buffer layers and magnetostrictive film before patterning should be also undertaken, for example by optical deflectometry [TIE08].
Despite the observed low sensitivity, the use of a hard magnetic material with high coercivity enables the demonstration of a bipolar sensor response for fields up to 0.5 T at room temperature. The field range where a reversible behavior is observed should by the way be extended in decreasing the temperature, as a result of the increased coercivity [MOU99].

Finally, a puzzling large magneto acoustic response of BAW (close to 1 GHz), observed for all the investigated devices, could be explained by the magnetic response of the SMA connector, partially made of Ni. Benefiting from a controlled magnetic field-sensitivity of a BAW in a non magnetic setup would be however an interesting perspective to improve accuracy of magnetic field detection. For instance, we can envision a resonator device combining magnetostrictive substrate on which a piezoelectric layer is deposited in order to obtain a BAW that could be magnetically sensitive through the volume device.

Future extensions of the work

Beyond the various points mentioned previously, an important element to go deeper in the understanding of hybrid multiferroics patterned devices would be to analyze the elastic coupling between the deposited magnetic layer and the piezoelectric substrate.
Recent studies using stroboscopic X-ray diffraction under synchrotron light have shown that the combination of atomic structural resolution with temporal resolution (ps time scale) allows the observation of the atomistic displacements in LNO 128Y for each time point within the SAW period [REU13]. These experiments show how the crystalline structure evolves under the acoustic wave propagation and its associated motion fields. Similar experiments could be envisioned on a piezoelectric/magnetostrictive system (delay line geometry) to analyse the structural evolution in both materials under the propagation of different waves and possibly under the application of an external magnetic field.
X-ray Resonant Magnetic Scattering (XRMS) at low angles (reflectivity configuration such as in [JAL13]) could also bring information on the evolution of magnetism under acoustic propagation with a possible depth resolution in the magnetic layer.

References

[GAN76] A. K. Ganguly, K. L. Davis, D. C. Webb and C. Vittoria, *Magnetic control of surface elastic waves in a novel layered structure,* J. Appl. Phys. **47**, 2696, (1976).
[GOM02] H. Gomonay and V. M. Loktev, *Magnetostriction and magnetoelastic domains in antiferromagnets*, Journal of Physics: Condensed Matter. **14**, 3959, (2002).
[JAL13] E. Jal, *Réflectivité magnétique résonante de rayons X mous : une sonde de la distribution d'aimantation complexe au sein de films minces*, PhD dissertation, Université de Grenoble, Institut Néel, (2013).
[MOU99] A. Mougin, *Nanosystèmes magnétostrictifs de $TRFe_2$ (110) (TR=terre rare): croissance, morphologie et propriétés magnétiques*, PhD dissertation, Université H. Poincaré, Nancy, (1999).
[PEN06] W. Y. Peng and H. Zhang, *Magnetostriction studies in an antiferromagnetic polycrystalline $Mn_{42}Fe_{58}$ alloy*, Appl. Phys. Lett. **89**, 262501, (2006).
[REU13] T. Reusch, F. Schulein, C. Bomer, M. Osterhoff, A. Beerlink, H. J. Krenner, A. Wixforth and T. Salditt, *Standing surface acoustic waves in $LiNbO_3$ studied by time resolved X-ray diffraction at Petra III*, AIP Advances. **3**, 072127, (2013).
[TIE08] N. Tiercelin, V. Preobrazhensky, P. Pernod and A. Ostaschenko, *Enhanced magnetoelectric effect in nanostructured magnetostrictive thin film resonant actuator with field induced spin reorientation transition*, Appl. Phys. Lett**. 92**, 062904, (2008).
[YAM79] H. Yamamoto, M. Naoe, S. Yamanaka, M. Yamaguchi and H. Kogo, *Variable surface acoustic weve delay line consisting of a magnetic thin film on a $LiNbO_3$ substrate,* Jap. J. of Appl. Phys**. 18**, 209-213, (1979).
[ZHO14] H. Zhou, *Etude théorique et expérimentale de systèmes à ondes de surface dans des structures multicouches piézomagnétiques pour des applications en contrôle santé intégré de MEMS par imagerie acoustique non linéaire*, PhD dissertation, IEMN, Lille, (2014).

Résumé (Français)

Dans l'introduction, nous avons explicité qu'il est possible d'agir sur l'aimantation (polarisation) via un champ électrique (respectivement magnétique) au travers du couplage magnétoélectrique qui existe au sein même de matériaux combinant un ordre ferroélectrique et un ordre ferromagnétique. Néanmoins, ces matériaux multiferroïques sont rares à l'état naturel et sont fonctionnels dans des gammes de température ne permettant pas la réalisation d'applications. Une possibilité pour obtenir cette combinaison d'ordre ferroique est d'associer au sein d'un matériau hybride (une multicouche, par exemple) deux matériaux possédant chacun son propre ordre ferroïque. Le système obtenu est appelé multiferroïque hybride. Dans ces matériaux composites, le couplage entre ordres ferroïques peut s'opérer au niveau de l'interface : l'application d'un champ électrique sur un matériau piézoélectrique peut engendrer une modification de l'état magnétique d'un matériau magnétique ; réciproquement, l'application d'un champ magnétique entraine une modification de l'aimantation qui peut engendrer une variation de l'état de contrainte dans un matériau piézoélectrique. Ces deux effets peuvent être couplés, comme dans les dispositifs magnétiques à ondes acoustiques de surface. Dans ces systèmes, le matériau piézoélectrique génère une onde acoustique par effet piézoélectrique inverse qui agit sur la dynamique d'aimantation du matériau ferromagnétique. Qui plus est, la dynamique d'aimantation peut en retour agir sur la propagation de l'onde elle-même. Cet effet s'ajoute au cas statique où un champ magnétique extérieur est appliqué et peut modifier la propagation de l'onde de surface par les contraintes magnétostrictives.
Dans une première étape, ce travail de thèse a porté sur la synthèse de ces matériaux hybrides en utilisant deux méthodes de croissance : l'épitaxie par jets moléculaires et la pulvérisation cathodique magnétron. Lors d'une seconde étape et dernière étape, ces multiferroïques hybrides ont été utilisés pour la réalisation de dispositifs magnétiques à ondes acoustiques de surface.

Première partie : Matériaux ferroélectriques/piézoélectriques et ferromagnétiques pour le développement de multiferroïques hybrides

Dans le premier chapitre de cette partie, le phénomène de la ferroélectricité a été décrit. Un ferroélectrique est un matériau qui possède une polarisation électrique à l'état naturel. Cette polarisation peut être renversée sous l'action d'un champ électrique externe et n'apparaît qu'en dessous d'une certaine température que l'on nomme température de Curie. Ce renversement n'est pas réversible et traduit l'apparition d'une hystérèse. Qui plus est, un matériau ferroélectrique est aussi pyroélectrique et piézoélectrique en raison de sa structure cristallographique particulière. La pyroélectricité représente la variation de polarisation d'un matériau sous l'effet d'une variation de température. La piézoélectricité est l'apparition d'une polarisation sous contrainte mécanique extérieure. Il existe beaucoup de matériaux ayant ces différentes propriétés, mais ce travail de thèse s'axe principalement sur le Niobate de Lithium ($LiNbO_3$ ou LNO) - un matériau qui appartient comme le Tantalate de Lithium ($LiTaO_3$) aux ferroélectriques de type ABO_3. La structure consiste en des plans d'atomes d'Oxygène dans une configuration hexagonale déformée. La température de Curie du $LiNbO_3$ est d'environ 1210 °C.
Malgré le caractère ferroélectrique de ce composé, le but est d'utiliser ses propriétés piézoélectriques. Pour cette raison, les équations constitutives de la piézoélectricité ont été explicitées afin d'appréhender les paramètres physiques sous-jacents. Il en résulte des lois reliant la contrainte au champ électrique. Il est à noter que ce matériau est ici utilisé sous forme de cristal congruent (proche de la stœchiométrie) suivant différentes coupes cristallographiques.

Dans le second chapitre, il a été logique de décrire le phénomène du ferromagnétisme, c'est-à-dire la propriété d'un matériau ayant une aimantation spontanée pouvant être renversée sous l'action d'un champ magnétique extérieur. Parmi les différents matériaux du tableau périodique, les métaux de transition et les Terres Rares (TR), aussi appelés lanthanides, présentent un ordre magnétique. Pour

chacun de ces matériaux, les différents termes d'énergies internes magnétiques ont été explicités. Premièrement, le magnétisme des métaux de transition relève d'un magnétisme dit itinérant. Ces matériaux possèdent des fonctions d'ondes spatialement étendues et sont fortement couplées au réseau cristallin, ce qui a pour effet de réduire nettement le moment orbital. Cela donne une énergie d'échange importante entre les moments magnétiques mais une anisotropie magnétocristalline et une magnétostriction faible. En effet, ces deux dernières énergies sont liées au moment orbital et au champ cristallin. Cette forte énergie d'échange assure que l'ordre ferromagnétique subsiste jusqu'à des températures relativement élevées, de l'ordre de 700 °C. Dans les Terres Rares, les fonctions d'ondes sont localisées, ce qui permet un couplage spin-orbite et un moment orbital fort, donc une énergie magnétocristalline ainsi qu'une magnétostriction forte. Néanmoins, c'est l'énergie d'échange qui est faible et le magnétisme résultant n'existe principalement que pour des températures bien inférieures à la température ambiante.
Dans ce travail, même si des matériaux tel le Nickel sont utilisés pour la réalisation des multiferroïques hybrides, le principal but de cette étude de croissance est d'obtenir un composé hautement magnétostrictif à température ambiante, afin de pouvoir l'utiliser pour des dispositifs industriels. Des atomes de Terres Rares ont donc été combinés avec des atomes de métaux de transition ($TRFe_2$) car ces matériaux bénéficient de la forte anisotropie magnétocristalline et de la magnétostriction des terres rares, ainsi que de la forte énergie d'échange des métaux de transition. Les structures de $TRFe_2$ sont cubiques en phase de Laves ($Fd\bar{3}m$). Les atomes de Terres Rares forment une structure de type diamant où la moitié des sites tétraédriques est occupée par des atomes de terres rares et l'autre moitié est occupée par des tétraèdres réguliers d'atomes de Fer. Le composé de $TbFe_2$ a été spécifiquement choisi car il possède le record de magnétostriction à température ambiante ($\lambda_{111} = 2460.10^{-6}$), ainsi qu'une température de Curie de 425 °C.
Comme pour les Terres Rares et les métaux de transition, les différentes énergies et les processus mis en jeu dans le $TbFe_2$ ont été explicités. Il a spécialement été montré que l'anisotropie magnétocristalline engendre une direction de facile aimantation suivant les directions de type $< 111 >$ à température ambiante. Qui plus est, les phénomènes de magnétostriction ont été expliqué plus en détail. Ils sont de différentes natures mais l'effet le plus important est la magnétostriction de Joule. Comme tout effet magnetostrictif, celui-ci traduit le changement d'état magnétique lorsque le cristal subit une déformation. Néanmoins, cet effet est anisotrope et provient de l'interaction entre les électrons et leurs environnements atomiques. Les équations constitutives de ce phénomène pour la structure cubique des $TRFe_2$ ont été écrites.
Finalement, les couches magnétiques qui ont été réalisée dans le cadre de cette thèse sont des couches minces. Lorsque l'épaisseur devient nanométrique, des effets de surface ou d'interface ainsi que des effets de forme peuvent apparaître et modifier le magnétisme des matériaux. Il y a par exemple l'effet du champ démagnétisant, *i.e.* l'anisotropie de forme qui a induit une réorientation de l'axe de facile aimantation dans la géométrie « résonateur » des dispositifs magnétiques à ondes acoustiques de surface. Des effets de contraintes peuvent aussi affecter le magnétisme des composés. Cet effet a été utilisé lors des étapes de croissance afin de favoriser certaines directions de facile aimantation.

Deuxième partie : Synthèse d'hétérostructures piézoélectriques/magnétostrictives - Propriétés magnétiques

Dans cette deuxième partie, la fabrication de multiferroïques hybrides a été entreprise avec deux différentes techniques de dépôt : l'épitaxie par jets moléculaires pour le $TbFe_2$; et la pulvérisation cathodique magnétron pour le Nickel et les multicouches de [Co/IrMn].

Le premier chapitre présente l'état de l'art concernant la croissance épitaxiale de $TRFe_2$ sur saphir d'une part, et la croissance épitaxiale ou non de différents matériaux sur des substrats de LNO d'autre part. Parmi les résultats importants, il y a la croissance épitaxiale de $TRFe_2$ (110) sur des substrats d'Al_2O_3 $(11\bar{2}0)$. Celle-ci peut être réalisée grâce à une couche tampon de Nb (110) d'une épaisseur de 50 nm déposée à 700 °C, suivie d'une couche de Fe d'une épaisseur de 1,5 nm déposée à 500 °C. Ce processus permet l'obtention d'un alliage avec un faible désaccord paramétrique pour la croissance des phases de Laves. Cela favorise spécifiquement la croissance de $TRFe_2$ (110). Dans ce cas, les relations épitaxiales

dans le plan sont : [001] $TRFe_2$ // [001] NbFe et $[1\bar{1}0]$ $TRFe_2$ // $[1\bar{1}0]$ NbFe. Les températures de dépôt sont comprises entre 460 °C et 660 °C et l'aimantation obtenue est contenue dans le plan de l'échantillon avec deux directions de facile aimantation $< 1\bar{1}1 >$ favorisées par l'anisotropie magnétocristalline et l'anisotropie de forme. La croissance de $TRFe_2$ (111) peut être obtenue sur Al_2O_3 $(11\bar{2}0)$ en utilisant une couche tampon de Mo (110) déposée à 750 °C. Les relations d'épitaxie dans le plan sont : $[11\bar{2}]$ $TbFe_2$ // [001] Mo et $[1\bar{1}0]$ $TbFe_2$ // $[1\bar{1}0]$ Mo, ce qui correspond à une Orientation Relative (OR) dite R30 entre fcc (111) et bcc (110). Malgré la direction de croissance [111], les directions $< 1\bar{1}1 >$ à 20 ° du plan sont favorisées énergétiquement pour l'orientation de l'aimantation en raison de l'anisotropie de forme. Pour finir, la principale étude qui a guidé ce travail de thèse a été rapportée. Dans cette dernière, la croissance épitaxiale de $TbFe_2$ (111) est réalisée sur du LNO coupe Z pour une température de dépôt de 550 °C, en utilisant une double couche tampon de Ti/Mo déposée respectivement à 100 °C et 750 °C. Les relations d'épitaxie dans le plan ne sont pas explicitées mais il est à noter que ce composé possède une anisotropie magnétique perpendiculaire qui est stabilisée grâce à une dilatation du paramètre de maille suivant la direction de croissance. Malgré le succès de la croissance de $TbFe_2$ sur la coupe Z du LNO, les auteurs soulignent les difficultés liées à la faible stabilité du LNO à haute température avec une possible diffusion de Li.

Dans le deuxième chapitre de cette partie, les différents substrats utilisés dans le cadre de cette étude ont été présentés. Ils sont au nombre de trois et sont utilisés pour des raisons différentes : (i) La coupe Z du LNO est utilisée pour sa symétrie hexagonale de surface pouvant faciliter la croissance épitaxiale de $TbFe_2$; (ii) la coupe LNO 128Y (plan de coupe perpendiculaire à la direction tournée de 128° dans le sens anti-horaire autour de X et à partir de Y) possède une symétrie de surface rectangulaire et est utilisée pour un couplage électromécanique raisonnable mais une génération d'onde acoustique de surface sans perte vers le volume ; (iii) la coupe LNO 41Y (plan de coupe perpendiculaire à la direction tournée de 41° dans le sens anti-horaire autour de X et à partir de Y), qui ne possède aucune symétrie de surface, est utilisée pour un fort couplage électromécanique malgré quelques pertes vers le volume des ondes acoustiques de surface.
La dégradation du substrat de LNO avec l'élévation en température a été ensuite étudiée. Il a été observé que le substrat se déplétait en Oxygène et en Lithium.

Dans le troisième chapitre, la croissance épitaxiale de $TbFe_2$ sur la coupe LNO Z associée à des couches tampons de Ti, Mo, Nb, Ti/Nb et Ti/Mo a été détaillée. Pour ces différentes couches tampons, les analyses RHEED et celles obtenues en diffraction de rayons X ont permis de déterminer les relations d'épitaxie. Le Ti, déposé à 100 °C, croît selon la direction [0001] et présente dans le plan des directions cristallographiques tournées de 30° par rapport au LNO (0001). Le Nb et le Mo sur Ti sont obtenus avec une direction de croissance [110] et forment respectivement dans le plan 3 ou 6 domaines qui suivent les relations de type Nishiyama-Wasserman ou Kurdjumov-Sachs par rapport au réseau hexagonal sous-jacent de Ti (Nb [001] // Ti $[11\bar{2}0]$ et Mo $[1\bar{1}1]$ // Ti $[11\bar{2}0]$). Sur le LNO, l'épitaxie est de type R30, *i.e.* Mo-Nb [001] // LNO $[1\bar{1}00]$. Concernant la croissance de Nb ou de Mo sur LNO ou sur Ti, la température optimale de dépôt est de 450 °C. Pour des températures supérieures, les couches n'accrochent pas à la surface. En définitive, il a été montré que la qualité des couches tampons de Mo ou de Nb est améliorée lorsqu'elles sont déposées sur Ti, *i.e.* avec une barrière supplémentaire d'interdiffusion avec le substrat. Cependant, les couches de Mo ont toujours révélé de meilleures qualités cristallographiques que celles de Nb.
Concernant le matériau magnétique, le $TbFe_2$ est polycristallin quand il est déposé sur Nb, peu importe la température de dépôt. Néanmoins, sur Ti/Nb, le $TbFe_2$ déposé pour une température optimale de 650 °C croit selon [110] avec trois domaines tournés de 60° dans le plan et dont les directions sont alignées avec celles du Nb sous-jacent. Malheureusement, les diverses caractérisations structurales montrent une faible qualité cristallographique. Sur Ti, Mo et Ti/Mo, le $TbFe_2$ déposé pour une température optimale de 650 °C croit selon [111] avec des relations dans le plan : $TbFe_2$ $[11\bar{2}]$ // Ti $[11\bar{2}0]$ // LNO $[1\bar{1}00]$ ou $TbFe_2$ $[11\bar{2}]$ // Mo [001] // LNO $[1\bar{1}00]$ avec deux variants tournés de 60° autour de la direction de croissance. Sur Mo et Ti/Mo, c'est donc une nouvelle fois une OR de type R30, peu importe le nombre de domaines cubiques sous jacents. Une remarque intéressante est que les relations d'orientation sont toujours identiques par rapport au réseau cristallographique de LNO. Pour ces trois dernières couches

tampons, les clichés RHEED obtenus attestent d'une bonne qualité cristalline malgré une rugosité marquée. Une largeur à mi-hauteur d'environ 1,5°-2° est mesurée en diffraction de rayons X pour la rocking curve autour de la réflexion (111), ce qui est satisfaisant au regard de la complexité de ce type de croissance. Il est cependant notable que la meilleure qualité cristallographique est obtenue pour une couche tampon de Ti.
Concernant les propriétés magnétiques, les films obtenus avec une direction de croissance [111] présentent une anisotropie perpendiculaire, *i.e.* une direction de facile aimantation selon la direction de croissance, liée aux contraintes épitaxiales (dilatation suivant la direction de croissance) générées lors du refroidissement depuis la température de dépôt. Ce phénomène est plus précisément lié aux différences de coefficient d'expansion thermique entre le substrat et la couche magnétique. Le $TbFe_2$ [110] déposé sur Ti/Nb possède quant à lui une anisotropie planaire en raison d'une compression du paramètre de maille suivant la direction de croissance. Il est à noter que, dans le plan, une isotropie magnétique est trouvée pour tous ces composés. Cet effet est surprenant mais est potentiellement lié à la dispersion planaire des directions cristallographiques. Contrairement à l'étude présentée dans l'état de l'art, nos composés présentent une aimantation à saturation plus faible que celle du composé massif (800 $kA.m^{-1}$). Une possible explication de cette faible valeur est l'interdiffusion de la couche magnétique avec le substrat et les couches tampons. L'aimantation la plus élevée est obtenue avec des couches tampons de Ti/Mo.

Pour ce qui est de la croissance épitaxiale de $TbFe_2$ sur les coupes de LNO 128 et 41Y, la croissance cristalline de $TbFe_2$ (111) déposé à 650 °C sur ces substrats non conventionnels est difficile mais a pu être réalisée en utilisant une couche tampon de Mo (110) déposé à 650 °C. Les films ne présentent pas un caractère monocristallin mais sont en réalité des multi-domaines pour la couche tampon comme pour la couche magnétique. Des OR-3D, similaires à celles obtenues sur LNO Z-cut, sont notamment observées ($TbFe_2 < 1\bar{1}0 >$ // Mo $< 1\bar{1}0 >$ // LNO $< 11\bar{2}0 >$ et $TbFe_2 < 11\bar{2} >$ // Mo $< 001 >$ // LNO $< 1\bar{1}00 >$). C'est donc une nouvelle fois une relation de type R30 entre Mo et LNO et entre $TbFe_2$ et Mo dans ces plans parallèles. Malgré l'OR-3D commune entre les différents réseaux, l'énergie libre de surface associée aux différents plans cristallins joue un rôle important puisque des domaines spécifiques sont sélectionnés parmi ceux qui sont équivalents. Trois domaines de Mo et un seul domaine de $TbFe_2$ sont stabilisés sur LNOZ, alors que deux domaines de Mo et deux ou trois domaines de $TbFe_2$ avec leurs variants associés se développent sur LNO 128Y et LNO 41Y. La qualité cristalline du $TbFe_2$ est limitée sur ces substrats, comme le révèle l'extension spatiale de l'intensité diffractée dans les figures de pôles. Ces films présentent cependant des caractéristiques magnétiques satisfaisantes, avec notamment une aimantation à saturation en accord avec la valeur du composé massif. L'axe de facile aimantation se trouve dans le plan de l'échantillon, le long de la direction X+90° du LNO, ce qui reste inexpliqué pour le moment.

Concernant la croissance de matériaux magnétiques par pulvérisation cathodique magnétron, la croissance de Nickel (50 nm et 200 nm) à température ambiante sur les trois différentes orientations de substrat a été entreprise. Les résultats obtenus par diffraction de rayons X montrent une texture selon la direction [111] du Nickel. Ce résultat est obtenu grâce à une couche tampon de 5 nm de Tantale amorphe qui permet aux plans denses du Nickel de croître. Concernant les résultats magnétiques, la géométrie de dépôt a permis d'induire un axe facile d'aimantation suivant la direction X du LNO pour le Nickel de 50 nm déposé sur les coupes de LNO 41Y et Z. De manière surprenante, le dépôt sur LNO 128Y s'est révélé isotrope. Dans tous les cas, l'aimantation est orientée dans le plan de la couche. En ce qui concerne le Nickel de 200 nm d'épaisseur, le comportement magnétique dépend également du substrat sur lequel la couche est déposée. Le Nickel déposé sur LNO Z-cut présente une aimantation planaire avec une isotropie magnétique dans le plan. Une composante perpendiculaire de l'aimantation est néanmoins présente. Concernant les dépôts réalisés pour cette épaisseur sur les deux autres substrats, une aimantation perpendiculaire est stabilisée avec le développement de « strong stripes », *i.e.* domaines magnétiques alternativement alignés « up » et « down ». Cet effet a pu être mis en évidence grâce aux cycles d'hystérésis caractéristiques de ce phénomène pour un champ magnétique appliqué hors du plan. Toujours avec la même méthode de dépôt, des multicouches de $[Co(5nm)/Ir_{0,2}Mn_{0,8}(5nm)]_{15}$ sur une coupe de LNO 41Y ont été réalisées. Grâce au couplage ferromagnétique/antiferromagnétique à l'interface, l'existence d'une énergie d'échange permet d'induire un axe d'anisotropie d'ordre 1. Par

construction, cet axe de facile aimantation a été orienté suivant la direction X+90° du LNO grâce au recuit sous champ magnétique.

Les multiferrroiques hybrides produits dans cette partie ont permis d'analyser et de contrôler de diverses façons les réponses magnéto-acoustiques des dispositifs magnétiques à ondes acoustiques de surface. C'est le sujet de la troisième partie.

Troisième partie : Dispositifs magnétiques d'ondes acoustiques de surface (MSAW)

Dans le premier chapitre de cette partie, des informations générales sur les ondes acoustiques sont données, où il est notamment rapporté le fait que certaines peuvent se propager en surface tandis que d'autres se propagent dans le volume du matériau. Parmi les ondes de surface, les ondes de Rayleigh et les ondes quasi transverses horizontales/verticales de surface (QSHSAW/QSVSAW) sont spécifiquement discutées. L'onde de Rayleigh possède un déplacement elliptique, c'est-à-dire une composante de propagation longitudinale et une verticale. Les ondes transverses de surface ont quant à elles un déplacement essentiellement perpendiculaire à la direction de propagation. Les dispositifs piézoélectriques à ondes acoustiques de surface permettant de générer ces ondes ont ensuite été présentés. Deux géométries sont généralement utilisées : les lignes à retard ; et les résonateurs. La première géométrie est composée de deux IDT, un émetteur et un récepteur, sur un substrat piézoélectrique. Un IDT est composé de doigts métalliques interdigités qui permettent de générer une onde acoustique par effet piézoélectrique inverse lorsqu'une tension alternative lui est appliquée. L'onde acoustique qui se propage entre les deux IDT peut-être affectée par divers stimuli. Un résonateur n'est composé que d'un IDT qui joue le rôle d'émetteur et de récepteur. Dans ce cas, des réflecteurs de Bragg sont disposés de part et d'autre de l'IDT en surface du matériau piézoélectrique afin de réfléchir l'onde acoustique de surface. Ces systèmes à ondes acoustiques de surface permettent de mesurer une grande variété de stimuli, et il est connu que la fréquence de résonance ainsi que l'amplitude des signaux des dispositifs SAW comprenant un matériau magnétostrictif peut être en particulier modifiée sous champ magnétique. Des systèmes magnétiques SAW (MSAW) ont été proposés au cours de ces 50 dernières années à partir de matériaux magnétostrictifs. Plus précisément, on peut citer l'utilisation de couches de Ni, de $TbFe_2$ amorphe ou de multicouches de [$TbCo_2$/FeCo] déposées sur un substrat de Niobate de Lithium ou de quartz. L'état de l'art concernant les deux géométries explicitées ci-dessus a été présenté, bien que ce soit la géométrie de résonateur qui a été choisi pour la suite de ce travail dans le but de réaliser facilement des interrogations sans fils. Parmi les nombreux résultats, deux effets sont principalement étudiés. La variation en amplitude du signal dans les travaux concernant des effets de dynamique d'aimantation ; ainsi que la variation de fréquence de résonance (et donc de la vitesse de l'onde) dans des applications de type capteur. Concernant les effets de dynamique d'aimantation, la communauté scientifique a travaillé avec des géométries de ligne à retard. Les auteurs ont principalement obtenu des réponses magnéto-acoustiques dépendantes de l'anisotropie magnétique, et donc de la direction et de l'intensité du champ magnétique appliqué. Les formes obtenues sont dues à des variations des constantes élastiques, aux possibles hystérèses magnétiques ainsi qu'à des effets de champ magnéto-élastique dynamique créés par la propagation d'une onde accoustique dans un matériau ferromagnétique. Des modèles ont été développés afin de rendre compte de ces phénomènes. Concernant l'étude de la variation en fréquence, les deux géométries ont été étudiées. Malheureusement, les études ne corrèlent pas/peu la réponse magnéto-acoustique à la réponse magnétique et bien souvent, aucune caractérisation magnétique n'est présentée. Une seule étude sérieuse du point de vue magnétique existe, celle de Zhou *et al.*. Ces auteurs ont développé un modèle piézomagnétique équivalent afin de comprendre les réponses magnéto-acoustiques. Ils annoncent eux aussi que ce sont les variations des constantes élastiques en fonction du champ magnétique ainsi que le champ magnéto-élastique dynamique qui sont responsables des réponses magnéto-acoustiques pour différents types d'ondes, comme l'onde de Rayleigh et l'onde transverse horizontale de surface.
Cependant, parmi toutes ces études, la détection de champ magnétique par un dispositif SAW est encore limitée à de faibles champs magnétiques avec une sensibilité faible, et la possibilité de mesurer sans fil des champs bipolaires et/ou des champs élevés n'a pas été démontrée. Par ailleurs, si la réponse acoustique du dispositif ne présente pas d'ambiguïté liée à la réponse magnétique de l'élément

magnétostrictif, une corrélation précise entre réponse magnéto-acoustique et propriétés magnétiques reste à établir et à formaliser pour les différentes géométries de dispositifs et les différentes directions de mesure. Pour finir, la réponse magnéto-acoustique hors du plan n'a été que très peu étudiée et donne une variation quasi nulle de la fréquence de résonance. Derechef, cela représente une contrainte quant à la fabrication potentielle de capteurs industriels.

Après avoir défini les interrogations existantes dans ce domaine de recherche, le deuxième chapitre s'est concentré principalement sur les étapes de nano-fabrication. Les dispositifs réalisés permettent d'obtenir pour un même matériau deux directions perpendiculaires de propagation des ondes dans le plan de surface. Plusieurs longueurs d'onde et taux de métallisation sont aussi disponibles. Dans la suite de ce même chapitre, un modèle électrique a été développé afin de décrire les paramètres importants qui caractérisent les résonateurs. Les caractérisations électriques ont ensuite été exposées. Cela a permis de connaitre les fréquences de résonance des différentes ondes pour tous les dispositifs utilisés.

Les premières mesures sont rapportées dans le troisième chapitre, consacré aux dispositifs à base de Nickel de 50 nm sur LNO. C'est principalement le décalage de fréquence de résonance et non la variation en amplitude qui a été étudié. Les réponses magnéto-acoustiques des dispositifs (onde de Rayleigh et onde transverse de surface) ont été analysées pour différentes directions d'application du champ magnétique dans le plan et en comparaison des propriétés magnétiques du film de Nickel. Les résultats démontrent la sensibilité de l'onde acoustique au champ magnétique et il apparait également que la réponse magnéto-acoustique présente un phénomène d'hystérèse marqué pour un champ appliqué perpendiculairement à la direction de propagation des ondes, peu importe le magnétisme de l'échantillon mesuré avant les processus de nano-fabrication. Les réponses magnéto-acoustiques suivant la direction de propagation des ondes sont réversibles et les formes obtenues sont typiques de la variation des constantes élastiques sous champ suivant un axe de difficile aimantation. Par ailleurs, le modèle piézomagnétique équivalent développé par Zhou *et al.* a été utilisé afin de comprendre les formes des courbes et de montrer que les réponses magnéto-acoustiques réversibles ou hystérétiques apparaissent suivant un axe difficile et facile respectivement. Ces résultats ont donc démontré une possible réorientation de l'axe de facile aimantation dans le plan suivant les IDT, *i.e.* perpendiculaire à la direction de propagation des ondes, et donc le rôle de l'anisotropie de forme. Qui plus est, ce modèle a aussi mis en exergue l'impact du champ magnéto-élastique dynamique créé sous excitation acoustique. C'est d'ailleurs ce dernier qui est à l'origine de la variation de la réponse magnéto-acoustique pour un champ appliqué suivant l'axe facile ou pour un champ supérieur à la saturation magnétique. Bien que le modèle ne permette pas de simuler la réponse magnéto-acoustique lorsque le champ magnétique est appliqué perpendiculairement au plan du dispositif, des mesures expérimentales ont été menées. Une réponse hystérétique a pu être observée bien qu'une variation d'aimantation non hystérétique ait été mesurée. Il est en de même pour tous les capteurs étudiés. Pour finir, une interrogation à distance sur un capteur a été réalisée et le résultat, bien qu'attendu, s'est révélé probant.

Dans le quatrième chapitre, la corrélation entre le magnétisme et les réponses magnéto-acoustiques a été particulièrement étudiée. Tout d'abord, il a été possible de corréler le magnétisme des capteurs avec les réponses magnéto-acoustiques. En effet, grâce à des mesures de magnétorésistance anisotrope réalisées sur les IDT de Nickel, il a été démontré qu'un changement d'anisotropie dans les IDT par rapport au film continu apparaissait. Qui plus est, des simulations micromagnétiques ont confirmé que l'anisotropie de forme associée aux IDT conduit à un axe facile selon les IDT. La réponse réversible est donc obtenue lorsque le champ est appliqué suivant un axe difficile et la réponse irréversible lorsque le champ est suivant un axe facile. L'utilisation de matériaux magnétiques doux permet donc d'utiliser la forme des IDT afin de contrôler les réponses magnéto-acoustiques.
Concernant la réponse magnéto-acoustique hors du plan, des mesures de magnétométrie vectorielle ont montré que le comportement des composantes planaires de l'aimantation est à l'origine de cette hystérèse. Un moyen d'éviter l'hystérèse perpendiculaire est alors de supprimer l'hystérèse des composantes planaires, comme cela a été confirmé avec un système multicouches [Co/IrMn] où le champ d'échange dû à l'IrMn impose une anisotropie unidirectionnelle. Cela permet un renversement continu, sans saut, de la composante planaire de l'aimantation lors d'un champ appliqué perpendiculairement au plan de la couche.

Finalement, si le comportement hystérétique peut représenter un obstacle majeur à l'utilisation des dispositifs en tant que capteur, il est à noter que le comportement reste parfaitement réversible tant que le champ n'atteint pas le champ coercitif. L'utilisation de composés à fort champ coercitif tel le $TbFe_2$ ouvre alors la perspective au développement de capteurs bipolaires hauts champs. Néanmoins, le principal but était d'augmenter la sensibilité grâce à la forte magnétostriction du $TbFe_2$. Ce but n'a pas été atteint, principalement en raison de la présence de couche(s) tampon(s) et la dégradation du LNO lors de la montée en température pour les dépôts de couches minces.

Pour finir, le dernier chapitre a rassemblé des mesures dans des géométries moins conventionnelles. En effet, les dispositifs réalisés à base de Nickel de 200 nm ont montré la suppression de l'hystérèse de la réponse magnéto-acoustique grâce à une morphologie en domaines à aimantation perpendiculaire. La présence de ces domaines a pu être vérifiée grâce à une étude par microscopie à force magnétique. Puis, la réponse magnétique d'une onde de volume (BAW) proche de 1 GHz a été étudiée. Cette réponse est présente sur tous les dispositifs synthétisés lors de cette thèse, y compris sur un dispositif SAW non magnétique (avec des IDT en Aluminium). La réponse des capteurs présente une forte variation en amplitude mais est isotrope en fonction de la direction du champ magnétique appliqué. Il a été démontré qu'elle provenait des connecteurs placés entre le capteur et l'appareil de mesure, mais que cet effet n'influait pas sur les réponses magnétiques des ondes de Rayleigh et QSVSAW/QSHSAW.

En conclusion de ce travail de thèse, nous avons apporté beaucoup de réponses quant à l'utilisation de ces dispositifs en tant que capteurs magnétiques. Tout cela grâce à une compréhension du magnétisme et de la structure des matériaux actifs intégrés au dispositif.
En terme d'amélioration ou d'optimisation des systèmes hybrides, il sera préalablement nécessaire d'étudier plus attentivement les barrières chimiques que sont les couches tampons ainsi que la dégradation du Niobate de Lithium quand il est chauffé. Cela pourra être réalisé à l'aide de techniques de caractérisations de chimie de surface présentes *in-situ* dans l'instrument Davm (tube d'interconnection sous ultra-vide) de l'IJL. Une piste de recherche consistera à utiliser des substrats stoichiométriques, ainsi que de nouvelles combinaisons de matériaux.
Au delà de ces expériences, il sera nécessaire d'approfondir le rôle du couplage élastique aux interfaces. Une question importante consiste à savoir dans quelle mesure une déformation du réseau de l'un des constituants du système hybride se transmet au second constituant. Nous avons pour projet de réaliser des mesures de diffraction de rayons X sous champ magnétique et/ou électrique statique afin d'observer la déformation du système hybride. Nous pourrons ainsi évaluer le rôle de la cristallinité, des couches tampons, et de la morphologie des films magnétiques sur le couplage élastique. Puis, des mesures de diffraction de rayons X résolues en temps ont montré récemment la possibilité de suivre les perturbations du réseau cristallin (propagation d'une onde acoustique) lors d'une excitation électrique. Nous avons aussi pour projet de répéter ces expériences sur les systèmes hybrides.
Enfin, d'un point de vue industriel, il faudra évidemment augmenter l'amplitude de variation de fréquence en fonction du champ appliqué dans les dispositifs magnétiques à ondes acoustiques de surface. Cela sera envisageable par des changements de taux de métallisation ainsi que par l'utilisation d'ondes confinées dans le matériau magnétique. De multiples pistes quant aux diverses fonctionnalités liées aux effets de formes et *tutti quanti* sont aussi poursuivies et actuellement en cours d'exploration par un doctorant de l'équipe 405 dans la continuité de ce travail de thèse.

APPENDICES

This section is devoted to appendices.
Appendix A presents the two methods used during this work for thin film growth: the molecular beam epitaxy and the sputtering. Appendix B presents the calculation to determine the easy magnetization axis in strained $TbFe_2$ films. Appendix C presents the various X-ray diffraction setups and experiments used throughout this thesis. Appendix D presents the common types of orientation relationships between (110) bcc and (111) fcp or (0001) hcp surfaces. Appendix E recalls the main aspects of the RHEED analysis technique. Finally, appendix F gives complementary information on the magnetic properties of magnetic materials exhibiting strong stripes or exchange bias.

Appendix A: Thin film deposition techniques

Molecular Beam Epitaxy (MBE)

Epitaxy is a term derived from Greek "epi" meaning above and "taxis" meaning in an ordered manner. The word epitaxy is thus used for atoms deposition on a substrate or on a buffer layer in an ordered manner. MBE refers to the epitaxy achieved by using a highly controlled molecular beam. The now well-established MBE technique started to develop in the 1960´s, and has been since used in research studies and industrial production. It is nowadays used to grow a large number of structures including semiconductors, metals, insulators, oxides, organic materials. One of the key elements of MBE equipments is the vacuum level. Absolute pressures in the range of 10^{-10} -10^{-11} Torr enable to avoid contamination of the surfaces, obtain a large mean free path of atomic fluxes, which provides an optimized control of deposition parameters.
Pictures of the MBE setup used during this work (outside (a) and inside (b)) are shown in Figure 107.

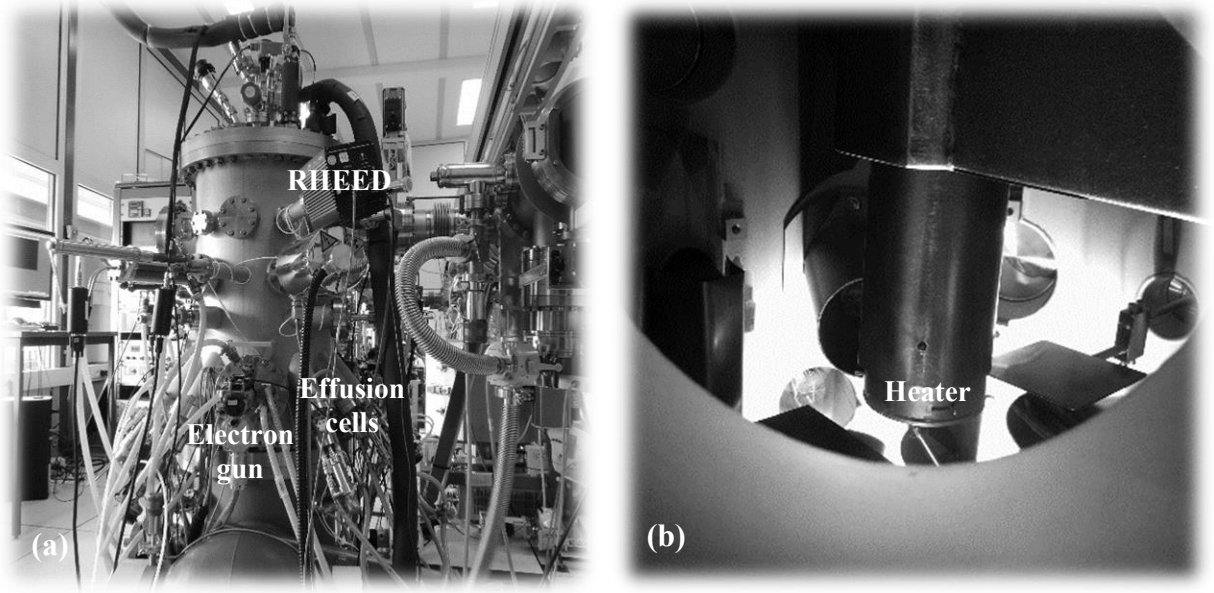

Figure 107. Outside view of the MBE chamber showing effusion cells, electron gun and RHEED characterization equipment (a). Inside view showing the sample holder and the heater (b).

Pressure control: achieving an ultrahigh vacuum

The expression UHV (Ultra High Vacuum) means that pressures are lower than 10^{-7} Torr. The evaporation chamber is pumped with a turbo molecular pump (36000 rev/min) connected to a primary pump. The light elements being not easily pumped, a Titanium sublimation pump helps improving the vacuum. A cryogenic trap that adsorbs molecules on its surface finally completes the vacuum techniques during a sample growth. The chamber is equipped with a mass spectrometer that allows the determination of residual gas pressures and thus the detection of possible contaminants or leaks.

The evaporation sources

Two types of evaporation sources are attached to the MBE setup:

(i) Effusion cells are used for materials that can be evaporated at low or moderate temperatures (maximum 2000 °C for high temperature cells). A crucible hosting the material to be evaporated or sublimated is heated by a filament located around or close to the crucible (Joule effect). The choice of the crucible is based on evaporation temperature and possible reactivity with the element. For some materials, it is necessary to use a supplementary liner in order to avoid a chemical reaction with the crucible. The cells temperatures are regulated (Shimaden or Eurotherm temperature controllers) to approximately ± 0.1 °C to insure a high stability of the evaporated flux and thus of the deposition rate.
Six effusion cells are available in the MBE setup. Three cells have been used in this work for Terbium, Iron and Gold, as detailed in the Table 14.

Material	Evaporation temperature range (°C)	Crucible/Liner
Tb	1280-1350	Ta/no liner
Fe	1220-1320	Ta/Al_2O_3
Au	1000-1100	Ta/Al_2O_3

Table 14. Type of crucible/liner and evaporation temperature range for materials evaporated from effusion cells in this thesis.

(ii) Electron guns are used for materials with evaporation temperatures above 2000 °C. A 8 kV electron beam is swept (deflecting magnetic field) on the material surface to heat it and yield the material evaporation. Once again, it is necessary for certain materials to use a supplementary liner in order to avoid a chemical reaction with the Cu crucible. A quartz crystal microbalance is positioned above each e-gun crucible to monitor the evaporated flux during the deposition process. A feedback loop between the thickness controller and the e-guns power supply adjusts the electron beam current to insure a stable evaporation rate.
Molybdenum, Titanium and Niobium have been evaporated from electron guns, as detailed in the Table 15.

Material	Evaporation power range (W)	Crucible/Liner
Mo	800-1400	Cu/C
Ti	320-400	Cu/C
Nb	1440-1680	Cu/no liner

Table 15. Type of crucible/liner and evaporation power range used for material evaporated from electron guns in this thesis.

Control of the deposited thickness

The control of the material flux during deposition is crucial to control the thickness of the layers. In the case of alloys, the control and stability of relative atomic fluxes for the different elements is essential to reach the targeted stoichiometry and insure a good homogeneity.
Several quartz crystal microbalances associated to an IC6 controller (Inficon) can be used in the MBE setup. In a first approximation, the quartz oscillation frequency varies linearly with the mass deposited on its surface and thus with the thickness of the deposited material. This allows determining the deposition rates of the different elements at the quartz position. A preliminary calibration (X-ray reflectometry) might be necessary to rely the deposition rates at the quartz and at the substrate position. As mentioned previously, a quartz crystal microbalance is positioned above each e-gun crucible to monitor the evaporated flux during the deposition process. The feedback loop ensures a stable deposition rate. A supplementary quartz microbalance can be inserted at the sample position. This one is used to

determine the deposition rate from effusion cells prior a sample fabrication. The stabilized power supply connected to temperature controllers ensures a stable deposition rate from the cells during the deposition proess.

$TbFe_2$ alloy

In order to get the right $TbFe_2$ stoichiometry, the atomic flux of Fe must be twice the atomic flux of Tb. Thus:

$$2.\frac{v_{Tb}(nm.s^{-1}).Density_{Tb}}{Molar\ mass_{Tb}} = \frac{v_{Fe}(nm.s^{-1}).Density_{Fe}}{Molar\ mass_{Fe}}$$

$$v_{Tb}(nm.s^{-1}) = \frac{1}{2}.v_{Fe}(nm.s^{-1}).\frac{Density_{Fe}}{Density_{Tb}}.\frac{Molar\ mass_{Tb}}{Molar\ mass_{Fe}}$$

$$v_{Tb}(nm.s^{-1}) = 1.36326.v_{Fe}(nm.s^{-1})$$

The molar masses are 55.84 $g.mol^{-1}$ and 158.92 $g.mol^{-1}$ for Fe and Tb respectively [PER11]. The densities are 7.874 $g.cm^{-3}$ and 8.219 $g.cm^{-3}$ for Fe and Tb repectively [PER11].
The usual deposition rates for Fe and Tb are between 0.005 $nm.s^{-1}$ and 0.02 $nm.s^{-1}$.

Capping layer

Iron and Terbium can easily oxidized in air. It is necessary to cover all samples with a capping layer. Multiple candidates have been tested but Gold was our final choice. Gold is deposited between 50 and 150 °C for several reasons: it slightly oxidizes in air, it is not magnetic and it absorbs some electromagnetic radiation. A thickness of 5 nm is chosen.

Sputtering process

This technique is carried out in a vacuum chamber using a cold Ar plasma. The substrate on which the material is deposited is mounted on a spot located approximately at 10 cm from the target. Since the sample is not located in the plasma, it does not cause any degradation of the surface. Deposition is often performed at room temperature by cooling the sample. Ar is introduced into the enclosure at typical pressure of 10^{-3} - 10^{-4} Torr. However, it is also possible to work under a reactive atmosphere, with a chemically active gas chosen as a function of the materials to be deposited. A plasma is created by electric discharge, by negatively polarizing the cathode (connected to the target (the material to deposit)) at DC voltage of few V to several kV. The plasma ions, attracted by the cathode, bombard the target and tear apart atoms (or clusters of atoms), which then condense on the substrate. This process is only valid for depositing metallic and conductive materials. In the case where insulating materials are required, it is not possible to apply a constant voltage since there would be accumulation of electrical charges brought by the ions at the level of the target. An AC deposition technique (RF-sputtering) is therefore used: the target is alternately polarized positively and negatively at high frequency (13.56 MHz). The alternation of the sign makes it possible to evacuate the electrical charges. In order to increase the rate of deposition, there is a way to confine plasma ions by use of a magnetic field: this technique is called magnetron sputtering. One or more magnets of strong magnetization are installed under the target in order to confine the plasma near the target. This has the effect of increasing the ionization of the gas and therefore the density of the plasma.
Picture of our magnetron sputtering setup is shown in Figure 108.

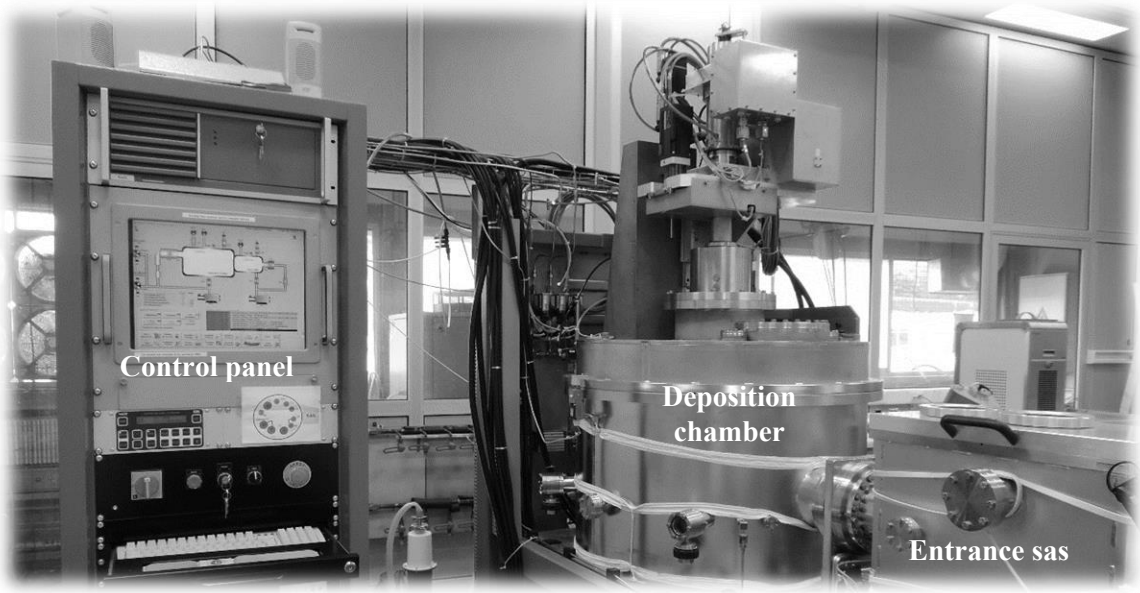

Figure 108. Magnetron sputtering setup showing control panel, deposition chamber and entrance sas load lock chamber.

Control of the thickness deposited

For a given value of Ar pressure and RF or DC power, the deposition rate is constant and reproducible. The sample-holder is moved on top of the target, forth and back along one axis during the process, which ensures homogeneity in thickness over the surface. The flow is pre-calibrated with reflectometry or profilometer steps.

Interest and difference with MBE process

Although epitaxial growth is generally achieved by MBE, the sputtering technique can also in some cases provide deposits with high crystalline quality and order. The main difference between these two techniques comes from the deposition rate and the working pressure. With sputtering process, it is possible to obtain a very high deposition flux and knowing that the deposits are often made at room temperature, the layer production can be very fast. That's why sputtering is superior to MBE for the vast majority of industrial purposes. MBE is simply too cost prohibitive to be a feasible option to make affordable products. Nevertheless, the working pressure of sputtering process is limited by the sputter gas. Thin films layers can then contain a lot of impurities and structural defects.

References

[PER11] D. L. Perry, *Handbook of inorganic compounds*, CRC press, second edition, (2011).

Appendix B: Easy magnetization axis in a strained $TbFe_2$ epitaxial film

As explained in the first part dealing with the properties of ferromagnetic materials, a lattice strain can induce a change in the direction of magnetization. This appendix presents the calculation to determine the easy magnetization direction (the magnetization direction cosines) in a strained $REFe_2$ film; numerical results are only given for the $TbFe_2$ compound.

The energy contribution that depends on the magnetization direction is the sum of the magnetocrystalline anisotropy (depending on K_i), the magnetoelastic energy (depending on b_i) and the shape anisotropy:

$$\begin{aligned} U = {} & K_1\left(\alpha_x^2\alpha_y^2 + \alpha_x^2\alpha_z^2 + \alpha_y^2\alpha_z^2\right) + K_2\left(\alpha_x^2\alpha_y^2\alpha_z^2\right) + K_3\left(\alpha_x^4\alpha_y^4 + \alpha_x^4\alpha_z^4 + \alpha_y^4\alpha_z^4\right) \\ & + b_0\left(\varepsilon_{xx} + \varepsilon_{yy} + \varepsilon_{zz}\right) + b_1\left(\alpha_x^2\varepsilon_{xx} + \alpha_y^2\varepsilon_{yy} + \alpha_z^2\varepsilon_{zz}\right) \\ & + b_2\left(\alpha_x\alpha_y\varepsilon_{xy} + \alpha_x\alpha_z\varepsilon_{xz} + \alpha_y\alpha_z\varepsilon_{yz}\right) - \frac{\mu_0}{2}\vec{M}.\overrightarrow{H_D} \end{aligned}$$

This expression can be simplified in $REFe_2$ since K_3, b_0 and b_1 are generally neglected compared to other anisotropy and magnetoelatic constants:

$$\begin{aligned} U = {} & K_1\left(\alpha_x^2\alpha_y^2 + \alpha_x^2\alpha_z^2 + \alpha_y^2\alpha_z^2\right) + K_2\left(\alpha_x^2\alpha_y^2\alpha_z^2\right) \\ & + b_2\left(\alpha_x\alpha_y\varepsilon_{xy} + \alpha_x\alpha_z\varepsilon_{xz} + \alpha_y\alpha_z\varepsilon_{yz}\right) - \frac{\mu_0}{2}\vec{M}.\overrightarrow{H_D} \end{aligned}$$

The point is to determine the magnetization direction cosines that lead to the lowest energy.
Since experiments permit to determine easily the strain perpendicular to the growth plane $\varepsilon_\perp$ and possibly the stain in the growth plane $\varepsilon_{//}$ (assumed isotropic), Cartesian strains ε_{ij} have to be expressed as a function of $\varepsilon_\perp$ and $\varepsilon_{//}$.
For this, we use the relation: $\varepsilon_{\vec{n}} = \{\vec{n}\}^t(\varepsilon)\{\vec{n}\}$, $\vec{n}$ being the direction in which the strain $\varepsilon_{\vec{n}}$ is observed. Different sets of $\vec{n}$ vectors are chosen depending on the geometry of the system, *i.e.* on the growth direction.

$REFe_2$ (110) growth

[110] is the growth direction, while [001] and $[1\bar{1}0]$ are in-plane perpendicular directions. These directions are expressed in the initial Cartesian coordinate systems:

$[1\bar{1}0]$ direction: $\vec{n}_1 = \frac{\sqrt{2}}{2}\vec{\imath} - \frac{\sqrt{2}}{2}\vec{\jmath}$

[110] direction: $\vec{n}_2 = \frac{\sqrt{2}}{2}\vec{\imath} + \frac{\sqrt{2}}{2}\vec{\jmath}$

[001] direction: $\vec{n}_3 = \vec{k}$

The corresponding strains are calculated:

$$\begin{cases} \varepsilon_{\vec{n}_1} = \frac{1}{2}\varepsilon_{xx} + \frac{1}{2}\varepsilon_{yy} - \varepsilon_{xy} = \varepsilon_{//} \\ \varepsilon_{\vec{n}_2} = \frac{1}{2}\varepsilon_{xx} + \frac{1}{2}\varepsilon_{yy} + \varepsilon_{xy} = \varepsilon_\perp \\ \varepsilon_{\vec{n}_3} = \varepsilon_{zz} = \varepsilon_{//} \end{cases}$$

For this growth direction, the symmetry gives $\varepsilon_{xx} = \varepsilon_{yy}$. ε_{xz} and ε_{yz} are neglected and, as mentioned before, in-plane strains are assumed isotropic, *i.e.* $\varepsilon_{\vec{n}_1} = \varepsilon_{\vec{n}_3}$.
One can eventually deduce the following relations:

$$\begin{cases} \varepsilon_{xx} = \varepsilon_{yy} = \frac{\varepsilon_\perp + \varepsilon_{//}}{2} \\ \varepsilon_{xy} = \frac{\varepsilon_\perp - \varepsilon_{//}}{2} \\ \varepsilon_{zz} = \varepsilon_{//} \end{cases}$$

Therefore, magnetoelastic energy becomes: $E_{m.e} = \frac{b_2(\varepsilon_\perp - \varepsilon_{//})\alpha_x\alpha_y}{2}$

Shape anisotropy for this growth direction is written: $E_D = \frac{\mu_0 {M_s}^2(\alpha_x+\alpha_y)^2}{4}$

And the resulting total energy is:

$$U = K_1\left(\alpha_x^2\alpha_y^2 + \alpha_x^2\alpha_z^2 + \alpha_y^2\alpha_z^2\right) + K_2\left(\alpha_x^2\alpha_y^2\alpha_z^2\right) + \frac{b_2(\varepsilon_\perp - \varepsilon_{//})\alpha_x\alpha_y}{2} + \frac{\mu_0 {M_s}^2(\alpha_x+\alpha_y)^2}{4}$$

With the room temperature values of K_1 (-6.3×10^6 J.m^{-3}), K_2 (6×10^5 J.m^{-3}) and b_2 (-3.7×10^8 J.m^{-3}) given in Table 1 and Table 2 and the value of 800 kA.m^{-1} for the saturation magnetization in $TbFe_2$, one can calculate (Wolfram Mathematica software) the equilibrium magnetization direction for various $(\varepsilon_\perp - \varepsilon_{//})$ values (Figure 109 (a)).

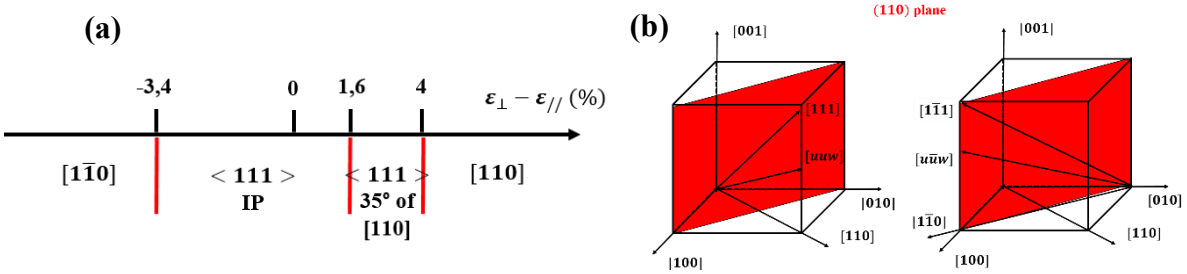

Figure 109. Evolution of the easy magnetization direction in a strained $TbFe_2$ epitaxial film for a [110] growth direction (a). Sketch of the different directions obtained in cubic symmetry (b). The growth plane is in red.

When only the magnetocrystalline energy is taken into account, the direction of easy magnetization is identical to the bulk material. Therefore, the easy magnetization direction lies along arbitrary $< 111 >$ (since K_1 is negative [ATZ76]). However, the demagnetizing field pulls the magnetization towards the plane of the layer. Therefore, the magnetization is distributed along the in-plane $< 111 >$ directions. For increasing positive shear strain, the magnetization tends towards the out of plane $< 111 >$, at approximatively 35° from the perpendicular [110] direction. When the strain becomes higher, the magnetization rotates ($< uuw >$ directions) towards [110]. On the contrary, for increasing negative shear strains (absolute value), the magnetization rotates in the layer plane ($< u\bar{u}w >$ directions) towards the [1$\bar{1}$0] direction. One can notice the asymmetry in these limit values (between positive and negative strains), due to the additional energy required to overcome the demagnetizing energy and align the magnetization out of the plane.

$REFe_2$ (111) growth

[111] is the growth direction, while [11$\bar{2}$] and [1$\bar{1}$0] are in-plane perpendicular directions. These directions are expressed in the initial Cartesian coordinate systems:

[1$\bar{1}$0] direction: $\vec{n}_1 = \frac{\sqrt{2}}{2}\vec{\imath} - \frac{\sqrt{2}}{2}\vec{\jmath}$

[111] direction: $\vec{n}_2 = \frac{\sqrt{3}}{3}\vec{\imath} + \frac{\sqrt{3}}{2}\vec{\jmath} + \frac{\sqrt{3}}{3}\vec{k}$

[11$\bar{2}$] direction: $\vec{n}_3 = \frac{\sqrt{6}}{6}\vec{\imath} + \frac{\sqrt{6}}{6}\vec{\jmath} - 2\frac{\sqrt{6}}{6}\vec{k}$

As for the previous case, one can calculate the corresponding strains along these in-plane and perpendicular directions. Since the symmetry leads here to $\varepsilon_{xx} = \varepsilon_{yy} = \varepsilon_{zz}$ and $\varepsilon_{xy} = \varepsilon_{xz} = \varepsilon_{yz}$, the following relations are eventually obtained:

$$\begin{cases} \varepsilon_{xx} = \varepsilon_{yy} = \varepsilon_{zz} = \frac{1}{3}(\varepsilon_{\perp} + 2\varepsilon_{//}) \\ \varepsilon_{xy} = \varepsilon_{xz} = \varepsilon_{yz} = \frac{1}{3}(\varepsilon_{\perp} - \varepsilon_{//}) \end{cases}$$

which leads to the magnetoelastic energy: $E_{m.e} = \frac{b_2(\varepsilon_{\perp}-\varepsilon_{//})(\alpha_x\alpha_y+\alpha_x\alpha_z+\alpha_y\alpha_z)}{3}$

Shape anisotropy for this growth direction is written: $E_D = \frac{\mu_0 {M_s}^2(\alpha_x+\alpha_y+\alpha_z)^2}{6}$

And the resulting total energy is:

$$U = K_1(\alpha_x^2\alpha_y^2 + \alpha_x^2\alpha_z^2 + \alpha_y^2\alpha_z^2) + K_2(\alpha_x^2\alpha_y^2\alpha_z^2) + \frac{b_2(\varepsilon_{\perp} - \varepsilon_{//})(\alpha_x\alpha_y + \alpha_x\alpha_z + \alpha_y\alpha_z)}{3} + \frac{\mu_0 {M_s}^2(\alpha_x + \alpha_y + \alpha_z)^2}{6}$$

With the same constants and the same numerical protocol than for $TbFe_2$ (110) growth, one can calculate the equilibrium magnetization directions for various $(\varepsilon_{\perp} - \varepsilon_{//})$ values (Figure 110 (a)).

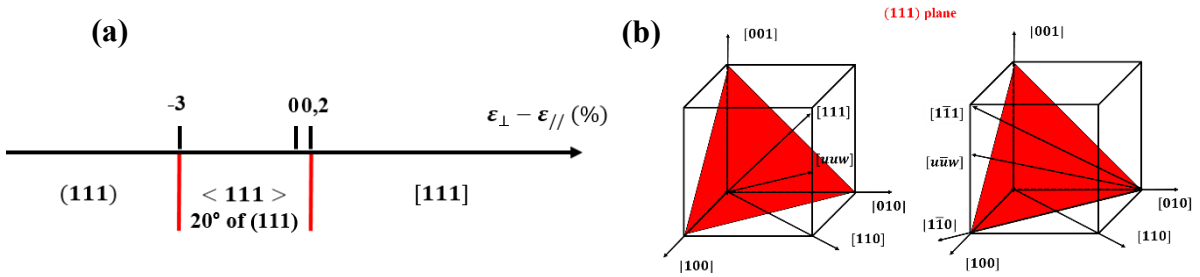

Figure 110. Evolution of the easy magnetization direction in a strained $TbFe_2$ epitaxial film for a [111] growth direction (a). Sketch of the different directions obtained in cubic symmetry (b). The growth plane is in red.

Once again, for zero shear strain, the demagnetizing field pulls the magnetization towards the < 111 > closest to the plane (at 20° from the growth plane). For increasing negative shear strains (absolute value), the easy magnetization rotates towards the (111) growth plane, without specific in-plane anisotropy. For increasing positive shear strains, a relatively moderate strain value brings the magnetization axis collinear to [111], *i.e.* normal to the sample plane. This direction is favored by both the magnetoelastic energy and the magnetocrystalline energy that counterbalance the demagnetizing field.

References

[ATZ76] U. Atzmony and M. P. Daniel, *Non major cubic symmetry axes of easy magnetization in rare-earth-iron Laves compounds*, Phys. Rev. B. **13**, 4006, (1976).

Appendix C: X-ray diffraction experiments

The X-Ray Diffraction (XRD) is a commonly used non-destructive approach for the structural analysis of thin films. Different configurations (detailed in the following) can easily bring valuable information on the structural quality, orientation and strained state of the film.

Experimental setups

Two different setups have been used during this work:

(i) XRD experiments have been performed using a PanAnalytical X'Pert Pro diffractometer with a wavelength of 0.154056 nm (K_α wavelength of the Copper anode). Dedicated primary and secondary optical blocks (respectively mounted before the sample and before the detector) enable high resolution and high sensitivity measurements in the small and large angle ranges.
The primary optical block is an hybrid monochromator composed of mirror and a channel-cut Germanium crystal. The mirror performs a pre-collimation of the divergent beam projected by an X-ray tube to a quasi-parallel beam. The K_α spectral component is separated by the monochromator crystal. The secondary optical block is composed of either a Parallel Plate Collimator (PPC), *i.e.* a set of parallel plates, or a Triple Axis monochromator to obtain a maximal resolution (but reduced intensity) to measure strain. This latter optical block is composed of two (220) Ge crystals configured to obtain three consecutive reflections and thus to limit the angular divergence of the diffracted X-ray beam. Moreover, a PIXcel detector with extremely high dynamic range and low noise is used behind the secondary block.
(ii) Pole figures and high temperature XRD measurements have been performed with a D8 discover (Bruker) instrument with a wavelength of 0.178901 nm (K_α wavelength of the Cobalt anode). This diffractometer is in "constant 2θ" configuration with a 300 mm diameter goniometric circle equipped with an Euler circle. An inclination angle χ of the sample is available over the [0° - 80°] range. The main advantage of such a geometry is the possibility of using heavy loads such an oven. Measurements can thus be carried out with a DHS1100 chamber at temperatures up to 1000 °C at atmospheric pressure. The primary optic is a polycapillary lens giving a parallel or pseudo-parallel beam. A fast detector type LynxEye (PSD: Position Sensitive Detector) with a 2.9° acceptance angle is used.

Large angle X-ray diffraction experiments

When incoming X-rays with a wavelength λ are scattered by the crystal lattice, constructive interferences occur when the Bragg's law given by: $n\lambda = 2d_{hkl}\sin(\theta)$ is satisfied. d_{hkl} is the interplanar distance between parallel (*hkl)* atomic planes, n is an integer and θ is the angle between the incoming X-ray beam and the atomic planes. X-rays are diffracted at an angle 2θ respect to the incident beam.
Two types of configurations have been used during this work: the symmetrical (specular) one and the non-symmetrical one.

Symmetrical configuration

In the specular geometry (Figure 111), the scattering vector $\vec{q}$ (defined as the difference between scattered and incident wave vectors) is collinear to the vector normal to the film surface ($\vec{n}$). In this case, the atomic planes that can lead to X-ray diffraction are the ones parallel to the surface plane. The θ

Bragg angle appearing in the Bragg's law is the angle between incoming X-rays and the surface, and the angle between scattered X-rays and the surface.
XRD experiments in specular geometry are performed in rotating both the sample (ω) and the detector (2θ) so that the scattering vector direction remains unchanged. The intensity is collected as a function of the angle, and Bragg peaks are observed when the conditions of diffraction are satisfied.

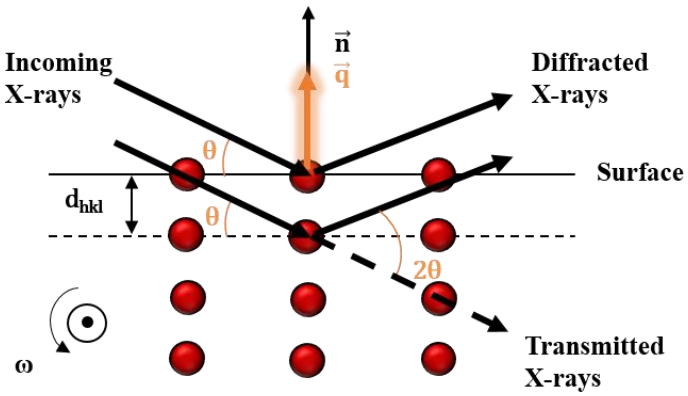

Figure 111. Sketch of the large angle X-ray diffraction experiment in symmetrical configuration (see text).

This commonly used configuration allows to determine several important structural parameters.
(i) The identification of the observed Bragg peaks gives information on the atomic planes parallel to the surface plane, *i.e.* on the growth direction. The occurrence of Bragg peaks related to different (*hkl*) sets would reveal the presence of several growth directions, *i.e.* of domains with different orientations.
(ii) The position of the Bragg peak is directly linked to the inter-reticular distance, *i.e.* to the lattice constant along the perpendicular direction (the growth direction). An accurate measurement and comparison with the bulk materials (see Table 16) allows us determining the possible lattice strain in this perpendicular direction.

Material (Space group)	Lattice constants (nm)
$LiNbO_3$ ($R\bar{3}c$)	a = b = 0.5149 c = 1.386
Ti ($P63/mmc$)	a = b = 0.2951 c =0.47
Nb ($Im\bar{3}m$)	a = b = c = 0.33
Mo ($Im\bar{3}m$)	a = b = c = 0.3145
Ni ($Fm\bar{3}m$)	a = b = c = 0.353
Co ($Fm\bar{3}m$)	a = b = c = 0.355
$IrMn_3$ ($Fm\bar{3}m$)	a = b = c = 0.378
$TbFe_2$ ($Fd\bar{3}m$)	a = b = c = 0.5196

Table 16. Materials, space groups and lattice constants used in this PhD work.

(iii) The width of the Bragg peak is related to the structural coherence length ξ along this perpendicular direction, *i.e.* the length over which the average lattice constant can be considered constant.

$\xi = \frac{2\pi}{\Delta q - \Delta q_o}$, where Δq (with $q = \frac{4\pi \sin(\theta)}{\lambda}$ (nm^{-1})) is the FWHM of the Bragg peak and Δq_o the width due to the instrumental resolution. The substrate being considered as a perfect crystal, this instrumental resolution can be reasonably estimated by the substrate's Bragg peak FWHM.
(iv) A final important information can be obtained in a slightly different measurement configuration: the intensity measurement when the sample is rotated around the Bragg peak position (ω), the detector being kept at fixed position. This so-called "rocking curve" corresponds to a tilt of the scattering vector (fixed amplitude) in the scattering plane. The FWHM of the rocking curve corresponds to the dispersion of the normal of the diffraction planes, the so-called "mosaicity", and is a good estimate of the crystalline order quality.

The non-symmetrical configuration

In the non-symmetrical geometry (Figure 112), the scattering vector $\vec{q}$ is no more collinear to $\vec{n}$. The angles between incoming X-rays and the surface and between the surface and diffracted X-rays are different. This configuration permits to probe atomic planes that are not parallel to the surface, those sharing a common zone axis that is perpendicular to the scattering plane (the normal to the plane sheet, also rotation axis for ω in Figure 112).

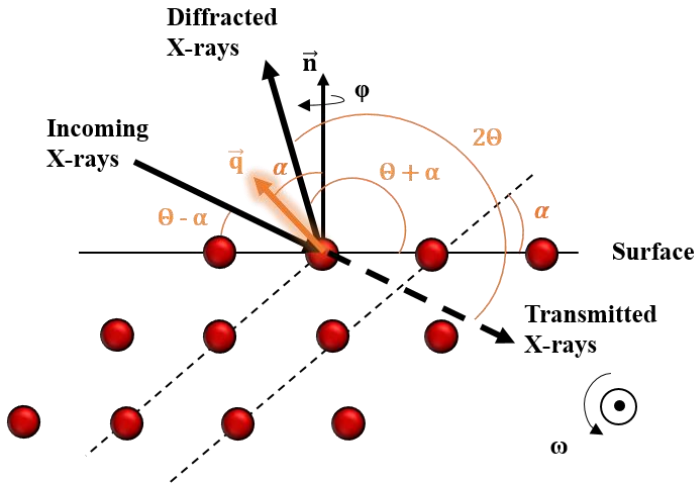

Figure 112. Sketch of the X-ray diffraction in non-symmetrical configuration (see text).

Three different types of investigation have been performed in this configuration:
(i) *The determination of the in-plane orientation knowing the growth direction.*
The idea consists in measuring selected asymmetrical Bragg reflections (ω and 2θ angles are fixed to satisfy the Bragg's law, knowing the α angle) while rotating the sample around its surface normal (φ angle, see Figure 112), thus performing so-called "φ scans". Asymmetrical Bragg reflections are chosen because the corresponding diffracting planes share a direction of interest with the surface plane. As explained previously, these atomic planes would scatter the X-ray beam only when the direction of interest is brought perpendicular to the scattering plane. The occurrence of several φ angles where intensity is measured can be related to the symmetry of the system or reveal the existence of several domains or variants. The measurement of the φ dependence of several different asymmetrical Bragg reflections is generally required to get a complete description of the in-plane orientation and possible occurrence of domains.
Such measurements have been extensively performed to analyze the in-plane and relative orientations of various materials (LNO, Mo, Ti, Nb and $TbFe_2$). The Table 17 gathers for the different materials the measured asymmetrical reflections and the corresponding in-plane directions that can be thus determined.

Material	Searched plane	Associated directions
LNO Z-cut	$(11\bar{2}9)$ $(30\bar{3}12)$	$<1\bar{1}00>$ $<11\bar{2}0>$
Ti (0001)	$(11\bar{2}4)$ $(10\bar{1}3)$	$<1\bar{1}00>$ $<11\bar{2}0>$
Nb/Mo (110)	(310) (121) (222) (301)	$<001>$ $<1\bar{1}1>$ $<1\bar{1}0>$ $<1\bar{1}3>$
$TbFe_2$ (111)	(440) (642)	$<1\bar{1}0>$ $<11\bar{2}>$
$TbFe_2$ (110)	(620) (422)	$<001>$ $<1\bar{1}1>$

Table 17. Asymmetrical Bragg reflections measured with φ scans for the different materials and in-plane directions that can be deduced.

(ii) *The determination of a common off specular direction shared by different layers*.
Once the in-plane orientation determined, the measurement consists in a scan along a direction which is tilted respect to the normal to the surface (scattering vector direction fixed). This allows us determining various sets of atomic planes (tilted from the surface) parallel to each other in the different layers.
(iii) *The determination of the crystal orientation and the possible occurrence of several domains in case of complex growth*.
This approach consists in measuring so-called "pole figures" to determine the various possible locations in space of directions perpendicular to a given set of atomic planes (poles).
Experimentally, the X-ray source and detector positions are chosen and fixed for a given Bragg reflection. Multiple scans are then performed in rotating the sample around its normal (φ) for different inclination angles (χ) respect to the scattering vector. Intensity is measured when the sample's orientation permits to bring the pole of interest along the scattering vector. The results are presented as pole figures where the center corresponds to the sample's normal and the outer circle corresponds to the sample plane. The distance ρ between the center and the measured pole is simply related to the χ angle. Such pole figures can be directly compared to stereographic projections (or stereograms).
Stereograms are commonly used to represent a 3D crystal orientation in a 2D plane. The principle is sketched in Figure 113: a direction X cuts the sphere in a point P called the *spherical projection*. The *stereographic projection* p is the intersection point of the (SP) direction (connecting the south pole S and P) with the equatorial plane. The various stereographic projections in the equatorial plane form the stereogram.
The comparison of experimental poles with the stereograms expected for various orientations permits to analyze the symmetry of the system, the orientation of the crystal lattice respect to the sample and the possible occurrence of differently oriented crystalline domains. The comparison of pole figures measured for the different materials present in a layered system can also bring relevant information on the 3D orientation relationships between the different lattices.

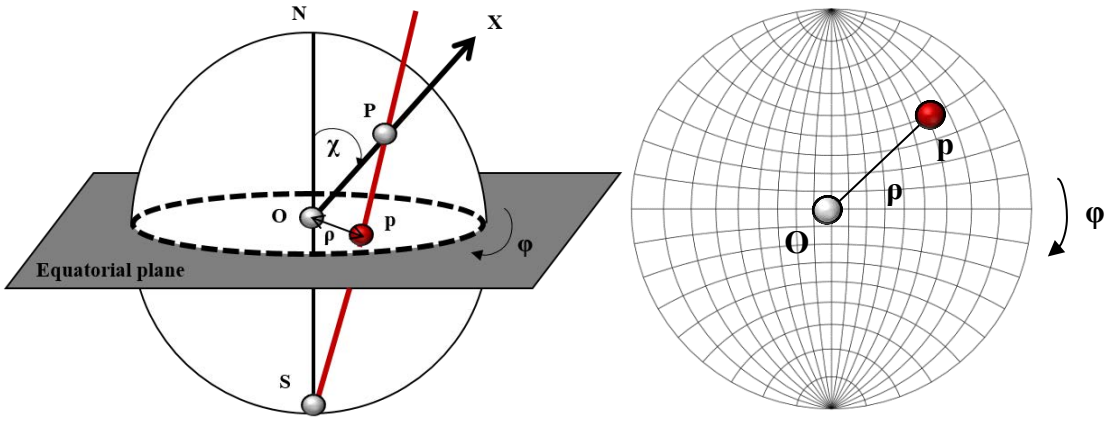

Figure 113. Principle of the stereographic projection (see text).

Appendix D: Orientation relationships between (110) bcc and (111) fcc / (0001) hcp surfaces

This section recalls the orientation relationships commonly observed/reported between the (110) surface of a bcc crystal and the (111) surface of a fcc or (0001) surface of a hcp crystal. (111) fcc and (0001) hcp both present the same hexagonal symmetry and the main directions $< 1\bar{1}0 >$ and $< 11\bar{2} >$ of (111) fcc are equivalent to $< 11\bar{2}0 >$ and $< 1\bar{1}00 >$ of (0001) hcp respectively. The nearest neighbor distances are the same. Only the case of (111) fcc will thus be presented here.

Figure 114 shows the (111) fcc lattice and the (110) bcc lattice. The nearest neighbor distance in fcc is called y and the nearest neighbor distance in bcc is called x.

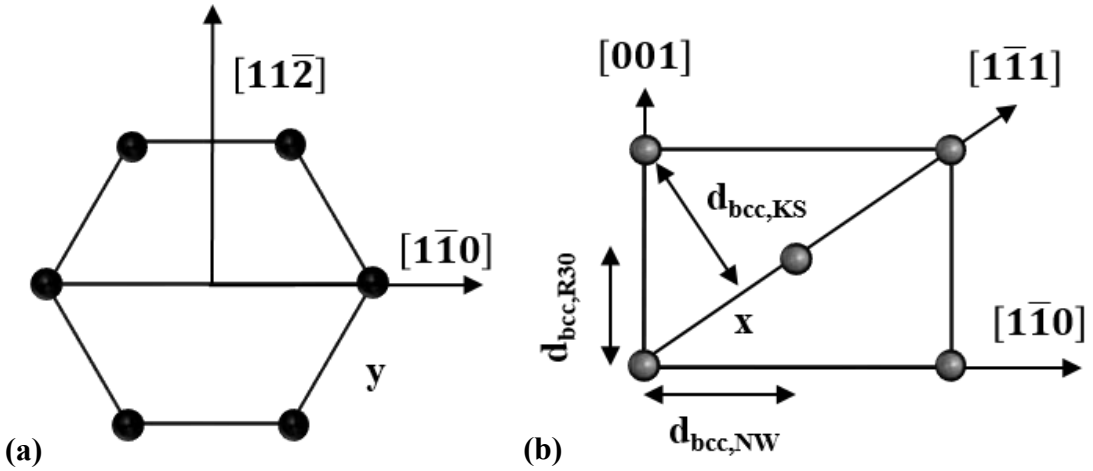

Figure 114. Sketch for (111) fcc (a) and (110) bcc (b) with nearest-neighbor distances y and x. $d_{bcc,\ KS}$, $d_{bcc,\ NW}$ and $d_{bcc,\ R30}$ are the densely-packed row distances corresponding to the KS, NW and R30 orientations.

Three OR for the (111) fcc / (110) bcc interface are basically predicted by the rigid-lattice theory: the Nishiyama-Wassermann (NW) [HEL98], the Kurdjumov-Sachs (KS) [HEL98], and the R30 [HOM87]. The orientations are given by the alignment of densely-packed rows in (111) fcc and (110) bcc and are most likely when the distances between the corresponding rows are close in the two crystals. The equality between d_{fcc} and d_{bcc} for the different possible OR leads to a criteria based on the ratio between nearest neighbor distances $r = x/y$ [PAI90] in the case of bcc on fcc (Figure 114).
These possible OR for a bcc (110) deposited on fcc (111) are gathered in Table 18 (with the corresponding values of the *r* parameter) and illustrated in Figure 115. The angle θ corresponds to the angle between [001] bcc and [1$\bar{1}$0] fcc [PAI90].

	In-plane orientation relationship	Distance between parallel atomic rows	Relative orientation (θ (°))	r parameter ($r = \frac{x}{y}$)
NW_x	bcc [001] // fcc [$1\bar{1}0$]	$\sqrt{\frac{2}{3}}x = \frac{\sqrt{3}}{2}y$	0	1.0607
NW_y	bcc [$1\bar{1}0$] // fcc [$11\bar{2}$]	$\frac{x}{\sqrt{3}} = \frac{y}{2}$	0	0.8661
KS	bcc [$1\bar{1}1$] // fcc [$1\bar{1}0$]	$\frac{2}{3}\sqrt{2}x = \frac{\sqrt{3}}{2}y$	5.26	0.9186
$R30_x$	bcc [001] // fcc [$11\bar{2}$]	$\frac{\sqrt{2}}{\sqrt{3}}x = \frac{y}{2}$	30	0.6123
$R30_y$	bcc [$1\bar{1}0$] // fcc [$1\bar{1}0$]	$\frac{x}{\sqrt{3}} = \frac{\sqrt{3}}{2}y$	30	1.5

*Table 18. Possible orientation relationships for a bcc (*110*) deposited on fcc (*111*) depending on the r parameter. The θ angle corresponds to the angle between [*001*] bcc and [*$1\bar{1}0$*] fcc.*

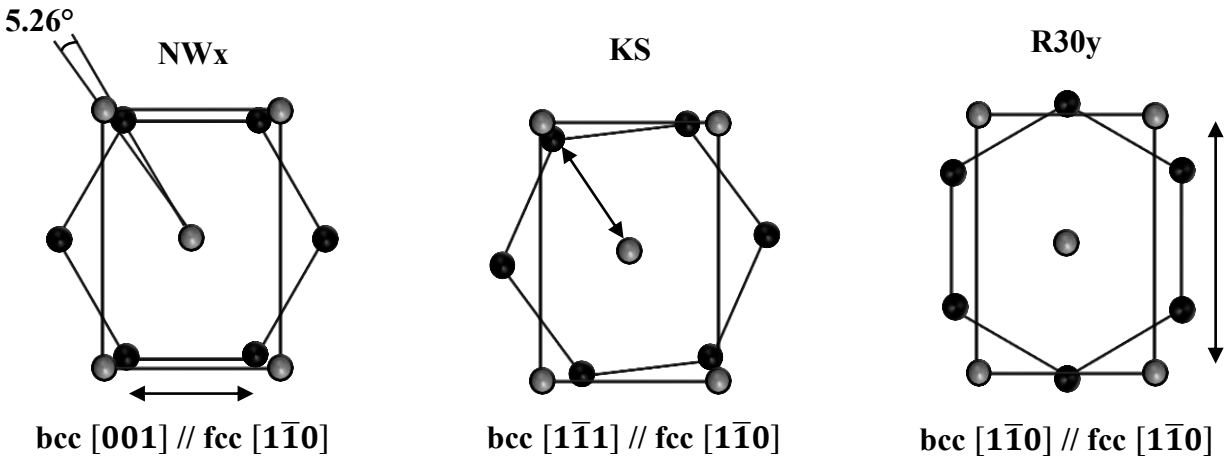

*Figure 115. Possible in-plane orientation relationships at the bcc (*110*) / fcc (*111*) interface. The double arrow represents the common direction between the two lattices.*

Given the hexagonal symmetry of the (111) fcc plane, those possible OR would most likely give rise to several domains for the (110) bcc crystal. The following paragraphs give complementary information on those equivalent domains and on the resulting in-plane directions that could be identified by RHEED analysis or X-ray φ scans.

Nishiyama-Wassermann growth

Three different orientations of (110) bcc can satisfy the NW-OR on (111) fcc (Figure 115). The corresponding domains (sketched with red, blue and green colors in Figure 116) are tilted by 60° from each other. The resulting succession of in-plane directions correspond to alternating $< 001 >$ and $< 1\bar{1}0 >$ directions separated by 30°, each being flanked at approximatively ± 5 ° by respectively $< 1\bar{1}1 >$ and $< 1\bar{1}3 >$ directions.

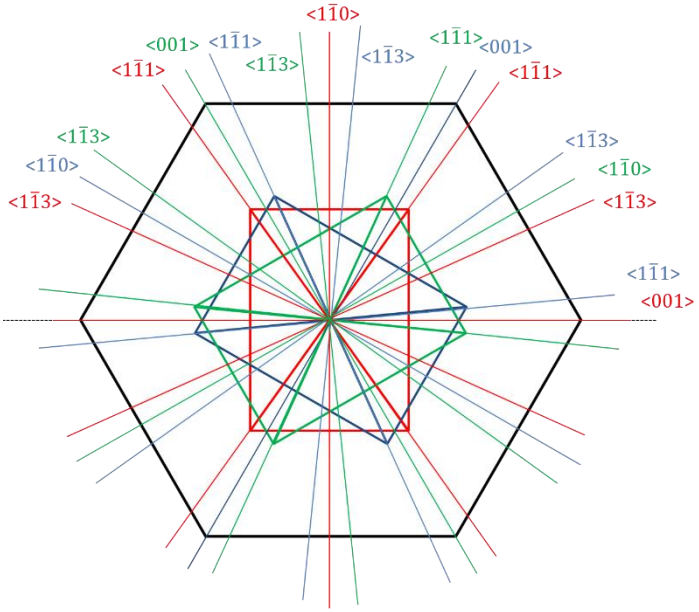

Figure 116. Schematic representation of the bcc in-plane directions when three (110) bcc domains (blue, red and green) grow on (111) fcc with NW-OR. The lattice parameters are not respected.

R30 growth

Three different orientation of (110) bcc can satisfy the R30-OR on (111) fcc (Figure 115). The corresponding domains (sketched with red, blue and green colors in Figure 117) are tilted by 60° from each other. As for the NW case, the resulting succession of in-plane directions correspond to alternating $< 001 >$ and $< 1\bar{1}0 >$ directions separated by 30°, each being flanked at approximatively ± 5 ° by respectively $< 1\bar{1}1 >$ and $< 1\bar{1}3 >$ directions.

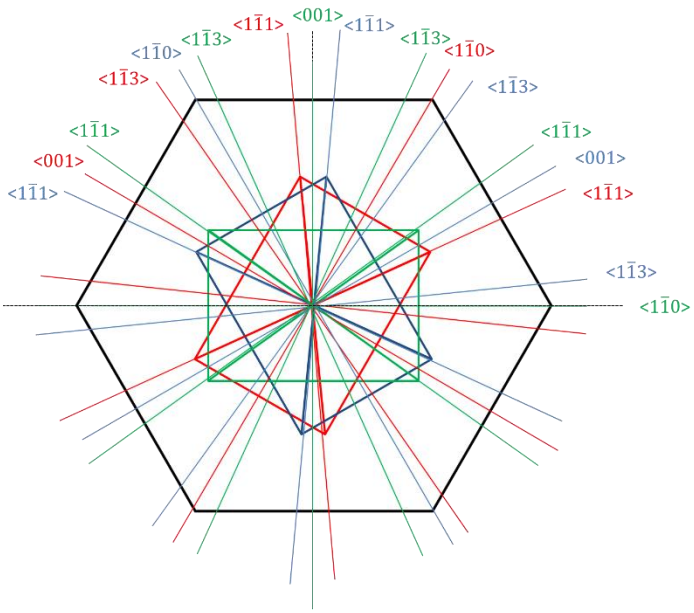

Figure 117. Schematic representation of the bcc in-plane directions when three (110) bcc domains (blue, red and green) grow on (111) fcc with R30-OR. The lattice parameters are not respected.

Kurdjumov-Sachs growth

In the case of the KS-OR, six different orientations of (110) bcc can stabilize (Figure 115). Two equivalent in-plane $< 1\bar{1}1 >$ bcc directions can namely align with each of the three equivalent in-plane $< 1\bar{1}0 >$ fcc direction. The resulting succession of in-plane directions is thus relatively complex, as sketched in Figure 118. One can nevertheless notice the succession of $< 1\bar{1}1 >/< 001 >/< 1\bar{1}1 >/< 001 >/< 1\bar{1}1 >$ and $< 1\bar{1}3 >/< 1\bar{1}0 >/< 1\bar{1}3 >/< 1\bar{1}0 >/< 1\bar{1}3 >$ (dotted ellipses in Figure 118). $< 1\bar{1}1 >$ and $< 1\bar{1}3 >$ directions at the center (in black in Figure 118) are associated to two different domains. They are aligned with the main directions of the (111) fcc surface and thus separated by 30°.

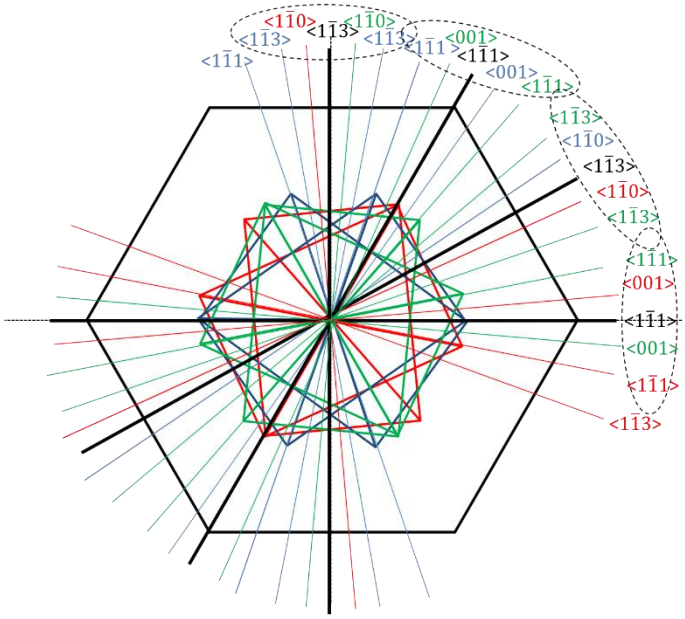

Figure 118. Schematic representation of the bcc in-plane directions when six (110) bcc domains grow on (111) fcc with KS-OR. The lattice parameters are not respected.

References

[HEL98] 0. Hellwig, K. Theis-Briihl, G. Wilhelmi, A. Stierle and H. Zabel, *Growth of fcc (111) on bcc (110): new type of epitaxial transition observed for Pd on Cr*, Surface Science. **398**, 379-385, (1998).
[HOM87] H. Homma, K. Y. Yang and I. K. Schuller, *Role of lattice matching in epitaxy: Novel Ce Phase and new fcc-bcc epitaxial relationship*, Phys. Rev. B**. 36**, 18, (1987).
[PAI90] S. M. Paik and I. K. Schuller, *New calculational method for epitaxial energy: Application to an axial commensurate interface*, Phys. Rev. Lett**. 64**, 16, (1990).

Appendix E: RHEED analysis

Equipment

The Reflection High-Energy Electron Diffraction (RHEED) setup installed on the MBE chamber is a Staib instrument. The electrons are emitted from a Tungsten filament heated up to 2500 °C. They are accelerated by a high voltage (30 kV, which corresponds to a wavelength of 0.00698 nm) and directed to the sample surface with an angle smaller than 1° (low penetration depth). The electrons then interact with the atoms of the surface. The diffracted beam is intercepted by a fluorescent screen. A CCD camera records the diffraction patterns that can be observed on a monitor. A dedicated software enables the analysis of these patterns: the measurement of diffracted intensity, of characteristic inter-streaks distances…

Brief elements on the theory of diffraction [MOU99]

In a periodic crystal, the positions of the lattice nodes are given by: $\vec{r_i} = m_1\vec{a} + m_2\vec{b} + m_3\vec{c}$
and the positions of the atoms respect to the lattice nodes are given by: $\overrightarrow{\rho_n} = u_n\vec{a} + v_n\vec{b} + w_n\vec{c}$
m_1, m_2 and m_3 are integers, $\vec{a}$, $\vec{b}$, $\vec{c}$ are the main vectors of the lattice, u_n, v_n and w_n are relative integers strictly smaller than 1.
For a scattering vector $\vec{q} = \vec{k} - \overrightarrow{k_0}$ ($\overrightarrow{k_0}$ and $\vec{k}$ represent respectively the wave vector of the incident wave and of the scattered wave) and a diffusion factor f_n, the amplitude scattered by the crystal is:

$$A(\vec{q}) = \sum_{i,n} f_n(\vec{q})\exp(i\vec{q}.(\overrightarrow{r_i} + \overrightarrow{\rho_n}))$$

where the sum is performed on all the atoms n and sites i of the lattice.
It is possible to separate the contribution of the elementary mesh and thus to define the structure factor $F(\vec{q})$ [HEH97]. The total scattered intensity is finally:

$$I(\vec{q}) = A(\vec{q})A^*(\vec{q}) = |F(\vec{q})|^2.\zeta(\vec{q})$$

with the structure factor: $F(\vec{q}) = \sum_n f_n(\vec{q})\exp(i\vec{q}.\overrightarrow{\rho_n})$

and the interference function: $\zeta(\vec{q}) = \frac{sin^2(\frac{N_1\vec{q}.\vec{a}}{2})}{sin^2(\frac{\vec{q}.\vec{a}}{2})}.\frac{sin^2(\frac{N_2\vec{q}.\vec{b}}{2})}{sin^2(\frac{\vec{q}.\vec{b}}{2})}.\frac{sin^2(\frac{N_3\vec{q}.\vec{c}}{2})}{sin^2(\frac{\vec{q}.\vec{c}}{2})}$

N_1a, N_2b and N_3c are the crystal dimensions.
The interference function is a periodic function of the reciprocal lattice vectors. It is maximal when the scattering vector is a vector of this reciprocal lattice, which constitutes the Laue conditions:

$$\vec{q}.\vec{a} = 2\pi h$$
$$\vec{q}.\vec{b} = 2\pi k$$
$$\vec{q}.\vec{c} = 2\pi l$$

where h, k and l are integers.
For a surface ($N_3 = 1$), the third factor of the interference function is equal to 1. The Laue conditions are reduced to those relative to $\vec{a}$ and $\vec{b}$, with constant interference function along $\vec{c}$. The reciprocal lattice consists of rods perpendicular to the surface, as it is sketched in Figure 119.
The obtained diffraction pattern is the intersection of the reciprocal lattice and the Ewald sphere, centered at the origin of the reciprocal lattice and with radius $\left|\overrightarrow{k_0}\right| = \left|\vec{k}\right| = \frac{2\pi}{\lambda}$. For a perfectly monochromatic electronic beam and an ideal surface, the diffraction pattern should be constituted of points (Figure 119). In real cases, the beam is not perfectly monochromatic which yields a finite thickness of the Ewald sphere, the radius of which is moreover much larger than reciprocal lattice

parameters. The reciprocal space rods are thus almost tangent to the Ewald sphere and the resulting diffraction pattern is constituted of streaks.

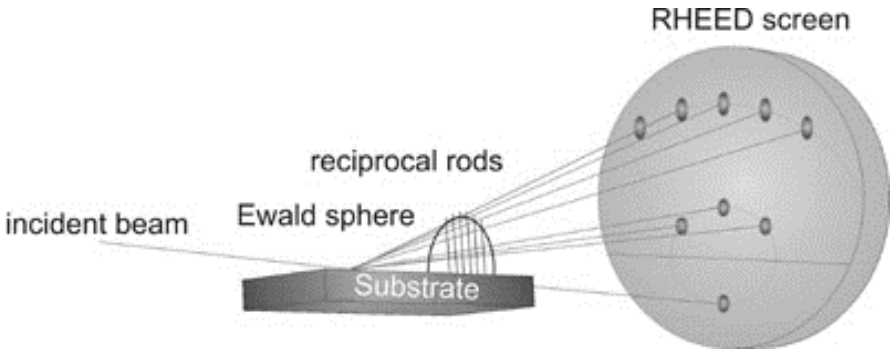

Figure 119. RHEED diffraction by a perfect surface.

RHEED diffractions patterns

Depending on the various deposition parameters (temperature, rate, thickness, substrate…), a deposited layer may exhibit different types of atomic order: single crystalline, polycrystalline or even amorphous. Corresponding RHEED diffraction patterns are drastically different and thus bring relevant information on the structural quality of the film and on the parameters that have to be controlled to optimize this quality:
(i) A high diffuse background without clear diffraction pattern reveals an amorphous layer.
(ii) The presence of rings (observed for all azimuthal angles) reveals a polycrystalline film. The detailed analysis of the diffracted rings can give information on a possible texture axis.
(iii) Streaks patterns observed for specific azimuthal angles are characteristic of a smooth crystalline surface. The analysis of those azimuthal angles and corresponding diffraction patterns permits to determine the surface reciprocal lattice, as it is shown in the following paragraph. One can deduce the surface symmetry and lattice constants; these can be interestingly compared to the substrate's and bulk material's ones in order to investigate epitaxial relationships and possible lattice strains.
More or less elongated dots (or dotted lines) may arise in the presence of islands that give rise to a 3D diffraction process (the electron beam is transmitted though islands). Dots are thus generally indicative of a rough surface.

In practice, a mixture of these different cases can be also observed: RHEED patterns with a high diffuse background, streaks more or less clear, rings more or less visible…

Example of RHEED pattern indexation

The Figure 120 presents an example of the RHEED patterns collected along two perpendicular azimuths of the LNO Z-cut surface. Each of these patterns is observed with a six-fold symmetry, *i.e.* when the sample is rotated by 60°.
The symmetry reveals the hexagonal surface lattice and inter-streaks distances, related to the distances in the reciprocal lattice, permit to orientate the surface lattice. When the incident electron beam is parallel to a $< 11\bar{2}0 >$ direction, the inter-streaks distance is inversely proportional to distance between these atomic rows, *i.e.* $a\frac{\sqrt{3}}{2}$. When the incident electron beam is parallel to a $< 1\bar{1}00 >$ direction, the inter-streaks distance is inversely proportional to distance between these atomic rows, *i.e.* $\frac{a}{2}$. One can easily check the $\sqrt{3}$ ratio between the inter-streaks distances measured along the two azimuths.

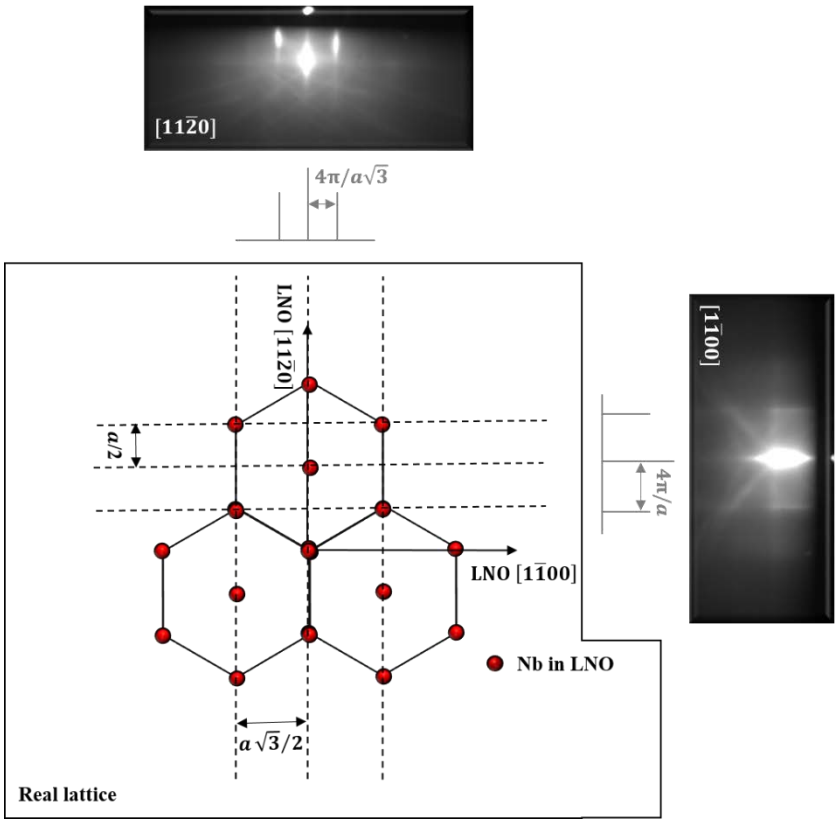

Figure 120. Surface hexagonal lattice for a LNO Z-cut surface and associated RHEED patterns observed along two perpendicular azimuths. The lattice parameters between real and reciprocal space are not respected.

RHEED pattern from a stepped surface

The case of stepped surfaces is interesting to be recalled here since LNO substrates with 128Y and 41Y -cuts do not correspond to high symmetry surface planes as it is the case for LNOZ. These surfaces, as well as those obtained after a material deposit grown on these surfaces, may thus give rise to patterns specific of stepped surfaces.
A stepped surface is sketched in Figure 121 (a). In this case, atomic planes (with an in-plane a lattice constant) are tilted by an angle α respect to the macroscopic surface. They are separated by steps of height x, which give rise to a surface periodicity (between step edges): $D = \frac{x}{\sin(\alpha)}$.

Such stepped surfaces possess two reciprocal lattices, one from the periodicity of the atoms on the terraces (a) and a second from the periodic arrangement of steps (D) [MIL82, HOT77]. Those two sets of reciprocal rods may have different broadness, depending on the size of terraces. The resulting diffraction pattern corresponds to the intersection of both reciprocal lattices with the Ewald sphere.
A simple sketch is given in Figure 121 (b), where the resulting pattern appears as tilted rows of dots. The distance between the spots on a same line is related to the distance x (steps' height) on the real surface, while the angle between the spot rows and the vertical direction corresponds to the angle between atomic planes and the macroscopic surface.

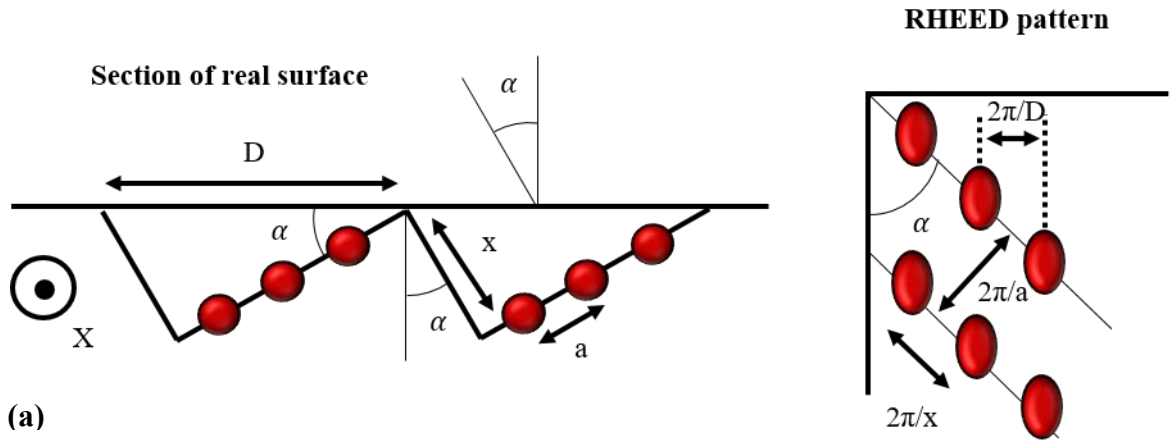

Figure 121. Sketch of a RHEED pattern (b) obtained from a stepped surface (a).

References

[HEH97] M. Hehn, *Elaboration, étude des propriétés structurales et magnétiques de couches et réseaux de plots submicroniques à base de Cobalt*, PhD dissertation, Université Louis Pasteur, Strasbourg, (1997).
[HOT77] F. Hottier and J. B. Theeten, *Comparative LEED and RHEED examination of stepped surfaces: Application to Cu (111) and GaAs (001) vicinal surfaces*, Surface Science**. 65**, 563-577, (1977).
[MIL82] R. H. Milne, *Investigation of stepped copper surfaces by RHEED*, Surface Science**. 122**, 474-490, (1982).
[MOU99] A. Mougin, *Nanosystèmes magnétostrictifs de $TRFe_2$ (110) (TR=terre rare): croissance, morphologie et propriétés magnétiques*, PhD dissertation, Université H. Poincaré, Nancy, (1999).

Appendix F: Magnetic stripes / Exchange bias phenomenon

Magnetic stripe domains: a particular domain state in samples with perpendicular magnetization

Since the improvement of ionic thinning and ultrahigh vacuum deposition techniques, it has been possible to study the evolution of the domain structure as a function of the thickness of a thin film. A large variety of magnetic configurations was evidenced depending on the thickness of the thin magnetic layer. They are represented in Figure 122 for a typical magnetic thin film with a perpendicular anisotropy.

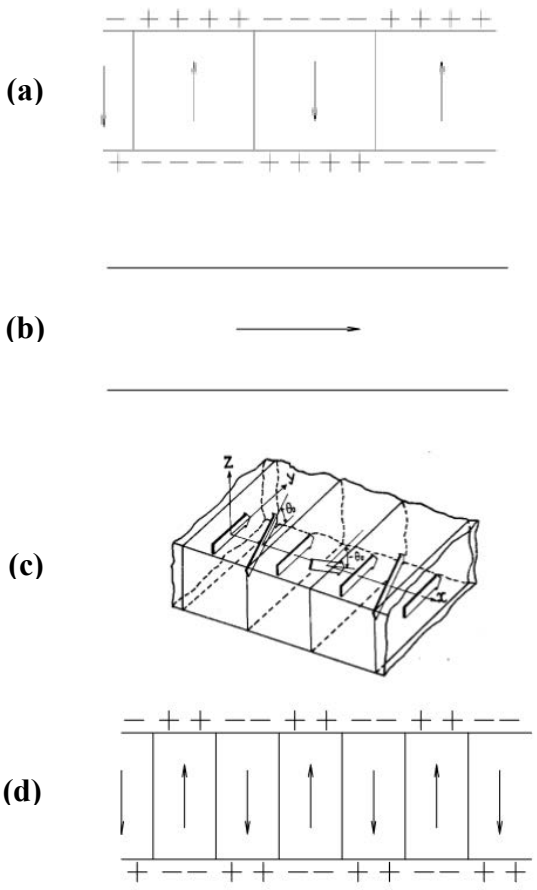

Figure 122. Evolution of the magnetization distribution in a magnetic thin film with perpendicular anisotropy as a function of the film thickness. Typical configurations observed for a Co layer: from 0 to several atomic planes (a), from several atomic planes to 20 nm (b), from 20 nm to 30 nm (c) and from 30 nm to several microns (d) [HEH97].

When the film thickness ranges between zero and several atomic planes, it is possible to get a state with perpendicular magnetization with extended domains or a single domain state. In this thickness range, the magnetization is oriented perpendicular to the layer because of the perpendicular anisotropy (Figure 122 (a)). When the thickness increases and exceeds several nanometers, the perpendicular anisotropy is no longer large enough to overcome the shape anisotropy and to maintain the magnetization perpendicular to the plane of the layer: the magnetization is reoriented in the plane of the layer

(Figure 122 (b)). The domain structure then consists of large in-plane magnetized domains of a few micrometers in diameter. By increasing the thickness further, the magnetization starts to oscillate out of the plane in a periodic manner to save part of the perpendicular anisotropy energy and reduce the demagnetizing field. While most of the magnetization remains in the plane of the layer, a small perpendicular component of magnetization is created in the form of bands with alternately positive and negative components of magnetization perpendicular to film plane (Figure 122 (c)). Saito [SAI64] predicted that the domain structure is transformed into a weak stripe structure for magnetic films with perpendicular anisotropy whose thickness is larger than:

$$h_1 \approx 27\left(\frac{8}{\pi^2}\right)^2 \sqrt{\frac{A{M_s}^4}{K^3}}$$

where K is the magnetocrystalline anisotropy constant, A is the exchange constant and M_s the saturation magnetization

When the thickness of the layer reaches [HEH97, KIT46]:

$$h_2 \approx 6.8\sigma_w\left(\frac{M_s}{K}\right)^2$$

where σ_w corresponds to the wall surface energy (180° Bloch walls in this case) and can be expressed as $\sigma_w = 4\sqrt{AK}$, the weak stripe structure transforms into a strong stripes structure, where the magnetization is totally out of the plane at the center of each magnetic stripes stabilized by an in-plane component on each wall (Figure 122 (d)).

The presence of strong stripes induces a particular and characteristic variation of magnetization versus a magnetic field applied perpendicular to film plane. As exposed in Figure 123 for a 200 nm thick Ni layer deposited on LNO 41 Y-cut, the variation of magnetization is linear with applied field, which is often attributed to a hard axis of magnetization. However, the hysteresis that appears close to the saturation is characteristic of the stripe domains nucleation. Starting the cycle from positive saturation (i), a slight decrease of the magnetization occurs due to the transformation of residual magnetic bubbles that were not eliminated during the field sweep to its maximum. As the applied field decreases (ii), the radius of the residual bubbles increases to reach a critical radius at the nucleation field H_n for which the bubbles are subjected to elliptical deformation (iii). Bubbles then deform into short stripes, which results in a jump in the magnetization curve. When the magnetic field decreases, stripes tend to grow by displacement of the walls resulting in a quasi-linear variation of the magnetization as a function of the applied field (iv). The demagnetizing field tends to stabilize the domain structure by opposing a magnetic pressure to the applied field and therefore stabilizes the stripe domains with a remanent magnetization close to zero at zero applied field. For negative applied fields, short stripes connect themselves to give rise to short stripes with an opposite magnetization sense by a process of wall propagation (v, vi and vii). These short stripes are transformed into cylindrical and residual bubbles when the applied field exceeds –Hs (viii).

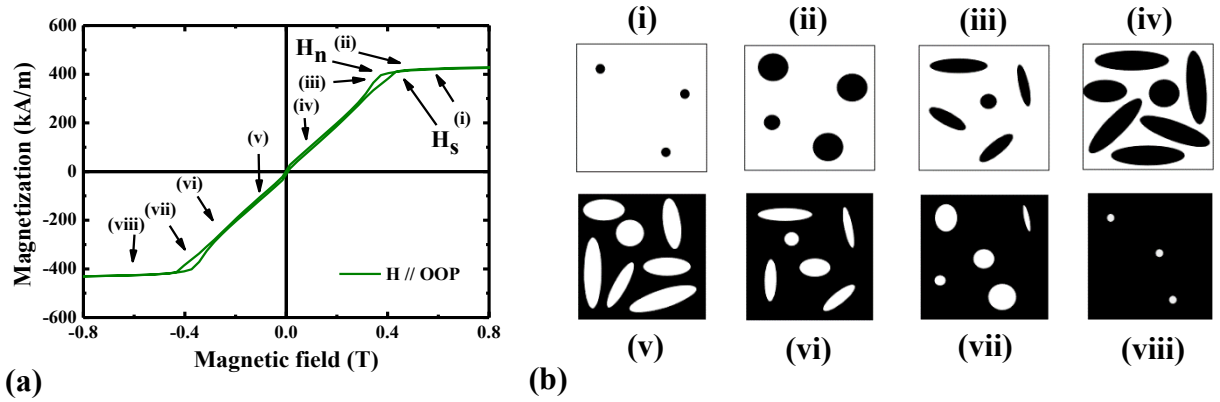

Figure 123. Hysteresis loop with the magnetic field applied perpendicular to the sample plane of 200 nm thick Nickel film deposited on LNO 41 Y-cut (a). Expected magnetic configurations at different stages of the hysteresis loop (magnetization "up" and "down" in black and white respectively) (b) [HEH97].

Several models can describe the evolution of the nucleation field (H_n) or perpendicular saturation field ($H_{s,OOP}$) with the thickness of the magnetic film. In our case, we will use a theory related to domains in the form of bubbles (the state close to saturation). Near saturation, the bubbles are far from each other and are considered independent, which jusitifes a description according to Thiele's model [THI71]. These fields can thus be written as:

$$H_{s,OOP} = 4\pi M_s \left(1 - 1.596 \sqrt{\frac{\sigma_w}{4\pi {M_s}^2 h}}\right)$$

$$H_n = 4\pi M_s \left(1 - 2.66 \sqrt{\frac{\sigma_w}{4\pi {M_s}^2 h}}\right)$$

where h is the thickness of the ferromagnetic film.

Exchange bias phenomenon

Let's consider a bilayer made of a ferromagnetic (FM) thin layer in contact with an antiferromagnetic (AFM) thin layer such that the Néel temperature T_N (416 °C for $Ir_{0.2}Mn_{0.8}$ [NOG99]) of the AFM is lower than the Curie temperature T_C (1086 °C for Co [MAL04]) of the FM. When the bilayer is cooled through T_N with an applied field to saturate and orientate the magnetization of the FM layer, an exchange bias and thus unidirectional anisotropy are induced in the FM layer. The hysteresis loop of the FM material is shifted from zero field, generally in the direction opposite to the cooling field (Figure 124).

The phenomenon of exchange bias can be qualitatively understood by assuming an exchange interaction at the FM/AFM interface. When a field is applied in the temperature range $T_N < T < T_C$, the FM spins line up with the field, while the AFM spins remain random (Figure 124). When cooling to $T < T_N$ in the presence of a magnetic field, the spins of the first monolayer of the AFM next to the FM align ferromagnetically (or antiferromagnetically) to those of the FM (assuming interface interaction). The next monolayer of the antiferromagnet will have to align antiparallel to the previous layer as to complete the AFM order, and so on.
For $T < T_N$ and by considering that all materials react in a single domain state, the hysteresis loop of Figure 124 can be described as the following: starting from negative applied field, the FM magnetization is first saturated and negative (i). For positive fields, the FM spins start to reverse (ii). However, for sufficiently large AFM anisotropy, the AFM spins remain unchanged. Therefore, the interfacial interaction between the FM and AFM spins at the interface tries to align the FM spins with the AFM spins at the interface. In other words, the AFM spins at the interface exert an additional force on the FM spins to keep them in their original position. Therefore, the FM spins have one single stable configuration. The field required to reverse completely the FM layer will be larger if it is in contact with an AFM, because an extra field is needed to overcome the additional energy (iii). When the field is decreased back, the FM spins will on the contrary start to reverse at a smaller field, due to the interaction with the AFM spins, which now exert a torque in the other direction (iv). Thus, the uniaxial anisotropy has one favored sense, *i.e.* it is unidirectional.

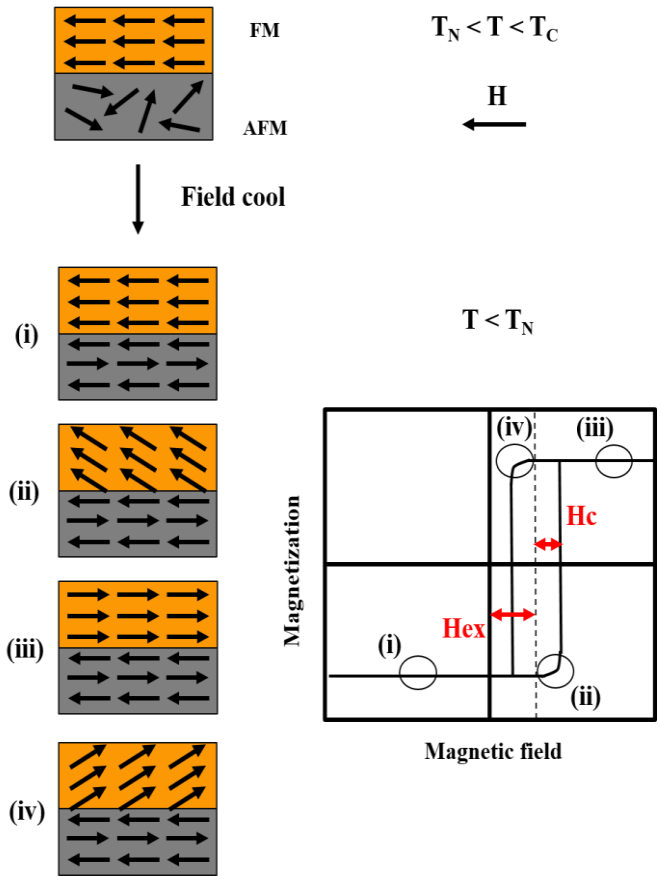

Figure 124. Naïve view of the spin configuration in a FM/AFM bilayer before (top sketch) and after field cooling (i) and at different stages of an hysteresis loop (i) to (iv). In this case, the exchange coupling is positive and the system has been field-cooled in a negative field.

On this figure, H_{ex} is the exchange field resulting from the exchange coupling $J_{FM/AFM}$ at the interface between FM and AFM layers. The exchange field can be written as:

$$H_{ex} = -\frac{J_{FM/AFM}}{Ms_{FM}t_{FM}}$$

where $J_{FM/AFM}$ depends strongly on the materials, roughness, crystallographic orientation as well as the texture. $J_{FM/AFM}$ = 1×10^{-4} J.m^{-2} in [Co(5nm)/$Ir_{0.2}Mn_{0.8}$(5nm)] multilayers and Ms_{FM} = 1420 kA.m^{-1} for Co [MAL04]. t_{FM} represents the thickness of the ferromagnetic layer. The dependence on $1/t_{FM}$ emphasizes the fact that it is mainly an interfacial phenomenon. With [Co(5nm)/$Ir_{0.2}Mn_{0.8}$(5nm)] multilayers, an exchange field of approximatively 15 mT is expected. With this formula, it can be seen that the use of multilayers (repeatability) and thin layers should maximize the exchange field. An important remark concerns the sign of the exchange field. The ferromagnetic reversal can be shifted towards positive or negative fields depending on the sense of the cooling field but also on the sign of the interface exchange constant (often positive).

The exchange bias vanishes above a temperature denoted as the blocking temperature T_B (between 126 °C and 246 °C for $Ir_{0.2}Mn_{0.8}$ [NOG99]) that can be in some cases much lower than the bulk T_N. The origin of this effect is partly related to the grain size and thickness of the AFM layer, through finite size effects. In other words, AFM films with large grains tend to have $T_B \approx T_N$, while systems with very thin films have $T_B < T_N$. The sketch previously shown in Figure 124 is thus partially true. In the case where $T_B < T < T_N$, there is no exchange bias but just a change in the coercive field.

References

[HEH97] M. Hehn, *Elaboration, étude des propriétés structurales et magnétiques de couches et réseaux de plots submicroniques à base de Cobalt*, PhD dissertation, Université Louis Pasteur, Strasbourg, (1997).
[KIT46] C. Kittel, *Theory of the structure of ferromagnetic domains in films and small particles*, Phys. Rev. **70**, 965, (1946).
[MAL04] G. Malinowski, *Transport dépendant du spin et couplage d'échange : de la jonction tunnel au capteur magnétique intégré*, PhD dissertation, Université H. Poincaré, Nancy, (2004).
[NOG99] J. Nogués and I. K. Schuller, *Exchange bias*, J. Mag. and Magn. Mat**. 192**, 203-232, (1999).
[SAI64] N. Saito, H. Fujiwara and Y. Sugita, *A New Type of Magnetic Domain Structure in Negative Magnetostriction Ni-Fe Films*, J. Phys. Soc. Japan. **19**, 1116, (1964).
[THI71] A. A. Thiele, A. H. Bobeck, E. Della Torre and U. F. Gianola, *The energy and general translation of cylindrical magnetic domains*, Bell Syst. Tech. Journal**. 50**, 711, (1971).

Croissance de systèmes hybrides piézoélectriques/magnétostrictifs pour des capteurs magnétiques à ondes acoustiques de surface en géométrie de résonateurs

Le développement de matériaux avec différents ordres ferroïques couplés (multiferroïques) motive d'intenses activités de recherche. Une combinaison particulièrement intéressante est celle des paramètres d'ordre magnétique et électrique qui, dans le cas favorable où ceux-ci sont couplés, ouvre la voie au contrôle électrique de l'aimantation. Celui-ci peut être envisagé via la manipulation de la polarisation d'un ferroélectrique ou des déformations d'un piézoélectrique Les propriétés du matériau ferroélectrique/piézoélectrique peuvent être inversement modifiées par l'état d'aimantation, ce qui laisse envisager des applications dans le domaine des capteurs de champs magnétiques. Ce travail s'inscrit dans l'étude de systèmes piézoélectrique/magnétostrictif, avec un intérêt spécifique porté à l'influence de l'aimantation sur les ondes acoustiques de surface (SAW) générées dans le dispositif. Nous avons ainsi déposé des couches polycristallines de Ni, des multicouches [Co/IrMn], ainsi que des couches épitaxiées de $TbFe_2$ sur des substrats de Niobate de Lithium (LNO) de différentes orientations. Sur LNO Z-cut, la croissance de $TbFe_2$ est réalisée en utilisant différentes couches tampons simples ou doubles qui permettent d'obtenir des directions de croissance [111] ou [110] avec des anisotropies magnétiques respectivement perpendiculaire et planaire. Sur des substrats de coupe 128Y et 41Y, la croissance s'avère beaucoup plus complexe mais il est néanmoins possible d'obtenir un film cristallisé de $TbFe_2$ multidomaines avec des relations d'orientation 3D similaires à celles obtenus sur LNO Z-cut, que ce soit entre la couche magnétique et la couche tampon, ou entre la couche tampon et le substrat. Des dispositifs magnétiques à ondes acoustiques de surface (MSAW) ont été ensuite fabriqués dans une géométrie de résonateur permettant une interrogation à distance aisée. La fréquence de résonance des dispositifs MSAW est sensible à l'application d'un champ magnétique externe, via des effets statiques liés à l'orientation de l'aimantation sous champ et via des effets dynamiques d'origine magnétoélastique liés à l'excitation acoustique. Nous avons examiné les réponses magnéto-acoustiques des différents dispositifs, en corrélation étroite avec les propriétés magnétiques statiques, en particulier l'anisotropie, la coercivité et l'hystérèse. Un modèle piézomagnétique équivalent a été utilisé pour simuler certaines de ces réponses. De manière générale, nous montrons qu'un choix judicieux du matériau magnétique et le contrôle de ses propriétés permettent d'élaborer des capteurs spécifiques : un matériau magnétique doux permet de contrôler l'anisotropie de la réponse acoustique via la forme des IDT; un matériau magnétique dur ouvre la voie au développement de capteurs de forts champs magnétiques; un système à anisotropie d'échange dont on peut contrôler la réversibilité de la réponse magnétique permet d'envisager un capteur de champ magnétique hors plan.

Growth of hybrid piezoelectric/magnetostrictive systems for magnetic devices based on surface acoustic wave resonators

The development of materials with different coupled ferroic orders (multiferroics) drives an intense research activity. A particularly interesting combination is the case where magnetic and electrical orders are simultaneously present, which, in the favorable case where these are coupled, opens the way to the electrical control of magnetization. This can be achieved in manipulating the polarization in a ferroelectric or the strains in a piezoelectric compound. Ferroelectric or piezoelectric properties can inversely be influenced by the magnetic state, an interesting feature for the development of magnetic field sensors. This work aims in the investigation of piezoelectric/magnetostrictive systems, more especially in the role of the magnetization and of the magnetization versus field behavior on the surface acoustic waves (SAW). Polycristalline Ni films, [Co/IrMn] multilayers and epitaxial $TbFe_2$ films have been deposited on Lithium Niobate (LNO) substrates of different orientations. On LNO Z-cut, various single or double buffer layers have been used to achieve the $TbFe_2$ epitaxial growth, along either [111] or [110] directions and with either perpendicular or in-plane magnetic anisotropy. On LNO 128Y and 41Y substrates, the growth is more complex but it is nevertheless possible to obtain crystalline multidomains $TbFe_2$ films with 3D orientation relationships similar to those obtained on LNO Z-cut, both between the magnetic and the buffer layers, and between the buffer layer and the substrate. Magnetic surface acoustic wave (MSAW) devices have been patterned in a resonator geometry that enables an easy wireless interrogation. The MSAW device resonance frequency is sensitive to an external magnetic field, both via static effects related to the field-induced magnetization changes, and via magnetoelastic dynamic effects related to the acoustic excitation. We have investigated the MSAW magneto acoustic responses of the various devices in close connection with the static magnetic properties, especially the anisotropy, the coercivity and the hysteresis. An equivalent piezomagnetic model could support some of these observations. We show more generally that the proper choice of magnetic material and the control of the magnetic properties helps to build up specific sensors: soft magnetic materials enable to tailor the anisotropy of the MSAW response by engineering the IDT's shape; hard magnetic materials enable to achieve high field unipolar or bipolar field response; exchange-biased systems in which the reversibility of the magnetic response is achieved let envision the development of sensors for out-of-plane magnetic fields.